Continuous Processing and Analysis of Synthetic Aperture Radar Interferometry Data to Support Deformation Monitoring

---

Madeline Stefania Evers

Doctoral Thesis
Karlsruhe, 2025

Continuous Processing and Analysis of Synthetic Aperture Radar Interferometry Data to Support Deformation Monitoring

Zur Erlangung des akademischen Grades einer

DOKTORIN DER INGENIEURWISSENSCHAFTEN (Dr.-Ing.)

von der KIT-Fakultät für
Bauingenieur-, Geo- und Umweltwissenschaften
des Karlsruher Instituts für Technologie (KIT)

genehmigte

DISSERTATION

von

Madeline Stefania Evers
aus Paderborn

Tag der mündlichen Prüfung:	14.11.2025
Referent:	Prof. Dr.-Ing. Stefan Hinz Institut für Photogrammetrie und Fernerkundung Karlsruher Institut für Technologie
Korreferent:	Prof. Dr.-Ing. Franz J. Meyer Geophysical Institute & Alaska Satellite Facility University of Alaska Fairbanks

Karlsruhe (2025)

Madeline Stefania Evers
Continuous Processing and Analysis of Synthetic Aperture Radar Interferometry Data to Support Deformation Monitoring
Doctoral Thesis
Date of examination: 14.11.2025
Referees:
Prof. Dr.-Ing. Stefan Hinz
Prof. Dr.-Ing. Franz J. Meyer

Karlsruhe Institute of Technology
Department of Civil Engineering, Geo and Environmental Sciences
Institute of Photogrammetry and Remote Sensing
Kaiserstr. 12
76131 Karlsruhe

Abstract

Monitoring the surface deformation of large infrastructure elements, such as dams, is part of assessing their structural health. Unexpected surface deformation or a change in the temporal pattern of the deformation can indicate either structural damage to the infrastructure element itself or a nearby ground surface deformation phenomenon, which in turn can damage the infrastructure element. Hence, regular analysis of their surface displacement is a crucial task.

Persistent Scatterer Interferometry (PSI) is a remote sensing technique well-suited for monitoring the surface deformation of large infrastructure elements and thus, contributes to assessing their structural health. The technique exploits the phase of Synthetic Aperture Radar (SAR) images to estimate surface displacement rates. The technique has several strong suits. One, it is capable of providing ground surface deformation datasets with an accuracy of submillimeter for the TerraSAR-X (TSX) sensors and millimeter for the Sentinel-1 (S1) sensors for displacement rates in the line-of-sight of the sensor. Second, it can be utilized without any personnel or sensors on site. Third, under favorable conditions, a dense grid of measuring points is far more achievable than it is using the Global Navigation Satellite System. Additionally, the launch of the S1 satellites has provided users with a steady stream of SAR images, which has promoted recent developments in the field to shift from analyzing a distinct time span to continuously updating ground surface deformation datasets with new incoming data. However, frequent processing of a continuously expanding dataset presents challenges concerning both the PSI processing itself and the systematic analysis of the resulting ground surface deformation data.

Concerning the PSI processing itself, a continuously expanding dataset raises questions regarding persistent scatterer density, processing efficiency, and the comparability of results from different updates. Within the scope of this thesis, three different strategies to continuously process a steady stream of SAR images with PSI are presented and evaluated. The first strategy is to always process all available SAR images, i.e., a growing dataset. The second strategy is to process the steady stream of SAR images in consecutive non-overlapping subsets, and the third strategy is to use overlapping consecutive subsets, similar to a sliding-window. In order to take full advantage of the possibility to re-use intermediate results given by the third strategy, the PSISlider processing chain was implemented. The strategies are evaluated and compared to each other based on key processing parameters. It could be concluded that the third strategy is the approach best-suited for processing a steady stream of SAR images for monitoring tasks. It provides a relatively constant number of PS, while keeping the processing time and needed hard disk space limited. Additionally, the strategy allows for quickly paced updates and ensures comparability of intermediate

results.

Additionally, a need for automatic post-processing procedures to extract relevant information on the temporal pattern of ground surface deformation datasets was identified. The often used mean deformation velocity maps, neglect any acceleration, deceleration or periodic behavior of deformation phenomena and thus, can be misleading. Therefore, the post-processing tool PSDefoPAT® was designed to extract the underlying time series model in the displacement time series resulting from advanced DInSAR processing. The tool assigns each displacement time series a best-fitting time series model using a sequence of statistical tests. Additionally, a standardized visualization of the PSDefoPAT® results was designed to facilitate an easy interpretation of the results. The capabilities of the tool were tested and demonstrated on synthetic and real displacement time series.

Further, challenges that can arise from tailoring a monitoring system for a specific large infrastructure element were addressed. Monitoring large infrastructure elements, such as dams, can lead to a need for data that has a wide coverage and a high spatial resolution. This demand can only be met using two sets of SAR images. For example, S1 SAR images that fulfill the requirement of wide coverage and high-resolution TSX SAR images that fulfill the requirement of high spatial resolution. However, their different spatial resolution and wavelengths make the datasets unequally complex to process. The two processing steps affected the most by this are the PS selection and the phase unwrapping process. It is suggested to combine different selection criteria so that they complement each other. Applying this approach to a TSX SAR time series, mapping the deformation of the Parapeiros-Peiros Dam, increased the number of PS and with that effectively closed significant gaps on the dam body, which prevented the mapping of its surface deformation. As for phase unwrapping, the process can be supported by reconstructing an idealized deformation-induced phase based on displacement time series models extracted with PSDefoPAT® from a simpler-to-process dataset. Applying the approach to a complex-to-process dataset resulted in an improvement of the displacement time series.

All three aspects contribute to moving forward from only analyzing a distinct time span to continuously updating ground surface deformation datasets with new incoming data in the context of infrastructure monitoring with PSI. Additionally, they also address a systematic approach to post-processing to extract relevant information.

Kurzfassung

Die Überwachung von Oberflächendeformationen großer Infrastrukturelemente, wie z.B. die Absperrwerke von Talsperren, ist Bestandteil der Beurteilung ihrer strukturellen Integrität. Unerwartete Oberflächendeformationen oder eine Veränderung in ihrem zeitlichen Verhalten kann als Indikator für einen strukturellen Schaden oder eine Bodendeformation, die die Infrastrukturelemente beschädigt, dienen. Aufgrund dessen ist eine regelmäßige Beurteilung der strukturellen Integrität eine entscheidende Aufgabe. Persistent Scatterer Interferometry (PSI) ist eine Methode der Fernerkundung, die sich zur Überwachung der Oberflächendeformationen großer Infrastrukturelemente gut eignet. Die Methode bestimmt aus der Phaseninformation von Synthetic Aperture Radar (SAR)-Aufnahmen die Oberflächendeformation. Eine Stärke der Methode ist, dass sie die Oberflächendeformation in Blickrichtung des Sensors mit einer Genauigkeit im Bereich von Submillimetern für die TerraSAR-X (TSX) Sensoren und im Bereich von Millimetern für die Sentinel-1 (S1) Sensoren bestimmen kann. Eine weitere Stärke ist, dass weder Personal vor Ort noch das Anbringen von Sensoren notwendig sind. Außerdem ist es mit PSI erheblich einfacher, unter günstigen Bedingungen ein enges Messpunktnetz bereitzustellen als mit Global Navigation Satellite System Stationen. Mit dem Start der S1-Mission kommt noch hinzu, dass dem Nutzer eine kontinuierliche Abfolge von SAR-Aufnahmen weltweit zur Verfügung steht. Dies hat die Entwicklung zu einer kontinuierlichen Auswertung eines sich regelmäßig aktualisierenden Datensatzes maßgeblich unterstützt. In diesem Zusammenhang ergeben sich einige Fragen bezüglich der eigentlichen Prozessierung und der systematischen Analyse der berechneten Oberflächendeformationsdatensätze.

Die PSI-Prozessierung eines sich stetig erweiternden Datensatzes wirft Fragen bezüglich der Persistent Scatterer (PS)-Dichte, der Effizienz und Vergleichbarkeit der Ergebnisse der jeweiligen Aktualisierungen auf. Im Rahmen dieser Arbeit werden drei unterschiedliche Strategien zur kontinuierlichen Verarbeitung eines sich stetig erweiternden Datensatzes mittels PSI vorgestellt und evaluiert. Die erste Strategie beinhaltet die kontinuierliche Prozessierung aller zur Verfügung stehenden SAR-Aufnahmen bei jeder Aktualisierung. Mit der zweiten Strategie wird der Ansatz verfolgt, die SAR-Aufnahmen in aufeinanderfolgenden sich zeitlich nicht überlappenden Teildatensätzen zu prozessieren. Die dritte Strategie berücksichtigt bei der Prozessierung aufeinanderfolgende sich zeitlich überlappende Teildatensätze, in Anlehnung an das Sliding-Window-Prinzip. Damit die im Rahmen der dritten Strategie bestehenden Möglichkeiten zur Wiederverwendung von Zwischenergebnissen vollständig ausgenutzt werden können, wurde die PSISlider-Prozessierungskette entwickelt. Die Strategien wurden bezüglich, für die Prozessierung relevanter, Schlüsselparameter ausgewertet und einander gegenübergestellt. Es wurde festgestellt, dass die

dritte Strategie am besten geeignet ist zur kontinuierlichen Verarbeitung eines sich stetig erweiternden Datensatzeses. Die Strategie ermöglicht eine relativ stabile PS Anzahl und benötigt eine begrenzte Prozessierungszeit und begrenzten Speicherplatz. Zusätzlich bietet die Strategie die Möglichkeit eng aufeinanderfolgende Aktualisierungen zu liefern und die Zwischenergebnisse zu vergleichen.

Im Weiteren wurde die Notwendigkeit für automatisierte Post-Prozessierungsverfahren zur Extraktion relevanter Informationen aus Oberflächendeformationsdatensätzen identifiziert. Die häufig genutzten Karten der mittleren Geschwindigkeit berücksichtigen weder eine Beschleunigung oder Entschleunigung noch ein periodisches Verhalten der Deformationsphänomene, was zu Fehleinschätzungen führen kann. Aus diesem Grund wurde das Persistent Scatterer Deformation Pattern Analysis Tool (PSDefoPAT®) entwickelt, um zeitliche Muster in Versatzzeitreihen zu erkennen. PSDefoPAT® weist jeder Versatzzeitreihe basierend auf statistischen Tests ein best-fitting Zeitreihenmodell zu. Zusätzlich wurde eine standardisierte Visualisierung der Ergebnisse entwickelt, um die Interpretation zu vereinfachen. Außerdem erfolgte der Test des Tools PSDefoPAT® auf simulierten und realen Versatzzeitreihen.

Der dritte Aspekt bezieht sich auf die Anpassung des Überwachungssystems an ein spezielles Objekt oder eine Region. Zur Überwachung großer Infrastrukturelemente, wie z.B. einer Talsperre, sind Daten notwendig, die eine gute räumliche Abdeckung und Auflösung aufweisen. Dies ist nur mittels zweier SAR-Datensätze umsetzbar. Daten der S1-Satelliten erfüllen beispielsweise die Anforderung der räumlichen Abdeckung, während Aufnahmen der TSX-Satelliten den Ansprüchen bezüglich der räumlichen Auflösung Genüge tun. Die Sensoren unterscheiden sich meist nicht nur in ihrer räumlichen Auflösung und Abdeckung, sondern auch in ihrer Wellenlänge. Alle Faktoren haben einen Einfluss auf die Oberflächendeformation, die abgebildet werden kann, und die Komplexität der Datenauswertung. Dies macht sich in den Prozessierungsschritten der PS-Auswahl und der Phasenabwicklung bemerkbar. Eine Möglichkeit der PS-Dichtemaximierung bietet die Kombination meherer PS-Auswahlkriterien. Die Realisierung dieser Möglichkeit für die Auswertung des TSX-Datensatzes, der die Deformationen der Parapeiros-Peiros-Talsperre aufzeichnet, erhöhte die PS Anzahl. Dadurch konnten erhebliche Lücken auf dem Staudamm geschlossen werden, die zuvor eine Deformationsauswertung in diesem Bereich umöglich machten. Die Phasenabwicklung kann mittels einer rekonstruierten durch Deformation verursachten Phase unterstützt werden. Die rekonstruierte durch Deformation verursachte Phase wird basierend auf Zeitreihenmodellen berechnet, die aus einem einfacher zu prozessierenden Datensatz abgeleitet werden. Mit diesem Ansatz konnte eine Verbesserung der Ergebnisse des TSX-Datensatzes erzielt werden.

Alle drei Aspekte fördern den Übergang von zeitlich begrenzten Auswertungen hin zu einer kontinuiertlichen Analyse eines regelmäßig aktualisierten Datensatzes, sowie zu einer systematischen Auswertung der daraus resultierenden Ergebnisse.

Contents

Introduction

1

1.1 Motivation

Differential Synthetic Aperture Radar Interferometry (DInSAR) has been used to map ground surface deformation for the past decades. The technique was first applied to record the co-seismic deformation field of the Landers earthquake, which occurred in 1992 in California, USA [1, 2]. Since earthquakes are often linked to boundaries of lithospheric plates, studying their distribution, focal mechanism, and the associated co-seismic surface deformation is important to understanding the processes driving the crustal deformation of the Earth [3]. Both co-seismic deformation, i.e., deformation directly associated with an earthquake, and aseismic deformation, i.e., deformation alongside faults in between seismic events, offer important information on the seismic hazards of a region. An assessment that is becoming increasingly important, since the population in seismically active areas continues to grow and densify. The geophysical research field dedicated to describing and understanding these processes with geodetic methods is tectonic geodesy. The first surface deformation associated with an earthquake was mapped in the early 1890s. Geodetic triangulation and leveling measurements were taken before and after the Nobi earthquake in Japan (1891). However, until the end of the 20th century, conducting measurement campaigns to map surface deformation alongside faults or in association with earthquakes was a labor- and time-intensive, as well as costly endeavor. Only the development of remote sensing techniques such as the Global Navigation Satellite Systems (GNSS) and DInSAR in the 80s and 90s facilitated regular surveys of ground surface deformation over wide areas independently of weather and daylight conditions [4, 5]. The advantage of DInSAR over GNSS is that, under favorable conditions, providing ground surface deformation measurements over a dense grid of measuring points (MP) is far more achievable with DInSAR than with GNSS. However, since GNSS measurements often tend to be more precise and using permanently operating stations provides an uninterrupted time series of measurements, both methods are often used to complement each other. With an uptake in data availability in recent years, they quickly replaced traditional methods in the field of tectonic geodesy [4, 5]. Especially DInSAR found regular application in monitoring geohazards, other than surface deformation due to seismic events, such as slope instabilities [6, 7] and sinkholes [8].

The capabilities of DInSAR to measure ground surface deformation are limited by a loss of coherence due to temporal and geometric decorrelation [9, 10] and the misinterpretation of atmospheric phase contributions [11, 12] as phase induced by the topography or surface deformation of the imaged scene. These limitations led to the development of advanced DInSAR techniques such as Persistent Scatterer Interferometry (PSI) [13, 14], Small Baseline Subset Interferometry (SBAS) [15], and SqueeSAR^{TM} [16] (an integrated Persistent and Distributed Scatterers (PS and DS) algorithm). These advanced DInSAR techniques have in common that they use a time series of differential interferograms instead of only one to estimate ground surface deformation and thus can mitigate the earlier listed limitations of DInSAR. Especially, the capabilities of PSI to map ground surface deformation with millimeter precision have been demonstrated in various studies over recent years [17, 18, 19, 20].

PSI has been utilized to map and analyze naturally occurring and human-induced ground surface deformation. Examples of naturally occurring ground surface deformation are post-glacial uplift [21], aseismic creep alongside active faults [22, 23], slope instability [24], and sinkholes [25, 26]. Human-induced ground surface deformations are, for example, varying uplift and subsidence due to seasonal groundwater usage [27] or gas storage [28, 29] and subsidence due to continuing urbanization [30]. Additionally, PSI has been used to study the surface deformation of large infrastructure elements such as bridges [31], dams [32], or levees [33].

All the examples listed above are only snapshots of the observed deformation, i.e., only a specific time span and Area-of-Interest (AOI) is analyzed. However, the ground surface deformation most likely continues. With the launch of the Sentinel-1 (S1) Synthetic Aperture Radar (SAR) satellites S1-A in 2014, S1-B in 2016 (S1-B was only operational until December 2021) and S1-C in 2024, the amount of available SAR data capable of interferometry increased significantly. The S1 SAR mission was designed to systematically record SAR images with a repeat-pass time of 12 days worldwide and 6 days for European areas provided freely to the public. However, the S1-B satellite was only operational between October 2016 to December 2021. The loss of S1-B increased the repeat-pass time over Europe from 6 to 12 days. With the launch of S1-C a repeat-pass time of 6 days over Europe was achievable again. Even though the S1 SAR images have a low spatial resolution of 5 m in range and 20 m in azimuth [34, 35, 36, 37], they can still be used to evaluate the risk that geohazard-induced ground surface deformation poses to human settlements and infrastructure networks [38, 39, 40, 41]. The wide spatial coverage of S1 SAR images with 250 km wide recorded swaths [34] allows for assessments at the regional scale, so that with advanced DInSAR (e.g., with PSI) derived mean velocity maps and displacement time series can be used to extract active deformation areas [38, 41] and associate them with predefined geophysical deformation mechanisms [40] in order to create priority lists for Civil Protection Authorities [39]. Although all the described studies above intend for their products (e.g., maps of active deformation areas) to be regularly updated, newly incoming data is not continuously processed. The case study on monitoring ground surface deformation at a regional scale in Tuscany presented by Raspini et al. (2018) showcased an innovative near-real-time approach. The S1 SAR data for the region of Tuscany is scanned every 6 days for a change in the mean deformation velocity over the past

150 days. MPs with a velocity change greater than 10 $\frac{\text{mm}}{\text{year}}$ are earmarked as anomalies and recommended to be investigated further. The recent development in the use of advanced DInSAR techniques, such as PSI, for risk assessment or structural health monitoring, from processing and analyzing distinct time spans to continuously updating the results with new incoming data, led to the main research question of the present work:

How can the PSI technique contribute to the continuous monitoring of human settlements and large infrastructure elements?

Frequent processing of a continuously expanding dataset presents challenges concerning both the PSI processing itself and the systematic analysis of the resulting ground surface deformation data. A drawback of the PSI technique is that it only extracts ground surface displacement rates from pixels behaving coherently for the majority of the observation period [43, 44]. Thus, a continuously growing dataset with an expanding observation period is likely to result in a continuous loss of MPs. A lower MP density impedes an accurate assessment of the spatial pattern of the ground surface deformation and the extend of the affected area. Another aspect to consider, is the comparability of the ground surface deformation data after each update of the dataset, if processing is carried out independently of prior processing. Concomitant with independent processing, is the question of inefficiency. Since the majority of the SAR images in the dataset are repossessed each time the dataset is updated. All three aspects can be summarized by the first sub-question investigated in this thesis:

What processing approach for PSI would allow for a continuous long-term monitoring of an area or object of interest, taking into account MP density and comparability with historic data?

Each PSI analysis provides a map of the mean deformation velocity and a displacement time series of each MP identified in the dataset. Typically, the mean deformation velocity map is used to analyze the recorded ground surface deformation. The advantage of using the mean deformation velocity maps is that actively deforming areas, their spatial pattern, and extent can be easily assessed [38, 45]. A disadvantage is that the map does not offer information concerning the temporal deformation pattern, since the mean deformation velocity is estimated with the assumption of a constant velocity model. However, for monitoring purposes, the temporal deformation pattern is of particular interest, as presented in Raspini et al. (2019). They identified an acceleration in the deformation of a large area in the Northern Apennines as a consequence of rainfall and snow melt, which could have been underestimated or remained undetected by only analyzing the mean deformation velocity maps. In combination with the amount of data generated by a continuously operating surface deformation monitoring system, this illustrates the need for an automatic post-processing procedure to assess the temporal deformation pattern of MPs in the dataset. Thus, the second sub-question of the research presented is:

How can the results of PSI processing be utilized to provide information on the dynamic evolution of the deformation process?

Additionally, tailoring the monitoring system for large infrastructure elements for structural health monitoring (SHM), such as embankment dams, poses significant challenges. Dams are subject to various surface deformations that can either be localized, such as varying subsidence rates alongside the crest of the dam body, or occur on a larger scale, such as slope instabilities along the shoreline of the water reservoir [47, 48]. Thus, high-resolution and wide spatial coverage are needed. Meaning, in addition to S1 SAR images TerraSAR-X (TSX) images of vulnerable areas are needed. Due to the higher resolution (0.6 m in slant range and 1.1 m in azimuth direction [49, 50]) of high-resolution spotlight TSX data compared to IW swath S1 data, the spatial variability of the deformation pattern can be captured in greater detail. However, a high spatial variability of the deformation pattern can lead to challenges during processing, since some PSI algorithms, such as the Stanford Method for Persistent Scatterer (StaMPS) [14, 51, 52], require spatial smoothness of the deformation pattern for PS selection. Further, the wavelength of the SAR sensor used has an influence on the mapping of the ground surface deformation. Advanced DInSAR techniques, such as PSI, exploit phase differences, i.e., the differential phase, between acquisitions to measure deformation rates, which correspond to a fraction of the wavelength of the used SAR sensor. The differential phase is measured modulo 2π, making it ambiguous. A requirement to unambiguously unwrap the observed differential phase for PSI is that the phase difference of two neighboring MP over two consecutive differential interferograms is less than π, which corresponds to $\frac{\lambda}{4}$ [53]. Thus, making the high-resolution dataset with the sorter wavelength more complex to process in the case of highly spatially variable and rather quick deformation, which leads to the question:

How can PSI datasets that are complex to process due to their high-resolution and shorter wavelength still be used to map highly spatially variable and rather quick deformation?

All three sub-questions will be addressed in this thesis. The structure of the thesis and the approach to addressing the research questions is outlined in the next section.

1.2 Road Map to the Thesis

The following section outlines the structure of this thesis and the approach taken to address the research questions introduced in section 1.1. Three sub-questions emerge from the overriding topic of using PSI to continuously monitor human settlements and large infrastructure elements such as dams. The research questions are the following ones:

(1) How can the results of PSI processing be utilized to provide information on the dynamic evolution of the deformation process?

(2) How can PSI datasets that are complex to process due to their high-resolution and shorter wavelength still be used to map highly spatially variable and rather quick deformation?

(3) What processing approach for PSI would allow for a continuous long-term monitoring of an area or object of interest, taking into account MP density and comparability with historic data?

The thesis is structured into seven chapters, with the first chapter providing a motivation for and a road map of the thesis. The theoretical background of remote sensing techniques to map surface deformation based on Synthetic Aperture Radar Interferometry (InSAR) is outlined in Chapter 2. The chapter also provides an overview of the deformation a dam is subjected to throughout its life time and conventional methods used to monitor them, since a recently build dam in Greece is used in addition to the coastal city Patras to demonstrate the presented research. Chapter 2 includes elements of previously published articles. Text passages extracted from [54] M. Evers, A. Kyriou, K. Nikolakopoulos, and K. Schulz. “How to set up a dam monitoring system with PSInSAR and GPS”. in: *Proceedings of Earth Resources and Environmental Remote Sensing/GIS Applications XI* 11534 (2020), pp. 98–114 are marked with an orange line. The AOI, the area around the city of Patras, used to demonstrate the findings concerning the research sub-questions is introduced in chapter 3.

Each question listed above is addressed in an individual chapter, containing sections providing the problem statement and an overview of related work, addressing the theoretical fundamentals and approach to solve the problem, presenting a demonstration case and a discussion on the topic. The first sub-question is addressed in Chapter 4. In order to asses the dynamic evolution of the observed deformation process a post-processing tool referred to as Persistent Scatterer Analysis Tool (PSDefoPAT®) was developed. PSDefoPAT® fully automatically assigns a best-fitting time series model to the displacement time series of each MP in an advanced DInSAR dataset. In this chapter the fundamentals of time series analysis relevant for PSDefoPAT® are outlined and the capabilities of the post-processing tool are demonstrated on the example of the city of Patras in Greece and the newly build embankment Parapeiros-Peiros Dam south-west of the city. Additionally, PSDefoPAT® is tested on simulated displacement time series, whose noise level increases progressively. This chapter includes elements of previously published articles. Text passages extracted from [55] M. Evers, A. Thiele, H. Hammer, and S. Hinz. “PSDefoPAT—Persistent Scatterer Deformation Pattern Analysis Tool”. In: *Remote Sensing* 15 (2023), 1–26, paper no. 4646 are marked with a blue line. Additionally, although the following previously published articles are not quoted verbatim and are thus not marked in the text, they are referenced here because they address methodological concepts featured in Chapter 4. A preliminary version of PSDefoPAT® was presented in [56] M. Evers, H. Hammer, A. Thiele, and S. Hinz. “Psdefopat–Towards automatic model based psi post-processing”. In: *ISPRS Annals of the Photogrammetry, Remote Sensing and Spatial Information Sciences* 3 (2022), pp. 107–114. The user interface for operating PSDefoPAT® is introduced in [57] M. Evers, A. Thiele, H. Hammer, E. Cadario, K Schulz, and S. Hinz. “Concept to analyze the displacement time series of individual persistent scatterers”. In: *The International Archives of the Photogrammetry, Remote Sensing and Spatial Information Sciences* 43 (2021), pp. 147–154 and the user interface for the visualization of PSDefoPAT® is introduced in [58] M. Evers and A. Thiele. “Visualization of PSDefoPAT Results”. In: *EUSAR 2024; 15th European Conference on Synthetic Aperture Radar* (2024), pp. 359–364.

The second sub-question aims to accommodate PSI algorithms, such as the Stanford Method for Persistent Scatterer (StaMPS), for ground surface deformation that depending of the wavelength and repeat-pass time of the SAR sensor might be considered fast in the context of PSI and additionally are spatially highly variable. Such ground surface deformation patterns can be observed monitoring large infrastructure elements such as the Parapeiros-Peiros Dam making the processing of high-resolution SAR data difficult. This mostly affects the processing steps PS selection and phase unwrapping. Concepts overcome these hurdles are presented and demonstrated in Chapter 5. Although the following previously published articles are not quoted verbatim and are thus not marked in the text, they are referenced here, since they address methodological concepts used in Chapter 5. The concept to combine different PS selection criteria to maximize PS density is introduced in [59] M. Evers, A. Thiele, H. Hammer, and S. Hinz. “The Filling Process of an Embankment Dam Monitored with PSI”. in: *IGARSS 2022 - 2022 IEEE International Geoscience and Remote Sensing Symposium* (2022), pp. 1640–1643 and the concept to support the phase unwrapping with a reconstructed idealized deformation induced phase is introduced in [60] M. Evers, E. Cadario, and A. Thiele. “PSDefoPAT for Phase Unwrapping: Knowledge Transfer from Sentinel-1 to TerraSAR-X”. in: *IGARSS 2024-2024 IEEE International Geoscience and Remote Sensing Symposium* (2024), pp. 11052–11055.

For the third sub-question, addressed in chapter 6, three different processing strategies for a continuous monitoring with PSI: (A) a growing dataset, (B) consecutive non-overlapping time intervals and (C) consecutive overlapping time intervals are evaluated. Additionally, the PSISlider processing chain is introduced. Although the following previously published article is not quoted verbatim and is thus not marked in the text, it is referenced here, since it addresses methodological concepts used in Chapter 6. The three different processing strategies evaluated in this chapter are introduced in [61] M. Evers, H. Hammer, A. Thiele, and K Schulz. “Strategies for PS processing of large sentinel-1 datasets”. In: *The International Archives of the Photogrammetry, Remote Sensing and Spatial Information Sciences* 43 (2020), pp. 99–106.

The final chapter contains the synopsis of the thesis and an outlook on future research.

Theoretical Background

2

The following chapter is divided into two parts. The first section of the chapter outlines the theoretical background of remote sensing techniques to map surface deformation based on InSAR with a focus on PSI. The second section of the chapter, provides an overview on the surface deformation a dam is subjected to during its life time and the methods used to monitor them. Section 2.2 includes text passages extracted from [54] M. Evers, A. Kyriou, K. Nikolakopoulos, and K. Schulz. “How to set up a dam monitoring system with PSInSAR and GPS”. in: *Proceedings of Earth Resources and Environmental Remote Sensing/GIS Applications XI* 11534 (2020), pp. 98–114, which are marked with an orange line.

2.1 Synthetic Aperture Radar Remote Sensing Techniques

SAR is an imaging system that provides high-resolution images of, e.g., the surface of the earth, day and night, independent of weather conditions and cloud coverage [62]. It was developed in the 50ties to improve the resolution of conventional side-looking active radar imaging systems. A fine resolution in range, which measures the distance from the radar track to a scatterer, can be obtained by a short-duration radar pulse. The resolution in azimuth, which is the flight direction of the radar antenna, is directly tied to the beamwidth of the system. The azimuth resolution can be improved by increasing the antenna size and increasing the operating frequency of the system. However, even the largest feasible antenna size and highest practical operating frequency did not achieve the desired resolution. The key idea of SAR is to use the forward motion of the radar platform, e.g., an aircraft or satellite, to synthesize a very long antenna. The aircraft or satellite carries the side-looking radar antenna to different positions, at which the antenna transmits a radar pulse and receives its echo. The various positions can then be treated like individual antenna elements of a linear antenna array. However, in the case of a physical antenna array or real aperture, the transmission and reception at each dipole of the antenna array are simultaneous. For a synthetic array, the returned signal at each position of the radar platform is stored separately. Assuming the phase information of each returned pulse is recorded, a narrow-beamed antenna can be synthesized. This concept is known as SAR. It was first mentioned by C. Wiley in a report while working at Goodyear Aircraft Corporation in 1951. In 1953, a discussion between C. Sherwin of the University of Illinois, W. Hausz of General Electric Company, J. Koehler of the Philco Corporation, and L. Cutrona of the

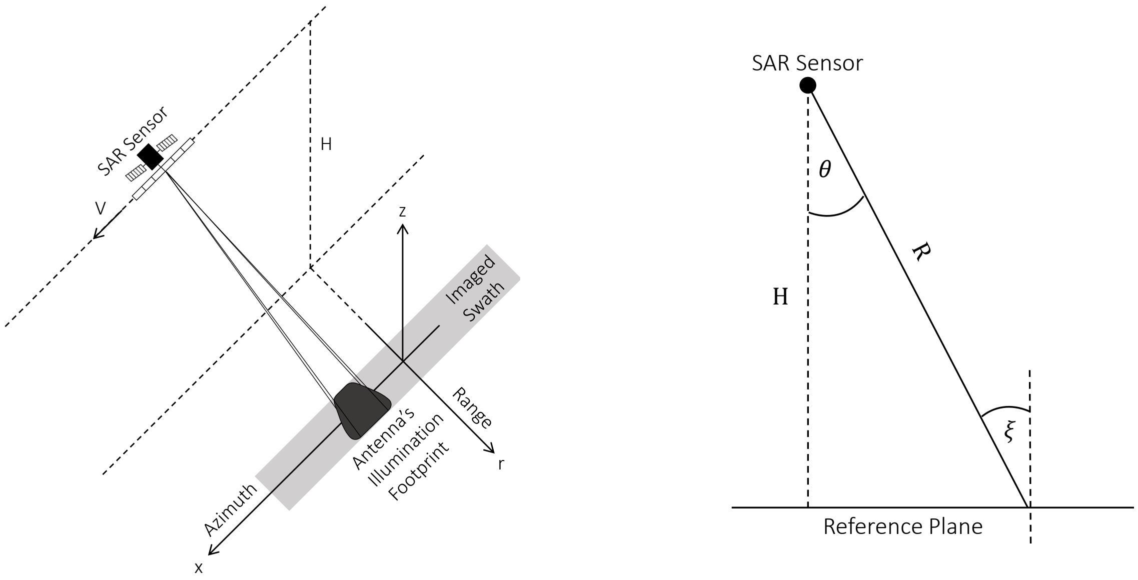

(a) Position of antenna footprint and sensor **(b)** Look θ and incidence angle ξ

Figure 2.1.: Side-looking imaging geometry of SAR [66, 10].

University of Michigan led to the Michigan project that evaluated the concept, starting with a roof-mounted antenna and later an aircraft as the platform. The first SAR data from the aircraft were recorded in August 1957, and the first strip map images of Fort Huachuca and Tucson in Arizona, USA, were created in the spring of 1958 [63, 64, 65]. In contrast to optical sensors, SAR sensors use a side-looking imaging geometry, as is depicted in Figure 2.1. Figure 2.1 (a) illustrates a SAR sensor moving along its path at an altitude H above the surface of the earth approximated by a reference (x, r)-plane. Its antenna is directed sideward to its illumination footprint rather than directly downwards. The x-axis represents the flight direction of the sensor, also referred to as the along-track or azimuth direction. The r-axis describes the across-track or range direction. The angle at which the antenna is steered towards the earth is the look angle θ. The incidence angle ξ refers to the angle at which the transmitted radar pulse reaches the reference plane regarding its normal. Both angles are depicted in Figure 2.1 (b), neglecting the curvature of the earth's surface. While moving along its track, the sensor emits microwave pulses into the antenna's illumination footprint at a fixed rate. This rate is called the pulse repetition frequency (PRF). Assuming that the microwaves propagate undisturbed from the antenna towards the earth, scattering only occurs close to its surface. The amplitude and phase of the backscattered signal depend on the physical and electrical properties of the individual scatterers in the illuminated scene. The backscattered signal of each pulse is received by either the same antenna they were transmitted from (mono-static SAR) or a different one (bi- or multi-static SAR). The individual received echoes are arranged 'side-by-side' as a 2D matrix for processing, making the SAR raw data resemble a hologram more than an image. The coordinates of the 2D matrix are slant range R, measuring the distance between the scatterer and the SAR antenna in its line-of-sight (LOS), and azimuth x, describing the

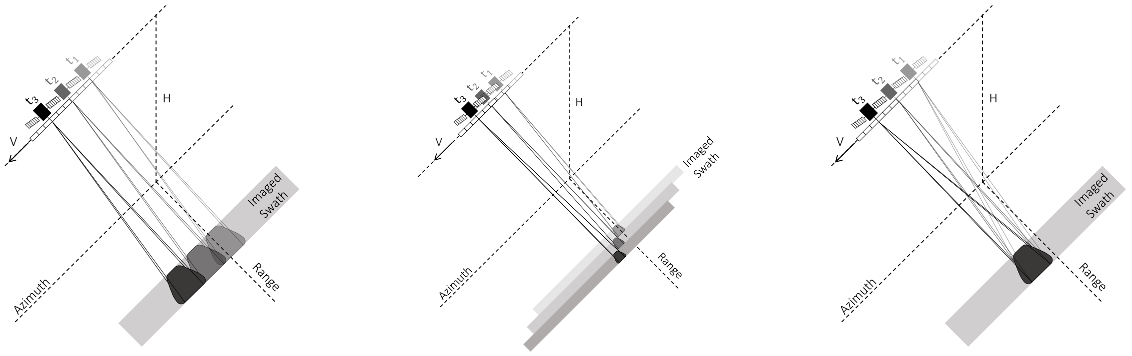

(a) Strip-map **(b)** ScanSAR **(c)** Spotlight

Figure 2.2.: Exemplary SAR acquisition modes [62]

position of the scatterer along the path of the sensor.

The resolution in azimuth is related to the SAR integration time, i.e., the time the SAR sensor illuminates a scatterer. The SAR integration time depends on the SAR acquisition mode. Commonly used modes are strip-map SAR, ScanSAR, and spotlight SAR. In the case of strip-map SAR, the scene is continuously recorded as the antenna's illumination footprint sweeps along the path of the sensor with a fixed look angle. The azimuth resolution of the SAR raw data is limited to the antenna footprint size, which is in the order of $\frac{R\lambda}{L}$ with L being the physical size of the antenna and λ the pulse carrier wavelength. For ScanSAR, the integration time is shorter since only separate bursts are illuminated. In between bursts, the antenna's look angle is changed so that a swath parallel to the previous one can be recorded, i.e., the SAR system operates in a stepped manner. The different bursts are stitched together during processing, resulting in a wide swath. A consequence of the high special coverage is a low resolution due to the short integration time. In contrast, for spotlight SAR, the antenna of the sensor is continuously steered towards a specific patch so that the integration time for the patch is elongated. This approach yields a higher azimuth resolution but a lower spatial coverage. The three acquisition modes are illustrated in Figure 2.2. The resolution in range is related to the bandwidth of the transmitted chirp pulse. The chirp is the frequency-modulated pulsed waveform commonly used for transmission by SAR sensors. The main frequency of the frequency-modulated pulsed waveform is the carrier frequency f_0 [62, 66, 67, 68]. Typical pulse carrier frequencies or wavelengths are (1) X-Band: 8-12 GHz or 2.5-3.75 cm, (2) C-Band: 4-8 GHz or 3.75-7.5 cm, (3) S-Band: 2-4 GHz or 7.5-15 cm, (4) L-Band: 1-2 GHz or 15-30 cm, and (5) P-Band: 0.5-0.25 GHz or 60-120 cm [62].

In order to create a focused SAR image, further processing is needed. Simply put, the process can be divided into two steps: (1) range compression and (2) azimuth compression. In the case of range compression, the transmitted chirp signals are compressed to short pulses, i.e., each line in range is multiplied by the complex conjugate of the spectrum of the transmitted chirp in the frequency domain. In the case of azimuth compression, the signal is multiplied by the complex conjugate of the expected return signal of a point target on the ground.

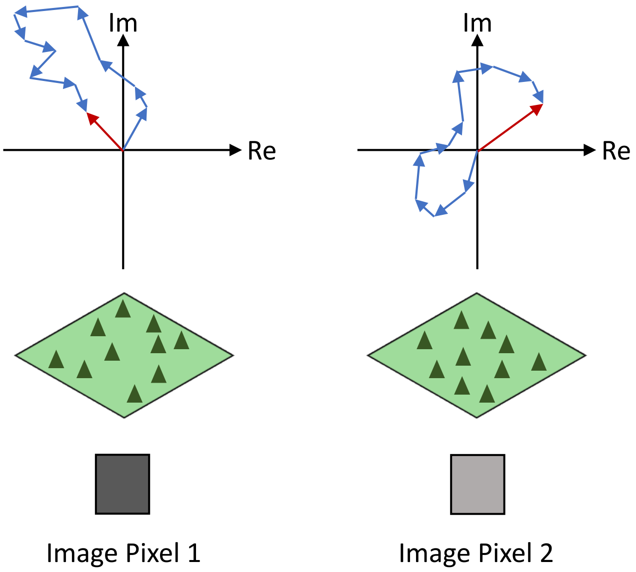

Figure 2.3.: Speckle effect in SAR images [62].

Once the SAR image is focused, effects such as speckle, foreshortening, shadow, and layover can be observed. These effects have their root in the SAR imaging geometry and the coherent nature of SAR data. The ground resolution cell corresponding to a pixel in the SAR image contains multiple randomly distributed scatterers. The microwave pulse transmitted from the SAR antenna interacts with each scatterer, and each scatterer produces a backscattered signal with an amplitude and phase. The coherent sum of these values is the phase and amplitude of the pixel in the final image. Constructive and destructive interference plays a role here, causing strong fluctuations in the backscattering over the image. This effect, called speckle, is illustrated in Figure 2.3. The figure shows the coherent summation of the backscattered signals of the randomly distributed scatterers in two exemplary ground resolution cells in the complex plane with a cartesian coordinate system. The vertical axis is the imaginary axis and the horizontal is the real axis.

Foreshortening, layover and shadow are a consequence of the side-looking image geometry of SAR. The three-dimensional position of objects in the recorded scene is only measured with two dimensions: slant range and azimuth. In the case of sloped terrain, this causes foreshortening, i.e., the slope facing the sensor appears compressed. Layover is extreme foreshortening, where a point higher on the slope is illuminated before one lower on the terrain, causing the lower point to be obscured in the final SAR image. Shadow refers to areas not illuminated by the SAR antenna [62, 66, 67, 68].

2.1.1 Synthetic Aperture Radar Interferometry

As stated previously, each pixel of a SAR image contains a measurement of the amplitude and phase of the signal backscattered by the area of the earth's surface the radar antenna illuminated. Both depend on the physical and electrical properties of the imaged area. While the amplitude can provide useful information on the recorded area by examining only one SAR image, two images are needed to extract information from the phase [62, 66]. In the late 1960s, Rogers and Ingalls were the first to utilize the phase of radar pulses in an interferometric manner to resolve uncertainties while mapping previously identified reflectivity features on the surface of the planet Venus. They used the earth-based Haystack and Westford radar antennas, located approximately 1200 m apart. The Haystack antenna transmitted radar pulses toward Venus. Both radar antennas received and recorded the reflected signal. The signals were combined using multiplicative interferometry. The complex cross-power of the received signals was calculated by multiplying one signal with the complex conjugate of the other. The resulting fringe pattern, i.e., the pattern caused by the 2π-ambiguity of the phase, was used to resolve the twofold hemispheric ambiguity hindering the exact positioning of previously observed features in the 2D reflectivity map of Venus [69]. A similar approach was later used to map the topography of the lunar surface facing the Earth. Again, the Haystack and Westford radar antennas were used as an interferometer. The fringe pattern resulting from calculating the phase difference between the recorded SAR images was used to determine the third dimension for a previously 2D map of the surface of the moon [70]. The first published work presenting lines of equal elevation based on a fringe pattern caused by the topography of the Earth was generated from airborne SAR data collected over Puerto Rico [71]. Based on these findings, different InSAR configurations were developed to map information on the surface of the Earth, such as the topography or the displacement of scatterers between acquisitions. All configurations have in common that at least two SAR images are combined to form an interferogram by multiplying the first image with the complex conjugate of the second image, resulting in the phase difference between the two images. To generate useful information from the images, at least one acquisition parameter needs to differ between the images [66]. In the case of the studies by Rogers and Ingalls (1969), Zisk et al. (1972), and Graham (1974), the divergent parameter was the location of the receiving antennas. Different information on the imaged area is generated depending on the deviant acquisition parameter. Table 2.1 provides an overview of the different InSAR configurations [66]. In the case of an across-track configuration, the images are recorded from different positions and, subsequently, with varying look angles. The difference is indicated with the perpendicular baseline $b_{\perp}$. Across-track InSAR can be used to reconstruct the topography of the imaged area. The divergent parameter in the case of along-track and differential InSAR is the point in time the images were recorded. The objective is to map the displacement of scatterers. Different phenomena can be observed depending on the temporal baseline, i.e., the time increment Δt between acquisitions. A difference in carrier frequency, as is the case for Δk-radar, can be used to eliminate the effects of the propagation medium and improve the accuracy of targets in range in the recorded SAR images [66]. This chapter presents the theoretical background of across-track and differential InSAR, focusing on the latter.

L.C. Graham [71] presented a concept to use synthetic interferometers to map the topography of the Earth in 1974 based on additive interferometry. Data from two radar antennas mounted on one aircraft with a vertical separation was used to generate a synthetic interferometer. Radar pulses were emitted from different positions along the flight path. The backscattered signal was recorded by both radar antennas and processed to form two focused SAR images. Simultaneously, the received signals from both antennas were combined by simple summation and subsequently processed in the same manner as the focused SAR images were, resulting in a synthetic interferometer. The collected data was combined with exact measurements of the position of the aircraft to extract lines of equal elevation for the imaged area. The concept was demonstrated using data collected in operational flights over Puerto Rico. The generated contour lines of equal elevation were in good agreement with conventionally generated topographic maps. Zebker et al. (1986) extended this concept to generate a high-resolution topographic map. Two airborne SAR images were obtained simultaneously by two spatially separated radar antennas over the San Francisco Bay Area. The images were pixel-wise combined using multiplicative interferometry to generate an interferogram containing the phase difference between the two images, also known as the interferometric phase, and the product of the two original amplitudes [72]. Later, the concept was adapted to accommodate the use of spaceborne

Defining Parameter	Configuration	Deviant Parameter		Extracted Information	Application
Perpendicular baseline	Across-Track	Orbit & Look angle		Position of scatteres	Topography reconstruction
Temporal baseline	Along-Track	Δt	ms to s	Displacement of scatteres	Ocean currents, Moving object detection
	Differential		Days		Glacier, Ice field flow, Lava flows
			Days to years		Subsidence, Seismic events, Volcanic activity, Crustal deformation
			ms to years		Sea surface Decorrelation time, Scene classification
Spectral baseline	Δk-Radar	Carrier frequency		Highly accurate range position	Exact ranging of targets, Elimination of propagation medium effects

Table 2.1.: Overview of possible InSAR configurations [66].

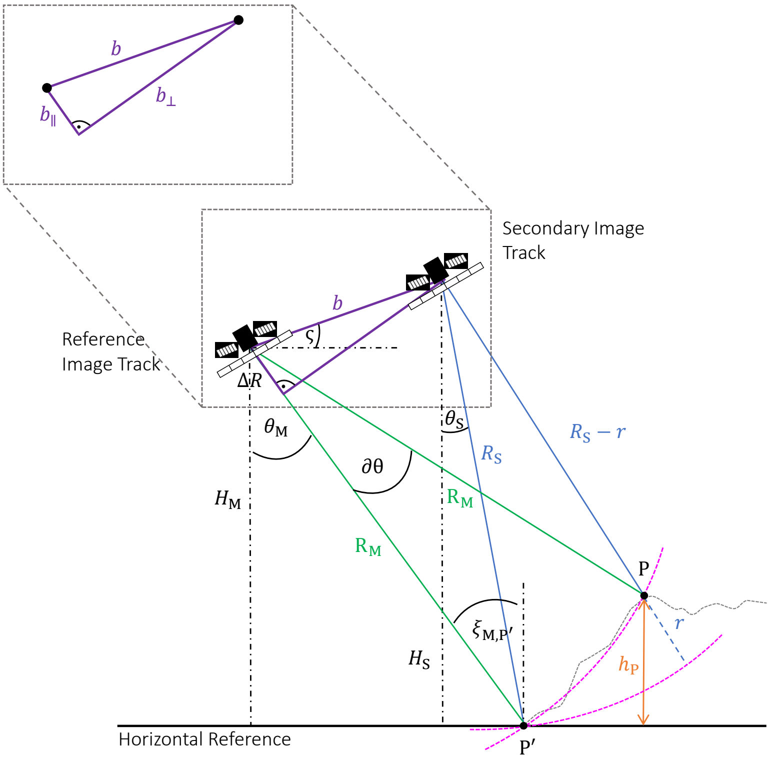

Figure 2.4.: Acquisition geometry for SAR interferometry [75, 10].

SAR data, imaging the same area but recorded at different times, i.e., repeat-pass interferometry [73, 74]. Figure 2.4 shows the acquisition geometry for spaceborne SAR interferometry. The images for SAR interferometry are not necessarily acquired simultaneously, i.e., repeat-pass instead of single-pass SAR interferometry. Before the images can be used to calculate an interferogram, they need to be aligned and resampled. The processing step is called co-registration and will be outlined later in this chapter. The image used as a geometric reference for co-registration is referred to as the reference image, while the second image is referred to as the secondary image. Together, they are also referred to as an interferometric pair. The orbits from which the images are recorded are referred to as the reference and secondary track, respectively. In Figure 2.4, it is assumed that the reference and secondary orbit tracks are parallel but at different altitudes, H_M and H_S. The spatial distance between them is defined as the spatial baseline b, which can be decomposed into a part perpendicular $b_\perp$ and parallel $b_\parallel$ to the LOS direction of the sensor. The angle between the baseline and its horizontal component is referred to as the baseline angle ς. Figure 2.4 also shows that the two ground resolution cells P' and P are located at the same slant range distance R_M in the reference image. In the secondary image the ground resolution cells are positioned at deviating slant range distances R_S and $R_S - r$ if they are located at different elevations on the imaged surface. The phase difference between the reference and secondary image is sensitive to this slant range difference, which is exploited in InSAR to reconstruct the topography of the imaged scene [10, 75]. The reference and secondary images consist of complex values on a regular grid. These complex values can be decomposed into the phase and amplitude of the backscattered signal for a specific ground resolution cell. The values, z_{M} and z_{S}, for pixels in the reference and secondary image covering the same ground resolution cells $\mathrm{P_M}$ and $\mathrm{P_S}$ respectively can be given as:

$$z_{\mathrm{M,P}} = \|z_{\mathrm{M,P}}\| \cdot e^{j\psi_{\mathrm{M,P}}}, \tag{2.1}$$

$$z_{\mathrm{S,P}} = \|z_{\mathrm{S,P}}\| \cdot e^{j\psi_{\mathrm{S,P}}}. \tag{2.2}$$

After the images are aligned and the secondary image is resampled to the geometry of the reference image, i.e., the secondary image is co-registered to the reference image, the interferogram for the common ground resolution cell P can be calculated as follows:

$$u_{\mathrm{P}} = z_{\mathrm{M,P}} \cdot z^{*}_{\mathrm{S,P}} = \|z_{\mathrm{M,P}}\|\|z_{\mathrm{S,P}}\| \cdot e^{j(\psi_{\mathrm{M,P}}-\psi_{\mathrm{S,P}})} = \|z_{\mathrm{M,P}}\|\|z_{\mathrm{S,P}}\| \cdot e^{j\Delta\psi_{\mathrm{P}}}. \tag{2.3}$$

Neglecting effects due to the propagation medium, the observed phase ψ_{P} only depends on the slant range distance between the sensor and the ground resolution cell P and the scattering characteristics of the resolution cell.

$$\psi_{\mathrm{M,P}} = -\frac{2\pi \cdot 2R_{\mathrm{M,P}}}{\lambda} + \psi_{\mathrm{scat,M,P}} \tag{2.4}$$

$$\psi_{\mathrm{S,P}} = -\frac{2\pi \cdot 2R_{\mathrm{S,P}}}{\lambda} + \psi_{\mathrm{scat,S,P}} \tag{2.5}$$

Here, $\psi_{\mathrm{scat,P}}$ denotes the phase due to the scattering properties of the ground resolution cell, λ the wavelength of the SAR system, and R_{P} the distance from the sensor to the ground resolution cell. Assuming that the scattering characteristics do not change in between acquisitions, the phase difference $\Delta\psi_{\mathrm{P}}$ can be calculated as follows:

$$\Delta\psi_{\mathrm{P}} = \psi_{\mathrm{M,P}} - \psi_{\mathrm{S,P}} = -\frac{4\pi}{\lambda}(R_{\mathrm{M,P}} - R_{\mathrm{S,P}}) = -\frac{4\pi}{\lambda}\Delta R_{\mathrm{P}}, \tag{2.6}$$

and its derivative is:

$$\partial\Delta\psi = -\frac{4\pi}{\lambda}\partial\Delta R. \tag{2.7}$$

In order to estimate the elevation h_{P} of the ground resolution cell P above a reference plane, ΔR_{P} needs to be measured. Based on the acquisition geometry, presented in Figure 2.4, ΔR_{P} can be approximated as:

$$\Delta R_{\mathrm{P}} = b \cdot sin(\theta_{\mathrm{P,M}} - \varsigma). \tag{2.8}$$

This equation cannot be used to accurately estimate ΔR_{P}, due to orbit inaccuracies and the ambiguous nature of the phase differences, i.e., the absolute phase differences are only given modulo 2π. How this ambiguity can be resolved is outlined in Section 2.1.4. However, the derivative of Equation 2.8 can be used to describe the relationship between changes in ΔR and θ.

$$\partial\Delta R = b \cdot cos(\theta^{0}_{\mathrm{P,M}} - \varsigma)\partial\theta \tag{2.9}$$

Here, $\theta^0_{\mathrm{P,M}}$ is an initial value for the look angle obtained from an arbitrary reference plane, such as a sphere or ellipsoid. Combining Equation 2.7 and 2.9, the relationship between a change in the look angle and a change in the interferometric phase can be written as:

$$\partial\Delta\psi = -\frac{4\pi}{\lambda} \cdot b \cdot cos(\theta^0_{\mathrm{P,M}} - \varsigma)\partial\theta. \tag{2.10}$$

A change in the interferometric phase can also be expressed as the difference between the observed phase ψ_{P} and the expected phase for the reference body ϑ_{P} based on the orbit geometry:

$$\partial\Delta\psi = \psi_{\mathrm{P}} - \vartheta_{\mathrm{P}}. \tag{2.11}$$

The height of the SAR satellite can be expressed in geometrical terms as:

$$H_{\mathrm{M}} = R_{\mathrm{P,M}} \cdot cos(\theta^0_{\mathrm{P,M}}), \tag{2.12}$$

and a change of the height of the satellite for the ground resolution cell P can be written as:

$$\partial H_{\mathrm{M}} = -h_{\mathrm{P}} = R_{\mathrm{M,P}} \cdot sin(\theta^0_{\mathrm{P,M}})\partial\theta. \tag{2.13}$$

Equation 2.13 can be solved for the elevation h_{P} of the ground resolution cell P above a reference body employing Equation 2.10, which results in:

$$h_{\mathrm{P}} = -\frac{\lambda R_{\mathrm{M,P}} \cdot sin(\theta^0_{\mathrm{P,M}})}{4\pi b^0_{\perp,\mathrm{P}}}\partial\Delta\psi \tag{2.14}$$

with

$$b^0_{\perp,\mathrm{P}} = b \cdot cos(\theta^0_{\mathrm{P,M}} - \varsigma). \tag{2.15}$$

With Equations 2.14 and 2.15, it is possible to reconstruct the topography of an imaged area from its interferometric phase and generate a digital elevation model (DEM). The height of ambiguity can be used as a rough estimate of the elevation change between two points in an interferogram, since it corresponds to a full 2π phase shift, i.e., one complete fringe. The change in elevation causing a 2π phase shift can be estimated using [10]:

$$h_{2\pi} = \left|\frac{\lambda R_{\mathrm{M}} \cdot sin(\theta^0_{\mathrm{M}})}{2b^0_{\perp}}\right|. \tag{2.16}$$

In addition to topography, fringes in an interferogram can be caused by the displacement of scatterers on the imaged surface. The processes of isolating the interferometric phase contribution due to the displacement of scatterers from the contribution caused by the topography of the imaged scene are referred to as DInSAR. The theory behind DInSAR is outlined in the next section.

2.1.2 Differential Synthetic Aperture Radar Interferometry

The interferometric phase is not only sensitive to the topography of the imaged scene, but also to the displacement of scatterers on the ground surface between acquisitions. Goldstein et al. (1987) first exploited this to map ocean currents in Francisco Bay. Airborne SAR data collected simultaneously with two L-band antennas, displaced in along-track direction with an 18.5 m baseline, was used to generate an interferogram. The phase difference captured in the interferogram is related to the real-time displacement of scatterers on the water surface, and thus, the tidal current flow out of the San Francisco Bay could be mapped. Gabriel et al. (1989) presented a study using multiple repeat-pass SAR images to map small elevation changes in the Imperial Valley, California. Two interferograms with one SAR image in common were calculated and subtracted from one another, removing the part of the interferometric phase due to the local topography. The remaining part of the interferometric phase, referred to as the differential phase, reveals elevation changes between image acquisitions. The potential of DInSAR holds for monitoring ground surface deformation due to geophysical processes, such as earthquakes or aseismic creep alongside active faults, was recognized early on [75]. The first differential interferogram mapping ground surface deformation due to an earthquake was presented 1993 capturing the co-seismic displacement field of the Landers earthquake in California [1]. The differential interferogram was generated using two SAR images recorded with ERS-1 data and an external DEM to simulate and remove the topographic phase. In a second study, the displacement field of the Landers earthquake was studied using three ERS-1 SAR images, one taken before the earthquake occurred and two afterward. The SAR images are arranged to form a deformation pair, capturing the deformation due to the earthquake, and a topographic pair, which is ideal for calculating the topographic phase and is unaffected by deformation. Both pairs have one image in common, which serves as the geometric reference, i.e. the reference image, for both interferograms. The topographic interferogram is scaled using the ratio of the corresponding perpendicular baselines $\frac{b_{\perp,\mathrm{defo}}}{b_{\perp,\mathrm{topo}}}$ and subtracted from the deformation interferogram, resulting in a differential interferogram [2]. The approach used by Gabriel et al. (1989) and Zebker et al. (1994) is referred to as three-pass DInSAR, while the approach presented by Massonnet et al. (1993b) is two-pass DInSAR. In case there is no external DEM and no suitable third SAR image to form the topographic pair in combination with one image from the deformation pair, four SAR images can be used to calculate the differential interferogram. Four-pass DInSAR is comparable to three-pass DInSAR if the topographic and deformation interferograms are aligned correctly [10]. The advantage of three-pass or four-pass DInSAR is that no data other than SAR data is required. On the other hand, a significant drawback is the risk of misinterpreting non-topographic contributions to the interferometric phase as a topographic-induced phase. The assumption that the topographic pair is unaffected by deformation only holds true in case of abrupt deformations, such as those observed due to an earthquake. In addition, the importance of the phase contribution due to atmospheric changes was underestimated when the approach

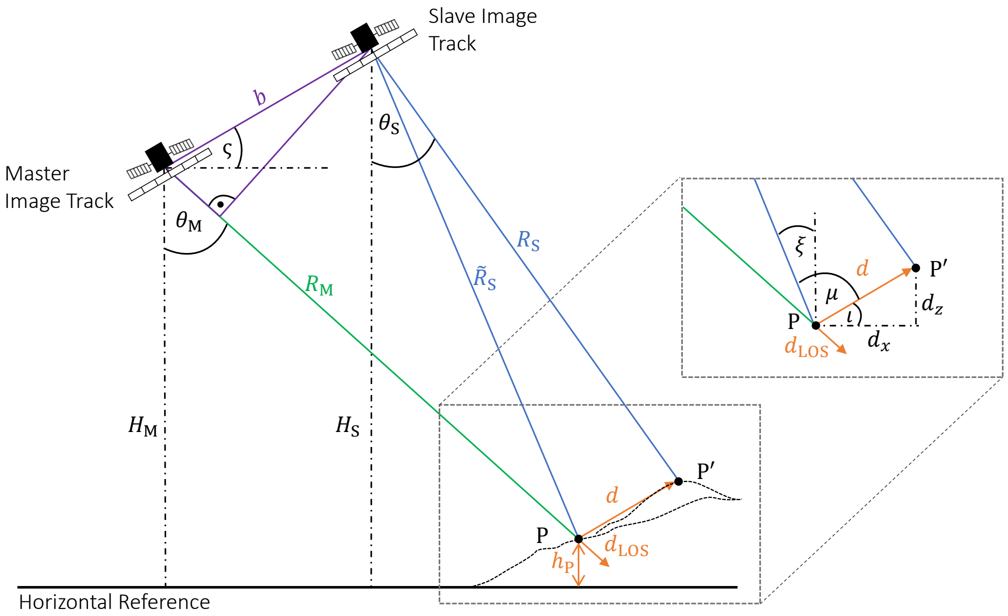

Figure 2.5.: Acquisition geometry for two-pass DInSAR [10].

was presented. In the case of two-pass DInSAR, using a DEM ensures that only the fringe pattern due to the local topography is eliminated. However, the accuracy of the DEM is pivotal [78]. In this work, the focus will be on two-pass DInSAR to form the differential interferograms needed for PSI.

The acquisition geometry for spaceborne two-pass DInSAR is presented in Figure 2.5. A displacement of the scatterers from position P to P’ contributes to a range difference in addition to the local topography and, subsequently, the interferometric phase for the corresponding pixel in an interferogram. If the displacement rates d of scatterers are the wanted information and not the local topography, the reference and secondary images would ideally be recorded from the same position with a zero spatial baseline in between them to limit the influence of the local topography. However, operating an InSAR satellite constellation with a zero baseline is often not possible or feasible [10]. The interferometric phase $\Delta\psi_{d_{\mathrm{LOS}},P}$ related to the displacement d_{LOS} can be written as [79]:

$$\Delta\psi_{d_{\mathrm{LOS}},\mathrm{P}} = \frac{4\pi}{\lambda} \cdot d_{\mathrm{LOS}}. \tag{2.17}$$

Combining Equation 2.14 and 2.17 and considering that reference phase ϑ_{P} is given as:

$$\vartheta_{\mathrm{P}} = \frac{4\pi}{\lambda} b \cdot sin(\theta^0_{\mathrm{P}} - \varsigma), \tag{2.18}$$

the observed interferometric phase can be written as:

$$\Delta\psi_{\mathrm{P}} = \frac{4\pi}{\lambda} \cdot (b \cdot sin(\theta^0_{\mathrm{P}} - \varsigma) - d_{\mathrm{LOS}} - \frac{b^0_{\perp,\mathrm{P}}}{R_{\mathrm{M,P}} \cdot sin(\theta^0_{\mathrm{P}})} h_{\mathrm{P}}). \tag{2.19}$$

2.1.3 Steps of DInSAR Processing

Filtering and multilooking aside, the process to generate a differential interferogram can be roughly divided into four steps: (1) co-registration of the SAR images, (2) interferogram generation, (3) removal of the flat-earth contribution, and (4) removal of the topography-induced phase contribution. Co-registering the interferometric image pair is necessary because even though the SAR images recorded in repeat-pass interferometry cover roughly the same patch of ground surface, they do not align perfectly due to slightly deviating orbit tracks. The correct alignment of the SAR images down to the sub-pixel

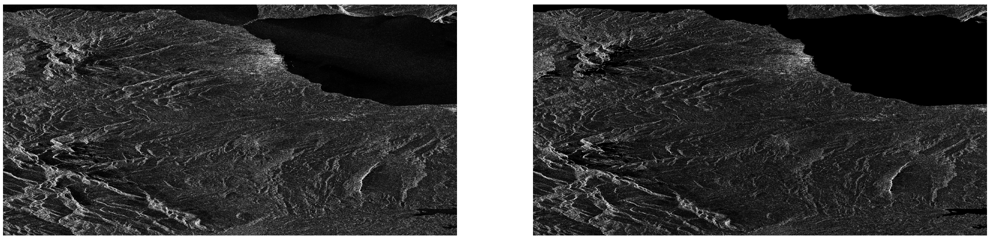

(a) Exemplary SLC taken by S1 on 02/15/2017

(b) Exemplary SLC taken by S1 on 03/17/2017

(c) Interferogram

(d) Phase induced by an idealized flat-earth

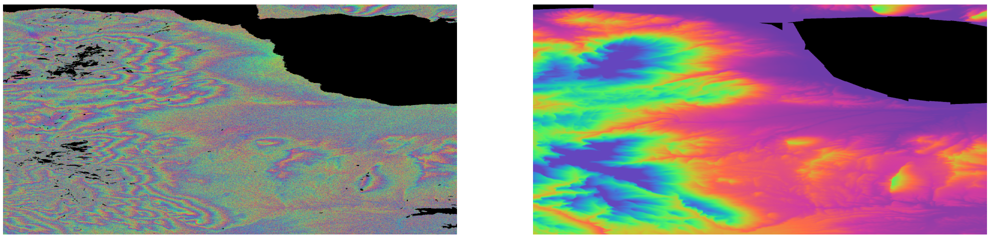

(e) Flattened interferogram

(f) Phase induced by topography

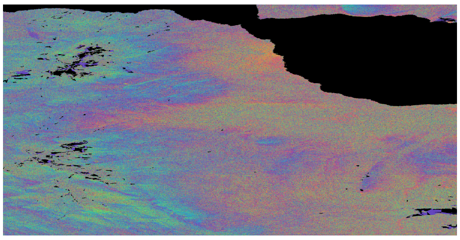

(g) Differential interferogram

Figure 2.6.: Processing steps of DInSAR on the example of the North-West of the Peloponnese Peninsula, Greece. For all seven images the azimuth direction extends from the upper left to the lower left corner and the range direction from left to right.

level, however, is required to generate coherent interferometric products. The parameter coherence describes the correlation between two SAR images. The value varies between 1 and 0, with 1 indicating a high correlation and 0 a low correlation. More details on coherence is provided in Sub-section 2.1.5. Errors in alignment would lead to a loss of coherence. The misalignment of images is corrected in a process referred to as co-registration. One SAR image, the reference image, serves as the reference image, and for the second image the azimuth and range offsets are calculated, and the image is resampled to match the reference image [10, 77, 80]. The azimuth shift depends on the start and stop times during image acquisition, while the shift in range corresponds to the length of the parallel component of the baseline divided by the posting in range. Realigning the images is divided into two steps: (1) coarse and (2) fine registration. For the coarse registration, the images are usually aligned by using common points within the images derived from a visual inspection or by using data on the satellite's orbit and timing as a reference. Fine registration relies on automatic correlation algorithms to achieve accurate alignment on a sub-pixel level. There are two types of algorithms: (1) coherent and (2) incoherent registration. The difference is that for coherent registration, the complex values of the phase and amplitude are used for cross-correlation, while for incoherent registration, only the phase values, the amplitude values or the squares of the amplitude are used. While coherent methods are very accurate, they tend to fail for large effective baselines. The cross-correlation of the amplitude squares, i.e., the powers, is a commonly used incoherent approach for fine registration. The cross-correlation is calculated in windows, preferably evenly distributed over the images, and the respective correlation peak provides the offset vectors restricting the 2D polynomial to estimate the offset of every pixel in the images. The secondary image can then be resampled to match the reference image. Accuracy up to $\frac{1}{20}$ of a pixel can be achieved [10]. However, Just and Bamler (1994) showed that an accuracy $\frac{1}{8}$ is enough to mitigate a loss of coherence due to misregistration. An example of a co-registered interferometric image pair is shown in Figure 2.6 (a) and (b). The images were recorded with the S1 satellites in Interferometric Wide (IW) Swath mode and with a descending acquisition geometry on the 02/15/2017 and 03/17/2017. The image from the 02/15/2017 serves as the reference image. After the SAR images are accurately co-registered, pixel-wise multiplying the first image with the complex conjugate of the second yields an interferogram (see Equation 2.3). An Example of an interferogram is shown in Figure 2.6 (c). The interferometric phase is given in modulo 2π and displayed in a cyclic color code. The fringe pattern featured in the interferogram in Figure 2.6 (c) shows a clear pattern in range, which is only disturbed by phase contributions from the local topography. This fringe pattern is caused by a systematic decrease of the interferometric phase with an increase in range and look angle, even for flat surfaces. Therefore, this contribution to the interferometric phase is referred to as the flat-earth contribution or more general reference phase. The flat-earth contribution is usually subtracted to reveal the interferometric phase induced by the topography of the imaged scene [10, 62, 66]. Such a flattened interferogram is shown in Figure 2.6 (e). The displayed fringe pattern matches the local topography. The topography-induced phase can be estimated and removed using either an external DEM or a second interferogram [1, 2]. Figure 2.6 (f) shows the topography-induced phase generated by using an external DEM, and Figure 2.6 (g) shows the interferogram after the topographic contribution to the phase has been removed, i.e., the differential interferogram. The last two processing steps are resolving the 2π ambiguity of the differential phase and calculating the displacement, which are outlined in detail in the next section.

2.1.4 Phase Unwrapping

The differential phase presented in Figure 2.6 (g) cannot be directly used to estimate the displacement of each pixel in the differential interferogram. Firstly, the differential phase is not necessarily equivalent to the deformation-induced phase. The differential phase does also include phase contributions induced by residual topography, orbit inaccuracies and changes in soil moisture, vegetation or atmospheric conditions [10]. Secondly, a major drawback of any technique based on SAR interferometry is that the phase is only given modulo 2π, i.e., the phase is wrapped.

$$\psi = \phi - k \cdot 2\pi \tag{2.20}$$

Here, ψ represents the observed wrapped phase and ϕ the unwrapped phase. The process of retrieving the correct number of phase cycles k needed to be added to ψ to reconstruct ϕ is referred to as phase unwrapping (PU). It is a crucial step. However, it is an ill-posed inverse problem. Multiple combinations of a phase value and the ambiguity number or number of phase cycles can result in the same wrapped phase value. The input to any 2D phase unwrapping problem is a 2D matrix containing the wrapped phase values, i.e., an interferogram. An intuitive approach to retrieve ϕ would be to integrate the phase differences from pixel to pixel [74, 82]. This approach assumes that the sampling rate of the wrapped phase is high enough so that the unwrapped phase difference between adjacent pixels is less than π or, in more general terms, half a phase cycle [83]. In other words, if the unwrapped phase difference between all adjacent pixels in an interferogram is less than π (or half a phase cycle), there are no ambiguities. In this case, its gradient field is irrotational, i.e., the integration of the phase differences is independent of the integration path. The gradient field of the interferogram can then be employed to determine ϕ using a simple integration process starting at a chosen reference point. However, in reality, the unwrapped phase difference between adjacent pixels is not always less than π due to noise, abrupt changes in the topography of the imaged scene, the deformation or effects like layover [82]. These effect can introduce two types of errors in the unwrapped phase: (1) local errors, where only a few pixels are affected, or (2) global errors, where the error propagates through the entire scene. The example given in Table 2.2 (a) shows a 2D matrix filled with wrapped phase values, where 1 equals a full phase cycle. Scanning

0.0	0.1	0.2	0.3
0.2	0.2	0.3	0.4
0.9	0.8	0.5	0.5
0.8	0.7	0.6	0.5

(a) Wrapped phase values

0.0	0.1	0.2	0.3
0.2	0.2	0.3	0.4
-0.1	-0.2	-0.5	-0.5
-0.2	-0.3	-0.4	-0.5

(b) Unwrapping row by row first

0.0	0.1	0.2	0.3
0.2	0.2	0.3	0.4
-0.1	-0.2	0.5	0.5
-0.2	-0.3	0.6	0.5

(c) Unwrapping column by column first

Table 2.2.: PU example of a 2D matrix based on the example given in [74].

the matrix row by row first and then column by column (see Table 2.2 (b)) while always adding an integer number of phase cycles to minimize the phase differences reveals an inconsistency between the second and third rows. Here, the phase difference between adjacent matrix elements surpasses half a phase cycle. Scanning the columns first and then the rows of the 2D matrix (see Table 2.2 (c)) also results in an inconsistency. Varying the order of scanning the data and integrating the phase differences yielded different results. The example, therefore, shows that if phase inconsistencies are present in the data, the integration of the phase differences is not path-independent. Another approach to show the path dependence is to evaluate the closed-path integration for 2x2 matrix elements by summing their phase differences clockwise, which is demonstrated in Table 2.3. If the integration is path-independent, the value of the closed-path integration is zero. If it is not zero, the value is either plus or minus a full phase cycle. In that case, the data features a phase inconsistency, which is either referred to as a minus or plus residue, depending on the sign of the closed-path integration [74, 82]. Any integration path that encloses a residue leads to an inconsistency in the unwrapped result unless the integration path encloses an equal number of minus and plus residues. The first 2D unwrapping algorithm designed explicitly for SAR interferometry applications relies on identifying the residues and placing branch cuts between residues of opposite signs. During the integration, these branch cuts guide the integration path so that no residues may be encircled and no global errors arise in the unwrapped result [74]. Over the years, other algorithms have been presented. They can be divided into three categories: (1) path-following, (2) optimization-based, and (3) integrated de-noising and unwrapping methods. The common idea of path-following PU algorithms is to choose reliable integration paths [82]. This

0.0		0.1		0.2		0.3
	0		0		0	
0.2		0.2		0.3		0.4
	0		+		0	
0.9		0.8		0.5		0.5
	0		0		0	
0.8		0.7		0.6		0.5

Table 2.3.: Closed-path integration of the PU example of a 2D matrix based on the example given in [74].

can be done by detecting and balancing residues and then choosing integration paths that do not cross their connecting branch cuts (e.g., [74]) or by using quality maps to guide the integration path, assuming that pixels with good quality are less likely to cause PU errors (e.g., [84]). Optimization-based PU algorithms aim to minimize the difference between the unwrapped phase gradient and the gradient of the observed wrapped phase (e.g., [85]). The last category of PU algorithms tries to simultaneously de-noise and unwrap the phase, assuming that separating these steps may introduce unnecessary processing errors (e.g., [74]).

As already mentioned, any phase noise hampers the application of PU algorithms and may lead to unwrapping errors, independent of the PU algorithm applied [82]. The noise overlaying the signal can be described using a dimensionless correlation parameter referred to as the coherence between an interferometric image pair. The closer the value is to 1, the better the correlation between the images [9, 86]. The influences of the coherence and other effects obscuring the deformation or topography-induced phase contribution in an interferogram are discussed in the following section.

2.1.5 Limits of Conventional DInSAR

Coherence and Decorrelation

The parameter providing an estimation for the correlation between an interferometric image pair is the coherence γ, which ranges from 0 to 1. A value close to 1 indicates a high correlation between the interferometric image pair and a value close to 0 indicates a low correlation. The coherence can be estimated using the following equation:

$$\gamma = \frac{E\{z_\mathrm{M} z_\mathrm{S}^*\}}{\sqrt{E\{|z_\mathrm{M}|^2\}E\{|z_\mathrm{S}|^2\}}}. \tag{2.21}$$

The expectation values $E\{\}$, needed to estimate the coherence, would ideally be obtained on the basis of a large number of interferograms acquired at the same time under the same conditions. However, this approach is highly unpractical in the case of SAR data [10].

Even though, SAR data is not generally considered ergodic, since the statistic of the data is dependent on the content of the imaged scene, i.e. terrain, buildings and vegetation, for phase observations of local uniform regions stationarity and ergodicity can be assumed. Thus, the maximum likelihood estimator of the coherence magnitude $|\widehat{\gamma}|$ can be estimated by exchanging the ensemble averages with spatial averages obtained over I pixels neighboring the pixel in question [10, 87]:

$$|\widehat{\gamma}| = \frac{|\sum_{i=1}^{I} z_\mathrm{M}^{(i)} z_\mathrm{S}^{*(i)}|}{\sqrt{\sum_{i=1}^{I} |z_\mathrm{M}^{(i)}|^2 \sum_{i=1}^{I} |z_\mathrm{S}^{(i)}|^2}}. \tag{2.22}$$

The number I pixels neighboring the pixel in question depends on the imaged scene. Firstly, the number needs to be large enough to ensure that the results are statistically reliable, and secondly, the number needs to be small enough to ensure local stationarity and ergodicity [88].

The coherence indicates the reliability of the interferometric phase measurement, thus providing a local measurement for the quality of an interferogram. A number of factors can lead to a loss of coherence. The most relevant are:

(1) receiver noise,

(2) temporal decorrelation and

(3) geometric decorrelation.

The influence of the thermal noise of the SAR receiver can easily be expressed in terms of the signal-to-noise ratio (SNR) [9]:

$$\gamma_{\text{thermal}} = \frac{1}{1 + SNR^{-1}}. \tag{2.23}$$

Geometric decorrelation describes the angular dependencies of the scattering reflectivity of the imaged scene. The difference in imaging geometry induced by the spatial baseline between acquisitions gives rise to three phenomena contributing to the geometric decorrelation of the SAR images [62].

The first is a consequence of the difference in incidence angles between the interferometric image pair due to their spatial baseline and is also referred to as baseline decorrelation γ_{rgn}. The phase and amplitude of a specific pixel result from the random coherent interference of the many closely spaced individual scatterers making up the corresponding ground resolution cell. Assuming that the composition of the individual scatterers does not change between image acquisitions, the interference pattern will still differ due to a difference in the acquisition geometry, i.e., diverging incidence angles ξ. The difference in the interference pattern leads to a loss of coherence [73]. The influence of the diverging imaging geometry on the correlation between an interferometric pair, depending on the difference in incidence angles $\Delta\xi$, can be written as:

$$\gamma_{\text{rgn}} = 1 - \frac{2cos(\xi)|\Delta\xi|o_r}{\lambda}. \tag{2.24}$$

Here, o_r is the resolution in range and λ the carrier wavelength of the SAR system. If the baseline angle ς is zero, i.e. the baseline has only a horizontal component, the equation can alternatively be expressed using the baseline b:

$$\gamma_{\text{rgn}} = 1 - \frac{2|b|cos^2(\xi)o_r}{R_{\text{Path}}\lambda}. \tag{2.25}$$

The parameter R_{Path} is the distance between the sensor and the center of the resolution element in slant range. Equation 2.25 shows that the decorrelation of an interferometric pair increases with an increasing perpendicular baseline. The baseline at which the interferometric image pair completely decorrelates is referred to as the critical baseline [9]. The contribution to the geometric decorrelation due to differences in the incidence angle mainly maps into a decorrelation in range direction [62]. The decorrelation in azimuth γ_{az} is caused by either a difference in squint angle, i.e., the angle between the sensors' LOS and the direction perpendicular to the orbit track or crossing orbits. The difference in the imaging geometry causes the reflectivity spectrum of the imaged surface to be mapped differently into the data spectrum of the reference and secondary images, i.e., a difference in the doppler centroid frequency. Only the overlapping parts of the data spectrum correlate. The correlation for the interferometric image pair decreases linearly with an increasing difference in the doppler centroid frequency [10].

To this point, only surface decorrelation has been considered. However, the geometric decorrelation will be enhanced if the ensemble of scatterers is distributed in a volume. Due to the different imaging geometry for the interferometric image pair, the vertical component of the reflectivity spectrum of the imaged scene is projected differently into the SAR images [89]. The volumetric decorrelation γ_{vol} is directly related to the vertical distribution $F(z)$ of the scatterers in the ground resolution cell through a Fourier transformation relationship

$$\gamma_{\text{vol}} = e^{ik_z z_0} \frac{\int_0^{h_\text{v}} F(z') e^{ik_z z'} dz'}{\int_0^{h_\text{v}} F(z') dz'} \tag{2.26}$$

with

$$k_z = \frac{2\pi}{h_{2\pi}} \tag{2.27}$$

and h_v indicates the height of the volume and z_0 is a reference height [62]. The different contributions to the geometric decorrelation are combined multiplicatively:

$$\gamma_{\text{geo}} = \gamma_{\text{rgn}} \gamma_{\text{az}} \gamma_{\text{vol}}. \tag{2.28}$$

Additionally, changes to the composition of scatterers in the ground resolution cell or its dielectric characteristics between acquisitions add to the degree of decorrelation. Causes can be seasonal changes in vegetation, the movement of leaves or grass due to wind, the freezing or thawing of the surface layer, or human activities. This type of decorrelation is referred to as temporal decorrelation. It depends on environmental parameters, such as the type of land cover, sensor parameters, such as the wavelength, and the temporal baseline, i.e., the amount of time between acquisitions [62, 66]. Some features, such as areas with dense forest, tend to decorrelate easily [90, 91], while others, such as man-made structures, can be stable over long periods of time [92].

Atmospheric Phase Delay

Another factor to consider is the influence of varying atmospheric conditions on the travel time of radar signals. InSAR and DInSAR rely on precise measurements of time delays and differential phase shifts in order to calculate geometric distances and thus estimate the local topography or ground surface deformations. Artifacts in the fringe pattern of interferograms, most likely related to a change in the atmospheric conditions between image acquisitions, have already been observed in the first differential interferogram mapping the co-seismic displacement field of the Landers earthquake. The differential interferogram shows a 25-by-20 km large feature that cannot be explained by local topography, i.e., a DEM error, or ground surface deformation. The feature is not present in every differential interferogram mapping the co-seismic displacement field but in every differential interferogram generated with the SAR image acquired in July 1992, supporting the presumption that a change in the atmospheric conditions is the cause [93]. A similar artifact has been observed in two of ten interferograms mapping the deflation of Mount Ethna between May 1992 and October 1993 [94]. Goldstein et al. (1995) conducted a study concerning the effects of varying atmospheric conditions on the travel path length of radar signals in repeat-pass InSAR. Using SAR data acquired over the Mojave Desert in California on three separate days with two wavelengths, 24 cm and 5.7 cm (L- and C-band, respectively), they demonstrated the non-dispersive nature of the observed effect. This characteristic suggests that the predominant part of the atmospheric signal in interferograms originates in the troposphere, rather than the ionosphere. Additionally, no correlation was found between topography and the results. However, a correlation with time delays derived from water vapor radiometer data for the three days of the SAR images could be established. In contrast, later studies showed that the atmospheric phase delay is influenced by atmospheric stratification. Thus, a topography-related component does exist, and a variation in the density of free electrons in the ionosphere results in a group delay and phase advance for a radar signal traversing the ionosphere, which are inversely proportional to frequency squared. In the case of InSAR and DInSAR measurements only the shift in the phase is relevant [95, 96, 97, 98, 99, 100].

So far in this chapter, the assumption has been made that the radar signal propagates at a constant known velocity from the sensor to the imaged surface and back. That is, however, not true if the radar signal propagates through the inhomogeneous atmosphere of the Earth. The atmosphere of the Earth has a slightly higher refraction index than free space, i.e., the propagation velocity of the radar signal is lowered, resulting in an additional time delay [11]. The difference between the refraction index of free space and the refraction index of a propagation medium is referred to as the refractivity index. In the case of the propagation of microwaves through the atmosphere, three factors significantly influence the refractivity index. One, the stratification of the atmosphere. The atmosphere can be imagined as multiple thin layers, each having a different constant refractivity. Second, the distribution of water vapor significantly influences the refractivity index of the troposphere at a specific slant range distance R from the radar sensor. The water vapor content and its distribution are variable over time and space. Second, the refractivity index of the ionosphere is influenced significantly by its density of free electrons, which depends on the activity of the sun, the atmospheric density profile, the magnitude and orientation of the magnetic field of the Earth, as well as the geographic location, and the time of day. All factors contaminate the measured time delays and differential phase shifts with spatially and temporally variable additional time delays. These additional time delays can be falsely interpreted as local topography or ground surface deformation [11, 96, 97, 101].

The phase shift ψ of a radar signal propagating through a medium depends on the refraction index $n(R)$ of the medium, the wavelength λ, and the slant range distance R from the sensor:

$$\psi = \frac{2\pi}{\lambda} n(R) \cdot R. \tag{2.29}$$

The refraction index of free space is $n(R)= 1$. In case the radar signal passes through the atmosphere of the Earth, the refraction index changes to $n(R)= 1 + 10^{(-6)} N(R)$, with $N(R)$ being the refractivity index of the neutral atmosphere. The change of the refraction index from the value 1, in the case of free space, to the neutral atmosphere of the Earth is always positive and very small, hence the factor 10^{-6}. Thus, Equation 2.29 changes to:

$$\psi = \frac{2\pi}{\lambda} R + \frac{2\pi \cdot 10^{-6} N(R)}{\lambda} R - 2\pi \frac{2 \cdot 40.28}{c \cdot f_0^2} \cdot \mathrm{TEC} = \frac{2\pi}{\lambda} R + \frac{2\pi}{\lambda} \Delta R - 2\pi \frac{2 \cdot 40.28}{c \cdot f_0^2} \cdot \mathrm{TEC} \tag{2.30}$$

with

$$\Delta R = 10^{-6} N(R) \cdot R. \tag{2.31}$$

Here, TEC is the column density of free electrons integrated along the vertical, also referred to as total electron content. Equation 2.30 expresses the additional phase shift, added to the observed phase ψ, in terms of three contributions: (1) the hydrostatic, (2) wet and (3) the ionospheric delay [11, 97]. The contribution due to hydrostatic delay is influenced by the pressure ν in the atmosphere, while the contribution due to water vapor by only the partial pressure of the water vapor e. Both contributions are influenced by the temperature ϖ in the atmosphere and can be approximated by:

$$\Delta R = 7.76 \cdot 10^{-5} \int_0^{R_{\text{Path}}} \frac{\nu}{\varpi} dR + 3.73 \cdot 10^{-1} \int_0^{R_{\text{Path}}} \frac{e}{\varpi^2} dR \tag{2.32}$$

Here, R_{Path} represents the total length of the propagation path. The constants preceding the integrals are valid for normal variations in humidity, pressure, and temperature, and for frequencies up to 30 GHz within about 0.5 %. The theoretical value for the additional phase shift, calculated with Equation 2.32, deviates from the observed one for a number of reasons [11].

First, the phase shift depends on the atmospheric conditions, such as pressure, temperature, and the partial pressure of water vapor along the propagation path of the signal, which is not easy to acquire for all points recorded in the SAR images. Therefore, the values along the propagation path are approximated based on values observed at the surface and models describing their altitude dependencies. Secondly, the models relating the values for pressure, temperature, and partial pressure of water vapor at the surface to the values along the propagation path of the signal only consider vertical slices of the atmosphere instead of inclined ones corresponding to the incidence angle of the radar system. If the atmospheric conditions are spatially variable due to turbulent mixing, the observed values of a reference point at the surface might not be closely related to the values along the actual inclined propagation path. Similarly, in Equation 2.30 the density of free electrons is integrated along a vertical column instead of an inclined one. Thus, the third term of Equation 2.30 needs to be multiplied by a geometry-dependent factor to account for the typically non-nadir looking SAR systems. Thirdly, the equation above implies that the propagation path of the radar signal is a straight line, even though the true propagation path is curved due to refraction. Discrepancies due to the curved propagation paths can be neglected since only differential distances are of interest for InSAR and DInSAR.

Despite all these discrepancies, the total additional two-way phase delay can be deduced with the following equation:

$$\Delta\psi = \frac{4\pi}{\lambda}\frac{\Delta R}{cos(\theta)} - 2\pi\frac{2 \cdot 40.28}{c \cdot f_0^2} \cdot \text{TEC}. \tag{2.33}$$

Here, θ is the look angle. The second term in Equation 2.30 and the first term in Equation 2.33 shows that the tropospheric phase delay is strictly proportional to $\frac{1}{\lambda}$ and that ΔR is independent of the wavelength. The last term in Equation 2.30 and 2.33 shows that the ionospheric phase delay is dependent on the carrier frequency f_0 of the SAR system [10, 11, 97, 98].

In the case of the tropospheric phase delay, measurements with different frequencies will experience the same additional time delay, and the effect cannot be determined by employing multi-frequency measurements. It is also not possible to measure the refractivity index of the atmosphere with sufficient accuracy, spatial resolution, and temporal sampling to eliminate the effect entirely from interferograms. GNSS can eliminate features with a long wavelength (λ>10 km) if methods on time series or networks are employed. In addition, the atmospheric phase delay is not easily distinguished from phase signatures due to topography, ground surface deformation, or orbital errors that map as linear trends into the entire interferogram [10, 11]. In the case of the ionospheric phase delay, approaches such as Split Bandwidth InSAR or Multi-squint InSAR are sensitive to ionospheric gradients and thus, can be used to correct for the ionospheric influence [96].

As for the magnitude of the error caused by the tropospheric delay, a distinction needs to be made between repeat-pass InSAR to estimate topography and two- and three-pass DInSAR to map ground surface deformation. For topography estimation, studies [11, 12] have shown that the magnitude of the height error is inversely proportional to the perpendicular baseline $b_\perp$. Thus, longer baselines produce smaller errors. The relationship between phase inaccuracies ε_ψ and height errors ε_h can be calculated with [11, 86]:

$$\varepsilon_h = \frac{\lambda R \cdot sin(\theta)}{4\pi \cdot b_\perp} \varepsilon_\psi \tag{2.34}$$

A change of 20 % in humidity between SAR image acquisitions, for example, can lead to a 290 m error in the topography estimation for a 100 m baseline and less than 100 m error for a 400 m baseline.

In the case of two-pass interferometry, the relationship between phase inaccuracies ε_ψ and deformation errors ε_d is independent from the perpendicular baseline [11]:

$$\varepsilon_d = \frac{\lambda}{4\pi} \varepsilon_\psi \tag{2.35}$$

In addition, potential phase inaccuracy introduced by errors in the DEM, which is used to correct for topographically induced phase, needs to be considered. The inverse of Equation 2.34 can be used to estimate the phase inaccuracy. For example, a DEM with an effective error of 10 m leads to a phase error of 0.25 rad for an L-band radar with a perpendicular baseline of 100 m, pointing at a 45° angle off nadir at 300 km range. A phase error of 0.25 rad results in a deformation error of 0.5 cm. Assuming that the external DEM used for two-pass DInSAR is correct, a 20 % change of humidity in the atmosphere in between SAR image acquisitions would lead to a deformation error of 10 cm.

For three-pass interferometry, the effect of the atmospheric phase delay on two interferograms needs to be considered. Here, the deformation error ε_d depends on the baseline component parallel to the LOS of the sensor from the topography pair $b_{\|,\,\mathrm{topo}}$ and the deformation pair $b_{\|,\,\mathrm{defo}}$:

$$\varepsilon_d = \frac{\lambda}{4\pi} \sqrt{1 - \frac{b_{\|,\mathrm{defo}}}{b_{\|,\mathrm{topo}}} + \frac{b^2_{\|,\mathrm{defo}}}{b^2_{\|,\mathrm{topo}}}} \varepsilon_\psi. \tag{2.36}$$

If equal parallel baseline lengths, as in the example for two-pass DInSAR, can be assumed, the deformation error or three-pass DInSAR resulting from a 20 % change in humidity between acquisitions results in a 14 cm error. Generally speaking, the deformation error of three-pass DInSAR due to influences of varying atmospheric conditions is $\sqrt{2}$ times the error of two-pass DInSAR [11].

As previously stated, the magnitude of the ionospheric induced error depends on the carrier frequency f_0 of the SAR system, for example, with a P-band or L-band system a phase advance of 7.5 or 2.6 cycles per TEC unit (which equals a TEC of 10^{16}), can be observed, respectively. In the case of SAR systems with shorter wavelengths, such as C- or X-band, 0.61 or 0.34 cycles per TEC unit can be observed, respectively [98].

As mentioned above, determining the atmospheric phase delay deterministically is impossible. However, one approach is to develop a mathematical model that describes its behavior stochastically and employ a time series of differential interferograms to estimate the atmospheric phase screen (APS) [10]. A time series of differential interferograms can also be used to identify features that exhibit high coherence over a long time span [102] and use these features to mitigate the influence of temporal and geometric decorrelation as well as varying atmospheric conditions [103]. Algorithms exploiting a multi-image framework to estimate reliable deformation rates are referred to as advanced DInSAR. The most important algorithms are introduced in the next section.

2.1.6 Advanced Differential Synthetic Aperture Radar Interferometry

Overview of Noteworthy Advanced DInSAR Algorithms

Usai et al. (1997) suggested using highly coherent pixels to mitigate the effects of temporal and geometric decorrelation in order to monitor slow-moving deformation. In order to identify such pixels, they examined a series of interferograms over Groningen in the Netherlands. The area is affected by subsidence due to gas extraction. They were able to identify a subset of pixels that kept a coherence higher than 0.8 for the entire examined time span. The identified highly coherent features were mainly of anthropogenic origin. Calculating the differential phase of these features showed that most of them also exhibited a stable phase over the examined time span. The research of Usai et al. (1997) laid the foundation for the development of a number of algorithms referred to as advanced DInSAR techniques. All advanced DInSAR algorithms have in common that they exploit a series of differential interferograms instead of only one to estimate reliable deformation rates. The key idea of advanced DInSAR is outlined in the following section. Noteworthy advanced DInSAR algorithms will briefly be introduced and their key features are summarized in Table 2.4. However, the focus will be on the two most relevant for the presented research, PSInSAR^{TM} [13], the first complete advanced DInSAR algorithm to be presented, and the StaMPS [14, 51]. Both algorithms employ a single-reference image configuration, but they use different pixel selection criteria. The StaMPS algorithm is adapted to provide reliable deformation measurements in urban and non-urban areas, while the approach of PSInSAR^{TM} tends to favor urban environments. Since the source code of StaMPS is publicly available, it functions as the basis for the research presented in the following chapters.

The backscattered signal of a ground resolution cell is the coherent sum of the radar echo of its individual scatterers. Slight changes in the imaging geometry or a change in the composition of the individual scatters lead to a different coherent sum and thus a loss of coherence over time [9, 10, 62, 73]. Two types of scatterers are typically associated with advanced DInSAR because they maintain coherence, Persistent Scatterer (PS) and Distributed Scatterer (DS). The ground resolution cell of a PS pixel is dominated by one scatterer, minimizing the influence of the other scatterers in the ground resolution cell and thus reducing the effects of decorrelation [13, 14]. DS pixels are characterized by their similarity to adjacent pixels. Spatial averaging is used to maintain coherence over time [16].

The first complete algorithm exploiting PS pixels to estimate reliable deformation rates is the PSInSAR$^{\text{TM}}$ [13]. The algorithm uses a single-reference image time series of differential interferograms and the amplitude dispersion index D_A as a measure of the phase stability to select a subset of pixels as PS. Aligning the secondary images with the reference image, generating interferograms, and subtracting the topography-induced phase contribution aside, the PSInSAR$^{\text{TM}}$ algorithm can be divided into four steps:

(1) Preliminary selection of pixels as PS

(2) Model and subtract the phase contributions due to
    a) DEM errors and
    b) a surface deformation with a constant velocity

(3) Estimate APS and correct the originally observed phase for it

(4) Recalculate DEM errors and the surface deformation model

The signal of each pixel in a differential interferogram consists of a complex reflectivity g superimposed with complex circular gaussian noise n. Both the real (n_{R}) and imaginary (n_{I}) component of the noise are characterized by a power σ_n^2. In order to select a subset of the pixels as PS candidates (PSC), the distribution of their amplitude values A_w over the observation time is examined. In general, their distribution can be described by the Rice distribution, whose shape depends on the SNR. For low SNR, the Rice probability density function (PDF) approaches a Rayleigh distribution and a Gaussian distribution for high SNR. If a high SNR can be assumed, the standard deviation of the amplitude values σ_A can be approximated by the standard deviation of the real component $\sigma_{n_{\mathrm{R}}}$ of the noise, which is equal to standard deviation of the imaginary component $\sigma_{n_{\mathrm{I}}}$. With that the phase stability σ_v can be approximated as follow, in the case of high SNR:

$$\sigma_v \simeq \frac{\sigma_A}{m_A} \equiv D_A \tag{2.37}$$

Here, m_A denotes the mean of the amplitude values and D_A the amplitude dispersion index. Ferretti et al. (2002) considers pixels with $D_A < 0.25$ to be PSC. The wrapped differential phase ψ of each selected PSC is the sum of multiple phase contributions:

$$\psi_{\mathrm{Diff}} = W\{\phi_{\mathrm{Atmo}} + \Delta\phi_{\mathrm{Topo}} + \phi_{\mathrm{Defo}} + \Delta\phi_{\mathrm{Orbit}} + \phi_{\mathrm{Noise}}\} \tag{2.38}$$

Here, $W\{\}$ is the wrapping operator, ϕ_{Atmo} the absolute phase due to a change in atmospheric condition in between acquisitions, $\Delta\phi_{\mathrm{Topo}}$ the residual absolute topography-induced phase due to DEM errors, ϕ_{Defo} the absolute deformation-induced phase, $\Delta\phi_{\mathrm{Orbit}}$ the residual absolute due to orbit uncertainties and ϕ_{Noise} the phase noise. In addition to the phase contributions listed in Equation 2.38, the differential phase is influenced by environmental factors such as soil moisture [104]. However, they are not listed Equation 2.38 because

the PSInSAR^{TM} algorithm [13] does not consider them. In an iterative process, starting with the phase values of the differential interferograms with small spatial and temporal baselines, PSInSAR^{TM} estimates the phase contributions induced by deformation and residual topography using a constant velocity model and exploiting their proportionality to the baseline. Phase contributions due to orbit uncertainties and varying atmospheric conditions are estimated as a phase ramp. In the next step, the estimated phase contributions are subtracted from the differential phase, leaving phase residues due to atmospheric phase effects not modeled in the estimated phase ramp and phase noise. The remaining atmospheric effects are estimated by spatially smoothing the residual phase. Once the complete APS is estimated, interpolated, and subtracted from the original differential interferograms, the phase contributions due to deformation and residual topography are recalculated. Small phase residuals may reveal further PS pixels. Similar algorithms have been developed by Werner et al. (2003), Interferometric Point Target Analysis (IPTA), and Kampes et al. (2006), who adapted the LAMBDA method usually used for GNSS analysis to PSI. The IPTA includes low spectral phase diversity as a selection criterion to accommodate smaller datasets. The initial selection of pixels is later refined using the standard deviation of the phase with respect to the estimated linear deformation model. Kampes et al. (2006) included the signal-to-clutter ratio as a selection criterion and allowed for deformation models other than a linear model. The StaMPS algorithm is a modification of the standard PSI algorithms developed to maximize the selection of PS pixels in non-urban areas, where approaches based on thresholding the amplitude dispersion index underperforms. The algorithm selects pixels based on their phase characteristics and thus allows for the selection of pixels characterized by low-amplitude natural targets. Additionally, the algorithm does not assume any specific deformation model, only spatial smoothness [14, 51, 52]. Perssini et al. (2011) introduced the concept of temporary PS with the quasi-PS technique. In general, advanced DInSAR algorithms targeting PS pixels are referred to as PSI.
The above-listed algorithms all use a single-reference image configuration. Alternatively, multiple reference images can be used to calculate differential interferograms with small spatial and temporal baselines. This approach was first introduced by Berardino et al. (2002). SBAS mainly targets DS pixels. The optimization for small baselines and spectral filtering reduces the effects of decorrelation [15]. Spectral filtering is not advised in PSI, since, due to the resulting coarse resolution, it may increase decorrelation [108]. Two other algorithms with similar approaches were presented by Mora et al. (2003) and Schmidt and Bürgmann (2003). Both the original SBAS algorithm and the one presented by Schmidt and Bürgman (2003) assume spatial smoothness of the observed surface deformation. The latter additionally assumes a temporal smoothness of the surface deformation. Mora et al. (2003) expect a linear surface model. Another noteworthy algorithm is SqueeSAR^{TM} [16], which processes PS and DS jointly. The algorithms and their key features are summarized in Table 2.4.

Algorithm	Baseline Configuration	Main Scattering Mechanism	Pixel Selection Criteria	Deformation Model Assumptions
Ferretti et al. (2002)	Single-Reference Image	PS	Amplitude dispersion	Linear model in time
Werner et al. (2003)	Single-Reference Image	PS	Amplitude dispersion & spectral phase diversity	Linear model in time
Kampes et al. (2006)	Single-Reference Image	PS	Amplitude dispersion & signal to clutter ratio	Different types of models
Berardino et al. (2002)	Small baselines	DS	Coherence	Spatial smoothness
Mora et al. (2003)	Small baselines	DS	Coherence	Linear model in time
Schmidt and Bürgmann (2003)	Small baselines	DS	Coherence	Spatial and temporal smoothness
Hooper et al. (2004, 2007,2007)	Single-Reference Image	DS	Amplitude dispersion and phase characteristics	Spatial smoothness
Perssini et al. (2011)	Subset of differential interferograms depending on the target	Temporary PS	Quasi-PS approach	Linear model in time
Ferretti et al. (2011)	Multi-Reference Image	PS and DS	Statistical homogeneity test	

Table 2.4.: Key features of different advanced DInSAR algorithms [53].

Stanford Method for Persistent Scatterer (StaMPS)

The PSI algorithm StaMPS [14, 51, 52], which serves as the base framework for the research presented in the following chapters, can be broken down into five steps:

(1) Selection of PSC,

(2) Iterative estimation of phase noise,

(3) Selection of PS,

(4) Estimation of displacement and

(5) Estimation of phase correction terms.

Steps 4 and 5 are executed iteratively to ease phase unwrapping and improve the estimates for the deformation rates.

In the first step, PSC selection, for each pixel, the amplitude values A_w in the SAR image time series are tested for zero entries. If a zero entry is detected, the corresponding pixel is excluded from the PSC selection process. The PSC selection is based on the amplitude dispersion index on a pixel-by-pixel basis using Equation 2.37. While Ferretti et al. (2002) used a strict threshold of $D_A < 0.25$ to select the initial subset of PSC pixels, StaMPS uses a more relaxed approach to thresholding. The default value is 0.4, but depending on the dataset, the threshold could also be set higher, or thresholding could be foregone entirely. The actual PS selection is based on an analysis of the phase values of Q differential interferograms, and selecting PSC is only performed to limit the need for computational power.

For the second step of the StaMPS algorithm, the estimation of the phase noise, the wrapped phase $\psi_{\text{Diff},i,q}$ of the ith pixel in the qth differential interferogram is described as follows:

$$\psi_{\text{Diff},i,q} = W\{\phi_{\text{Defo},i,q} + \phi_{\text{Atmo},i,q} + \Delta\phi_{\text{Orbit},i,q} + \Delta\phi_{\theta,i,q} + \phi_{\text{Noise},i,q}\} \tag{2.39}$$

The differential phase is the sum of five separate phase contributions:

(1) $\phi_{\text{Defo},i,q}$, induced by surface deformation,

(2) $\phi_{\text{Atmo},i,q}$, induced by varying atmospheric conditions between image acquisitions,

(3) $\Delta\phi_{\text{Orbit},i,q}$, induced by orbit inaccuracies,

(4) $\Delta\phi_{\theta,i,q}$, induced by the look angle error and

(5) $\phi_{\text{Noise},i,q}$, the phase noise.

In addition to the phase contributions listed in Equation 2.39, the differential phase is influenced by environmental factors such as soil moisture [104]. However, they are not listed Equation 2.39 because the StaMPS algorithm [13] does not consider them a separate contribution. Also, the difference in labeling the phase contributions between Equations 2.38 and 2.39 stems from Hooper et al. (2004, 2007, 2007) considering differences in the positioning of the phase centers between SAR images as a source of error for any inaccuracies in the height above the reference surface, in addition to errors in the DEM. Both error sources are accumulated in the term $\Delta\phi_\theta$ and according to Equation 2.10 can be estimated using:

$$\Delta\phi_\theta \approx \frac{4\pi}{\lambda} \cdot b_\perp(\theta)\Delta\theta \tag{2.40}$$

The equation describes a linear relationship between $\Delta\phi_\theta$ and a difference in look angle $\Delta\theta$ between reference and secondary images, hence the label look angle error. Pixels deemed PS pixels are characterized by a small phase noise component $|\phi_{\text{Noise}}|$. In order to estimate the phase noise, contributions to the differential phase other than noise need to be estimated and subtracted. The first three phase contributions $\phi_{\text{Defo},i,q}$, $\phi_{\text{Atmo},i,q}$, $\Delta\phi_{\text{Orbit},i,q}$, and part of the fourth $\Delta\phi_{\theta,i,q}$ are spatially correlated and can be estimated by using a bandpass filter in the frequency domain. The filtered phase $\tilde{\psi}_{\text{Diff},i,q}$ is then subtracted from the original phase $\psi_{\text{Diff},i,q}$, leaving only the spatially uncorrelated phase contributions and small residues for $\phi_{\text{Defo},i,q}$, $\phi_{\text{Atmo},i,q}$ and $\Delta\phi_{\text{Orbit},i,q}$, which are represented as $\delta_{i,q}$:

$$W\{\psi_{\text{Diff},i,q} - \tilde{\psi}_{\text{Diff},i,q}\} = W\{\Delta\phi^{\text{nc}}_{\theta,i,q} + \phi^{\text{nc}}_{\text{Noise},i,q} + \delta_{i,q}\} \tag{2.41}$$

The spatially uncorrelated part of the look-angle error can be estimated by fitting Equation 2.40 to the residual phase in a least-squares manner. Subtracting the estimated phase $\Delta\widehat{\phi}^{\text{nc}}_{\theta,i,q}$ leaves:

$$W\{\psi_{\text{Diff},i,q} - \tilde{\psi}_{\text{Diff},i,q} - \Delta\widehat{\phi}^{\text{nc}}_{\theta,i,q}\} = W\{\phi^{\text{nc}}_{\text{Noise},i,q} + \delta'_{i,q}\} \tag{2.42}$$

Here, $\delta'_{i,q}$ is the sum of any remaining phase contributions due to deformation, varying atmospheric conditions, orbit, and look angle inaccuracies, which are expected to be small. Based on the equations above, a measure for the variations of the residual phase is defined as:

$$\gamma_i = \frac{1}{Q}\left|\sum_{q=1}^{Q} exp\{j(\psi_{\text{Diff},i,q} - \tilde{\psi}_{\text{Diff},i,q} - \Delta\widehat{\phi}^{\text{nc}}_{\theta,i,q})\}\right| \tag{2.43}$$

The measure of residual phase variability γ can be used to calculate the probability $P(i \in \text{PS})$ with which the PSC pixel in question is a PS pixel. Estimating the phase noise accurately is an iterative step, weeding out the PSC pixels that are not a PS pixel. In the first iteration the PSC pixels are weighted with $\frac{1}{D_A}$ and in later iterations with $\frac{1}{[P(i \in PS)]^2}$. The process is terminated when the difference $\Delta\gamma$ between the current and previous iterations is smaller than 0.005. The selection of the final subset of PS pixels is based on $P(i \in \text{PS})$ and D_A. Following that, duplicates and PS pixels, which originate from scatterers in neighboring pixels, are excluded.

In order to calculate the deformation rates, the differential phase needs to be unwrapped. StaMPS employs a 3D optimization phase unwrapping algorithm [52, 111]. Delaunay Triangulation is used to define arcs connecting PS pixels in each differential interferogram, and the phase difference on each arc is calculated. The resulting phase difference time series is then unwrapped in time by first filtering the time series with a Gaussian window in the frequency domain, calculating the phase difference between timestamps of the filtered

time series. Following that, the time series is wrapped so that its values range between $-\pi$ and π. The wrapped time series is then integrated. The original phase difference time series for each arch is unwrapped on the basis that its absolute difference to the filtered and wrapped time series must be less than π. After unwrapping the arch time series, each interferogram is unwrapped in space. StaMPS uses the optimization routine of the statistical-cost network-flow algorithm for phase unwrapping (SNAPHU) [112]. The unwrapped phase still contains unwanted phase contributions induced by varying atmospheric conditions, orbit, and look angle inaccuracies. These unwanted contributions to the differential phase are estimated by filtering. The last two steps are executed iteratively, so that estimates for the unwanted phase contributions can be subtracted from the wrapped differential phase to ease phase unwrapping and improve the calculated deformation rates.
Independent of the specific algorithm, PSI is a well-established remote sensing technique and has been used in the last two decades to map naturally occurring surface deformation such as post-glacial uplift [21], aseismic creep alongside active faults [22, 23], slope instability [24, 113] and sinkholes [25, 26] as well as human induced surface deformation, e.g., varying uplift and subsidence due to seasonal groundwater usage [27] or gas storage [28, 29] and subsidence due to continuing urbanization [30]. Quickly, becoming an alternative in the scientific community, for applications where documenting surface deformation with ground-based geodetic methods is time- and labor-intensive [4, 5].
Additionally, PSI has been used to study the surface deformation of large infrastructure elements such as bridges [31], dams [32], or levees [33], clearly showing its potential to be incorporated into long-term monitoring of the structural health of large-scale human infrastructure.
In the following chapters, adaptations to the above introduced StaMPS algorithm to accommodate for a long-term continuous monitoring of large-scale human infrastructure and the risk of human settlements due to geo-hazards, as well as a post-processing tool to automatically asses the temporal development of the observed surface deformation are presented and demonstrated on S1 and TSX SAR data covering the city of Patras and the Parapeiros-Peiros Dam south-west of Patras, which is an embankment dam.

2.2 Overview on Dams

About 34 dam structures already existed worldwide around the time most ancient civilizations started to keep records [114]. The number increased to 300 by the end of the 16th century. Those dams were mainly used for water storage [48], while today's purposes of dams additionally include flood control, energy generation, irrigation, and recreation [115]. Until the turn of the 20th century, dam construction followed intuition rather than scientific rules. Only then engineers incorporated scientific considerations of soil mechanics and construction techniques. Every building site has its unique regional and local conditions, which need to be considered during the planning stage of a dam.

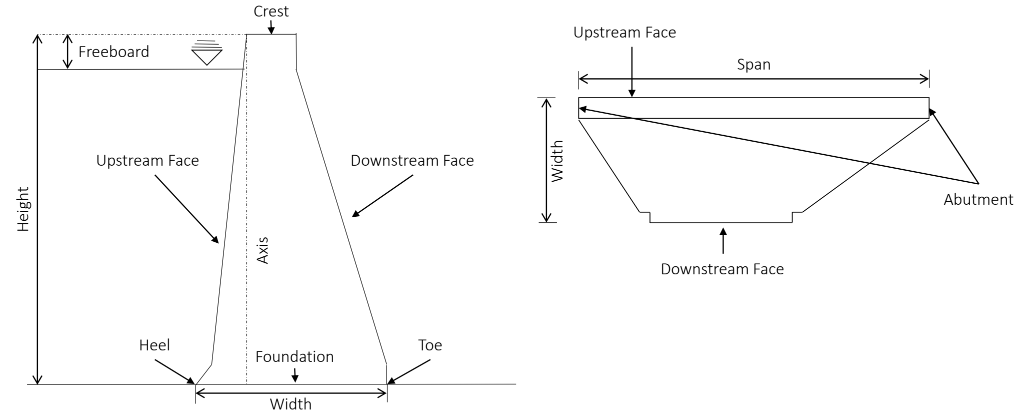

Figure 2.7.: The cross-section and plan view of a non-overflow section of a typical gravity dam [115, 117].

The local geology, morphology, topography, and hydrology do play a role in the safety and performance of a dam structure. Favorable conditions are, for example, adequate bearing capacity and low permeability of the foundation, a smooth and symmetrical valley with gentle slopes, high flanks around the reservoir with long seepage paths to neighboring valleys, no existing faults and seismic activity. However, dam sites hardly ever meet all the favorable conditions. Various dam construction types were developed to meet the unique set of characteristics of each dam site [48]. Most construction types can be categorized as either embankment (earth- and rockfill embankment dams) or concrete dams (gravity, arch and buttress dams). Each of them has its own characteristic merits and disadvantages, which need to be considered when choosing a construction type. Embankment dams, for example, are generally considered to be able to accommodate substantial deformation, while they have a weak resistance against overtopping. Concrete dams, on the other hand, are capable of withstanding overtopping for hours [116].

2.2.1 Construction Types

Concrete Dams

In the case of concrete dams, a further distinction between gravity, arch and buttress dams is made. Gravity dams are not only the most commonly used type of concrete dams, but they are also the most straightforward in design and construction. The dam body is designed to withstand the imposed pressure of the reservoir water purely by its weight. The structure usually consists of non-overflow and overflow sections [117]. A cross-section and plan view of a non-overflow section of a typical gravity dam is shown in Figure 2.7. Both the non-overflow and overflow section consists of a crest, downstream and upstream face. In the case of the non-overflow section, the downstream face is uniform and usually inclines in the order of 1:0.7 to 1:0.8. Located between the downstream and upstream face near-maximum reservoir water level is the crest. The crest is the highest point of the dam body and is designed to accommodate a road, withstand the impact of floating objects, and provide the desired freeboard. The term freeboard denotes the vertical difference between the maximum reservoir water level and the height of the dam body. The upstream face is usually approximately vertical. The overflow section differs from the non-overflow section in the sense that overflow is possible. The crest is lowered and curved, and the slope of the downstream face is made tangent to the crest. The overflow section might be overbuilt by a bridge to connect the roads on top of the non-overflow sections. The dam is built in blocks separated by transverse contraction joints. The joints extend vertically from the foundation to the crest and horizontally from the downstream to the upstream face. During the design stage, engineers need to consider the following loads:

(1) the dead load of the dam body,

(2) the pressure of earth and silt building up at the heel of the dam,

(3) ice pressure,

(4) wind pressure,

(5) varying temperatures,

(6) sub-atmospheric pressure,

(7) reaction of the foundation,

(8) pressure of the head- and tailwater (water on the upstream and downstream face) against the dam body,

(9) internal water pressure causing differential uplift within the body and

(10) imposing forces due to earthquakes.

Furthermore, due to their immense weight, gravity dams require a solid rock foundation [117]. A weak foundation may lead to differential settlement or sliding of the dam body resulting in cracking and possibly failure [116]. However, if a gravity dam is built on clay, shale, or other weak rock foundations, special treatment of the foundation to control seepage and ensure sliding resistance are necessary [117]. The advantages of gravity dams are their durability and their capability to withstand overtopping for several hours [116]. A buttress dam is similar to a gravity dam in the sense that it also utilizes its weight to withstand the pressure of the reservoir water. Additionally, a buttress dam employs the weight of the reservoir water over the upstream face to achieve stability. Figure 2.8 shows the cross-section and plan view of a typical buttress dam. The dam body consists of two main components: the sloping upstream deck and the buttresses. In comparison to a solid gravity dam, a buttress dam requires less concrete. However, its construction is complicated. In general, engineers have to consider the same loads while planning and

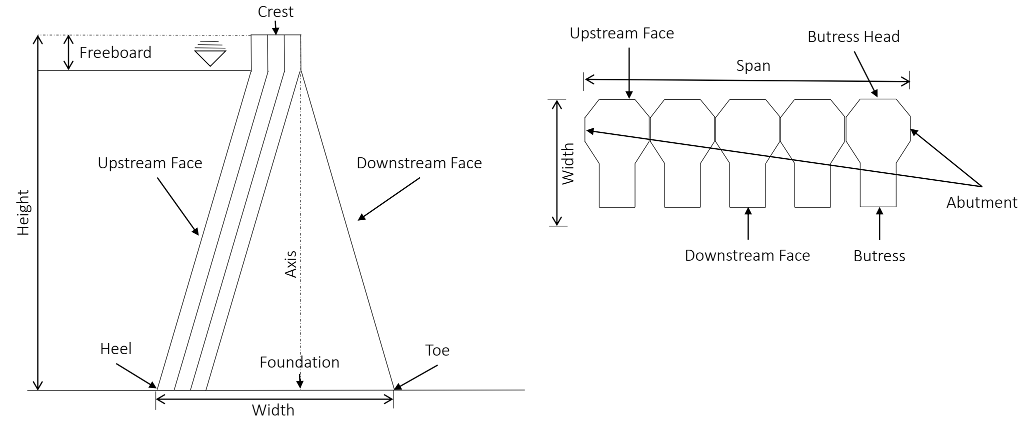

Figure 2.8.: The cross-section and plan view of a typical buttress dam [115, 117].

building a buttress dam as they do for a gravity dam [117].
The third type of concrete dams is the arch dam. It is the most efficiently designed type of concrete dam, but also the most complex one to plan and build [118]. Arch dams are further categorized into single- and double-curved arch dams. A single-curved arch dam is only curved horizontally, while a double-curved arch dam is curved horizontally and vertically [119]. The cross-section and plan view of a typical double-curved arch dam is shown in Figure 2.9. The hydrostatic load is transmitted to the valley walls and the foundation due to the curvature of the dam body. Therefore, the dam site does not only require a rock foundation, but also abutments with sufficient strength to support the arch thrust. Furthermore, arch dams are designed to withstand the same loads as a gravity dam. However, the expected temperature range of the dam needs special attention. A varying temperature changes the stress distribution within the dam body and thus affects its geometric form [119].

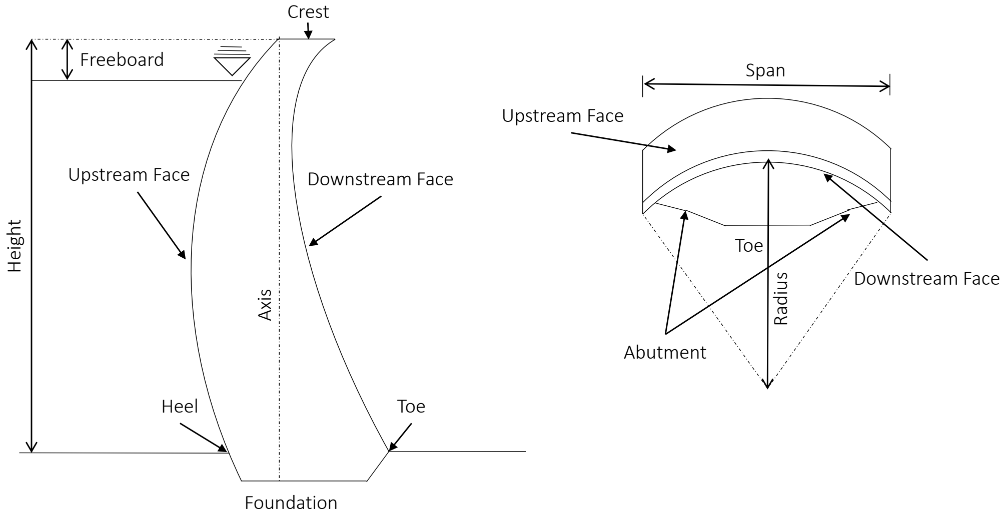

Figure 2.9.: The cross-section and plan view of a typical two-curvature arch dam [119].

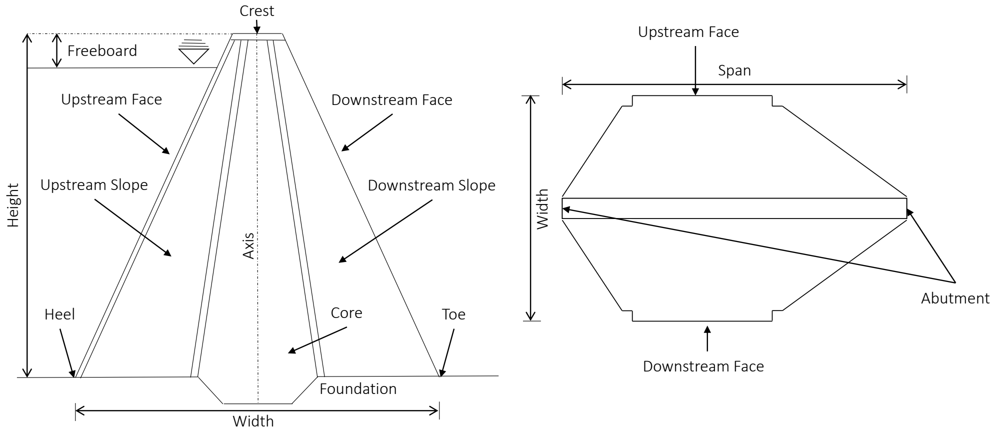

Figure 2.10.: The cross-section and plan view of a typical embankment dam [115].

Embankment Dams

In contrast to concrete dam structures, embankment dams are constructed using naturally occurring earth- or rockfill found at or near the dam site. They are the most commonly used type of dams. Up to 75 % of all dams worldwide are embankment dams [120]. Since the building materials are acquired locally, the exact choice of the material varies considerably, resulting in a unique structure for each dam. The most basic design only incorporates one type of cohesive soil with a low permeability. These types of embankment dams are referred to as homogeneous dams. However, the term homogeneous does only refer to the fact that a single type of soil is used. Characteristic soil parameters such as permeability are not uniform within the dam body. The soil is laid out in different layers during construction, which leads to zones of varying permeability. The usage of cohesive soils with a low shear strength, such as clay or silt, restricts the maximum height of homogeneous dams to 35 m. This type of dam has been built for millennia to secure the freshwater supply and for flood control. A more modern type of embankment dam is the zoned earth-fill embankment dam. This type of dam uses more than one type of soil arranged in horizontal zones consisting of soils with varying permeability. Usually, the permeability increases from the inner zones to the outer zones, while the deformability decreases in the same manner. This way of constructing an embankment dam has two advantages. First, non-cohesive soils can be used, which are easier to handle during construction. Second, non-cohesive soils develop a higher shear strength making steeper slopes possible. Steeper slopes lead to a reduction in the dam volume [48]. The cross-section of an embankment dam has a triangular shape, as is illustrated in Figure 2.10. The two slopes of the dam body are referred to as the upstream and downstream shoulder or slope. A protective layer made of tight, strong, and durable material usually covers their surfaces to prevent erosion. Erosion of the upstream shoulder occurs due to wave action. Therefore, the protective layer of the upstream slope needs to extend from at least a few meters below the minimum headwater level to the crest. Suitable materials to use are, for example, ingenious and metamorphic rock or strong limestone. The upstream shoulder itself should be free-draining to improve stability during drawdown events and prevent soil liquefaction during an earthquake. Erosion of the downstream slope is generally caused by rainfall or the local wildlife [121]. The downstream slope is covered from at least a few meters below the minimum tailwater level to the crest. The dam crest needs to be constructed so that it withstands the impact of floating objects, wave action, ice and wind pressure, as well as traffic accidents. The width of the crest depends on its usage. Just as concrete dams, most embankment dams accommodate a road on top of their crest [48]. The necessary freeboard needs to be determined conservatively because earth-fill dams, in particular, are vulnerable to overtopping. The core of a zoned embankment dam serves as the seepage barrier. It is either located centrally or sloping towards the upstream face [121]. Rockfill can also be used instead of earth-fill to construct an embankment dam. The main characteristic that distinguishes rockfill from earth-fill is the particle size. In the case of rockfill, the average particle size should be at least 5 cm. The permeable and free-draining rockfill is only used to construct the shoulders. The core is constructed with an impervious material such as clay. Alternatively, imperviousness can be ensured using a concrete sealing of the upstream slope. In contrast to homogeneous dams, rockfill dams can reach a height well over 300 m [122].

The advantage of an embankment dam, in general, is that it can withstand substantial deformation triggered by either earthquakes or differential subsidence of the foundation. For that reason, these dams do not require a solid rock foundation. However, a disadvantage is that they can hardly withstand overtopping. Therefore, their freeboard and associated spillway capacity need to be determined conservatively [121].

2.2.2 Expected Deformation of an Embankment Dam

In the same way as concrete dams, an embankment dam is subject to the following loads:

(1) the dead load of the dam body,

(2) the pressure of earth and silt building up at the heel of the dam,

(3) ice pressure,

(4) wind pressure,

(5) varying temperatures,

(6) sub-atmospheric pressure,

(7) reaction of the foundation,

(8) pressure of the head- and tailwater against the dam body,

(9) internal water pressure causing differential uplift within the body and

(10) imposing forces due to earthquakes [117].

An embankment dam is constructed to accommodate substantial deformation due to these loads. Nevertheless, to ensure dam safety, it is essential to understand the mechanisms initiating the deformation of the dam body. Within the scope of this thesis, we differentiate between three deformation patterns: (1) subsidence, (2) uplift, and (3) horizontal displacement. The first deformation pattern is a downwards directed deformation. The foundation and building material of the dam are subject to consolidation resulting in subsidence. The dead load of each newly added layer of earth- or rockfill increases the load acting on the layers below and the foundation. The imposed loads in the center and at the edges of the dam differ from one another. The varying imposed loads and the usage of different building materials lead to varying subsidence rates in the core and the shoulders. The consolidation process is expected to start during the construction period and continue during the first filling of the reservoir and long after [48]. Additional subsidence may be observed during the first filling of the reservoir. The increasing dead load of the reservoir water further compresses the foundation and construction material on the upstream face. Differential subsidence rates alongside the upstream side of the crest and the upstream shoulder are the consequences. Moreover, the possibility of collapse compression needs to be considered [47]. Unsaturated soils compact upon wetting [123]. In the case of an embankment dam, this phenomenon mainly affects the upstream shoulder and upstream side of the crest. It leads to differential subsidence, crest spreading, and longitudinal crest cracking. The magnitude of the subsidence rates depends on the type and placement technique of the construction material [47]. For most dams, the total subsidence of the crest amounts to less than 0.5 % of dam height three years after the construction ended and less than 0.75 % of dam height after ten years. The subsidence in the upstream and downstream shoulders can measure up to 2 % of the dam height, though higher values have been observed in the case of dry placed, poorly compacted rockfill [47]. Spatially, the maximum subsidence rate is usually located at 50 to 70 % of the height of the dam body [48]. The subsidence rates typically exhibit a linear trend over the logarithm of time. However, the long-term trend is significantly influenced by reservoir operations. Drawdown events are usually associated with periods of rapid acceleration of the subsidence rates [47]. The second deformation pattern is an upwards directed deformation. Buoyant uplift is a consequence of a decrease in the effective stress due to the increasing water load during the first filling of the reservoir. Only the upstream shoulder is affected by this phenomenon. The effects of collapse compression might obscure the observation of the buoyant uplift, since both phenomena coincide [47]. Thirdly, horizontal displacement downstream of the entire dam body is caused by an increased lateral tension within the dam body. The increase of the lateral tension inside the dam body originates from an increase in the water pressure in the upstream side of the core during the first filling. Since the displacement rate does not depend on the dam height, a range of absolute values can be provided. On the downstream side of the crest, total typical horizontal displacements range from 50 mm upstream to 200 mm downstream. On the upstream side of the crest and in the upstream shoulder, the displacement varies between 200 mm upstream and

200 mm downstream. The horizontal displacements on the downstream shoulder range from 0 mm to 250 mm downstream. However, larger horizontal displacements have been observed, for example, at the Suvartevann Dam. The dam experienced a downstream displacement of the crest of 1120 mm during the first filling. The general trend is a steady or slow displacement in a downstream direction, and the displacement rates usually approach near zero over time [47]. Some loads can trigger a combination of subsidence, uplift, and horizontal displacement. Seasonal variations of the reservoir water level can result in alternating uplift and subsidence of the dam body [125]. An earthquake can trigger abrupt short-term deformation in the form of subsidence or spreading of the dam body [126, 127] the horizontal displacement of the dam slopes, failure of the crest, or landslides sliding into the reservoir [48]. Soil liquefaction, also triggered by an earthquake, may additionally change the geometric shape of the dam body [124]. Furthermore, the stability of the slopes bordering the reservoir is of concern. A mass sliding into the reservoir causes large waves, and depending on the wave height may result in overtopping [48]. The above described deformations are summarized in Table 2.5.

Phenomena	Deformation Pattern	Location	Likelihood
Consolidation of foundation and building material	Subsidence	Entire dam body	Expected
Deadweight of the reservoir water	Subsidence	Upstream slope & Upstream side of the crest	Expected
Decreasing effective stress	Buoyant uplift	Upstream slope	Expected
Lateral tension	Horizontal displacement	Entire dam body	Expected
Collapse Compression	Subsidence	Upstream slope & Upstream side of the crest	Maybe
Drawdown Events	Subsidence	Entire dam body	Maybe
Seasonal varying water level	Subsidence & uplift	Entire dam body	Maybe
Sliding	Horizontal displacement & subsidence	Enclosing slopes	Unlikely
Soil liquefaction	Subsidence	Entire or parts of the dam body	Unlikely
Earthquake	Subsidence & horizontal displacement	Entire or parts of the dam body	Unlikely

Table 2.5.: Overview of the phenomena causing a deformation of a dam body [48, 47, 124].

2.2.3 Methods for Monitoring the Surface Deformation of an Embankment Dam

In order to control the safety and performance of a dam during its entire lifetime, a monitoring system must be set up. Regular inspections of the dam body, the reservoir, and the nearby environment for signs of subsidence, horizontal displacement, cracking, erosion, seepage, and undesired growth of vegetation need to be conducted. These inspections are supplemented by measurements recorded by several different instruments that are distributed on the dam body and its vicinity. While the selection of the type of instrument, its location, and a timely interpretation of the data is more important than the sheer number of instruments installed, engineers need to keep in mind the vulnerability of the instruments. Over time, the number of installed instruments, still working, will decline [48, 121]. In the case of an embankment dam, the main features to monitor are the deformation of the dam body and the quality and quantity of the seepage water. Further, it is recommended to monitor the earth and pore-water pressure inside the dam body using, for example, pressure cells and determine the phreatic line by analyzing data. Furthermore, the fluctuation of the groundwater should be controlled by installing groundwater observation holes along the toe of the dam. In seismically active areas, it is recommended to install at least one seismograph in the crest and at the bottom of the dam to register earthquakes. The water seeping through the dam is controlled for suspended particles to detect erosion inside the dam body. Its chemical composition is analyzed for the same reason. Therefore, a measuring weir is built at the deepest point along the toe of the dam. It is usually a trough made of concrete with a v-shaped outlet calibrated for direct readings [48]. The deformation of the dam body is usually only monitored on a limited number of control points. The locations of the control points must be chosen so that the behavior of the entire structure can be determined [125]. In the last century, geodetic triangulation and optical leveling networks have both been widely used to determine displacements. Geodetic triangulation provides 2D horizontal displacement, while optical leveling supplies vertical displacements. Concrete pillars on the crest of the dam and in stable areas in the vicinity are usually used as control points [128, 129, 130]. Optical leveling is an exact method. Vertical displacements can be measured with a precision of up to 2 $\frac{\text{mm}}{\text{km}}$. The disadvantages of the method are that it is very time-consuming, and it cannot be used continuously [125, 131]. Geodetic triangulation, in contrast to optical leveling, can be included in a continuous monitoring system, if robotic total stations are used. Reflectors are permanently installed on the dam, and a high-precision rangefinder measures their 3D coordinates [132, 133]. Both methods are usually complemented by measurements of local deformations utilizing, for example, extensometers and inclinometers [125]. In more recent years, the GNSS has been employed to determine the 3D coordinates of control points. In terms of time and cost-effectiveness, it is the most efficient method. No visibility between the control points and the reference point is needed, which allows the monitoring of larger areas. Expert operators are only needed for the initial set-up of the network and the data interpretation [134]. Another well-established instrument to monitor horizontal displacements is an optical collimator. The instrument measures the horizontal deviation in LOS between a stand-point and a portable target. The portable target can be deployed along the crest of the dam. The accuracy depends on the distance between the stand-point and the portable target, as well as changes in the atmospheric refractive index [135]. A precision on the sub-millimeter level can be achieved. Normal optical collimators need to be handled manually [136]. However, automatic collimators are used on some dams to measure horizontal displacement continuously [135]. Employing the method Terrestrial-Based Radio Frequency is a more innovative approach. The method provides 3D displacements of specific control points with an accuracy on centimeter-level vertically and millimeter-level horizontally [144]. Another approach to map the deformation of a dam is to not only measure the displacement of specific control points, but to use methods for areal deformation monitoring. Terrestrial Laser Scanning (TLS), for example, provides measurements of 3D distances with a high spatial density. The high density of measuring points might be exploited for change detection algorithms. However, the accuracy of the measurements is lower than the ones achieved using total stations.[145, 143]. Ground-based Synthetic Aperture Radar (GBSAR), on the other hand, provides high precision (± 1 mm) measurements of relative displacements in LOS direction [137]. The radar sensor moves along a rail track while emitting and receiving microwaves. The

Method	Measured Value	Accuracy	In Use
Geodetic Triangulation Network	Horizontal displacements	100/30 $\frac{\text{mm}}{\text{km}}$	yes
Optical Leveling Network	Vertical displacements	2 $\frac{\text{mm}}{\text{km}}$	yes
Inclinometer	Horizontal deformation along depth profile	± 7 mm	yes
Extensometer	Changes in length of an object over time	± 1 mm	yes
Optical Collimator	Horizontal displacements	Less then: ± 1 mm	yes
Terrestrial-Based Radio Frequency	3D displacements	Vertically: ± 1 cm Horizontally: ± 1 mm	experimentally
Terrestrial Laser Scanning	3D distances	± 2 mm to ± 25 mm	experimentally
GPS	3D Positions	± 15 mm	yes
GBSAR	Relative displacements in LOS	± 1 mm	experimentally
PSInSAR	Relative displacements in LOS	± 1 mm	experimentally

Table 2.6.: Overview of methods used to monitor dam deformation [19, 20, 128, 129, 130, 131, 134, 136, 137, 138, 139, 140, 141, 142, 143, 144].

system can be installed permanently in front of any given structure, making it suitable for carrying out near real-time deformation monitoring [146]. Another advantage is that no instruments need to be installed on the dam, and the deformation can be monitored from a safe distance. Furthermore, the system can be used under any weather and light conditions. However, the accuracy of the results depends on variations of the relative humidity between the sensor and the target. The fact that the relative displacements are measured in the LOS direction is a further disadvantage. Moreover, measuring the relative displacement in the LOS direction has the consequence that a movement perpendicular to the LOS direction is not detectable [126, 146, 147, 148, 149]. Spaceborne InSAR is similar to GBSAR. The difference is that the SAR sensor is installed on a satellite. In particular, the technique PSI has been used in a few case studies to reconstruct dam failures or analyze short periods of the lifetime of a dam [150, 151]. The technique itself and its advantages are further discussed in Section 2.1.6. The above described techniques and instruments to monitor the deformation of a dam body, the slopes enclosing the reservoir, and the surrounding area are summarized in Table 2.6.

3 Area-of-Interest, Datasets and Software

3.1 Area-of-Interest: North-West Peloponnese

The AOI is located in the Achaea prefecture in the north-west of the Peloponnese Peninsula, Greece. It covers about 2,100 km^2 of terrain. The AOI includes the cities of Patras and Rio, at the coastline of the Gulf of Patras and the westernmost part of the Gulf of Corinth, and more rural areas with small human settlements to the south and west. The terrain is flat at the coastline, but it quickly becomes mountainous inland with the Erymanthos and Panachaiko mountain chains in the south and east. The highest elevation in the area is at 2,200 m above sea level. Prominent features in the AOI are the Rio-Andirrio bridge and the newly built Parapeiros-Peiros Dam southwest of Patras. A map of the AOI and the location of the Parapeiros-Peiros Dam are presented in Figure 3.1. The AOI was selected because, due to its complexity, it provides many different examples of naturally occurring and anthropogenic ground surface deformation. The AOI is located in one of the most-seismically active areas of the world and is pervaded with various active faults, along which ground surface deformation can be observed. Additionally, it is one of Greece's most landslide prone areas. As for examples of anthropogenic ground surface deformation, the AOI features human settlements and infrastructure, which are affected

Figure 3.1.: AOI located in the North-West of the Peloponnese Peninsula.

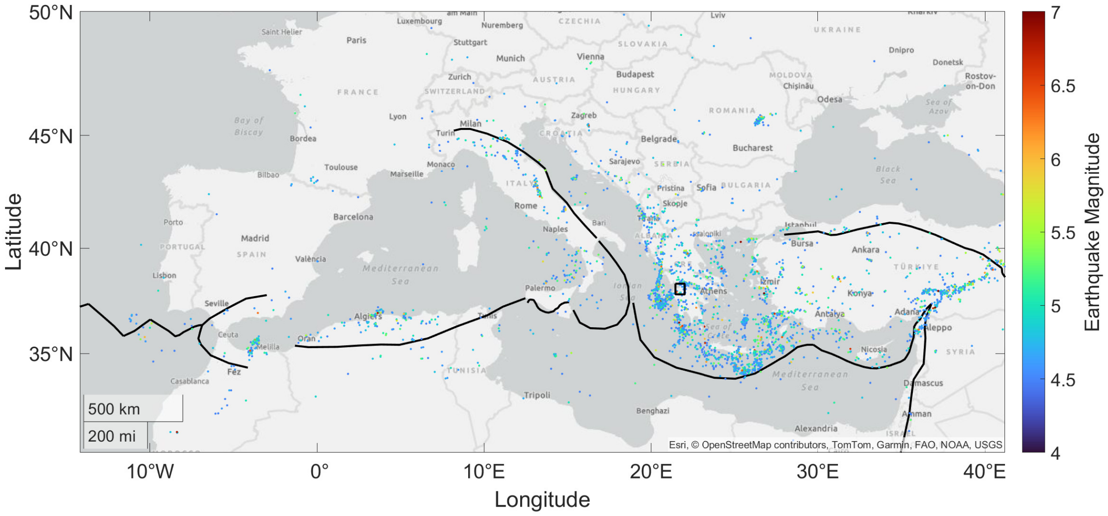

Esri, © OpenStreetMap contributors, TomTom, Garmin, FAO, NOAA, USGS

Figure 3.2.: The Mediterranean with tectonic plate boundaries (black lines) [152], earthquake epicenters (colored points) [153] for the time span from 2000 to 2025 and the AOI (black rectangle).

by the local geo-hazards, subsidence due to the continuing urbanization of the area and deformation due to environmental influences, e.g., expansion and shrinking due to a varying temperature. Overall various surface deformation phenomena can be observed at the same time in this area. This section provides a brief overview of the relevant causes for naturally occurring and human-induced ground surface deformation within the AOI, starting with seismotectonic setting of the area.

The first order seismotectonic model of the Mediterranean is defined by the relative motion between the Eurasian, African, and Arabian tectonic plates. The plate boundary between Eurasia and Africa starts at the Azores triple junction, i.e., where the Eurasian, African, and North American tectonic plates meet, and stretches through the Mediterranean south of Spain, mainland Italy, and Greece and lastly to Cyprus. If Eurasia is assumed to be stable, the African plate moves northward in a counter-clockwise manner. The plate boundary features a pure right-lateral strike-slip motion at the Gloria fault in the Atlantic and oblique convergence eastwards through the Mediterranean. The plates converge with a rate of 4.4 $\frac{\text{mm}}{\text{year}}$ at the longitude of Algiers and 5.5 $\frac{\text{mm}}{\text{year}}$ at the longitude of Cyprus. The tectonic plate boundaries [152] and earthquake epicenters [153] for the Mediterranean are displayed in Figure 3.2. The eastern Mediterranean exhibits significantly more seismic activity than the western Mediterranean, which is due to the more complex interaction of the tectonic plates. The relative motion of the Eurasian and African plates is disturbed in the eastern Mediterranean by two smaller rapidly moving tectonic plates, the Aegean and Turkish plates. The Aegean plate includes Greece, Crete and the western part of Turkey, while the Turkish plate consists of Cyprus and the remaining part of Turkey. The interaction of the Eurasian and Aegean plates is characterized by a strike-slip motion and spreading. With respect to Eurasia, the Aegean plate moves in a southwest direction towards the

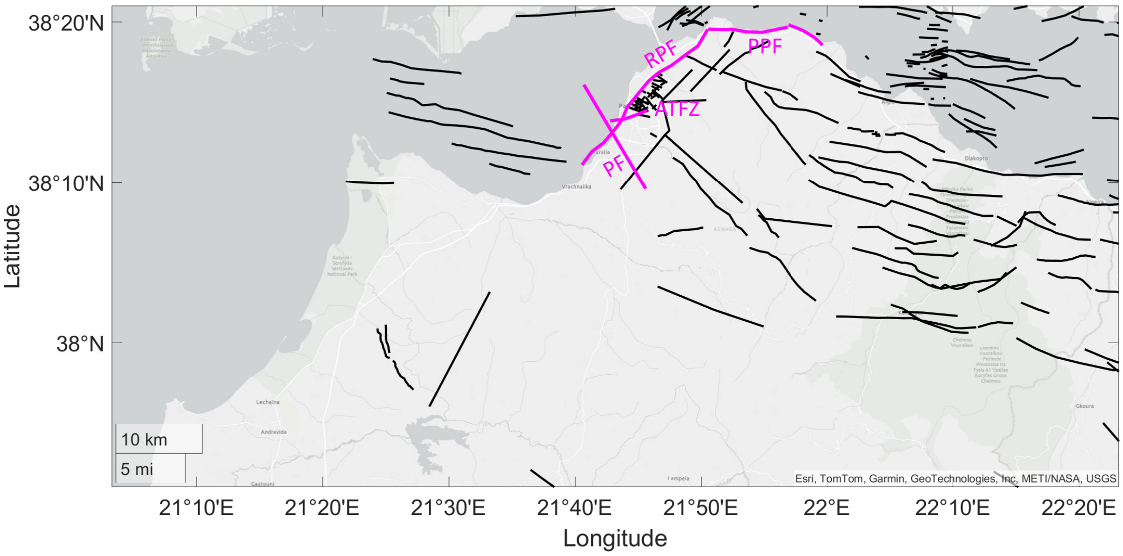

Figure 3.3.: The AOI with active fault traces (major faults in magenta and other faults in black lines) [159] and the location of the Parapeiros-Peiros Dam (marked in magenta).

African plate. At the Hellenic Trench, the oceanic lithosphere of the African plate is subducting underneath the continental lithosphere of the Aegean plate with a rate close to $4\,\frac{\text{cm}}{\text{year}}$ [154, 155, 156]. The Aegean plate itself is undergoing extension, which concentrates in several zones of graben development. Associated earthquake epicenters cluster in an about 200 km long and 40 km wide belt that cuts across the Hellenides from the Aegean to the Ionian Sea. The Gulf of Patras and the Gulf of Corinth are located at the center of this belt. Both are asymmetric grabens that form an about 140 km long rift belt separating the pre-Neogene folded basement of mainland Greece and the Peloponnese Peninsula. They intersect at a strait between Rio, on the northern coastline of the Peloponnese, and Nafpaktos, on the southern coastline of mainland Greece. It is one of the most rapidly extending regions of the world. About 500 active faults associated with this graben system cut across the North-West Peloponnese [157, 158]. The trace of major faults relevant for the AOI are presented in Figure 3.3. The Psathopyrgos fault (PPF) and the Rion-Patras fault (RPF) trace through the north-eastern part of the AOI along the coastline of the westernmost part of the Gulf of Corinth and eastern part of the Gulf of Patras. The Aigia Triada fault zone (ATFZ) cuts right through downtown Patras from the coastline eastwards inland. The Patras fault (PF) is located in the southern outskirts of Patras and traces from the coastline east-southwards inland. All traces were extracted from the 5th release of the NOAFAULTs database [159], which provides information on the fault geometry of 2,916 faults located in Greece based on 140 peer-reviewed publications. Studies such as [160], [161], and [162] have shown that the cities of Patras and Rio and surrounding areas are subject to ground surface deformation, possibly related to active faults. Together, the studies analyzed the ground surface deformation of the area between 1992 and 2017 using different SAR Sensors (ERS-1/2, ENVISAT, and Sentinel-1) and different advanced

DInSAR processing techniques (PSI [13, 14], SBAS [15], and SqueeSAR^{TM}[16]). All three studies observed contrasting zones of uplift and subsidence in Patras, subsidence in Rio, and near the Psathopyrgos Fault. Additionally, Elias and Briole (2018) observed subsidence in Selienitika and uplift in Aigion. Sakkas et al. (2018) documented an eastwards motion south of the Patras city.

In Addition to ground surface deformation due to tectonic faulting, most of the mountainous areas in the Achaia prefecture experience slope instability, which results in various degrees of ground surface displacement down slope [163]. In other words, the area is prone to landslides. Sabatakakis et al. (2013) established a landslide susceptibility map for Greece based 10 predisposing factors for landslides: (1) lithology, (2) slope angle, (3) elevation, (4) hydrographic network-drainage density, (5) rainfall, (6)climate, (7) seismicity, (8) land use, (9) road network density and (10) population density. Based on these predisposing factors, the Achaia prefecture features a moderate susceptibility for landslides at the coastlines and a very high susceptibility in the mountainous areas. About 600 landslides in the mountainous areas of the north-western Peloponnese have been detected based on advanced DInSAR data for the time from 1993 to 2017 [165]. Along with the cities of Patras and Rio and the mountainous areas affected by landslides, the AOI features large and important infrastructure elements such as the Parapeiros-Peiros Dam and the Rio-Andirrio bridge. Various studies have shown that large infrastructure elements are subject to deformation due to changing environmental temperature, compaction of their foundation, or as a consequence of internal damage [31, 32, 166].

Within the scope of this research, a focus will be on the Parapeiros-Peiros Dam. The dam is located south-west of Patras and features a 75 m high and 760 m long earth-fill embankment dam built between 2008 and 2017. The dam body impounds the water of the Parapeiros and Peiros Rivers, starting in September 2019. The associated freshwater reservoir was designed to hold $44{\cdot}10^6$ m^3 of water, to supply the surrounding region with fresh water. After construction, the dam body was expected to settle due to its foundation and building material consolidating. Additional settlement was expected to be triggered by the foundation and building material being exposed to the increasing load of the stored water during the first filling of the reservoir [167].

3.2 Datasets

Within the scope of this thesis, three distinct datasets are used to demonstrate the presented research. In this section, the SAR missions that provided the used data and the composition of the three distinct datasets are briefly outlined.

SAR images recorded with the S1-A and -B sensors, as well as images recorded with the TSX sensors, are used. Additionally, a TanDEM-X DEM was acquired to remove the topography-induced phase during advanced DInSAR processing. The S1 SAR mission is part of the European Copernicus program led by the European Union. The European Space Agency (ESA) is in charge of the space component of the mission. The mission objective is to systematically and regularly record SAR data for European land and coastal areas, tectonic and volcanic areas worldwide, and other areas of interest for the Copernicus services. The observation plan stipulates regular mapping of all land areas worldwide, with a few exceptions, with a repeat-pass time of 12 days worldwide and 6 days over Europe. The observation plan is based on employing two SAR satellites. S1-A was launched in October 2014 and S1-B in October 2016. On the 23rd December 2021, S1-B experienced an anomaly on its sub-power system, which resulted in a permanent loss of the satellite for the mission. The loss of S1-B led to an increase in repeat-pass time over Europe from 6 to 12 days, similar to the time before S1-B was launched. However, from October 2016 to December 2021, the satellites recorded all land and coastal areas of Europe with a 6-day repeat-pass in ascending and descending orbits with dual polarization (VV and VH) in C-Band (5.6 cm). The main acquisition mode of the S1 satellites is referred to as IW swath. A 250 km wide swath is recorded with 5 m resolution in range and 20 m resolution in azimuth [34, 35, 36]. An imaging mode referred to as Terrain Observation by Progressive Scans (TOPSAR) is employed for the wide swath coverage. This wide swath is achieved by periodically steering the SAR antenna to adjacent sub-swath parallel in range. The steering of the antenna has the consequence that only a finite number of radar echoes are emitted and recorded to image a specific patch on the surface, i.e., the SAR image consists of a number of bursts [168]. The S1 satellites record three parallel sub-swaths with nine bursts each. In order to map and analyze ground surface deformation of the entire described AOI, S1 SAR images with a descending acquisition geometry were acquired from the Copernicus Dataspace (`https://browser.dataspace.copernicus.eu/`).

The TSX twin satellites are Germany's first national remote sensing satellite mission, which was implemented in a private-public partnership between the German Aerospace Center (DLR) and EADS Astrium GmbH. The satellites were launched in June 2007 and 2010. The TSX mission had two objectives. The first is providing high-quality SAR data with various acquisition modes for commercial and scientific purposes. Different acquisition modes can be used, providing a high variability in spatial coverage and resolution. The different acquisition modes and their spatial coverage and resolution are listed in Table 3.1. Additionally, the satellites can operate in different polarizations, namely: (1) HH, (2) VV, (3) HV, and (4) VH. The second objective of the TSX satellites, the TanDEM-X mission, is to create a global DEM. To generate high-quality interferograms as input for the DEM generation, the SAR images are recorded in a bi-static manner, meaning one satellite transmits the radar signal but both satellites receive the backscattered signal. To achieve this, the twin satellites orbit the Earth in a Helix formation. Both satellites operate in X-band (3.1 cm) and have a repeat-pass time of 11 days. In contrast to the S1 satellites, the TSX satellites do not continuously record the Earth's surface. They need to be tasked [49, 50, 169].

Since one focus of this research was the newly built Parapeiros-Peiros Dam south of Patras,

Mode	Scene Coverage az x rg [km^2]	Resolution Class [m]
Wide ScanSAR	200 x (194 - 266)	40
ScanSAR	150 x 100	18
StripMap	50 x 30	3
Spotlight	10 x 10	1.7 - 3.5
High-Resolution Spotlight	5 x 10	1.4 - 3.5
300 MHz High-Resolution Spotlight	5 x (5 - 10)	1.1 - 1.8
Staring Spotlight	(2.5 - 2.8) - $\sim$ 6	0.24 az

Table 3.1.: Overview of TSX acquisition modes [49].

a time series of high-resolution spotlight (300 MHz) TSX SAR images was acquired from the DLR within the scope of a research proposal. The images were recorded with a descending acquisition geometry and a spatial resolution of 0.6 m in slant range and 1.1 m in azimuth direction. The DEM used for the advanced DInSAR processing of the SAR images was created within the scope of the TanDEM-X mission based on TSX data from 2011 to 2013. The DEM has a 30 m spatial resolution and a relative height accuracy of 2 m at flat and 4 m at steep terrain. Furthermore, the global change map for the AOI, based on SAR images recorded between September 2017 and mid-2020 [169], was acquired and added to the TanDEM-X 30 m DEM to consider the changed topography due to the 2017 finished Parapeiros-Peiros Dam.

Within the scope of this thesis, three distinct datasets are used to demonstrate the research presented. The datasets are different combinations of the data presented above. An overview is provided in Table 3.2. Dataset A consists of a S1 SAR images time series with 138 images. The images were recorded with the acquisition mode IW swath and a descending image geometry. The time series covers the North-West corner of the Peloponnese Peninsula in Greece for the time span from September 2019 to September 2022. The dataset is used in Chapter 4 to demonstrate the capabilities of the post-processing tool PSDefoPAT® and in Chapter 5 to discuss the presented approach to use extracted information concerning temporal and spatial deformation patterns from Dataset A to support the processing of Dataset B. Dataset B consists of 84 high-resolution (HS-300) TSX SAR images covering the area around the Parapeiros-Peiros Dam for the time span from September 2019 to September 2022. The images were also recorded with a descending imaging geometry. The dataset is used in Chapter 5. The final dataset, Dataset C, is

Dataset	Chapter	Satellite Mission	Acquisition Mode	Nr. SAR Images	Time Span
Dataset A	4 & 5	S1	IW	138	09/2019 - 09/2022
Dataset B	5	TSX	HS-300	84	09/2019 - 09/2022
Dataset C	6	S1	IW	300	11/2016 - 12/2021

Table 3.2.: Overview of the datasets used within the scope of this thesis.

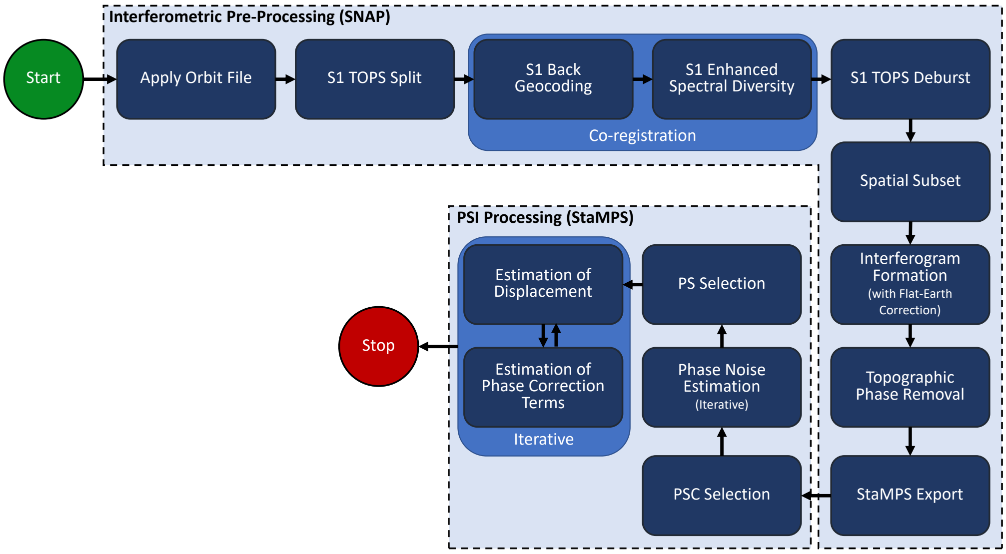

Figure 3.4.: Complete advanced DInSAR processing chain, where the interferometric processing was realized with SNAP and StaMPS serves as the PSI algorithm.

used in Chapter 6 to evaluate three different strategies for processing a steady stream of SAR images. The dataset consists of 300 S1 SAR images, which were recorded with the acquisition mode IW swath and a descending image geometry. The images record the North-West corner of the Peloponnese Peninsula in Greece for the time span from November 2016 to December 2021.

Even though Dataset C and Dataset A both use S1 images, they differ from one another for two reasons. Firstly, the surface deformation of the Parapeiros-Peiros Dam needed to be captured with TSX and S1 images for the same time span. Thus, the time span covered by Dataset A was selected to match that of Dataset B. In the case of Dataset C, the time series needed to cover a longer time span. Secondly, to avoid the influence of a switch in the temporal sampling of the S1 images, Dataset C was restricted to the time during which both S1-A and S1-B recorded images.

3.3 Software

The complete advanced DInSAR processing chain, used within the scope of this thesis and referred to as the conventional processing chain, is presented in Figure 3.4. It can be divided into two parts, (1) the interferometric pre-processing and the PSI processing. Within the scope of this thesis, the interferometric pre-processing is realized with the SeNtinel Application Plattform (SNAP) [170] provided free of charge by the ESA (`https://step.esa.int/main/download/snap-download/`). The needed steps and their sequence for processing S1 SAR images are presented in Figure 3.4. In the case TSX SAR images are processed, the steps: (1) Apply Orbit File, (2) S1 TOPS Split and (3) S1 TOPS Deburst

are skipped and the co-registration is carried out with a more general cross-correlation technique implemented in SNAP. In order to facilitate the automatized processing of large dataset the SNAP Graph Processing Tool (gpt) is operated using the python scripts.
The StaMPS [14, 51, 52] is used for the PSI processing, since it as commonly used and is freely available (`https://homepages.see.leeds.ac.uk/~earahoo/stamps/`). The general operating principle of the algorithm is presented in Sub-section 2.1.6. In order to take full advantage of the available hardware, parts of the StaMPS algorithm were re-implemented so that the entire algorithm can be executed within a Microsoft Windows based framework. To facilitate an easy reading of this thesis, the Microsoft Windows-adapted version of the StaMPS algorithm will simply be referred to as StaMPS, since the general operating principle was not changed. Adaptations to the StaMPS algorithm presented in Chapter 5 and Chapter 6 were implemented using the Microsoft Windows-adapted version of the StaMPS algorithm and necessary tests to verify their functionality are presented in the Appendix A.2.

4

Persistent Scatterer Deformation Pattern Analysis Tool

The following chapter includes text passages extracted from [55] M. Evers, A. Thiele, H. Hammer, and S. Hinz. “PSDefoPAT—Persistent Scatterer Deformation Pattern Analysis Tool”. In: *Remote Sensing* 15 (2023), 1–26, paper no. 4646, which are marked with a blue line

4.1 Problem Statement and State-of-the-Art

Earlier in this thesis, it was stressed that advanced DInSAR results are often evaluated and analyzed based on mean deformation velocity maps, which can be misleading because they are generated with the assumption of a constant velocity deformation model. While actively deforming areas and their spatial deformation patterns can be assessed at a glance, relying solely on them can lead to an underestimation or misinterpretation of the ground surface deformation. Many geophysical processes are often not sufficiently described by a linear trend. Ground surface deformation due to underground gas storage [28, 29], groundwater extraction [27] or the thermal expansion of large buildings [166] are periodic, while displacement rates of aseismic creep [22, 23] alongside tectonic faults or subsidence rates due to urbanization [30] can change over time and may result in a piecewise linear or quadratic trend.

To support civil protection authorities in assessing the risk to human settlements and infrastructure networks due to geohazards, identifying suitable mitigation measures, and implementing effective urban planning, it is essential to analyze the spatial patterns of ground surface deformation in conjunction with their temporal patterns. Changes in the temporal deformation pattern can act as a precursor to geohazard events or structural health failures of infrastructure elements. Thus, identifying the underlying temporal pattern of the ground surface deformation and any recent changes, e.g., acceleration, deceleration, or a varying amplitude of a periodic pattern, is a highly relevant task [39, 42, 171, 172]. With the launch of the S1 SAR satellites in 2014, 2016, and 2024, and the subsequent development of Ground Motion Services such as the European Ground Motion Service (EGMS), the door was opened to perform such analysis at a regional scale [40, 42, 173]. Manual inspection of the amount of accessible data is not feasible and poses a bottleneck for the operational use of advanced DInSAR products in monitoring tasks [174]. Thus, as emphasized in Section 1.1 automatic post-processing procedures to extract relevant information from the datasets are required to aid in the interpretation of ground motion datasets at a regional scale, providing a comprehensive picture of the evolution of movement [175]. Hence, the research question of how the results of advanced DInSAR processing can be utilized to provide information on the dynamic evolution of the deformation process.

A first attempt was presented by Cigna et al. (2011). They presented a semi-automated approach to identify potential changes in the underlying temporal pattern of displacement time series derived from advanced DInSAR processing. The proposed algorithm labels the individual displacement time series as either unaffected or affected. Unaffected in this context means that the MP is either stable and not moving or following an uninterrupted linear trend. Affected, on the other hand, is the label for MPs that undergo a change in their temporal deformation pattern. The approach was demonstrated using ERS-1/2 and RADARSAT-1 datasets, covering Naro in Italy from 1992 to 2000 and 2003 to 2007, which was affected by a seismic event in February 2005, reactivating ground instabilities. The systematic evaluation of advanced DInSAR enabled the mapping of areas where the temporal deformation pattern of MPs was affected by the event and those where it remained unaffected, thereby supporting civil protection authorities in identifying appropriate hazard mitigation measures. Berti et al. (2013) presented the first fully automatic algorithm to categorize advanced DInSAR displacement time series. The presented algorithm is based on a conditional sequence of statistical tests for six predefined time series models: (1) uncorrelated, (2) linear, (3) quadratic, (4) bilinear, (5) discontinuous with constant velocity, and (6) discontinuous with varying velocity. Although Berti et al. (2013) also acknowledge the possibility of periodicities in ground surface deformation, their algorithm does not incorporate time series models with a periodic component. The algorithm was developed and tested primarily to investigate slope instabilities. However, it is also noted that it could be used to analyze ground surface deformation caused by subsidence, soil swelling or shrinkage, or uplift due to deep injections. Chang and Hansen (2015) introduced an approach to systematically estimating kinematic models from interferometric displacement time series data based on multiple hypothesis testing. The developed algorithm utilizes hypothesis testing to estimate a mathematical model that describes the temporal deformation patterns. They consider the following set of time series models: (1) linear, (2) thermal expansion, (3) periodic with a fixed period of one year, (4) exponential, (5) the Kronecker delta function, and (6) the Heaviside step function or any combination of these time series models.

Contrary to the previously described algorithms, Boni et al. (2016) presented an approach for automatically categorizing the vertical and East-West components of advanced DInSAR displacement time series. Additionally, they analyze the average displacement time series of clusters rather than individual MPs. The algorithm considers linear, non-linear, and periodic deformation and consists of three steps. First, ascending and descending displacement time series are combined to decompose them into their vertical and East-West components. The second step aims to identify areas affected by the same type of deformation through statistical analysis. A cluster must have a minimum of three MPs with similar temporal deformation patterns. The average temporal pattern of the cluster is combined with geological, land-use, and hydrogeological data of the affected area to determine the underlying geological processes and triggering mechanisms or driving forces of the deformation. Bordoni et al. (2018) presented an automated approach to detect areas affected by ground surface deformation along slopes. The presented approach builds on previously published work by Boni et al. (2016). They added three steps. First, the MPs are divided into those located on slopes and those on plain areas. Secondly, MPs with uncorrelated trends are excluded from the analysis. Thirdly, the step to identify the underlying geological processes is tailored to slope instabilities, which allows them to categorize different portions of the same landslide into different types of slope movement related to landslide [177].

In contrast to the algorithms described above, the advanced DInSAR post-processing approach presented by Costantini et al. (2018) was developed for MPs identified on buildings. Similar to the approach presented by Boni et al. (2016) and Bordoni et al. (2018), the MPs are analyzed in clusters. The displacement time series of MPs in a cluster are averaged. The average displacement time series is labeled as either piecewise linear or a combined seasonal and linear displacement time series. MPs not included in one of the clusters are considered outliers and excluded from the analysis. The algorithm assumes that the AOI is an urban area with a dense MP grid. Mirmazloumi et al. (2022) presented an algorithm to automatically categorize advanced DInSAR displacement time series that builds on the algorithm presented by Berti et al. (2013). They consider the following seven categories: (1) stable, (2) linear, (3) quadratic, (4) bilinear, (5) discontinuous with constant velocity, (6) discontinuous with varying velocity, and (7) affected by unwrapping errors. The algorithm consists of five steps. First, MPs affected by phase unwrapping errors are excluded from the dataset. Secondly, the remaining MPs are tested to see whether they are stable or not, i.e., if they are affected by deformation. Their stability is determined by evaluating the significance of a linear regression fitted to the individual displacement time series. Thirdly, unstable MPs are examined for abrupt changes, i.e., a change point (CP). For MPs with no CP, a quadratic regression is carried out in the fourth step. MPs with a CP are tested for bilinearity, and subsequently, a test for equality of the slopes is conducted. Once the displacement time series are categorized, the fifth step is to recheck the time series for phase unwrapping errors. A test for underlying periodicity is conducted after the displacement time series are categorized according to their long-term trend. With this approach, they were able to categorize 77.8 % correctly. Festa et al. (2023) presented an automated approach to detect patterns of anthropogenic ground surface deformation in advanced DInSAR datasets to support risk assessment. They employ Principal Component Analysis and k-Means clustering. They first decompose the LOS displacement into its vertical and horizontal components and then perform a Principal Component Analysis, which serves as input for the k-Means clustering algorithm. The k-Means algorithm identifies clusters based on the temporal displacement patterns. Based on these clusters, the trend and periodic component of the average displacement time series are retrieved.

Most of the algorithms described above focus on a specific type of ground surface deformation, such as slope instabilities or subsidence. Even the most general ones focus on deformation, either driven by geophysical or anthropogenic processes. However, in order to integrate time series analysis of the displacement time series into broader monitoring systems, it should consider both geophysical and anthropogenically driven ground surface deformation. For example, Chang and Hansen (2015) consider periodic temporal deformation patterns but only with a fixed cycle length of one year, which is generally suitable for most natural ground surface deformation phenomena occurring in non-urbanized areas. However, it is not necessarily suitable for deformation processes in anthropogenic environments. Embankment dams, for example, deform in response to the water level of their reservoir [47], which can change due to water consumption or periods of heavy rainfall. Both phenomena often have a cycle length of one year, but can also have cycle lengths longer than a year, depending on the regional climate. Additionally, the water level changes in accordance with hydropower production, which depends on the power demand of the surrounding region and may not correspond to any naturally occurring processes. Another example of anthropogenic causes for ground surface deformation is the underground storage of gas [28, 29]. The ground surface deformation is influenced by the amount of gas either extracted from or pressed into the underground cavity, which depends on gas consumption and does not necessarily correspond to a periodicity of one year.

Another aspect to consider is that, in the case of continuous monitoring, the displacement time series continues to lengthen and may encompass more than two stages of the observed ground surface deformation. Therefore, time series analysis should allow for more than one change point. Also, when analyzing both geophysical and anthropogenically driven ground surface deformation, no assumption should be made concerning the spatial extent of the deformation phenomena. Especially, the deformation of an infrastructure element can be quite local.

In a nutshell, a post-processing procedure to identify the temporal pattern of actively deforming areas should function fully automatically, not assume the spatial extend of the observed surface deformation, include time series models that explain the temporal patterns of both geophysical and anthropogenically driven ground surface deformation, including time series models with multiple CPs and flexible cycle lengths, to integrate time series analysis of the displacement time series into broader monitoring systems. Subsequently, in this chapter, a fully automated algorithm for post-processing advanced DInSAR displacement time series is described. Its capabilities are demonstrated through two use cases. The first use case is the city of Patras and its surrounding region, and the second is the newly filled Parapeiros-Peiros Dam, located southwest of the city. The presented algorithm, the PSDefoPAT®, assigns each MP of an advanced DInSAR dataset a best-fitting time series model based on a series of statistical tests. This algorithm decomposes the displacement time series into its trend, periodic, and noise components. The periodic component can have cycle lengths other than one year, and the trend can be divided into multiple segments.

4.2 PSDefoPAT®—Time Series Analysis Approach

The Matlab-based tool PSDefoPAT® assigns each MP resulting from an advanced DInSAR algorithm a best-fitting time series model based on its associated displacement time series. The model provides information on the evolution of the deformation instead of only a snapshot as the mean velocity does [57, 56].

A time series is commonly defined as a sequence of measurements y_i of a specific variable, here the displacement of an MP between SAR image acquisitions, in chronological order but not necessarily equidistantly spaced. Time series analysis aims to determine a mathematical model that describes the evolution of the variable over time. A time series is often split into its trend, seasonal, cyclic, and residual components. The trend component describes the long-term evolution of a variable, while the seasonal and cyclic components describe behavior that repeats regularly. In the literature, the periodic behavior of a variable is referred to as seasonal if it is linked to seasonal effects, such as varying weather conditions over the course of a year. Periodicities linked to other causes are subsumed under the term cyclic [181, 182]. Here, we will refer to both components as periodic. The tool determines the trend $\hat{y}_\mathrm{T}$ and periodic $\hat{y}_\mathrm{P}$ components of a given time series separately from one another. The resulting deformation model $\hat{y}$ is the sum of the trend and periodic components, while the residual component $\hat{y}_\mathrm{R}$ represents the part of the time series that the model cannot explain.

$$\hat{y} = \hat{y}_\mathrm{T} + \hat{y}_\mathrm{P} + \hat{y}_\mathrm{R} \tag{4.1}$$

The tool can be used either manually or in an automated fashion. The main difference is that if the tool is used manually, the user must provide input during each processing step, and only selected MPs are processed. In contrast, if the tool is used in an automatized fashion, all MPs in the dataset are processed, and the user only has to provide input at the beginning of the process. The sequence of the processing steps for the automatized version of PSDefoPAT® is presented in Figure 4.1.

The processing chain given in Figure 4.1 can be divided into three topics:

(1) Time series de-noising,

(2) Estimating the periodic component,

(3) Estimating the trend component.

The thrid step, estimating the trend component, includes examining the displacement time series for CPs. The theoretical background of each topic is outlined in the next sub-section. Within the scope of this thesis, the focus will be on the automatized version of the post-processing tool, and an overview of the manual usage of the tool is provided in Evers et al. (2021). The approach used for the automatized version of the tool is demonstrated using two MPs selected from the PSI results of Dataset A, which is described in detail in Chapter 3. The MPs were selected so each processing step can be demonstrated and discussed based on an example. The first MP is referred to as MP I and is located at top of the dam body of Parapeiros-Peiros Dam in Greece. It was selected due to the piecewise linear trend of its time series. The second MP is called MP II and is located on the Rio-Antirio Bridge connecting the Peloponnese Peninsula to mainland Greece. This MP was selected because its displacement time series features a periodic component.
The relevant theoretical background on time series analysis and its realization in PSDefoPAT® are outlined in the next sub-section.

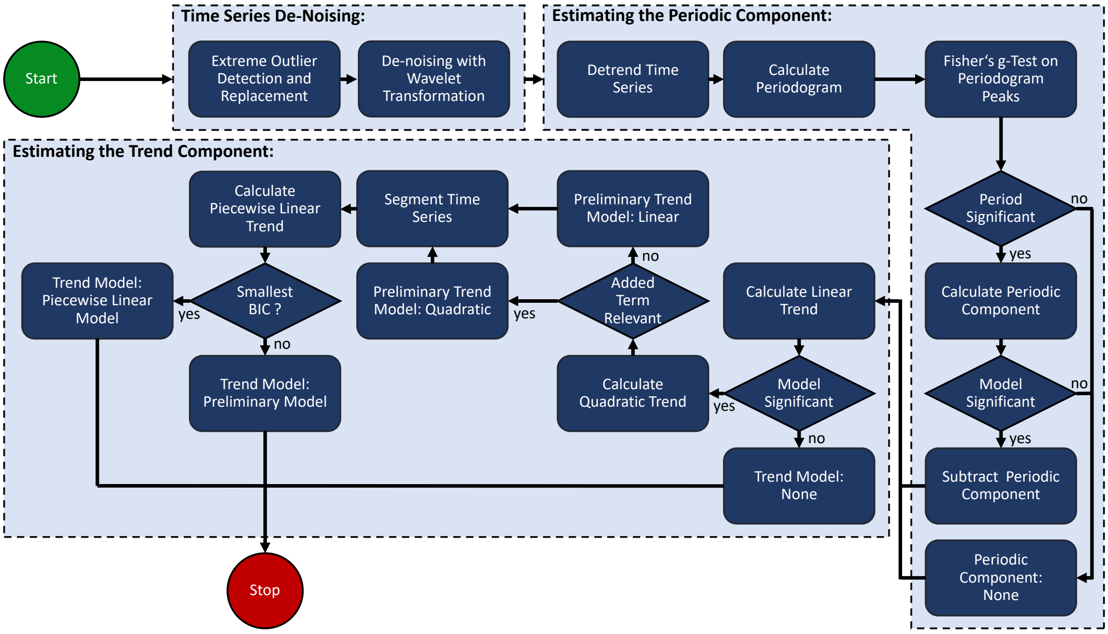

Figure 4.1.: Workflow of PSDefoPAT®.

4.2.1 Theoretical Background on Time Series Analysis

Time Series De-Noising

A time series can also be viewed as a combination of noise and a wanted signal. The wanted signal represents any pattern caused by the intrinsic dynamics of the observed process. The time series may additionally be affected by outliers. Outliers are unusual data points in the time series representing possible recording or processing errors. They can have a disruptive effect on time series model selection. PSDefoPAT® considers any data point y_i that deviates more than three times the scaled median absolute deviation from the median of the time series to be an extreme outlier. Extreme outliers are replaced using linear interpolation.

Smoothing or de-noising refers to the process of separating the wanted signal in the given time series from noise to reveal patterns previously obscured. An option to smooth the time series is the simple moving average, which replaces the data point y_T recorded at time point T with an average of y_T and J previous data points $y_{T-1}, ...y_{T-J}$ or an average of y_T and $\frac{J}{2}$ previous and subsequent data points $y_{T-\frac{J}{2}}, ..., y_{T-1}, y_{T+1}, ...y_{T+\frac{J}{2}}$. Similarly, the median could also be used instead of the average. However, a crucial point is to select the right size J of the window, in which the average or median is calculated. The size of the window determines how sensitively the moving average or median reacts to changes in the wanted signal. If the underlying pattern of the wanted signal remains unchanged, a large window is preferred, while a small window is preferable if the underlying pattern changes rapidly over time [181]. Thus, J would need to be selected with a priori knowledge of the time series. An alternative approach to extracting the wanted signal from the provided time series is de-noising using wavelet transformation (WT).

The key factor is that WT can be used to represent any signal. As with any transformation, WT shifts the time series from its original domain into another, possibly making operations such as signal compression or noise reduction easier to conduct [183]. The basic concept of WT is that piecewise regular signals can be described by base wavelet functions, similarly to how Fourier transformation is used to describe a periodic signal as a sum of sine and cosine functions [184].

The basic building block, also referred to as the mother wavelet $\zeta(t)$, of a wavelet basis is a wave-like function that oscillates around zero for a limited time. All other wavelets are generated by dilating or translating the mother wavelet.

$$\zeta_{s,o}(t) = \frac{1}{\sqrt{s}}\zeta\left(\frac{t-o}{s}\right) \tag{4.2}$$

The width of the wavelet non-zero part and its position in time are determined by the scaling parameter s and the translation parameter o [183, 185].

Noise reduction with WT requires wavelet coefficients derived with discrete wavelet transformation (DWT). The wavelet transform of signal $y(t)$ with N data points can be written in vector-matrix form as

$$X = \Gamma^{\mathrm{T}} y(t) \tag{4.3}$$

where X is a vector consisting of N wavelet coefficients χ_j and Γ is an $N \times N$ orthogonal matrix containing the wavelet-base vectors. The wavelet base is defined by wavelet filtering coefficients e_j. The number of coefficients varies depending on the wavelet base used. The Daubechies wavelet family, for example, is defined by $2n$ coefficients. In the case of the second-order Daubechies wavelet, n is 2. The coefficients are used to generate two filters: (1) a scaling filter S, which resembles a low-pass filter, and (2) a wavelet filter G, which is similar to a high-pass filter. The same coefficients define the filters, only in reversed order and with alternating signs. The filter matrices for a signal containing eight data points and n=2 can be written as follows [183]:

$$G = \begin{bmatrix} e_0 & e_1 & e_2 & e_3 & 0 & 0 & 0 & 0 \\ 0 & 0 & e_0 & e_1 & e_2 & e_3 & 0 & 0 \\ 0 & 0 & 0 & 0 & e_0 & e_1 & e_2 & e_3 \\ e_2 & e_3 & 0 & 0 & 0 & 0 & e_0 & e_1 \end{bmatrix} \tag{4.4}$$

and

$$S = \begin{bmatrix} e_3 & -e_2 & e_1 & -e_0 & 0 & 0 & 0 & 0 \\ 0 & 0 & e_3 & -e_2 & e_1 & -e_0 & 0 & 0 \\ 0 & 0 & 0 & 0 & e_3 & -e_2 & e_1 & -e_0 \\ e_1 & -e_0 & 0 & 0 & 0 & 0 & e_3 & -e_2 \end{bmatrix}. \tag{4.5}$$

The filters are used like a recursive pyramid decomposition algorithm, which provides a hierarchical multi-resolution representation of the analyzed signal [186].

At level 1, the scaling and wavelet filters are applied to a signal $y(t)$ with N data points, producing $\frac{N}{2}$ detail coefficients ${u_j}^1$ and $\frac{N}{2}$ approximation coefficients ${a_j}^1$. The application of the filters at resolution level m can be written as

$$a^m = G a^{m-1} \tag{4.6}$$

and

$$u^m = S a^{m-1} \tag{4.7}$$

where ${a_j}^{m-1}$ denotes the approximation coefficients at a previous resolution level. The original signal $y(t)$ can be considered ${a_j}^0$.

At level 2, the filters are applied to the approximation coefficients from level 1, resulting in $\frac{N}{4}$ detail coefficients and $\frac{N}{4}$ approximation coefficients. The process is repeated until the desired level is reached. The wavelet coefficients χ_j consist of both the approximation and detail coefficients at each resolution level. Thresholding is carried out after applying the filters to the desired resolution level. Since approximation coefficients ${a_j}^m$ contain the low-frequency part of the signal, which is usually less affected by noise, thresholding is

only applied to detail coefficients ${u_j}^m$ at each level [183, 187].
For this purpose, Donoho et al. (1995) introduced the universal threshold κ.

$$\kappa = \sqrt{2\log_2 N} \tag{4.8}$$

There are two approaches: (1) hard and (2) soft thresholding. Coefficient u_j is dismissed if its absolute value is less than κ and kept if it surpasses the threshold in case of hard thresholding.

$$u_j^{\text{hard}} = \begin{cases} 0, & |u_j| < \kappa \\ u_j, & |u_j| \geq \kappa \end{cases}$$

If soft thresholding is applied, the coefficient is also dismissed if its absolute value is smaller than κ. However, if the absolute value is larger than κ, it is shifted towards zero by subtracting κ.

$$u_j^{\text{soft}} = \begin{cases} 0, & |u_j| < \kappa \\ sign(u_j)(|u_j| - \kappa), & |u_j| \geq \kappa \end{cases}$$

Following thresholding, the remaining coefficients are used to reconstruct the signal [183, 187].

$$a^{m-1} = G^* a^m + H^* u^m \tag{4.9}$$

PSDefoPAT® applies DWT to the entire times series, employing Daubechies wavelets, after extreme outliers have been detected and replaced. The Daubechies wavelets are the most commonly used orthogonal wavelets for WT because, compared to other orthogonal wavelets, they have a short, compactly supported scaling function given an exponent number of vanishing moments. Additionally, examining the mean squared error between the original and reconstructed signals, as well as maximizing the SNR, Daubechies wavelets yield the best performance [189]. For the noise reduction step, soft thresholding is used because it provides a smooth and continuous time series after signal reconstruction [188]. The original displacement time series (black dots) of MP I and MP II, and the effective noise reduction can be observed in Figure 4.2.

Estimating the Periodic Component

After reducing the noise level of the time series, the next step to establish a best-fitting time series model is to estimate the periodic component $\hat{y}_{\text{P}}$. Displacement time series with a periodic component are often related to the varying water content or temperature of a material. Sine functions are typically used to approximate such phenomena.

$$\hat{y}_{\text{P}} = \beta_0 \cdot sin(2\pi \cdot \beta_1(t - \beta_2)) \tag{4.10}$$

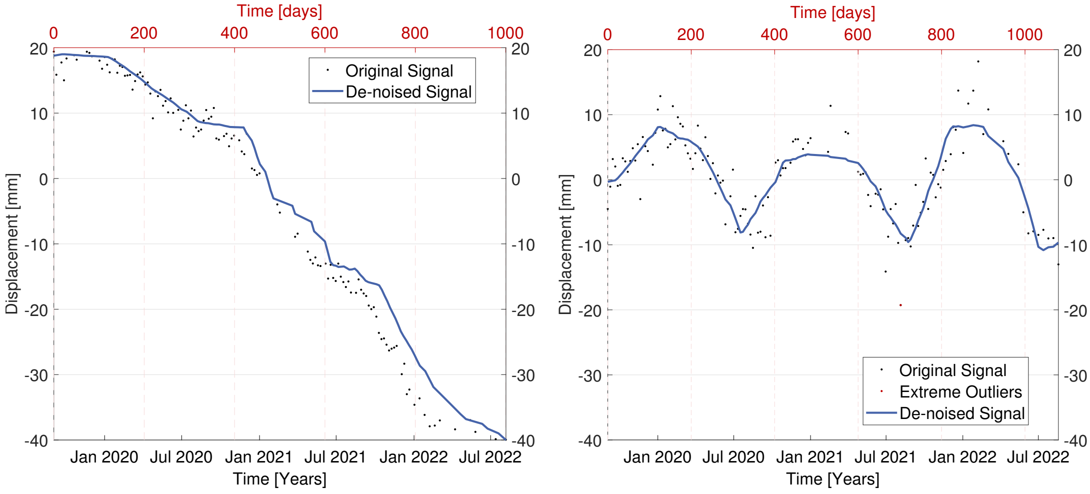

(a) MP I

(b) MP II

Figure 4.2.: Original (black) and de-noised displacement time series (blue) for (a) MP I and (b) MP II.

where t is the predictor variable, and β_0, β_1, and β_2 are the regression coefficients. They represent the amplitude β_0, frequency β_1, and temporal offset β_2 with respect to a usual sine function of the modeled time series. PSDefoPAT® uses a non-linear least squares approach to fit a sine function to the data points of a given time series. However, this approach requires an initial value for the frequency of the time series.

Fisher's test [190] is a well-known significance test designed to detect periodicities of unknown frequency in a given time series. The null hypothesis H_0 of Fisher's test assumes that the amplitude β_0 of the time series is zero and the signal y_i only consists of Gaussian noise.

$$H_0 : \beta_0 = 0 \tag{4.11}$$

The alternative hypothesis H_1 assumes that the time series contains a deterministic periodic component with an unknown frequency.

$$H_1 : \beta_0 \neq 0 \tag{4.12}$$

The g-statistic is used as a test statistic for this hypothesis. The statistic is defined by the spectral estimate $I(\omega)$ evaluated at Fourier frequencies ω_i [191].

$$\begin{aligned} g &= \frac{max_{1 \le i \le v} I(\omega_i)}{\sum_{i=1}^{v} I(\omega_i)} \\ \text{with } v &= \frac{N-1}{2} \end{aligned} \tag{4.13}$$

The P-value represents the probability of obtaining a value from the test statistic at least as extreme or more extreme than the one derived from the data, assuming that the null hypothesis is true. In other words, the P-value provides a measure of evidence against accepting the null hypothesis. The lower the P-value is, the less likely it is that the null hypothesis is true. In general, if the P-value is between 0.1 and 0.9, it is safe to assume that the null hypothesis is true. If the value is less than 0.02, there is strong evidence that the null hypothesis does not hold true. The threshold indicating whether or not to reject the null hypothesis is referred to as the level of significance α. If the P-value surpasses α, the null hypothesis is accepted, and if it is smaller, the null hypothesis is rejected. Typical values for α are 0.1, 0.05, and 0.01. A significance level of 0.05 is considered acceptable for falsely rejecting the null hypothesis [192, 193]. For PSDefoPAT®, the significance level is set to 0.05, meaning that the likelihood of the data supporting the null hypothesis is less than 5 %. The probability resulting from a g-statistic g^* for a specific peak can be calculated as follows [191]:

$$P(g \geq g^*) = 1 - \sum_{i=0}^{v} (-1)^i \frac{v!}{i!(v-i)!} (1 - i \cdot g^*)_+^{v-1} \tag{4.14}$$

Before Fisher's test is performed on the periodogram of a given time series, the time series is de-trended, i.e., a linear regression model is subtracted from the time series. This step eliminates the presence of the trend component in the periodogram. Afterward, if Fisher's test identifies a peak in the periodogram with a P-value lower than 0.05, and the associated period is larger than the smallest possible period and smaller than the time interval the time series covers, a sine function is fitted to the de-trended time series. An additional hypothesis test is performed to evaluate if model $\hat{y}_\mathrm{P}$ explains the de-trended time series sufficiently.

The null hypothesis H_0, in this case, assumes that regression model $\hat{y}_\mathrm{P}$ does not sufficiently describe the relationship between the data points of the de-trended time series and predictor variable t.

$$\begin{aligned} H_0 &: \beta_0 = \beta_1 = \beta_2 = 0 \\ H_1 &: \text{at least one } \beta_j \neq 0 \end{aligned} \tag{4.15}$$

The test statistic F_0 is calculated to determine whether the null hypothesis is rejected or not. The sum of squares due to the regression model SSR, the sum of squares due to the residual error SSE, the number of data points N, the number of predictor variables η, and the degree of freedom for the regression model τ define the F_0-statistic.

$$F_0 = \frac{SSR(N - \eta)}{SSE \cdot \tau} \tag{4.16}$$

The F_0-statistic is used to determine the P-value, which equals the area under the curve of the F-distribution between value F_0 and infinity. If the P-value does not exceed the specified level of significance α, the null hypothesis is rejected [192]. The threshold is set to 0.05 for PSDefoPAT®. In the case of MP I and MP II, the significance test only confirmed a periodic component for MP II. The fitted sine function and the de-trended time series of MP II are presented in Figure 4.3 (b).

If Fisher's test identifies a significant period and the subsequent hypothesis test on the

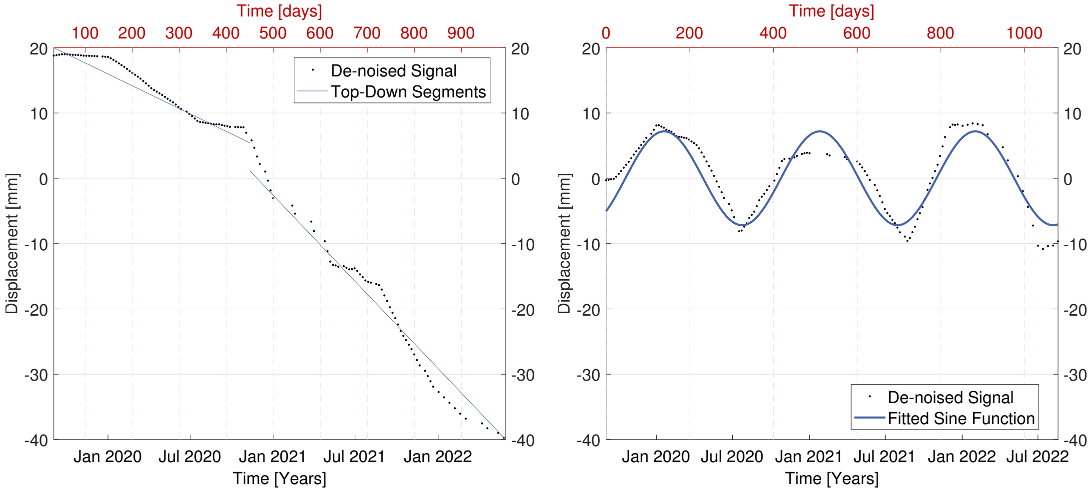

(a) MP I

(b) MP II

Figure 4.3.: (a) De-noised time series (black) and the identified segments (blue) for MP I, and (b) de-noised displacement time series (black) and fitted sine function (blue) for MP II.

fitted sine function results in a P-value lower than 0.05, the predicted values of the periodic component are subtracted from the de-noised time series. The resulting time series is referred to as de-seasonalized.

Estimating the Trend Component

The last step in determining the best-fitting model for any time series in PSDefoPAT® is estimating the trend component. This component describes the long-term evolution of a time series. Three different regression models are considered: (1) linear, (2) quadratic, and (3) piecewise linear trend models.

Linear or quadratic regression models can also be referred to as first- and second-degree polynomial regression models. In general, a k-degree polynomial model can be written as follows:

$$\hat{y}_{\mathrm{T}} = \beta_0 + \beta_1 t + \beta_2 t^2 + \ldots + \beta_k t^k \tag{4.17}$$

where β denote the regression coefficients; t, the predictor variable; and $\hat{y}_{\mathrm{T},i}$, the predicted data points. The number of regression coefficients is set to two for a linear regression model. Thus, the equation can be written as follows:

$$\hat{y}_T = \beta_0 + \beta_1 t \tag{4.18}$$

The first- and second-degree polynomial regression models are fitted to the presented data points using ordinary least squares (OLS). The idea is to minimize the squared difference between the measured data points y_i and the data points $\hat{y}_{\mathrm{T},i}$ predicted by the regression model [192].

$$\sum_{i}^{N}(y_i - \hat{y}_{\mathrm{T},i})^2 = \sum_{i}^{N}(y_i - (\beta_0 + \beta_1 \cdot t_i))^2 \tag{4.19}$$

The procedure is to first estimate a linear regression model, test for its significance, and only estimate the other regression models if a linear relationship between the data points and the predictor variable t could be established. The significance test is performed with an F_0-statistic. The level of significance α is set to 0.05, meaning that the likelihood for the data to support the null hypothesis is less than 5 %.

A quadratic regression model is fitted to the collected data points only if the linear regression significantly explains the relationship between the data points and the predictor variable. In order to determine if the additional term of the quadratic regression model contributes significantly to the explanation of the collected data points, another hypothesis test is performed. In this case, the null hypothesis H_0 assumes that the contribution of the term in question is not significant and can be removed from the regression model.

$$\begin{aligned} H_0 :&\beta_j = 0 \\ H_1 :&\beta_j \neq 0 \end{aligned} \tag{4.20}$$

Student's t-statistic is used as the test statistic for this hypothesis test instead of the F_0-statistic. The t-statistic is defined by the ratio of the regression coefficient β and the associated diagonal element of the variance-covariance matrix C_{jj}.

$$t_j = \frac{\beta_j}{C_{jj}} \tag{4.21}$$

The contribution of the term in question is considered significant if the associated P-value of the t_j-test statistic is lower than a predefined level of significance α. Here, the P-value is defined as the sum of the area underneath the curve of the t-distribution between $|t_j|$ and infinity, and $-|t_j|$ and negative infinity [181]. The quadratic regression model is accepted as the preliminary trend model if the P-value is less than 0.01. If not, the linear regression model is accepted as the preliminary trend model. In this case, a stricter level of significance α was chosen to avoid over-fitting.

The last regression model to be estimated is a piecewise linear model, also referred to as piecewise linear representation (PLR). A PLR represents a given time series with N data points as a sequence of M straight lines [194]. The transition point between the two segments is referred to as a CP. A PLR with only one CP cp_1 can be written as follows [195]:

$$\begin{aligned} \hat{y}_i =&\beta_0 + \beta_1 t + \beta_2(t - cp_1)\delta \\ \text{with } \delta =& \begin{cases} 0, & t < cp_1 \\ 1, & t \geq cp_1 \end{cases} \end{aligned} \tag{4.22}$$

In order to estimate the PLR of a given time series using a non-linear least squares approach, the number of segments and the location of the associated CPs need to be determined beforehand. Both can be determined using a time series segmentation algorithm. In the literature, a distinction is made between online and offline algorithms. Online algorithms do not have access to the entire time series to produce the best PLR, because they allow data points to be added to the time series in parallel to the execution of the algorithm. On the other hand, for offline algorithms, the time series remains unchanged during the execution of the algorithm, and all data points are taken into consideration to find the best PLR [196].

Keogh et al. (2004) sorts online and offline algorithms in three categories: (1) sliding-window, (2) top-down, and (3) bottom-up algorithms. Algorithms that fall in the category sliding-window are considered online algorithms because they do not factor in all the data points of the time series while determining the boundaries of the segments of the PLR. sliding-window algorithms start with the first couple of data points of the time series as the first segment and keep adding data points until the deviation of the approximated segment from the time series exceeds a user-specified threshold. The last added data point is removed and used to form a new segment.

In contrast, top-down and bottom-up algorithms are offline algorithms. Both require the entire time series to determine the boundaries of the segments. A top-down algorithm starts with the assumption that the entire time series is one segment. If the linear approximation of the segments deviates more than the user-specified threshold from the time series, the time series is divided into two segments. Afterward, each segment is recursively tested and further divided until the PLR fulfills the user-specified criterion. bottom-up algorithms, on the other hand, start with the finest possible segmentation of the time series and then merge adjacent segments as long as the resulting PLR does not surpass a user-specified criterion.

Further, there are three different ways to formulate the concrete task of all segmentation algorithms:

(1) Generating the best PLR for the given time series with K segments.

(2) Generating the best PLR of the given time series so that the maximum error of each approximated segment does not exceed a user-specified threshold.

(3) Generating the best PLR of the given time series so that the maximum combined error of all approximated segments does not exceed a user-specified threshold.

All three types of time series segmentation algorithms were implemented with a combination of the first and third formulations of the problem in mind. The first formulation of the task was used so that the number of segments used for the PLR could be limited. Additionally, the choice to use the third instead of the second formulation of the problem in combination with the first one was derived from the goal of PSDefoPAT® to find the best-fitting model of the entire time series and not individual segments. The tool uses the mean squared error to evaluate the segmentation. In Figure 4.3 (a), the estimated segments of the time series of MP I are marked with blue lines. The procedure for PSDefoPAT® is to compare the PLR of the given time series to the previously estimated preliminary trend model. For this reason, the Schwarz-Bayesian Information Criterion (BIC), which is a parameter that evaluates the goodness-of-fit of the regression model in question, is calculated. It is based on the sum of squared residuals or errors, which tends to minimize for more complex models. However, in contrast to criteria such as the adjusted coefficient of determination R^2_{adj} or the Akaike Information Criterion, it penalizes severely for adding complexity to the regression model and thus avoids over-fitting. The BIC can be calculated as follows [181]:

$$BIC = ln\left[\frac{SSE}{N}\right] + \frac{\eta \cdot ln(N)}{N} \tag{4.23}$$

where N is the number of data points and η is the number of predictor variables. The regression model with the lowest value for the BIC is selected as the final trend model.

Evaluation of the Best-Fitting Model and the Residual Component

After estimating the best-fitting model, the sum of the trend and periodic components, it is necessary to evaluate the quality of the selected model. How well the model reproduces the data points of the given time series is referred to as the goodness-of-fit. Two common parameters for the goodness-of-fit are the RMSE and the mean absolute error (MAE). The parameters can be calculated as follows:

$$RMSE = \sqrt{\frac{1}{N}\sum_{i=1}^{N}(y_i - \hat{y}_i)^2} \tag{4.24}$$

$$MAE = \frac{1}{N}\sum_{i=1}^{N}|y_i - \hat{y}_i| \tag{4.25}$$

where N is the number of data points y_i of the given time series and $\hat{y}_i$ represents the data points predicted by the selected model. Minimizing either parameter yields the best-fitting model in case of normally distributed errors. In the case of a Laplacian-like error, minimizing the MAE provides the best results. Thus, both parameters are reasonable first choices to evaluate the selected model [197].

Another parameter that describes the goodness-of-fit of a time series model is the already mentioned parameter adjusted coefficient of determination R^2_{adj}. Earlier in this section, it was stated that using R^2_{adj} leads to over-fitting, which is why it is not used in the context of model selection within PSDefoPAT®. However, its typical range, between 0 and 1, caters

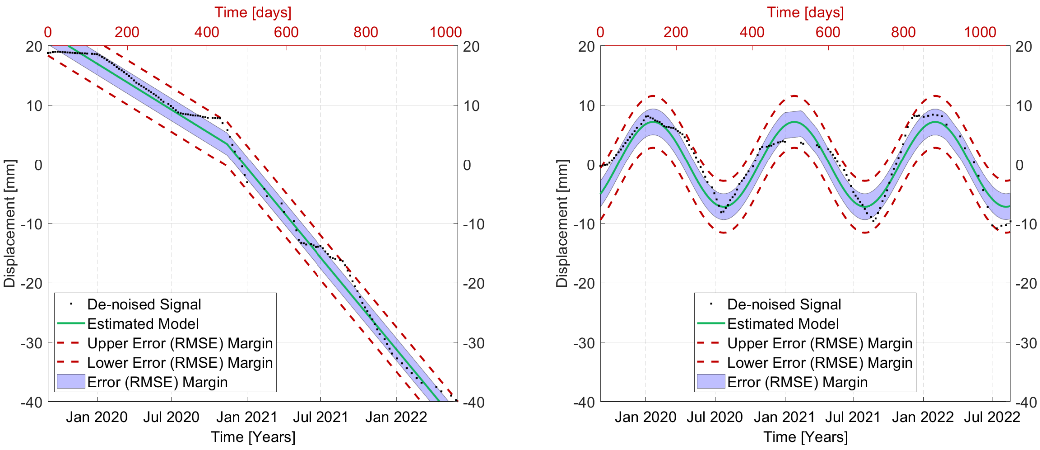

(a) MP I **(b)** MP II

Figure 4.4.: De-noised time series (black), estimated best-fitting model (green), and associated error margins (blue) for (a) MP I and (b) MP II.

to an intuitive analysis of the goodness-of-fit of the estimated models in a spatial context. The closer the value is to 1, the better the fit. The parameter is calculated as follows:

$$R^2_{\text{adj}} = 1 - \frac{SSR(N-1)}{SST(N-\eta-1)} \tag{4.26}$$

where η denotes the number of predictor variables in the time series model, N is the number of data points, and SST is the total sum of squares [198]. The estimated best-fitting displacement time series models of MP I and MP II are displayed in Figure 4.4 with the associated RMSE as upper and lower error margins. Their respective R^2_{adj} values are 0.99 and 0.90, which indicates a very good fit.

In order to facilitate an easy analysis of the extracted temporal patterns of the MPs, an intuitive standardized visualization is needed. Therefore, a graphic interface to review the fitted time series models of individual MPs and four standardized figures were designed. They are introduced using the example of Campi Flegrei in the next sub-section and applied to the PSDefoPAT® results of Dataset A in the next section.

4.2.2 User Interface and Visualization of the Results

Figure 4.5 shows the user interface of PSDefoPAT®. Both the manual and automated versions of the tool can be operated with the interface. It is structured into three areas, which are marked in red in Figure 4.5. Area I is located in the upper left corner of the interface. The output area is used to display the mean deformation velocity of the MPs in the dataset, here the PSI results of Dataset A for the Parapeiros-Peiros Dam. Area II, in the lower left corner, provides the user with a number of different functions, e.g., selecting an MP to analyze or starting the automated processing of the entire dataset. The user

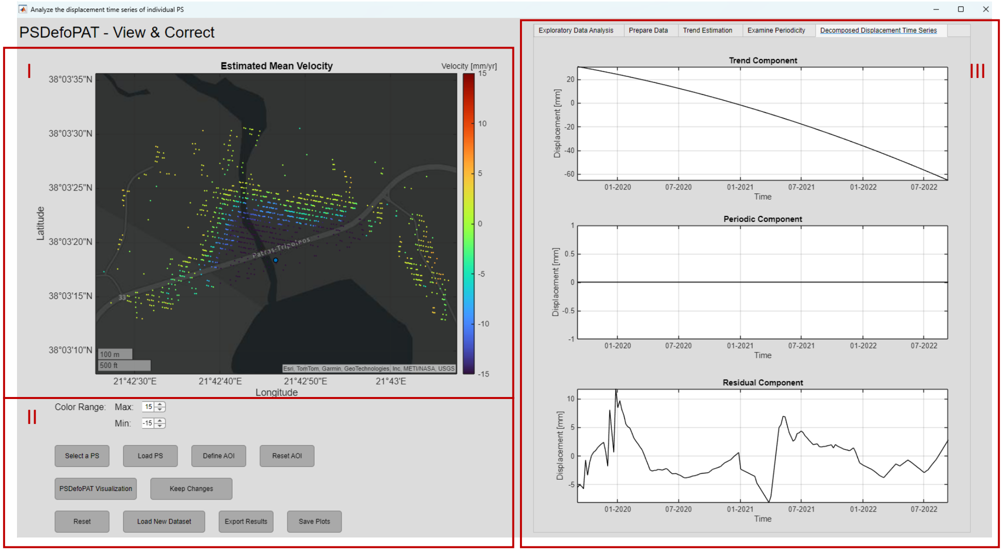

Color Range: Max: 15
Min: -15

Figure 4.5.: The user interface of PSDefoPAT® showing the components of a fully processed displacement time series.

has the opportunity to conduct the time series analysis of selected MPs themselves in the area of the interface located on its right side (Area III). Input on, e.g., outlier detection or change point detection for a PLR of the time series can be provided. More information on the manual processing of selected MPs can be found in Evers et al. (2021). In case the automated processing of the entire dataset is selected, the user has to provide initial input on the following:

(1) The maximum number of segments to be used in the PLR of the time series.

(2) The maximum error used to estimate the segments of a PLR.

(3) The type of segmentation algorithm to be used.

Once the parameters are set, they are valid for the entire dataset.
In addition to the user interface, presented in Figure 4.5, a standardized visualization of the PSDefoPAT® results has been developed. There are four standardized PSDefoPAT® figures that show selected features of the estimated time series model.

The plots display:

(a) The type of time series model selected for the trend component,

(b) The goodness-of-fit of complete time series model,

(c) Whether or not the time series features a periodic component and

(d) The amplitude of the periodic component.

The selected features are displayed for each PS in the dataset, even if the feature is not relevant to the respective time series model. For example, if a fitted time series model does not include a periodic component, the component's amplitude is set to zero and visualized in white. This is done so that the four standardized PSDefoPAT® figures show the same amount and distribution of scatterers, and thus a lack of scatterers or a deviation in their distribution does not irritate the analyst.

The area surrounding Campi Flegrei in South Italy was chosen as an example to illustrate the poignancy of the standardized PSDefoPAT® figures for the interpretation of the estimated time series models in a spatial context. The ground surface deformation phenomenon is well documented and not to complex. Campi Flegrei is an active volcanic caldera in South Italy, west of Naples. Historical evidence indicates volcanic activity in the area for the past 50,000 years, with the last eruption in 1538. Geodetic measurements, however, to monitor ground surface deformation associated with volcanic activity have only been conducted since 1905. The measurements document a period of deflation until 1950, followed by three episodes of uplift: (1) 1950–1952, (2) 1969–1972, and (3) 1982–1985. GNSS and DInSAR campaigns in recent years revealed that after a period of no significant ground surface deformation, the area has been subject to uplift again since 2011. In the 1950s, the period of unrest was not accompanied by felt seismicity. However, in more recent episodes, the magnitude of seismic events has progressively increased. The ground surface deformation and seismic events were also accompanied by other indicators of volcanic activity, such as degassing. It is unclear if the current unrest

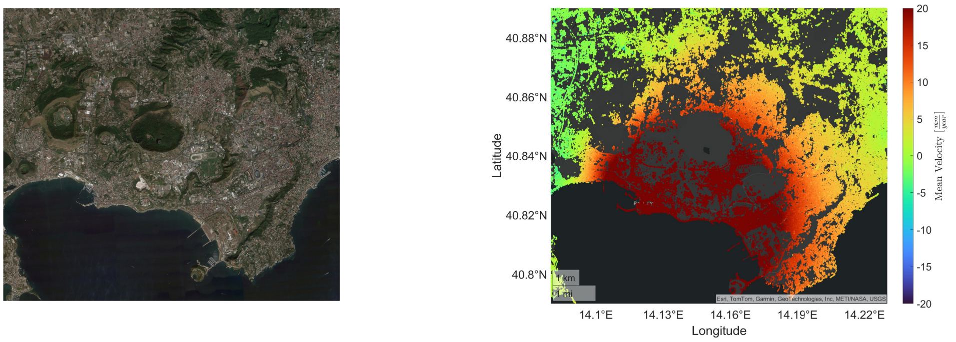

Esri, TomTom, Garmin, GeoTechnologies, Inc, METI/NASA, USGS

(a) Optical Satellite Image

(b) Mean Deformation Velocity

Figure 4.6.: Area of Campi Flegrei as (a) an optical image obtained from Google Earth and with (b) its mean deformation velocity in the LOS provided by the EGMS.

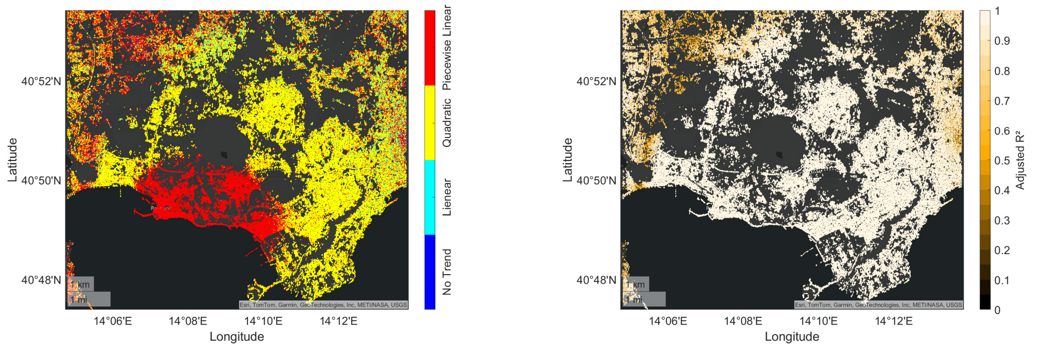

(a) Model type of the trend component **(b)** Goodness-of-fit

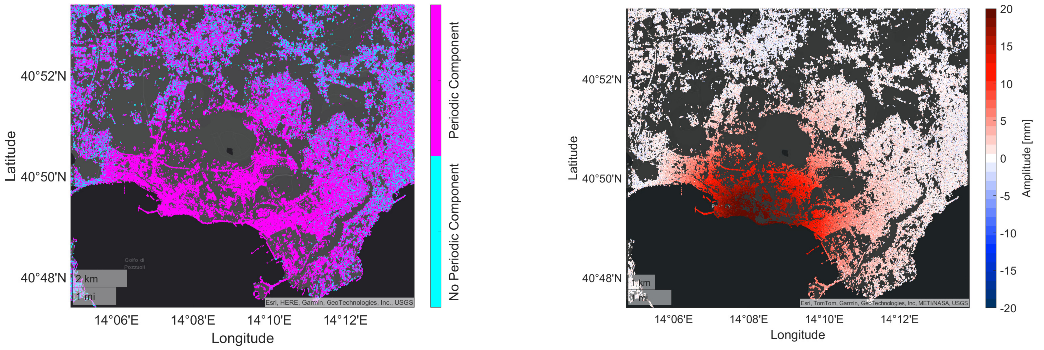

(c) Indication of a periodic component **(d)** Amplitude of the periodic component

Figure 4.7.: Selected features of the best-fitting time series models derived by PSDefoPAT® for MPs in the area of Campi Flegrei in South Italy.

is a precursor for an eruption and, if so, when the eruption will take place [199, 200]. Figure 4.6 shows (a) an optical satellite image provided by Google Earth of the area and (b) the mean deformation velocity in LOS of the sensor extracted from a fully processed PSI dataset provided by the EGMS (Product: Basic Descending) for the area for the time span of 2015 to 2021. The figure clearly shows a large actively deforming area colored in red and orange. However, the mean deformation velocity map shows no information concerning the temporal pattern of the deformation. Figure 4.7 shows the key features of time series models estimated with PSDefoPAT® for the area. Most MPs in the areas of Campi Flegrei possess time series models that include a periodic component, as can be seen in Figure 4.7 (c), and Figure 4.7 (d) that the amplitude of the periodic component decreases from the coastline inland. The type of regression model selected for the trend component is displayed in Figure 4.7 (a). A distinction is made between linear (cyan), quadratic (yellow), and piecewise linear (red) regression models. MPs with no trend are colored in dark blue. Figure 4.7 (a) indicates that the overall deformation pattern of Campi Flegrei can be split into two distinct clusters. The first cluster concentrates on the coastline and exhibits a piecewise linear long-term trend. The second cluster forms a semi-circle around the first cluster and extends more inland. Most MPs located in the area of the second cluster follow a quadratic long-term trend. For MPs outside the active deformation area (see Figure 4.6 (b), the choice of the regression model for the trend component varies with no apparent pattern. A look at the adjusted R^2 value depicted in Figure 4.7 (b) shows

that this area is associated with lower adjusted R^2 values, indicating a not sufficiently good fit of the model to the data. The example shows that using the four standardized PSDefoPAT® figures, clusters with similar temporal patterns become immediately evident to the analyst. In order to allow further exploration of the temporal deformation patterns of individual MPs another user Interface was designed. The user interface is presented in Figure 4.8. On the left side different function, such as selecting a specific MP to plot its displacement time series model, are available. The user interface features two maps next to each other. The map on the right side displays the goodness-of-fit of the estimated time series models and the map on the left side shows one of the four standardized PSDefoPAT® figures. The user can switch between the four figures by selecting a different tab. A more detailed description of the user interface is given in [58].
To demonstrate the capabilities of PSDefoPAT®, the tool is tested on synthetic and real-life displacement time series in the next two sections.

4.3 Test on Simulated Displacement Time Series

In order to test the capabilities of PSDefoPAT® a dataset with 16,000 simulated displacement time series was generated. The test dataset includes time series generated with one of the following time series models: (1) a linear trend, (2) quadratic trend, (3) piecewise linear trend, (4) purely periodic model, (5) a linear trend with a periodic component, (6) a quadratic trend with a periodic component, (7) a piecewise linear trend with a periodic component or (8) no model at all. For each model the test dataset features 2,000 time series. The simulated displacement time series were generated with regard to the two case studies, the city of Patras and the Parapeiros-Peiros Dam, presented in Section 4.4, for a time span of three years. The dataset includes displacement time series

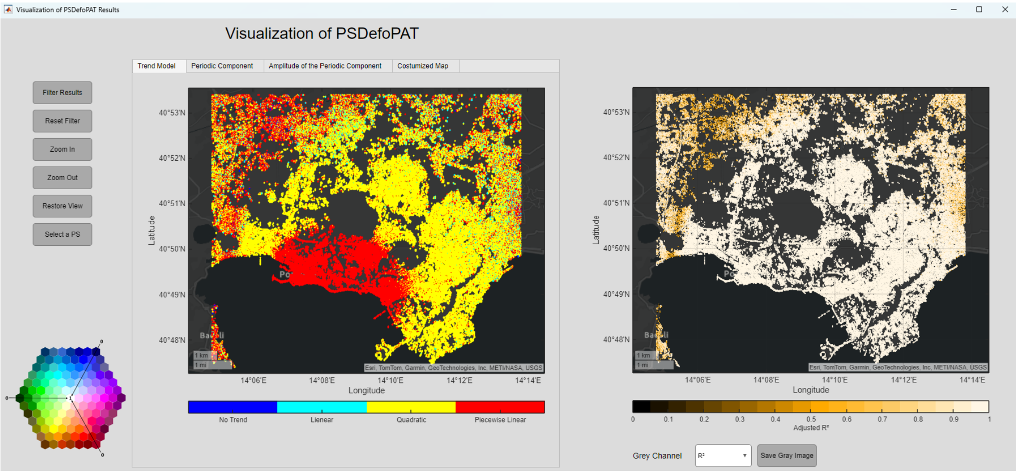

Figure 4.8.: User interface to explore and visualize the PSDefoPAT® results.

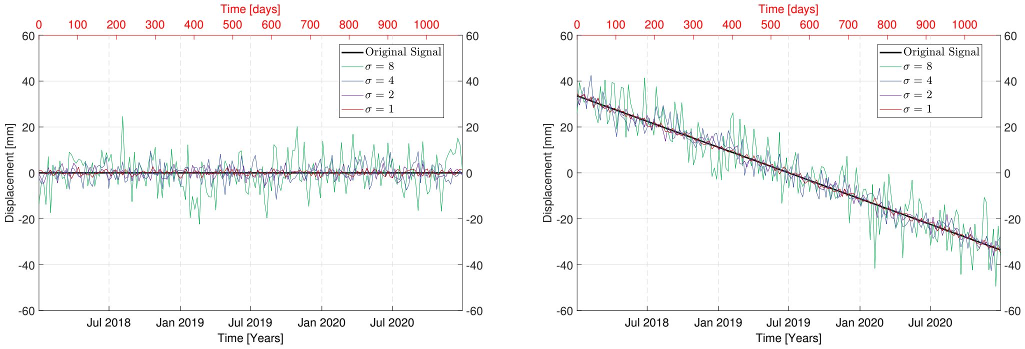

(a) No model **(b)** Linear trend

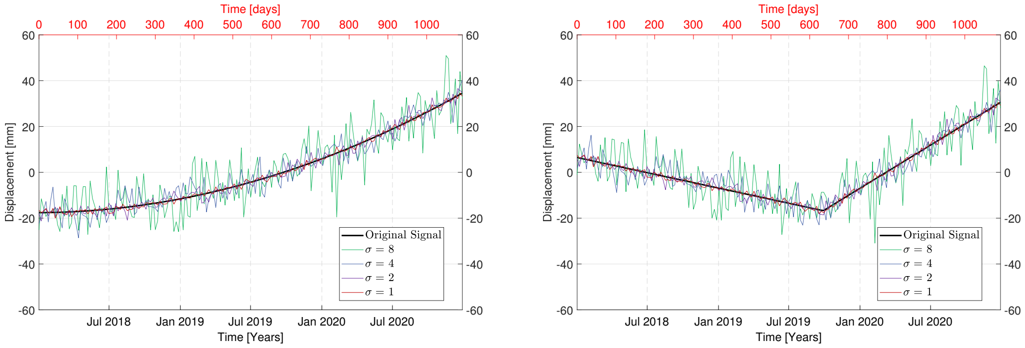

(c) Quadratic trend **(d)** Piecewise linear trend

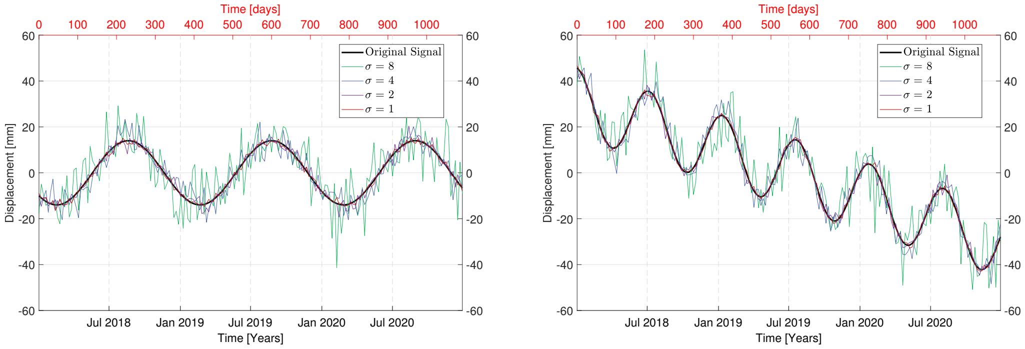

(e) Periodic signal **(f)** Linear trend & periodic signal

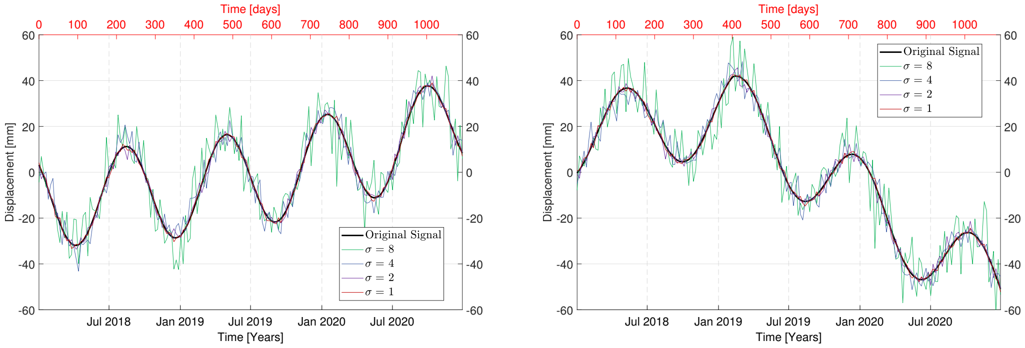

(g) Quadratic trend & periodic signal **(h)** Piecewise linear trend & periodic signal

Figure 4.9.: Synthetic displacement time series (black) for each time series model considered by PSDefoPAT® superimposed with noise following a Gaussian distribution with $\sigma = 1$ (red), $\sigma = 2$ (purple), $\sigma = 4$ (blue) and $\sigma = 8$ (green).

with an accumulated displacements between -300 mm and 300 mm over the time span and estimated mean deformation velocities between -97 $\frac{\text{mm}}{\text{year}}$ and 96 $\frac{\text{mm}}{\text{year}}$. The absolute maximum mean deformation velocity, taken into consideration, is roughly a fourth of the maximum displacement rate of 426 $\frac{\text{mm}}{\text{year}}$ that can theoretically be captured using S1 SAR sensor [53]. The maximum absolute mean deformation velocity observed in the two case studies presented in Section 4.4 is 40 $\frac{\text{mm}}{\text{year}}$. Thus, the mean deformation velocity of the simulated displacement time series is well within the bounds of what can be expected. Figure 4.9 shows exemplary time series for each model type, including no model (Figure 4.9 (a)). The simulated displacement time series without noise is displayed in black in Figure 4.9 (b) to Figure 4.9 (h). To test the limits of PSDefoPAT® the simulated displacement time series were superimposed with noise following a Gaussian distribution

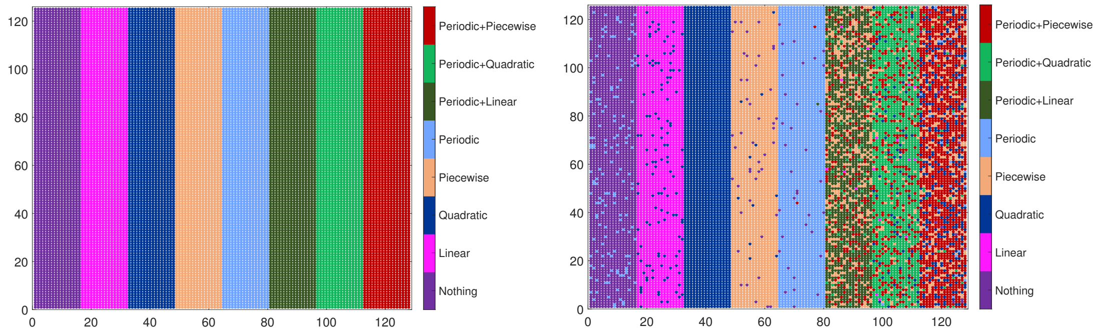

(a) Set labels **(b)** $\sigma = 1$

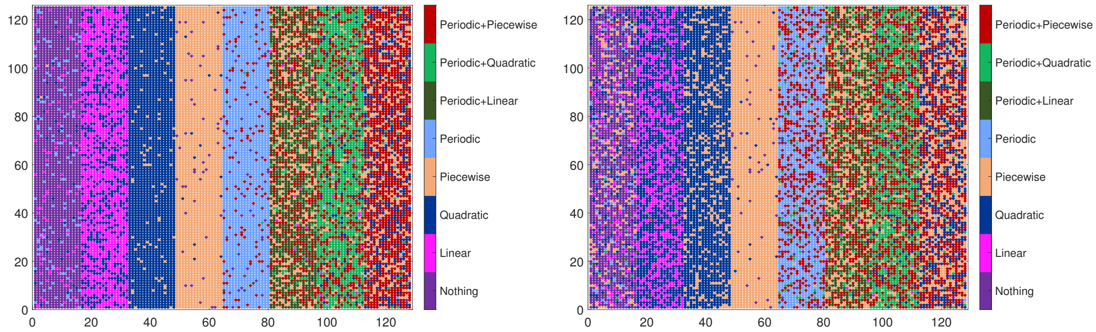

(c) $\sigma = 2$ **(d)** $\sigma = 4$

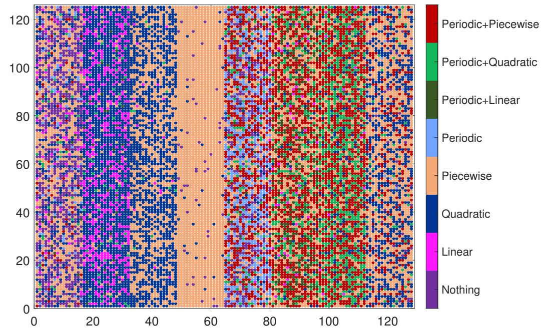

(e) $\sigma = 8$

Figure 4.10.: Type of time series models (a) set and estimated with PSDefoPAT® for 16,000 synthetic displacement time series superimposed noise following a Gaussian distribution with (b) $\sigma = 1$, (c) $\sigma = 2$, (d) $\sigma = 4$ and (e) $\sigma = 8$.

with $\sigma = 1$ (red), $\sigma = 2$ (purple), $\sigma = 4$ (blue) and $\sigma = 8$ (green). Naturally, displacement time series with a small deformation velocity are already quite noisy in the case of $\sigma = 1$ (red), while displacement time series with a high deformation velocity are still quite crisp in the case of $\sigma = 8$ (green), as can be observed in Figure 4.9 (a) and Figure 4.9 (h).

Figure 4.10 (a) shows the type of time series model set for each time series. The figure presents an easily recognizable striped pattern. Figure 4.10 (b) shows the type of time series model estimated with PSDefoPAT® in case the time series is superimposed noise following a Gaussian distribution with $\sigma = 1$. The striped pattern can be observed again. However, it is noticeable that some displacement time series are mislabeled. For Figure 4.10 (b) to Figure 4.10 (e) the noise level increases. As expected the number of mislabeled displacement time series increases as well. In total 2,465 time series are mislabeled, in the case the displacement time series are superimposed with noise following a Gaussian distribution with $\sigma = 1$, which is 15 % of the generated 16,000 displacement time series. For the case of noise following a Gaussian distribution with $\sigma = 8$ the number of mislabeled time series increases to 10,973 time series, which is 69 % of the generated displacement time series. However, the effect the noise has on estimating the time series model varies with the type of time series model. While the combination of a piecewise linear trend and a periodic component is already mislabeled 37 % of the time for noise following a Gaussian distribution with $\sigma = 1$, displacement time series that feature a quadratic or piecewise linear trend or a periodic component are mislabeled less than 10 % of the time. In the case of noise that follows a Gaussian distribution with $\sigma = 8$, displacement time series that feature piecewise linear trend and a periodic component is mislabeled 86 % of the time and displacement time series that follow a quadratic, piecewise linear trend or periodic pattern are mislabeled 45 %, 4 % and 72 % of the time. Further, in the case of higher noise levels and time series models that feature a change in their slope, such as piecewise linear or quadratic trend models, PSDefoPAT® tends to favour a piecewise linear trend. This is also valid for time series models combining a trend and periodic component. Also, in the case of time series models combining a trend and periodic component, the estimation of the periodic component is hampered by higher noise levels. This can also be observed in the table presented in Figure 4.11 (enlarged in the Appendix A.1). The table presents the set and estimated coefficients for exemplary displacement time series. The respective time series are presented in Figure 4.9 (d), Figure 4.9 (e) and Figure 4.9(f). In the case of the second time series (linear trend with periodic component) superimposed with noise following a Gaussian distribution with $\sigma = 8$, only the trend component of the time series is estimated. In this case PSDefoPAT® failed to estimate the periodic component. The time series also has the highest value for the RMSE. However, the value for R^2_{adj} is still quite good, probably a reflection of the good estimation of the trend component. Generally, as expected with an increase in noise the estimation of the coefficients worsens.

After testing the capabilities of PSDefoPAT® on simulated displacement time series, they are tested on two AOIs: (1) the city of Patras and (2) the Parapeiros-Peiros Dam. The

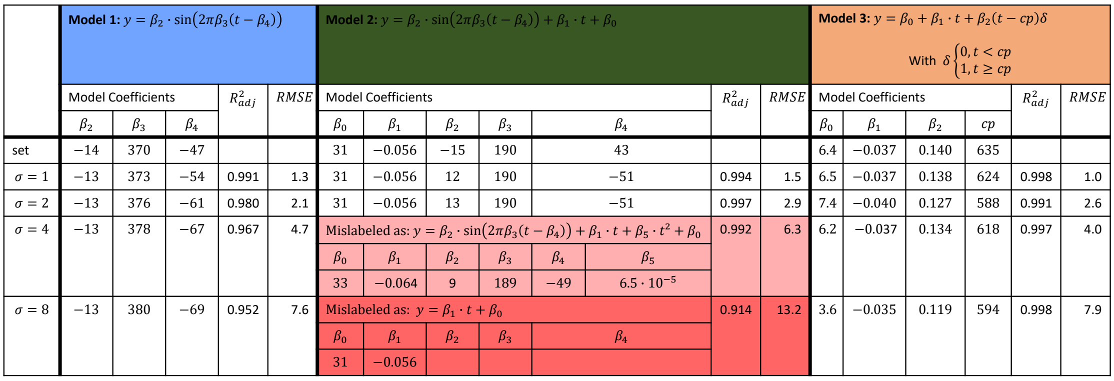

<table>
<tr><td rowspan="3"></td><td colspan="5">Model 1: $y = \beta_2 \cdot \sin(2\pi\beta_3(t-\beta_4))$</td><td colspan="8">Model 2: $y = \beta_2 \cdot \sin(2\pi\beta_3(t-\beta_4)) + \beta_1 \cdot t + \beta_0$</td><td colspan="6">Model 3: $y = \beta_0 + \beta_1 \cdot t + \beta_2(t-cp)\delta$
With $\delta \begin{cases} 0, t < cp \\ 1, t \geq cp \end{cases}$</td></tr>
<tr><td colspan="3">Model Coefficients</td><td rowspan="2">R^2_{adj}</td><td rowspan="2">$RMSE$</td><td colspan="6">Model Coefficients</td><td rowspan="2">R^2_{adj}</td><td rowspan="2">$RMSE$</td><td colspan="4">Model Coefficients</td><td rowspan="2">R^2_{adj}</td><td rowspan="2">$RMSE$</td></tr>
<tr><td>β_2</td><td>β_3</td><td>β_4</td><td>β_0</td><td>β_1</td><td>β_2</td><td>β_3</td><td colspan="2">β_4</td><td>β_0</td><td>β_1</td><td>β_2</td><td>cp</td></tr>
<tr><td>set</td><td>−14</td><td>370</td><td>−47</td><td></td><td></td><td>31</td><td>−0.056</td><td>−15</td><td>190</td><td colspan="2">43</td><td></td><td></td><td>6.4</td><td>−0.037</td><td>0.140</td><td>635</td><td></td><td></td></tr>
<tr><td>$\sigma = 1$</td><td>−13</td><td>373</td><td>−54</td><td>0.991</td><td>1.3</td><td>31</td><td>−0.056</td><td>12</td><td>190</td><td colspan="2">−51</td><td>0.994</td><td>1.5</td><td>6.5</td><td>−0.037</td><td>0.138</td><td>624</td><td>0.998</td><td>1.0</td></tr>
<tr><td>$\sigma = 2$</td><td>−13</td><td>376</td><td>−61</td><td>0.980</td><td>2.1</td><td>31</td><td>−0.056</td><td>13</td><td>190</td><td colspan="2">−51</td><td>0.997</td><td>2.9</td><td>7.4</td><td>−0.040</td><td>0.127</td><td>588</td><td>0.991</td><td>2.6</td></tr>
<tr><td rowspan="3">$\sigma = 4$</td><td rowspan="3">−13</td><td rowspan="3">378</td><td rowspan="3">−67</td><td rowspan="3">0.967</td><td rowspan="3">4.7</td><td colspan="6">Mislabeled as: $y = \beta_2 \cdot \sin(2\pi\beta_3(t-\beta_4)) + \beta_1 \cdot t + \beta_5 \cdot t^2 + \beta_0$</td><td rowspan="3">0.992</td><td rowspan="3">6.3</td><td rowspan="3">6.2</td><td rowspan="3">−0.037</td><td rowspan="3">0.134</td><td rowspan="3">618</td><td rowspan="3">0.997</td><td rowspan="3">4.0</td></tr>
<tr><td>β_0</td><td>β_1</td><td>β_2</td><td>β_3</td><td>β_4</td><td>β_5</td></tr>
<tr><td>33</td><td>−0.064</td><td>9</td><td>189</td><td>−49</td><td>$6.5 \cdot 10^{-5}$</td></tr>
<tr><td rowspan="3">$\sigma = 8$</td><td rowspan="3">−13</td><td rowspan="3">380</td><td rowspan="3">−69</td><td rowspan="3">0.952</td><td rowspan="3">7.6</td><td colspan="6">Mislabeled as: $y = \beta_1 \cdot t + \beta_0$</td><td rowspan="3">0.914</td><td rowspan="3">13.2</td><td rowspan="3">3.6</td><td rowspan="3">−0.035</td><td rowspan="3">0.119</td><td rowspan="3">594</td><td rowspan="3">0.998</td><td rowspan="3">7.9</td></tr>
<tr><td>β_0</td><td>β_1</td><td>β_2</td><td>β_3</td><td colspan="2">β_4</td></tr>
<tr><td>31</td><td>−0.056</td><td></td><td></td><td colspan="2"></td></tr>
</table>

Figure 4.11.: Estimated coefficients for three selected displacement time series.

city of Patras is affected by natural and anthropologically induced deformation, while the Parapeiros-Peiros Dam is only affected by anthropologically induced deformation.

4.4 Demonstration Case

In this section, the capabilities and applicability of PSDefoPAT® are demonstrated on Dataset A, which incorporates natural and anthropologically induced deformation and is described in detail in Chapter 3. The focus, in this chapter, is on two smaller areas, surrounding (a) the city of Patras and (b) the Parapeiros-Peiros Dam. The mean deformation maps are presented in Figure 4.12. In order to extract relevant information on their temporal and spatial deformation patterns, they were subjected to post-processing with PSDefoPAT®. For both case studies, it was decided to use the top-down segmentation algorithm and a maximum number of three segments to estimate the PLR of the displacement time series. The decision was made because out of the three implemented time series segmentation approaches the sliding-window approach performs the worst and the top-down approach out performs the bottom-up approach in case of longer segments [194]. However, the user can decide this for each dataset individually. The user can also specify the maximum allowed error for the PLR. Since PSDefoPAT® operates entirely automatically, the value cannot be set for each displacement time series individually. Here, the standard deviation of the de-seasonalized time series, i.e., the de-noised time series minus the estimated periodic component, was used as an adaptive measure that adjusts to each time series. It measures the range of deviations expected for the individual displacement time series. Its physical unit is mm, since the displacements are measured in mm. Its value is higher for a noisy displacement time series than for a crisp one. For the examples below, the error threshold for time series segmentation was set to $\frac{1}{2}$ the standard deviation of the de-seasonalized time series.

Figure 4.12 shows the mean deformation velocity for MPs identified in the coastal city Patras and its suburbs (see Figure 4.12 (a)), as well as for MPs identified on the dam

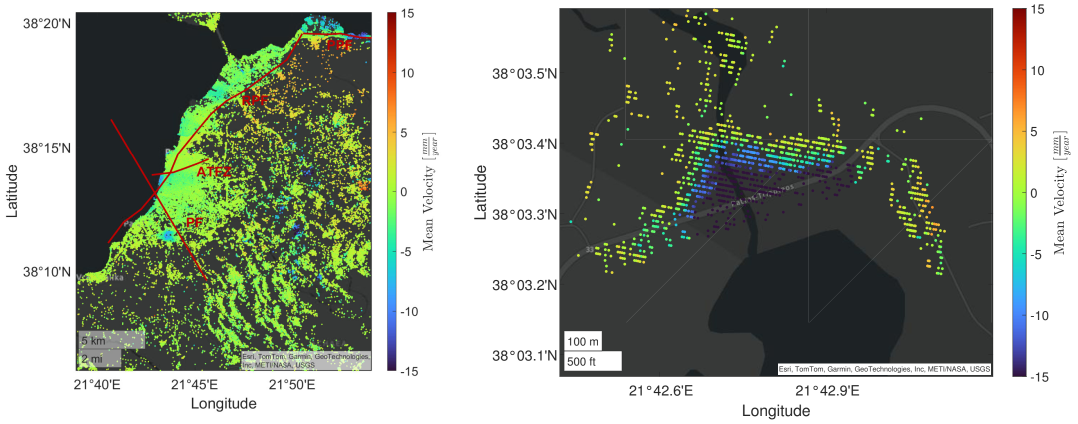

(a) City and suburbs of Patras **(b)** Parapeiros-Peiros Dam

Figure 4.12.: Mean deformation velocity of (a) City and suburbs of Patras overlaid with traces of active faults (red) extracted from NOAFAULTs database [159] and (b) the Parapeiros-Peiros Dam southwest of Patras.

body of the Parapeiros-Peiros Dam southwest of Patras (see Figure 4.12 (b)). The PSI analysis identified 156,767 MPs in Patras and its suburbs and 1,159 MPs on the dam body of the Parapeiros-Peiros Dam. The colormap in Figure 4.12 extends from 15 $\frac{\text{mm}}{\text{year}}$ (dark red) to -15 $\frac{\text{mm}}{\text{year}}$ (dark blue). The mean deformation velocities are measured in the LOS of the sensor. Thus, a negative velocity indicates a movement away from the sensor, and a positive velocity indicates a movement towards the sensor.

Most MPs in Figure 4.12 (a) are colored in green. The color green indicates that no ground surface deformation occurred during the observation period, which might be misleading. The mean deformation velocities are calculated with a linear fit, neglecting any changes or periodicity in the temporal deformation pattern. A purely periodic deformation pattern would be represented by a mean deformation velocity of 0 $\frac{\text{mm}}{\text{year}}$. As stressed in the beginning of the chapter, changes in the deformation pattern are highly relevant for assessing geo-hazard risks or the structural health of infrastructure elements. In Figure 4.12 (a) clusters of blue MPs noticeable in the south-east of the AOI. They are located in the mountainous regions of the AOI, which are known for landslides [164, 165]. Thus, it stands to reason to assume that the blue clusters are the result of actively moving landslides. Changes in their deformation pattern, can indicate an acceleration or deceleration of the movement due to heavy rain fall or snow melt [201] and may pose a threat to infrastructure or human settlements [202]. Thus, their temporal pattern is an important information.

Another blue colored area is located in the North of the AOI, east of the Rio-Antirio Bridge, directly at the coastline. The border of the cluster coincides with the trace of the western-most part of the PPF (marked in red in Figure 4.12 (a)). Additional clusters of blue colored MPs can be observed within the city of Patras and its suburbs. Following the coastline from North to South, a slight alternation between blueish and green colored areas can be observed. The pattern coincides with the traces of the RPF and the ATFZ (marked in red in Figure 4.12 (a)).

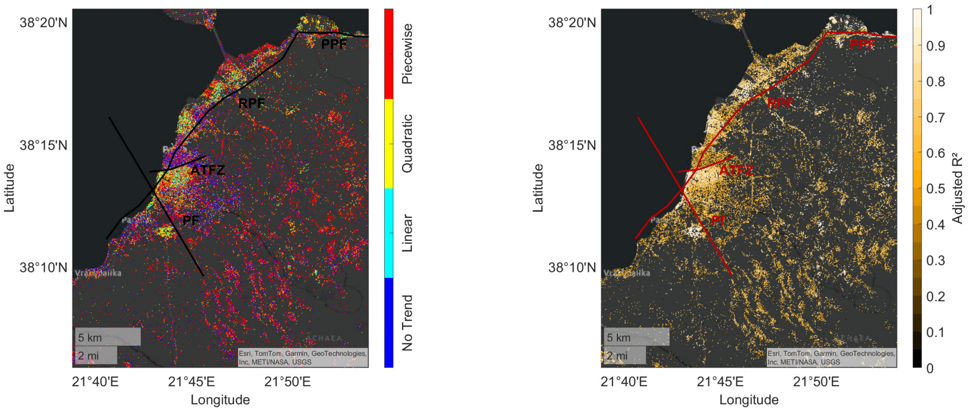

(a) Model type of the trend component

(b) Goodness-of-fit

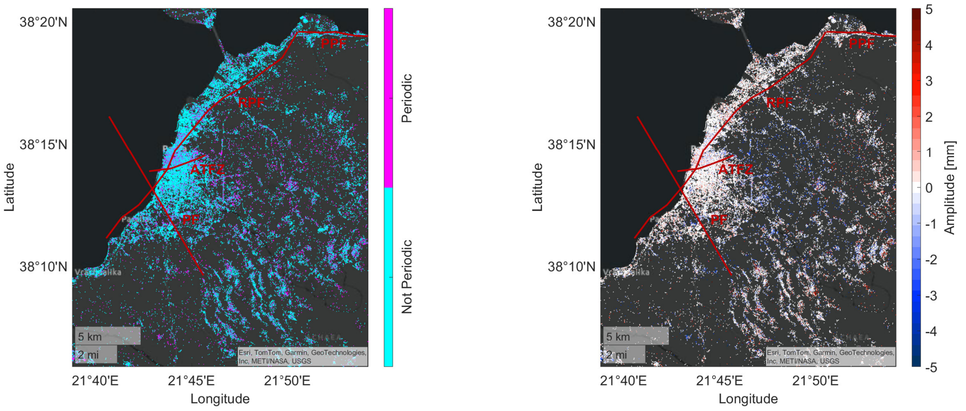

(c) Indication of a periodic component

(d) Amplitude of the periodic component

Figure 4.13.: Selected features of the best-fitting time series models derived by PSDefoPAT® for MPs in the area of the city of Patras at the North-West coastline of the Peloponnese Peninsula, Greece. The features are overlaid with traces of active faults extracted from NOAFAULTs database [159].

The surface deformation of the Parapeiros-Peiros Dam is displayed in Figure 4.12 (b). A movement away from the sensor can be observed with the highest mean deformation velocity of - 37 $\frac{\text{mm}}{\text{year}}$ at the center of the crown of the dam body. From the center of the crown, the magnitude of the surface deformation decreases towards the edges of the dam body. The observed spatial deformation pattern fits the pattern described in literature for embankment dams. Concerning the temporal pattern of the dam body, it is likely that the body does not deform evenly over time. The deformation of the dam body is mainly influenced by the consolidation of the foundation and building material, as well as their reaction to the rising pressure from the stored fresh water [48, 47].

As already stated, most MPs in Figure 4.12 (a) are colored in green, indicating no movement is taking place, but this can of course be misleading. However, many natural or anthropogenic deformation phenomena do exhibit a more complex temporal pattern and therefore do not follow the assumption of a constant velocity model. For example, ground surface deformation due to underground gas storage [28, 29], groundwater extraction [27] or the thermal expansion of large buildings [166] are periodic, while displacement rates of aseismic creep [22, 23] alongside tectonic faults or subsidence rates due to urbanization [30] can change over time and may result in a piecewise linear or quadratic trend. Consequently, the PSI results were further processed using PSDefoPAT®. The key features of the estimated time series models are visualized in Figure 4.13 and Figure 4.15, as described in Sub-section 4.2.2. The results for MPs identified in the city of Patras and its suburbs are presented in Figure 4.13. Figure 4.13 (a), presenting the city of Patras and its suburbs, shows distinct areas in which either a quadratic (yellow), piecewise linear (red), or no time series model (blue) was predominantly selected for the trend component. The areas alternate along the coastline. The transition from an area mainly experiencing a quadratic trend to an area where no trend could be identified in the center of Patras coincides with the ATFZ (marked in black). Further north, most MPs exhibit a quadratic trend component again. Here, the transition line is less sharply defined than at the ATFZ. The transition roughly matches an alternative trace of the RPF [160] to the one marked in black in Figure 4.13 (a). The area around the Rio-Antirio Bridge is divided into two parts. The MPs closer to the shore line follow a piecewise linear and more inland a quadratic trend. The MPs on the bridge itself are also divided in to clusters between no trend and a piecewise linear trend. Figure 4.13 (c) reveals those MPs that are additionally affected by thermal expansion. Hence, the periodic component. Figure 4.13 (a) also shows that the border of a cluster of MPs in the easternmost part of the AOI exhibiting a quadratic temporal pattern matches the trace of the PPF (marked in black). The overall goodness-of-fit presented in Figure 4.13 (b) exhibits a similar spatial pattern. Areas in which a quadratic trend was selected predominantly feature a high goodness-of-fit. Figures 4.13 (c) and (d) show whether or not the estimated time series model features a periodic component and the corresponding amplitude of the periodic component. MPs with

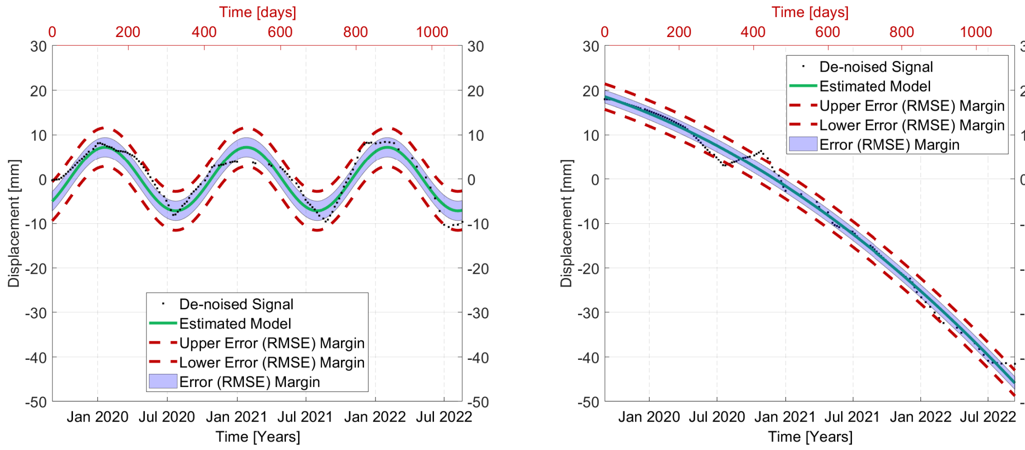

(a) MP II

(b) MP III

Figure 4.14.: De-noised time series (black), estimated best-fitting model (green), and associated error margins (blue) for (a) MP II, located on the Rio-Antirio Bridge, and (b) MP III, located in the mountainous area east of Patras.

a periodic component can mostly be found near and on the Rio-Andirrio bridge, close to the circular deformation pattern near the PF (see Figure 4.12 (a)) and in the mountainous areas to the south and east. Processing the displacement time series MPs in Patras and its suburbs shows that temporal deformation patterns along geophysical features such as active faults changes. Additionally, periodic deformation patterns such as can be observed on the Rio-Antirio Bridge, identifying which sections of the bridge are affected by thermal expansion.

Figure 4.14 shows the displacement time series (black) and the corresponding fitted time series model (green) for two exemplary MPs in the area of and surrounding Patras. MP II is located on the Rio-Antirio Bridge and exhibits a periodic pattern. The estimated time series model (green) clearly captures the periodic pattern, which would not have been apparent in the mean deformation velocity map shown in Figure 4.12 (a). MP III is located in the mountainous area east of Patras and thus, most likely related to a landslide. The displacement time series (black) follows a quadratic trend, i.e., the deformation velocity increases over time. Again, the increase in deformation velocity is information not provided by the mean deformation velocity map presented in Figure 4.12 (a).

While first example features a city, its suburbs and adjacent rural areas, the second example focuses on the area surrounding the Parapeiros-Peiros Dam. The PSDefoPAT® results for MPs identified on the dam body and adjacent are presented in Figure 4.15. Figure 4.15 (a) shows that a quadratic model (yellow) was predominantly selected for the trend component of MPs at the center of the dam body of the Parapeiros-Peiros Dam, while a piecewise

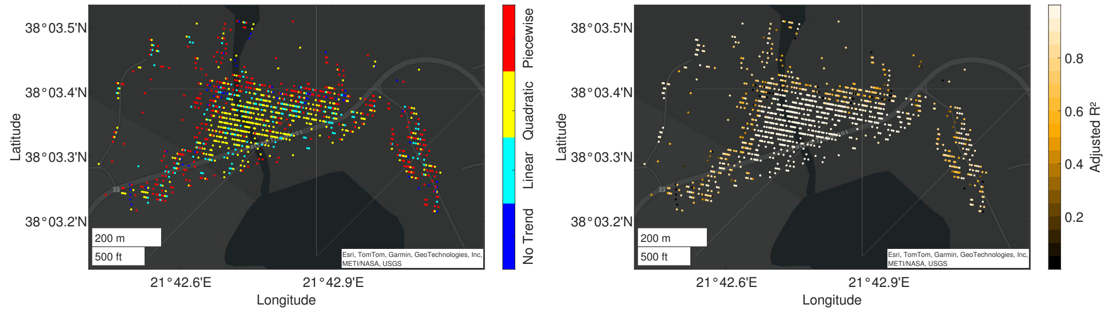

(a) Model type of the trend component **(b)** Goodness-of-fit

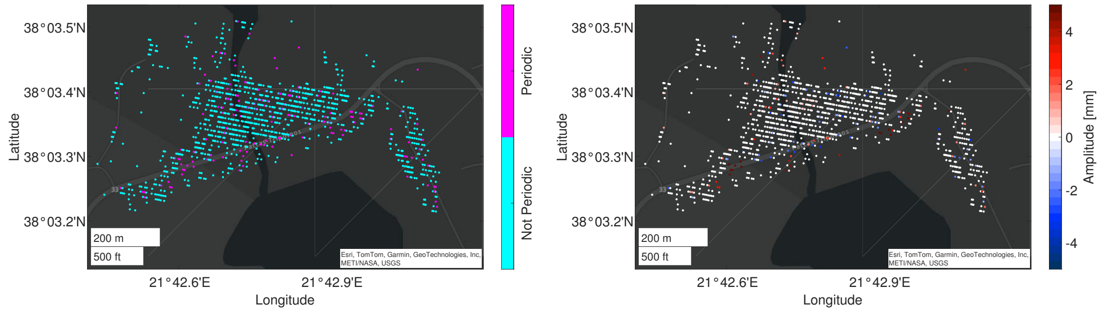

(c) Indication of a periodic component **(d)** Amplitude of periodic component

Figure 4.15.: Selected features of the best-fitting time series models derived by PSDefoPAT® for MPs in the area of the Parapeiros-Peiros Dam southwest of Patras.

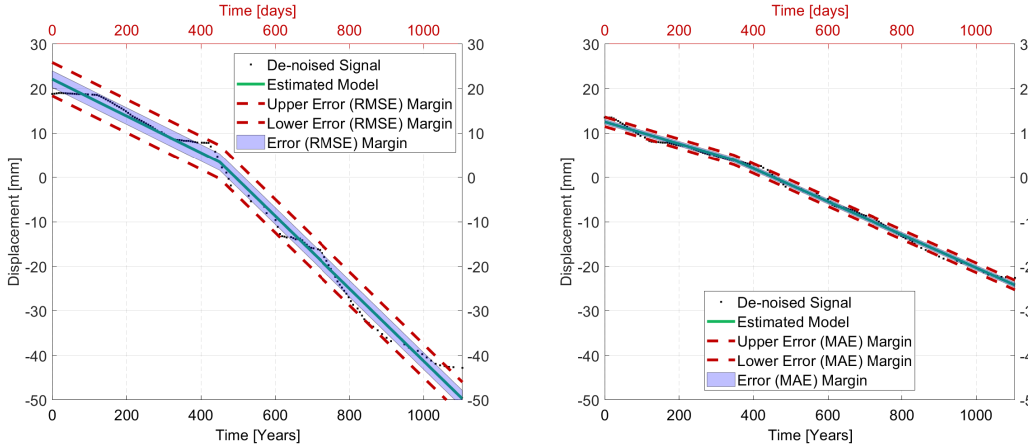

(a) MP II **(b)** MP III

Figure 4.16.: De-noised time series (black), estimated best-fitting model (green), and associated error margins (blue) for (a) MP I located on the crown and (b) MP IV located at the center of the dam body of the Parapeiros-Peiros Dam.

linear (red) model was selected for MPs towards the edges of the dam body. Areas with a high value for the goodness-of-fit in Figure 4.15 (b) match areas where a quadratic time series model was selected. Figures 4.15 (c) and (d) showed that only a few MPs feature a periodic component (magenta). Processing the displacement time series of MPs on the dam body of the Parapeiros-Peiros Dam reveals that the dam does not deform uniformly in time. The predominantly selected quadratic model shows that the mean deformation velocity changes over time. In the case of the dam, the velocity first increases, which matches the expectation. The water reservoir of the dam is flooded for the first time during the observation period of Dataset A and thus, the pressure and dead load on the dam body increases. Figure 4.16 shows the displacement time series (black) and the corresponding fitted time series model (green) for two exemplary MPs located on the dam body of the Parapeiros-Peiros Dam. MP I is located at the crown and MP IV is located at the center of the dam body. Both displacement time series (black) follow a piecewise linear trend and the second segment has a higher deformation velocity than the first. The displacement time series differ in the magnitude of the deformation. The MP located at the center of the dam body exhibits a slower deformation than the one on the crown, which is a deformation pattern expected for embankment dams [47, 48].

4.5 Discussion

Reflecting on the introduction to this thesis, a need for automatic post-processing procedures to extract relevant information on the temporal pattern of ground surface deformation datasets was identified. Advanced DInSAR results are often evaluated using their mean deformation velocity maps, which can be misleading because the mean deformation velocity is estimated with the assumption of a constant velocity deformation model. Thus, an acceleration, deceleration, or periodic pattern in the deformation processes is neglected. However, in Sub-section 4.1 it was stated that this kind of information is of special interest for local authorities to assess and mitigate any threat due to surface deformation. Additionally, in the case of a continuous processing of a steady stream of SAR images, analyzing the amount of produced advanced DInSAR results poses a bottleneck. The presented post-processing tool PSDefoPAT® addresses both issues. The tool assigns each MP in the dataset a best-fitting time series model, which provides the desired information on the dynamics of the observed ground surface deformation. Additionally, PSDefoPAT® is fully automated. The four standardized PSDefoPAT® figures presented in Section 4.2.2 show key features of the estimated time series models in a spatial context and facilitate an easy analysis of both the spatial and temporal pattern of the ground surface deformation in conjunction.

Testing PSDefoPAT® on synthetic displacement time series in Section 4.3 showed that, as could be expected, the reliability of PSDefoPAT® depends on the noise in the displacement time series. In the case of a low noise level, PSDefoPAT® correctly labeled 85 % of the synthetic displacement time series, with the exception of those that featured a trend in combination with a periodic component. About 30 % of them were mislabeled even in the case of low noise level. In the case of a high noise level, PSDefoPAT® only labeled 14% of the synthetic displacement time series correctly. As already stated it was expected to observe a decline in the accuracy of labeling the displacement time series with an increase in the noise present in the dataset. The application of PSDefoPAT® on the simulated displacement time series showcased this. It also stresses the importance of evaluating if the displacement time series in the dataset are crisp or noisy before applying PSDefoPAT® and to keep it in mind while interpenetrating the estimated time series models.

Nevertheless, the two case studies presented in Section 4.4 show that clusters of MPs that follow a specific time series model do roughly match known geological features such as active faults. Additionally, the case study of the Parapeiros-Peiros Dam showed that PSDefoPAT® provides relevant information on the dynamics of its surface deformation, which are mainly anthropogenically driven. Most MP on the dam body feature a quadratic trend, i.e., their deformation velocity changes during the observation period as a reaction to the flooding of its reservoir. Both case studies highlight the significance of moving on from mainly using the mean deformation velocity maps to interpret the results from advanced DInSAR results.

5

Processing Complex High-Resolution DInSAR Data

5.1 Problem Statement & State-of-the-Art

At the beginning of this thesis, it was stressed that tailoring a continuous advanced DInSAR processing chain to a specific large infrastructure element, such as a dam, for SHM can pose challenges. Dams often play a vital role in their region's socio-economic development [203] and, in the case of dam failure, pose a catastrophic threat to human settlements and the environment [204, 205]. Hence, implementing a SHM system to ensure their functionality and stability is important. Part of a SHM system is monitoring their surface deformation [125, 206]. Studies such as Tomas et al. (2013), Martire et al. (2014), Milillo et al. (2016a), Milillo et al. (2016b), and Ullo et al. (2019) have shown that advanced DInSAR techniques such as PSI are well suited to monitor the surface deformation of dams and provide vital information for SHM. Especially the study on the Mosul dam, conducted by Milillo et al. (2016b), showcased the advantages of advanced DInSAR and its potential contribution to the SHM of large infrastructure elements. In this study, ENVISAT, S1, and COSMO-SkyMed SAR data for the time spans from 2004 to 2010 and 2014 to 2016 were used to map the surface deformation of the Mosul dam, which is the largest hydraulic structure in Iraq and was built in an unfavorable geological setting, characterized by highly soluble materials. Grouting was necessary to close pathways opened by water infiltrating the foundation material. Limiting the water level in the reservoir and intervention by the US Army Corps of Engineers resulted in lower hydrostatic pressure on the foundation and a reduction in surface deformation. PSI analysis of the data revealed that the previously slowed-down deformation of the Mosul dam increased again after the Islamic State captured the structure, and grouting operations came to a stop. The study showcased one major advantage of using advanced DInSAR for SHM: no personnel or sensors are needed on site, making the technique well-suited for the SHM of remotely situated or hard-to-reach infrastructure elements. This is especially interesting for dams located in regions of geopolitical conflict, such as the Mosul Dam in Iraq, the Grand Ethiopian Renaissance Dam in Ethiopia [210] or the Enguri Dam in Georgia [211].

The dam that serves as an example within the scope of this thesis is the Parapeiros-Peiros Dam in Greece, which is introduced in detail in Chapter 3. The dam is of particular interest because it was only recently built and experienced the first filling of its reservoir. Hence, it was expected to undergo significant surface deformation. Dams are subject to various surface deformations that can either be localized, such as varying subsidence rates alongside the crest of the dam body, or occur on a larger scale, such as slope instabilities along the shoreline of the water reservoir [47, 48]. Hence, a wide coverage is needed to monitor large-scale deformation and a high spatial resolution to monitor vulnerable areas. This requirement can only be fulfilled by two sets of SAR images. For example, S1 SAR images fulfill the requirement of wide coverage, while high-resolution TSX SAR images fulfill the requirement of high spatial resolution. Due to the higher resolution (0.6 m in slant range and 1.1 m in azimuth direction [49, 50]) of high-resolution TSX data compared to S1 data, the spatial variability of the deformation pattern can be captured in greater detail and better localized, an important aspect for SHM. However, the different spatial resolution and wavelengths used by the S1 and TSX sensors, can result in SAR image time series that are unequally complex to process. The downside of a high spatial resolution is that a high spatial variability of the deformation pattern can lead to challenges during processing, since most PSI algorithms either use a predefined deformation model or enforce spatial smoothness of the deformation pattern during PS selection. Potential PS deviating from either option are not considered PS. The PSI algorithm used within the scope of this thesis, the StaMPS algorithm, requires spatial smoothness of the deformation pattern during PS selection.

Another challenge is the shorter wavelength λ of the TSX sensors (λ_{TSX} =3.1 cm [50]) compared to S1 (λ_{S1} =5.6 cm [34]). PSI exploits the difference in phase between two consecutive SAR images to measure displacements, which corresponds to a fraction of λ. Due to the ambiguous nature of the observed wrapped phase, a requirement to unwrap the observed phase is that the phase difference between two neighboring PS over two

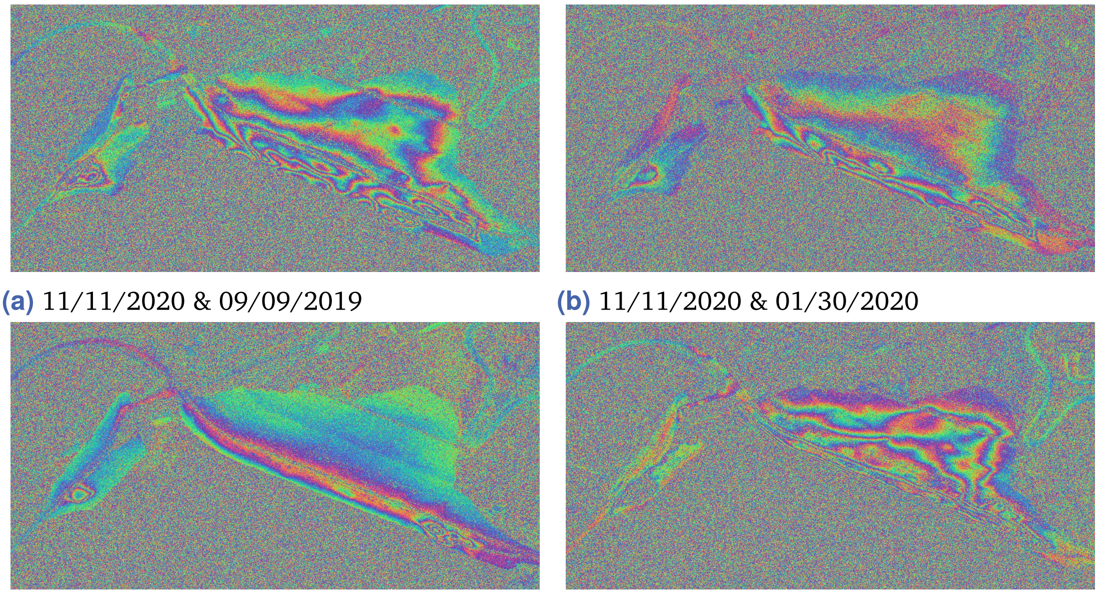
(a) 11/11/2020 & 09/09/2019
(b) 11/11/2020 & 01/30/2020

(c) 11/11/2020 & 01/27/2021
(d) 11/11/2020 & 09/02/2022

Figure 5.1.: Selected differential TSX interferograms mapping the ground surface deformation between September 2019 and September 2022 of the Parapeiros-Peiros Dam southwest of Patras.

consecutive differential interferograms is less than π [53]. The displacement resulting in a shift of π can be estimated using $\frac{\lambda}{4}$. Hence, the phase difference captured with TSX exceeds the threshold of π quicker than the ones captured with S1. This can result in multiple tightly arranged fringes, as can be seen in the differential interferograms presented in Figure 5.1. The figure shows the fringes, i.e., a phase shift of 2π, typically associated with DInSAR in the commonly used rainbow color scheme on the dam body of the Parapeiros-Peiros Dam during the filling of its reservoir. The displayed differential interferograms feature multiple deformation centers surrounded by multiple fringes. Since a displacement of $\frac{\lambda}{2}$ in LOS results in a full 2π phase shift [79], the displacement between the 11/11/2020 and 09/09/2019 on the dam body is about 4.7 cm (see Figure 5.1 (a)) and the displacement between the 11/11/2020 and 09/02/2022 on the dam body is about 7.8 cm (see Figure 5.1 (d)). It is also worth mentioning that the dam body is roughly 100,000 m^2 large and the differential interferogram for the 11/11/2020 and 01/30/2020 shows about four deformation centers in that relatively small area (see Figure 5.1 (b)). Thus, the spatial deformation pattern on the dam body is highly variable. Also, a mean deformation velocity of roughly - 40 $\frac{\mathrm{mm}}{\mathrm{year}}$ can be considered rather quick in the context of PSI processing. As already stated, both the spatial variability of the deformation pattern and the relatively quick movement, i.e. phase differences surpassing π, can cause issues during PSI processing. Thus, potentially making the high-resolution SAR dataset with the shorter λ more complex to process. The two vital processing steps mostly affected by this are: (1) PS selection and (2) Phase unwrapping.

As for the PS selection, Evers et. al (2022) reviewed the success different PS selection criteria had in selecting PS on Parapeiros-Peiros Dam for monitoring the surface deformation of embankment dams. The study concluded that the selection criteria defined by Ferretti et al. (2002) and Hooper et al. (2004) have the potential to complement each other in the case of monitoring highly spatially variable deformation of a large infrastructure element, such as dams. Additionally, Piter et al. (2024) faced a similar challenge while monitoring infrastructure for transportation using S1 SAR images. Here, the medium resolution of the sensor led to a low PS coverage. Piter et al. (2024) also proposed to improve the coverage by combining multiple pixel selection criteria.

In the case of phase unwrapping, unwrapping errors due to large phase differences in adjacent pixels are a known challenge in DEM reconstruction. The elevation difference that results in a 2π phase shift is referred to as the height of ambiguity (Equation 2.16 in Section 2.1.1) and is affected significantly by the spatial baseline. Larger spatial baselines result in a smaller height of ambiguity and thus, in larger phase differences between pixels and possibly unwrapping errors. Nevertheless, larger spatial baselines are still desired since they provide better height accuracy in DEM reconstruction. This issue was resolved for the TanDEM-X mission, whose objective it was to create a high-quality global DEM, through a multi-baseline acquisition plan. Interferograms with smaller baselines were recorded and unwrapped first. In a second step, interferograms with larger baselines were acquired and processed jointly with the small baseline interferograms. The small baseline interferograms were used to obtain the correct ambiguity number, i.e., multiplier needed to obtain the absolute phase (see Sub-Section 2.1.4) [213, 214]. In other examples, the phase difference was simply reduced by reconstructing the wrapped topography-induced phase from an already existing DEM of the area, often with low resolution, and subtracting the wrapped topography-induced phase from the interferometric phase, so that only the residual phase needs to be unwrapped [215, 216]. A similar approach, as was suggested by Evers et al. (2024), can be realized for advanced DInSAR datasets using the post-processing tool PSDefoPAT®, which is presented in Chapter 4. The tool extracts temporal and spatial deformation patterns from advanced DInSAR datasets by estimating a best-fitting time series for each displacement time series. The proposal to improve or ease the unwrapping process of a complex-to-process dataset is to extract displacement time series models from a simpler-to-process dataset, which records the surface deformation of the same area and for the same time span as the complex-to-process dataset, but with a different SAR sensor and a different acquisition mode. The time series models, extracted from a simpler-to-process dataset, can be used to reconstruct an idealized wrapped deformation-induced phase and subtract it from the differential phase of the more complex to process dataset prior to phase unwrapping. Thus, reducing the phase differences between adjacent PS over consecutive differential interferograms.

In this chapter, first, an approach for combining the selection criteria defined by Ferretti et al. (2002) and Hooper et al. (2004), so that they complement each other, is presented and demonstrated. Following that, an approach to support the unwrapping step of a complex-to-process dataset with a reconstructed idealized deformation-induced phase generated based on displacement time series models extracted from a simpler-to-process dataset is presented and demonstrated. Within the scope of this thesis, the complex-to-process dataset is Dataset B and the simpler-to-process dataset is Dataset A. Both datasets cover the area of the Parapeiros-Peiros Dam from September 2019 to September 2022 and are introduced in Chapter 3.

5.2 Adaptations to PSI Processing

In this section, the adaptation to the conventional advanced DInSAR processing chain, presented in Figure 3.4 in Chapter 3, needed for combining different PS selection criteria to support PS selection and the use of a reconstructed idealized deformation-induced phase to support the unwrapping process, are outlined and demonstrated.

The section is divided into two sub-sections. The first sub-section outlines the approach to combine different pixel selection criteria [59]. The second sub-section addresses the reconstruction of the idealized unwrapped deformation-induced phase ϕ_{defo} from the simpler-to-process dataset (Dataset A) based on the displacement time series models d_{model} provided by PSDefoPAT® [60]. This reconstructed ϕ_{defo} is then wrapped and used

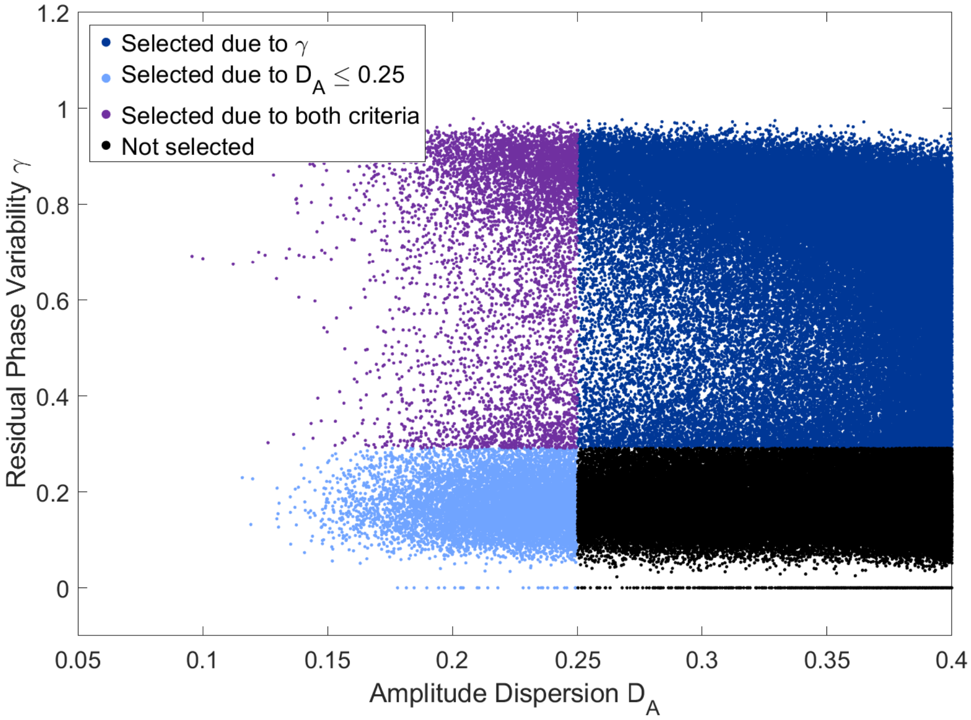

Figure 5.2.: Scatterer plot of D_A and γ for PSC.

as a correction term during the phase unwrapping of the complex-to-process dataset (Dataset B).

5.2.1 PS Selection Supported by Combining PS Selection Criteria

As already stated, a solution to increasing the number of PS, is to combine different selection criteria. Two commonly used PS selection criteria are the amplitude dispersion index D_A, first used by Ferretti et al. (2002), and the residual phase variability γ, introduced by Hooper et al. (2004). Ferretti et al. (2002) considers all pixels with $D_A \leq 0.25$ as PS pixels. while Hooper et al. (2004) considers all pixels with $D_A \leq 0.4$ as PSC pixels, whose γ is calculated in a second step. The threshold for γ is calculated for every dataset individually. It is estimated to be 0.3 for Dataset A and Dataset B. Pixels with $\gamma \leq \gamma_{\text{Threshold}}$ are not considered PS. Figure 5.2 (a) shows a scatterer plot between γ and D_A for PSC identified in Dataset B. The scatterers are colored based on which PS selection criteria they meet. The black colored PSC were not selected as PS, the dark blue colored PSC were selected as PS based on their γ, the light blue PSC were selected based on their D_A, and the purple PSC fulfill both criteria. Noticeably, there are PSC with a low D_A and γ beneath the threshold (light blue). Thus, they are not selected as PS by the PSI algorithm StaMPS. As stated in Section 5.1 the PSI algorithm StaMPS requires spatial smoothness of the spatial deformation pattern to accurately estimate the noise of the PSC. Figure 5.1 showed that this is likely not the case for Dataset B. Hence, negatively influencing the γ values for the PSC on the dam body. Assuming that the high spatially variable deformation pattern is the cause for the PSC being excluded, it stands to reason to re-integrate them after the PS selection process in StaMPS and processes both sets of PS pixels together without further altering the algorithm. Figure 5.3 (b) shows the mean deformation velocities in LOS of the sensor for pixels selected as PS by combining the selection criteria defined by Ferretti et al. (2002) and by Hooper et al. (2004). The coverage on the dam body is significantly better than only using the selection criteria by Hooper et al. (2004), which can be seen in Figure 5.3 (a). Combining the selection criteria resulted in an increase of PS form 50,608 to 60,346 on and around the dam body. The dam body is now sufficiently covered to observe its surface deformation. The mean deformation velocity map in Figure 5.3 (b) depicts a displacement of the dam body away from the sensor, which is in agreement with the surface deformation observed in the S1 dataset (results are presented in Chapter 4). However, inspecting the mean deformation velocity map in Figure 5.3 (b) reveals sharp transitions in the color gradient, which indicate phase unwrapping errors. Resolving these is addressed in the next sub-section.

5.2.2 Phase Unwrapping Supported by an Idealized Deformation-Induced Phase

Reconstructing the Idealized Deformation-Induced Phase

Reconstructing an idealized unwrapped deformation-induced phase ϕ_{defo} consists of seven steps, which are visualized in Figure 5.4. The first step is to use the time series model d_{model} estimated by PSDefoPAT® of each MP in Dataset A to estimate the displacement rates for the time stamps of Dataset B. Once the displacement rates for the new time stamps are acquired, the displacement rates need to be adjusted for the difference in the LOS of

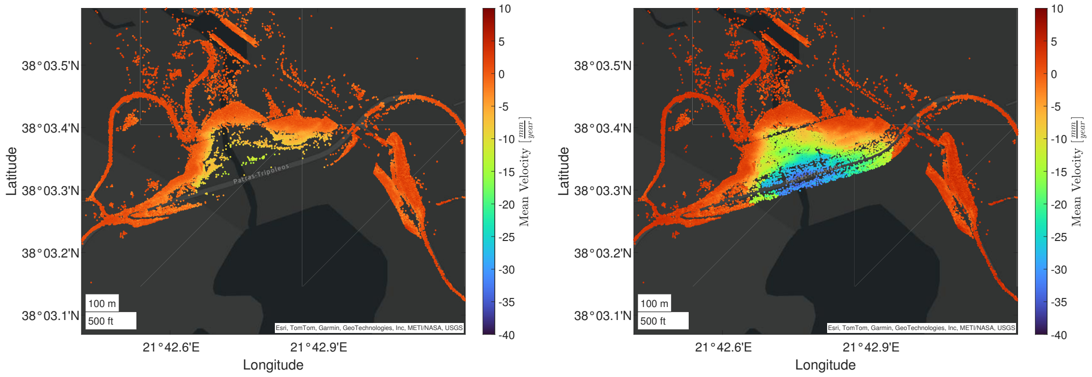

(a) Before

(b) After

Figure 5.3.: Mean deformation velocity map for the Parapeiros-Peiros Dam derived from the TSX SAR image time series (a) before and (b) after combining different selection criteria so that they complement each other.

the sensors and the date of the reference image between Dataset A (11/08/2020) and Dataset B (11/11/2020). If the dates of the reference images deviate from one another, the displacement time series needs to be shifted so that on the date of the reference image of Dataset B, the displacement is 0 mm. As for the adjustment, which needs to be made due to a difference in LOS between Dataset A and Dataset B. The following equation describes the relationship between the displacement d_{LOS} in LOS direction and the 3D displacement:

$$d_{\mathrm{3D}} = \begin{pmatrix} d_{\mathrm{u}} \\ d_{\mathrm{e}} \\ d_{\mathrm{n}} \end{pmatrix}, \tag{5.1}$$

i.e., vertical displacement d_{u} and displacement in the north-south d_{n} and east-west d_{e} direction [10]:

$$d_{\mathrm{LOS}} = d_{\mathrm{u}} \cdot cos(\xi) - sin(\xi) \cdot (d_{\mathrm{n}} \cdot cos(\varpi_{\mathrm{heading}} - \frac{3\pi}{2}) + d_{\mathrm{e}} \cdot sin(\varpi_{\mathrm{heading}} - \frac{3\pi}{2})). \tag{5.2}$$

The equation can also be used to estimate the sensitivity of a SAR sensor, capable of interferometry, to map ground surface displacement in each direction. A heading of $\varpi_{\mathrm{heading}} = 190.28°$ and a mean incidence angle of $\xi_{\mathrm{mean}} = 33.74°$ for the S1 images of Dataset A results in a sensitivity of 0.83 for vertical displacement and -0.10 and 0.55 for displacement in the north-south and east-west direction. For the TSX images of Dataset B with a heading of 189.08° and a mean incidence angle of 42.2°, the sensitivity is 0.74 for vertical displacement and -0.11 and 0.66 for displacement in the north-south and east-west direction. In addition, measurements with surface monuments on the dam body have shown that in the examined time span, the total horizontal displacement downstream of the dam body of the Parapeiros-Peiros Dam amounts to 1 cm, and the total vertical displacement amounts to 11 cm [167]. Since the horizontal displacement is less than one $\frac{1}{10}$th of the vertical displacement, and both datasets are most sensitive to the vertical component of the displacement, it stands to reason to only consider vertical displacement

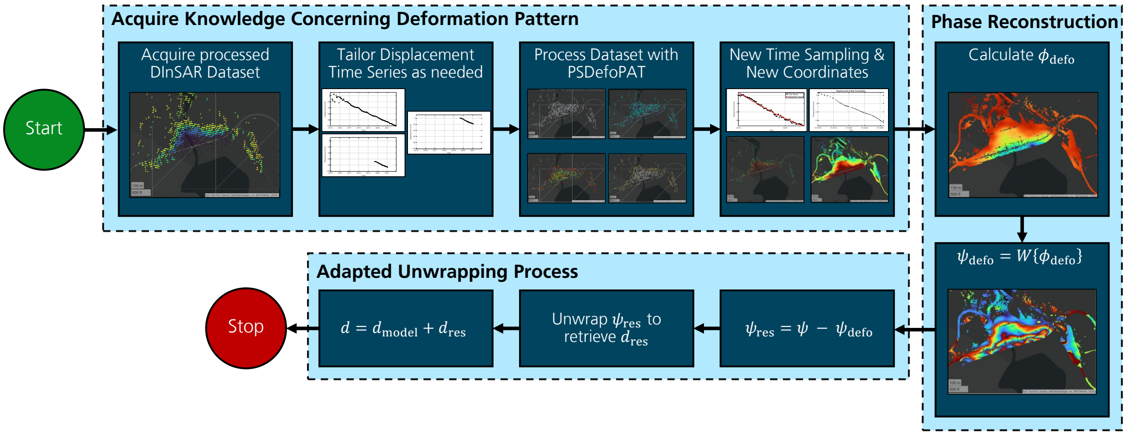

Figure 5.4.: Proposed workflow to reconstructing an idealized unwrapped deformation-induced phase ϕ_{defo}.

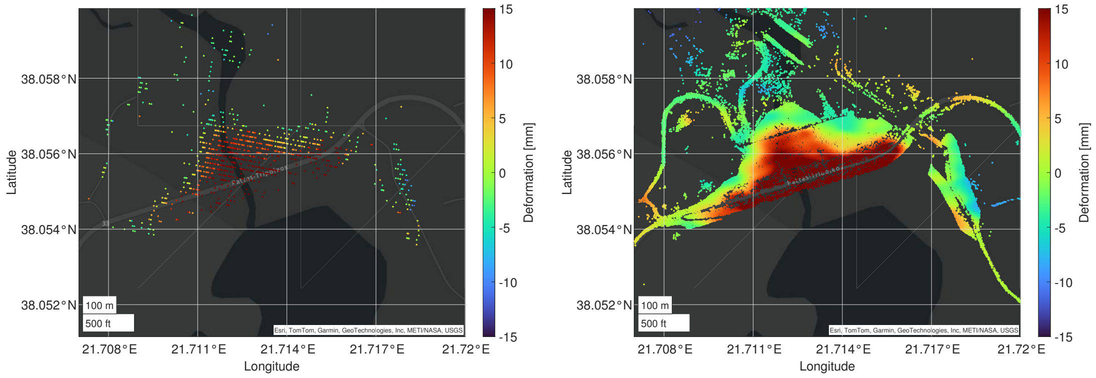

(a) Displacements at the coordinates of Dataset A

(b) Displacements at the coordinates of Dataset B estimated with interpolation

Figure 5.5.: Exemplary displacements for one differential interferogram at the coordinates of PS identified in (a) Dataset A and (b) Dataset B.

when adjusting the displacements derived from the displacement time series model for the LOS of Dataset B. Similar assumption have been made by Milillo et al. (2016a) and Ziemer et al. (2025) in order to compare displacement rates of dam bodies acquired with different sensors. Based on Equation 5.2, the following equations can be used to project the displacement d_{LOS} in LOS direction of S1 and TSX in their vertical component d_u:

$$d_{\mathrm{LOS,\ S_1}} = d_\mathrm{u} \cdot cos(\xi_{\mathrm{S_1}}) \tag{5.3}$$

and

$$d_{\mathrm{LOS,\ TSX}} = d_\mathrm{u} \cdot cos(\xi_{\mathrm{TSX}}). \tag{5.4}$$

Combining both equations allows to project the vertical component of $d_{\mathrm{LOS,\ S_1}}$ to $d_{\mathrm{LOS,\ TSX}}$:

$$d_{\mathrm{LOS,TSX}} = d_{\mathrm{LOS,\ S_1}} \cdot \frac{cos(\xi_{\mathrm{TSX}})}{cos(\xi_{\mathrm{S_1}})}. \tag{5.5}$$

The next step is to estimate the displacements at the coordinates of the PS found in Dataset B for each differential interferogram. This is done by fitting a surface to the displacements at the coordinates of the PS in Dataset A using thin-plate spline interpolation, which is an algorithm designed for the interpolation of scattered data. The interpolation is based on a weighted sum of locally defined thin-plate splines [218]. The regression surface of each differential interferogram is used to retrieve the displacement at the coordinates of Dataset B. An example of the original displacements at the coordinates of Dataset A and an estimation of the displacements at the coordinates of Dataset B using thin-plate spline interpolation is displayed in Figure 5.5. Making all the adjustments to the idealized displacement time series and estimating the displacements at the coordinates of PS in Dataset B, yields a set of idealized displacement maps that match the differential interferograms of Dataset B.

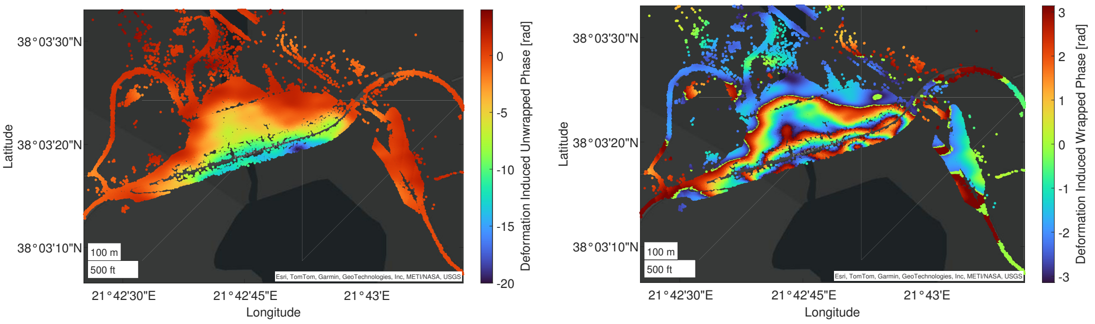

(a) Idealized ϕ_{defo} **(b)** Idealized ψ_{defo}

Figure 5.6.: The idealized (a) ϕ_{defo} and (b) ψ_{defo} resulting from the displacements presented in Figure 5.5.

The next step is to generate the idealized ϕ_{defo} based on the displacement maps. The relationship between d_{LOS} and ϕ_{defo} is [10]:

$$\phi_{\text{defo}} = \frac{4\pi}{\lambda} d_{\text{LOS}}. \tag{5.6}$$

Using Equation 5.6 yields a set of maps containing the idealized ϕ_{defo}, which is then wrapped. ϕ_{defo} and the wrapped idealized deformation induced phase ψ_{defo} resulting from the displacements presented in Figure 5.5 are presented in Figure 5.6. Once the phase is wrapped to an interval of $[-\pi, \pi)$, it can be incorporated into the phase unwrapping step of the advanced DInSAR processing chain, presented in Figure 3.4 in Chapter 3. Figure 5.7 shows an exemplary differential interferogram of Dataset B (a) before and (b) after ψ_{defo} was subtracted. It shows that this approach compensates for a significant part of the deformation pattern. The next paragraph outlines how the approach can be used to support the steps of phase unwrapping.

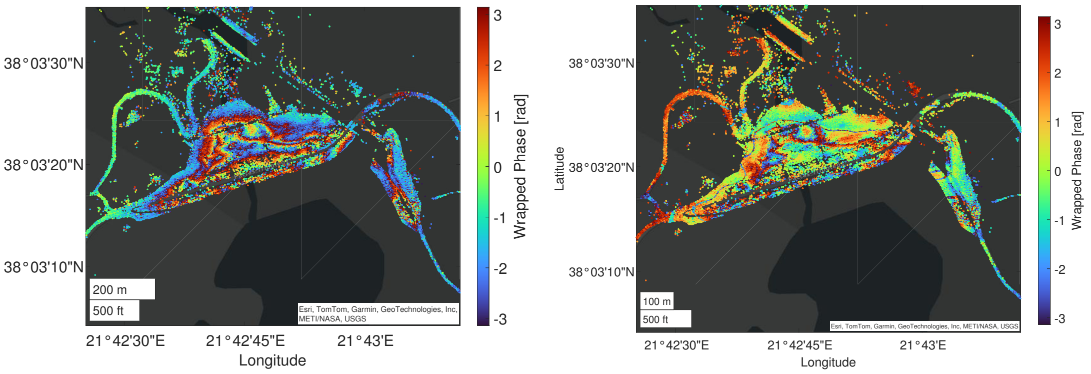

(a) Before **(b)** After

Figure 5.7.: The differential phase of an exemplary interferogram (a) before and (b) after subtracting the ψ_{defo}.

Phase Unwrapping with an Idealized Deformation-Induced Phase

Similarly, as it is done DEM reconstruction [215, 216], an already known deformation-induced phase can be used to aid the phase unwrapping step in a PSI analysis. As outlined in Sub-section 5.2.2, the idealized ϕ_{defo} is reconstructed using displacement rates based on time series models obtained from Dataset A, here a S1 SAR image time series. Once ϕ_{defo} is estimated and wrapped, it can be subtracted from differential interferograms of Dataset B, here a TSX SAR image time series. This step reduces the phase difference of MPs connected by the same arc and the difference of phase of an arc in subsequent differential interferograms. For successful unwrapping, the phase difference should be less than π [53, 82]. Since, the StaMPS PSI algorithm offers the option to subtract phase contributions resulting from changes in atmospheric conditions and the spatially correlated look angle error, the option to also subtract an idealized ψ_{defo} was added.
After subtracting the idealized ψ_{defo}, the established StaMPS phase unwrapping procedure is carried out, and the residual phase of the differential interferograms of Dataset B is unwrapped. Afterwards, the idealized ϕ_{defo} is added back to the now unwrapped residual phase, yielding a set of unwrapped differential interferograms for Dataset B. The mean deformation velocity map resulting from this approach is presented in Figure 5.8 (b). In comparison the mean deformation velocity map resulting not using this approach is presented in Figure 5.8 (a). Areas, in which the mean deformation map changed are marked in black. In those areas in Figure 5.8 (a) unwrapping errors in space can be observed. They are visible in form of sharp transition lines between colors (here green-yellow to red). In Figure 5.8 (b) these transition lines are more smooth. To show this in more detail, exemplary displacement time series of individual PS are presented in Figure 5.9. In this figure, unwrapping errors in time can be observed. They manifest in form of significant jumps in the displacement time series. Time windows, in which the displacement time series deviate significantly, are marked in black. It can be observed that

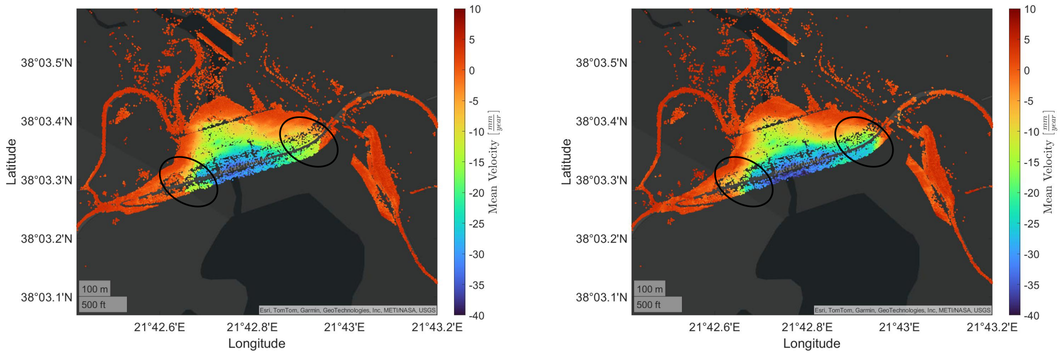

(a) Without subtracting ψ_{defo}

(b) With subtracting ψ_{defo}

Figure 5.8.: Mean deformation velocity maps for PS identified on the dam body after combining different PS selection criteria to complement each other (a) without and (b) with subtracting ψ_{defo} prioir to phase unwrapping

the phase unwrapping procedure was improved by the above presented approach resulting in far smoother displacement time series in some of the marked time windows. However, it is also noticeable that there is an artifact appearing in all magenta colored displacement time series in the middle of the time series, which is most likely an effect transferred from Dataset A.

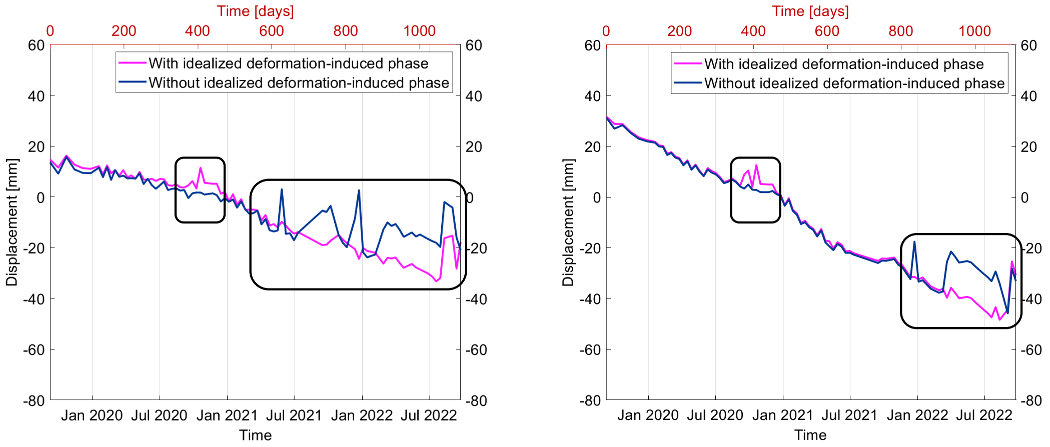

(a) PS on top of the crown

(b) PS at the center

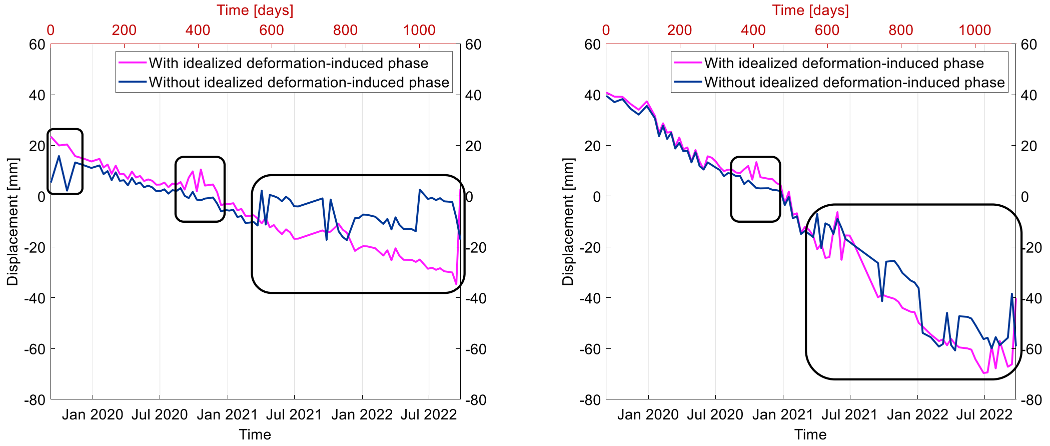

(c) PS on the right side

(d) PS on the left side

Figure 5.9.: Displacement time series of exemplary PS in Dataset B (a) on top of the crown, (b) at the center and (c) on the right and (d) left side of the downstream shoulder before (dark blue) and after (magenta) incorporating the deformation-induced phase. Time windows, in which the displacement time series deviate significantly are marked in black.

5.3 Discussion

At the beginning of the chapter, the parameters spatial resolution and wavelength of the used sensor are discussed as aspects that can determine the complexity of processing a dataset in the context of SHM, where the object of interest is expected to undergo significant deformation. Hence, SAR image time series recording the same deformation over the same time span with different sensors, e.g., S1 and TSX, are unequally complex to process.

A higher resolution allows for capturing spatial deformation patterns in greater detail and better localization, both important aspects for SHM. The downside is that a high spatial variability of the deformation pattern can lead to challenges during processing. This affects mostly the steos of PS selection and phase unwrapping. In this chapter, two approaches to support these steps are presented. In the case of PS selection, it is suggested to combine the criteria defined by Ferretti et al. (2002) and Hooper et al. (2004) so that the resulting set of PS complement each other. The approach is demonstrated on a TSX SAR image time series that maps the deformation process of the Parapeiros-Peiros Dam during the filling of its reservoir, a time in which the dam is expected to undergo significant deformation. Figure 5.3 shows that this approach increases the PS coverage on the dam body significantly. The number of PS increased form 50,608 to 60,346 on and around the dam body. This did not just simply lead to a densification of the PS, the approach effectively closed significant gaps in the coverage. Those gaps prevented the analysis of the surface deformation, the Parapeiros-Peiros Dam experienced, entirely. Hence, combining PS criteria is an effective approach to PS in complex-to-process datasets.

The second parameter, the wavelength, determines the displacement that results in a complete 2π phase shift, i.e., a fringe in a differential interferogram, and can be estimated by $\frac{\lambda}{2}$. Hence, shorter wavelengths result in more fringes that are tightly spaced than longer wavelengths. This can negatively influence the unwrapping process if it results in the phase difference between adjacent PS over consecutive differential interferograms exceeding π. Figure 5.1 shows that for the TSX SAR image time series, mapping the deformation of the Parapeiros-Peiros Dam during its filling process, this is likely the case. In this chapter, an approach to reduce these phase differences by incorporating the idealized deformation-induced phase reconstructed from the displacement time series model extracted with PSDefoPAT from the simpler-to-process dataset, here a S1 SAR image time series (Dataset A) is presented and demonstrated. The presented approach does result in improvements in the phase unwrapping step in and thus, smoother displacements in space and time, which is clearly shown in Figure 5.8 and Figure 5.9. However, Figure 5.9 also shows that unwanted effects can be transferred from the simpler-to-process dataset to the complex-to-process dataset. Hence, it is important that the time series models extracted from simpler-to-process dataset are smooth and without artifacts themselves. This also underlines the importance of noise reduction in PSDefoPAT®. Alternatively, displacement time series acquired with, e.g., GNSS, could be used instead of a simpler-to-process DInSAR dataset to avoid transferring any unwanted effects related to PSI processing.

6

Strategies to Process a Steady Stream of SAR Images

6.1 Problem Statement & State-of-the-Art

As stressed in Section 1.1, continuously analyzing a steady stream of SAR images for monitoring tasks entails frequent processing, which raises questions concerning an adequate processing strategy. In general, three different strategies are imaginable. The first strategy is to always process all available SAR images W_{total}, i.e. a growing dataset. This strategy will be referred to as Strategy A. The second strategy is to process the steady stream of SAR images in consecutive non-overlapping subsets, which will be referred to as Strategy B. The third strategy is to use overlapping consecutive subsets, similar to a sliding-window. This strategy will be referred to as Strategy C. All three strategies are visualized in Figure 6.1. In literature, there are already several examples of monitoring systems or services that process the steady stream of SAR images provided by the S1 mission continuously. The first example ever presented is the ground surface deformation monitoring system set up for the Tuscany region, presented by Raspini et al. (2018). The monitoring system utilizes a parallelized version of SqueeSAR$^{\text{TM}}$ [16] and generates updates of the ground surface deformation dataset of Tuscany with each newly available SAR image. After each analysis, local authorities are provided with a monitoring bulletin highlighting areas with deformation anomalies, making it one of the first Ground Motion Services (GMS) to be introduced. Regarding the proposed processing strategies above, the monitoring system of the Tuscany region falls under Strategy A.

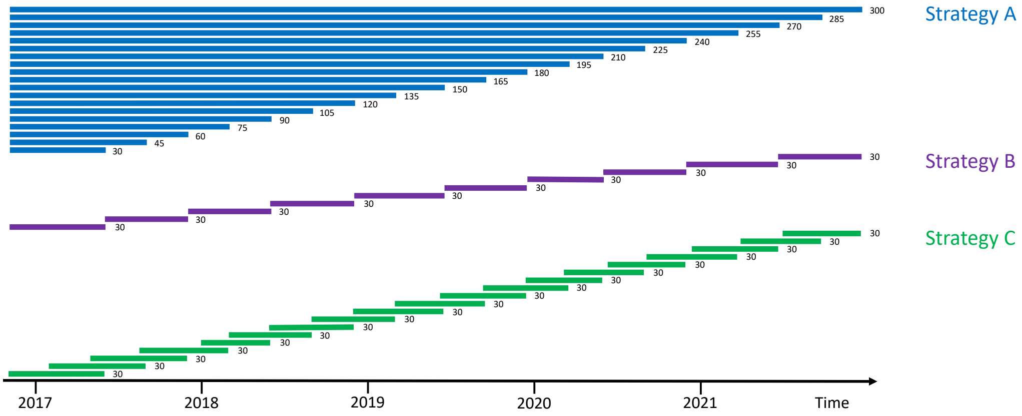

Figure 6.1.: Visualization of the three proposed processing strategies for PSI.

The first nationwide GMS presented was InSAR Norway (`https://insar.ngu.no/`). The primary objective of the service is to detect and map landslides. The baseline product was launched in November 2018. It was generated by the Norwegian Research Center (NORCE) utilizing S1 SAR images from 2015 to 2018. The German GMS, referred to as BodenBewegungsdienst Deutschland (`https://bodenbewegungsdienst.bgr.de/mapapps/resources/apps/bbd/`), was launched a year after the Norwegian GMS. The Federal Institute for Geosciences and Natural Resources (BGR) led the initiative, while the DLR carried out the processing of the S1 images covering Germany with a wide-area PSI approach. The baseline product was generated using the available S1 data from November 2014 to March 2019. The GMS on a continental scale is the EGMS (`https://egms.land.copernicus.eu/`). The service provides ground motion data for all European countries that support the Copernicus initiative, as well as the United Kingdom. The EGMS publishes an update of the ground motion data once a year, covering the past five years [173, 219]. While the EGMS falls under Strategy C, the exact processing strategy of InSAR Norway and the BodenBewegungsdienst Deutschland is unknown. Based on the products available online, it can be deduced that InSAR Norway also falls under Strategy C. It is currently possible to download the data from four distinct time spans (2015-2019, 2018-2022, 2019-2023, and 2020-2024), which overlap. In the case of the BodenBewegungsdienst Deutschland, only one time span (2019-2023) is available, making it difficult to deduce its processing strategies. Examples for Strategy B cannot be found in the literature.

Regarding the question of which processing strategy is the most suitable for continuous monitoring tasks, some considerations have to be made. A drawback of the PSI technique is that it only extracts ground surface displacement rates from pixels behaving coherently for the entire observation time [43, 44]. This restriction leads to a loss in PS density, the longer the examined SAR image time series gets [61]. Thus, a continuously growing dataset with an expanding observation period is likely to result in a continuous loss of PS. A lower PS density impedes an accurate assessment of the spatial pattern of the ground surface deformation and the extent of the affected area. This limitation mainly concerns Strategy A.

Raspini et al. (2018) counteracts this by employing SqueeSAR$^{\text{TM}}$ [16], a PS and DS algorithm, which increases the number of MPs.

Another option to prevent the decline of this PS density is to include temporary coherent PS pixels. Perissin and Wang (2012) and Dörr et al. (2022) presented advanced DInSAR algorithms that include temporary coherent PS pixels. The basic idea of the algorithm presented by Perissin and Wang (2012) is to loosen the restrictive conditions imposed by PSI techniques to identify PS. The approach is referred to as quasi-PS technique. Three key changes were made: (1) The SAR images are not required to be correlated with a unique common reference image, (2) the estimation of height and displacement of quasi PS is based on a pixel-specific subset of interferograms, and (3) spatial filtering is applied to improve the SNR. The algorithm presented by Dörr et al. (2022) builds upon the approach proposed by Hu et al. (2019), which leverages the distinct distributions of amplitude values for PS, coherent and incoherent DS. The amplitude value distribution for incoherent scatterers follows a Rayleigh distribution. The amplitude value distribution of PS, on the other hand, can be described by a Rice distribution with high SNR. Coherent DS have an amplitude value distribution fitting a Rice distribution with low SNR. In the case of temporary coherent scatterers, it is assumed that the distribution of amplitude values changes over the observation time. They employ hypothesis testing to identify scatterers that undergo a change in their amplitude dispersion. Dörr et al. (2022) introduce an additional phase-based change point detection algorithm, based on a likelihood ratio test, to iteratively refine the change date of the scatterers. For phase unwrapping, they adapted the algorithm implemented in StaMPS, allowing them to jointly unwrap the phase of PS and temporary PS. Applying their approach to a time series of S1 SAR images covering the Vietnamese city Ca Mau between November 2016 and November 2020 allowed them to increase the number of PS from 46,553 to 121,032.

Other aspects to consider, while processing a steady stream of SAR images, are the processing time, computational load and hard disk space. Concerning processing time, Raspini et al. (2018) attempts to reduce the processing time by parallelizing the SqueeSAR$^{\text{TM}}$ [16] algorithm. In contrast, a characteristic of Strategy B and Strategy C is to limit the number processed SAR images and thus, limit the processing time. Additionally, limiting the number processed SAR images will also reduce hard disk space. Another algorithm, which needs to mentioned in this context is the Sequential Estimator [221]. The algorithm recursively estimates and analyzes covariance matrix of wide-swath and long-term DInSAR time series to identify DS by dividing the dataset into small batches. The batch is compressed after processing and from each compressed batch an artificial interferogram is formed to link already processed data batches to the most recently acquired SAR acquisitions. Both, the computational load and hard disk space are reduced with this approach.

Additionally, the comparability of the ground surface deformation data generated with each update of the dataset is a concern. This mainly affects Strategy B and Strategy C. If processing is carried out independently for each subset, it is unlikely to observe the same PS in consecutive subsets. However, it stands to reason that being able to observe the same PS would be preferable for a monitoring system. In a previously conducted study, Evers et al. (2020) proposed to solve this by introducing two distinct reference images for co-registration and interferogram formation.

Further, concomitant with independent processing is the question of inefficiency. Since the majority of the SAR images in the dataset are reprocessed each time the dataset is updated, in the case of Strategy A and Strategy C. Implementing the PSI processing using two distinct reference images, as proposed by Evers et al. (2020), opens the door to re-using intermediate results. This potentially reduces processing time, required hard disk space, and performs more efficiently.

A final aspect is the pace in which updates are provided. Raspini et al. (2018) provides an update with each newly available SAR image, while most nation- or continental wide GMS

offer a yearly update [173, 219]. The pace of updates is mainly an issue for Strategy B. Since the subsets in Strategy B do not overlap, the user needs to wait until enough new SAR images have been recorded to conduct a PSI analysis. Strategy A and Strategy C allow for faster paced updates, as seen by Raspini et al. (2018).
In this chapter, the three proposed processing strategies are evaluated concerning their performance. Therefore, Dataset C, described in Chapter 3, is divided into subsets to simulate a steady stream of SAR images and processed according to each processing strategy, see Figure 6.1. In order to take full advantage of Strategy C, an adaptation of the advanced DInSAR processing chain, displayed in Figure 3.4, is presented. The adapted processing chain:

(1) uses two distinct reference images for co-registration and interferogram formation and

(2) re-uses intermediate results.

This processing chain is referred to as the PSISlider processing chain and will be presented in Sub-section 6.2.1.

6.2 Different Processing Strategies for PSI

In this section, the three different processing strategies to continuously process a steady stream of SAR images based on the advanced DInSAR processing chain, presented in Figure 3.4, are introduced. The processing strategies are:

(A) Growing dataset,

(B) Non-overlapping subsets and

(C) Overlapping subsets.

All three processing strategies are visualized in Figure 6.1. Additionally, in this section, changes made to the advanced DInSAR processing chain are outlined.

Strategy A: Growing Dataset

The first strategy represents the typically applied approach to processing SAR image time series. All W_{total} available SAR images are processed at once. To facilitate continuous monitoring, the dataset is regularly updated once a user-specified number W_{add} of new SAR images are available. The entire SAR time series is reprocessed with each update (following the processing chain presented in Section 3). In the case of Strategy A, the number of SAR images considered in each update W_{subset} is equal to W_{total}. Thus, W_{subset} continuously increases, likely leading to a loss in the number of PS N_{PS}.

Strategy B: Non-Overlapping Subsets

The second strategy is to process consecutive but temporally non-overlapping subsets. W_{subset} in each subset is kept constant. Since the consecutive subsets do not overlap temporally, the ground surface displacement maps and displacement time series are only updated once W_{subset} new SAR images have been recorded. The new subset is processed completely independently of all previous subsets (following the processing chain presented in Section 3). Therefore, each subset features a distinct reference image, making it challenging to compare results from the different subsets. Since W_{subset} is kept constant, it is likely that N_{PS} remains steady.

Strategy C: Overlapping Subsets

The third strategy is to process the steady stream of SAR images with temporally overlapping subsets, similar to a sliding-window approach. W_{subset} remains constant for all processed subsets. Each time a user-specified number W_{change} of new SAR images are available, W_{change} old SAR images are removed from and W_{change} new SAR images are added to the time series. The new subset is processed to update the ground surface deformation dataset. Since the consecutive subsets overlap, $W_{\text{keep}} = W_{\text{subset}} - W_{\text{change}}$ SAR images are taken on from the previous subset. This allows for the reference image to remain unchanged for a while and opens the door to re-using intermediate results. The processing chain corresponding to Strategy C is referred to as the PSISlider processing chain.

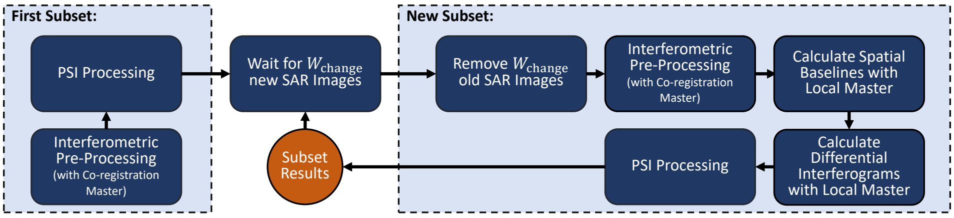

Figure 6.2.: Workflow for the PSISlider processing chain.

Advantages and Disadvantages of the Three Processing Strategies

Each strategy has its pros and cons. In case of the Strategy A, W_{subset} and the time span the dataset covers increases continuously, likely resulting in a decrease in N_{PS}. Since a pixel needs to be coherent over the majority of the time series to be considered a PS [43, 44]. The longer the time series gets, the less likely it is for this to occur. Another factor to keep in mind is that the results of a PSI analysis are typically presented in a mean deformation velocity map. In the case of a long time series, short-term deformation or changes in the deformation velocity are smothered in the mean deformation velocity map.

Strategy B and Strategy C exploit consecutive temporal subsets of W_{total} available SAR images, keeping W_{subset} and the time span the subsets cover roughly constant. Thus, it stands to reason that both strategies will potentially result in a relatively consistent N_{PS}. In addition, the shorter time span allows short-term deformation or deformation velocity changes to become recognizable in the mean deformation velocity maps.

A disadvantage of Strategy B is that each subset is processed independently, making it difficult to compare the results or possibly re-use intermediate results. Additionally, the absence of overlap between subsets results in users having to wait longer for updates of the mean deformation velocity map and its corresponding displacement time series. Before a new subset can be processed, W_{subset} new SAR images need to be recorded. Strategy A and Strategy C allow for a quicker pace in updating the ground surface deformation dataset, since W_{add} and W_{change} are generally smaller than W_{subset}.

In a nutshell, Strategy C is the most promising one, combining the advantages of Strategy A and Strategy B. The shorter time span and constant W_{subset} will potentially result in a relatively steady N_{PS}. The temporal overlap allows for a quicker pace in updating the results and potentially opens the door to re-using intermediate results from previous subsets.

The next section outlines the possibilities to re-use intermediate results and the adaptation made to the StaMPS PSI algorithm to facilitate the re-use in the PSISlider processing chain.

6.2.1 PSISlider - A Sliding-Window Approach for Persistent Scatterer Interferometry

As stated in the previous sub-section Strategy C is the most promising one out of the three strategies discussed. However, to take full advantage of re-using intermediate results, some adaptations to the conventional advanced DInSAR processing chain, presented in Figure 3.4, need to made. While processing a steady stream of SAR images with Strategy C, the first subset with W_{subset} SAR images is processed with the conventional advanced DInSAR processing chain. All subsequent subsets are processed according to the PSISlider processing chain, presented in Figure 6.2. One major difference in the two processing chains is the use of different reference images for co-registration and interferogram formation. All secondary images need to be co-registered to the same reference image independently of which image is used as the reference for interferogram formation. The reference image for co-registration will hereafter be referred to as the co-registration reference image, and the reference image for interferogram formation as the local reference image. Employing two different reference images has the consequence that:

(1) For new subsets only the W_{change} new SAR images are subjected to interferometric pre-processing with the co-registration reference image,

(2) Spatial baselines between secondary images and the local reference image need to be calculated and

(3) Differential Interferograms between secondary images and the local reference image need to be calculated.

However, using the same co-registration reference image for all subsets has the advantage, that the following intermediate results from previous subsets can be re-used during the PSI processing:

(1) D_A for PSC selection,

(2) The probability of a PSC being a PS $P(i \in \text{PS})$ for PS selection and

(3) The spatially uncorrelated look angle error $\Delta\widehat{\phi}^{\text{nc}}_{\theta,i,q}$.

Calculation of the Differential Interferograms and Spatial Baseline Between the Local Reference and Secondary SAR Images

As state previously, all SAR images in each subset are subject to interferometric pre-processing (following the processing chain presented in Figure 3.4) with the same co-registration reference image. Thus, before the PSI processing is carried out, spatial baselines and differential interferograms with the local reference image need to be calculated. The spatial baselines are estimated using a re-implementation of the process to estimate the vertical and horizontal baselines used by SNAP. A test to verify its functionality is presented in Appendix A.2.

The number of differential interferograms in a subset, generated with the co-registration reference image, is $Q = W_{\text{subset}} - 1$. The Q differential interferograms $u_{\text{LM,S}}$ between the local reference and the secondary SAR images are generated by complex multiplication of the differential interferograms $u_{\text{M,S}}$ between the co-registration reference and the secondary

SAR images with the differential interferogram $u_{\mathrm{M,LM}}$ between the co-registration reference and the local reference image. The operation can be expressed as follows:

$$u_{\mathrm{LM,S}} = \frac{u_{\mathrm{M,S}} \cdot u^{*}_{\mathrm{M,LM}}}{|z^{2}_{\mathrm{M}}|} \tag{6.1}$$

Here, $|z^{2}_{\mathrm{M}}|$ denotes the squared amplitude of the co-registration reference image. This approach results in Q-1 $u_{\mathrm{LM,S}}$. A test to verify the functionality of this approach is presented in Appendix A.2.

Re-using the Amplitude Dispersion Index for PSC Selection

Since consecutive subsets have W_{keep} SAR images in common, it is not necessary to recalculate D_A entirely for each subset. D_A from the previous subsets only needs to be corrected for the removed and added SAR images. StaMPS uses the following equation to calculate D_A:

$$D_A = \sqrt{\frac{W_{\mathrm{subset}} \cdot \Sigma_{w=1}^{W_{\mathrm{subset}}} A_w^2}{(\Sigma_{w=1}^{W_{\mathrm{subset}}} A_w)^2} - 1} \tag{6.2}$$

To facilitate the adjustment of D_A, the intermediate result from the sum of the amplitude values A_w and their square ${A_w}^2$ for each pixel are saved during the processing of the previous subset and edited for the removed and added SAR images. A test to ensure the functionality of this approach is presented in Appendix A.2.

Re-use of the Probability of a PSC Being a PS for PS Selection

The selection of the final subset of PS pixels is based on D_A and $P(i \in \mathrm{PS})$ (Step 3 in Sub-section 2.1.6), which is calculated based on γ.This γ is a measure for the phase noise of PSC pixels and is calculated iteratively (Step 2 in Sub-section 2.1.6). The influence of PSC pixels, which have a low probability of being a PS, decreases with each iteration of estimating $P(i \in \mathrm{PS})$. The value for $P(i \in \mathrm{PS})$ from the previous iteration is used to weigh the PSC pixels in each iteration, except for the first iteration. In the case of the first iteration, $\frac{1}{D_A}$ is used to weigh the PSC pixels. In the context of Strategy C, it is highly likely that consecutive overlapping subsets have many PS pixels in common. Therefore, instead of $\frac{1}{D_A}$, $\frac{1}{[P(i \in PS)]^2}$ with $P(i \in \mathrm{PS})$ from the previous subset is used to weigh the pixels during the first iteration of estimating the phase noise for PSC pixels in common for consecutive subsets. PSC pixels not present in the previous subset are weighed based on the mean $P(i \in \mathrm{PS})$ calculated over the closest neighboring PSC pixels.

This approach potentially lowers the number of iterations needed to fulfill the criterion, defined in Sub-section 2.1.6 to terminate the iteration process. On average, with the conventional processing chain, three iterations are needed to fulfill this criterion and with the PSISlider processing chain two iterations are needed on average.

Re-use of the Spatially Uncorrelated Look Angle Error

Another intermediate result that can be re-used from the previous subset is $\Delta\widehat{\phi}^{\text{nc}}_{\theta,i,q}$, which is relevant for the estimation of displacement and is calculated during the estimation of the phase correction terms (Step 4 and Step 5 in Sub-section 2.1.6). Both steps are carried out iteratively in succession. The goal is to improve phase unwrapping by subtracting $\Delta\widehat{\phi}^{\text{nc}}_{\theta,i,q}$ prior to phase unwrapping and then estimating $\Delta\widehat{\phi}^{\text{nc}}_{\theta,i,q}$ more accurately due to fewer unwrapping errors. $\Delta\widehat{\phi}^{\text{nc}}_{\theta,i,q}$ is estimated for each differential interferogram separately. Thus, in the context of Strategy C, it stands to reason to re-use the $\Delta\widehat{\phi}^{\text{nc}}_{\theta,i,q}$ estimated previously for those differential interferograms that consecutive subsets have in common. This approach lowers the number of iterations needed for the estimation of displacements and phase correction terms. On average, with the conventional processing chain, five iterations are needed to estimate all the phase correction terms, such as phase contribution induced by the atmosphere in the reference and secondary images or the spatially uncorrelated look angle error. In contrast with the PSISlider processing chain only needs three iterations.

Re-using intermediate results in the context of Strategy C had the purpose of reducing processing time, which all the presented adaptations effectively do. The processing time is one of the key parameters used in the next sub-section to evaluate the presented processing strategies.

6.2.2 Evaluation of the Processing Strategies

In the beginning of this chapter concerns regarding the processing time, PS density, processing efficiency and the compatibility of intermediate results in the context of continuously processing a steady stream of SAR images were raised. In order to identify a processing strategy most suited for the task, all three processing strategies were applied to Dataset C, which is described in detail in Chapter 3. The time span of Dataset C was set to the time between October 2016 and December 2021, resulting in $W_{\text{total}} = 300$ SAR images. Dataset C was restricted to the period where S1-A and S1-B provided SAR images with a 6-day repeat-pass time to avoid any influence on the results due to an irregular temporal sampling. The dataset was divided into subsets to simulate a continuous stream of SAR images (see Figure 6.1). The first subset for all three strategies consists of $W_{\text{subset}} = 30$ SAR images. In the case of Strategy A, a growing dataset, $W_{\text{add}} = 15$ SAR images were added to the time series for each subset. In total 19 subsets were needed. In the case of Strategy B, the consecutive non-overlapping subsets, each subset consists of $W_{\text{subset}} = 30$ SAR images. Thus, 10 subsets were needed. In the case of Strategy C, the consecutive overlapping subsets, each subset also consists of $W_{\text{subset}} = 30$ SAR images. For each subset, $W_{\text{change}} = 15$ new SAR images were exchanged for $W_{\text{change}} = 15$ old SAR images, resulting

$W_{\text{keep}} = 15$ SAR images remaining in the subset. In total 19 subsets were needed. The processing was carried out on a server with the following features:

Operating system: Micrososft Windows Server 2019 Standard
Processors: 4 x Intel(R) Xeon(R) CPU E7-8867 v3 @ 2.5 GHz
Random-Access Memory (RAM): 384 GB

In this section the processing strategies are evaluated concerning their performance. Therefore, the following key parameters were recorded during processing:

(1) Total processing time t_{total},

(2) PSI processing time t_{PSI},

(3) Number of PSC N_{PSC},

(4) Number of PS N_{PS} and

(5) Needed hard disk space M_{Space}.

The parameters t_{total}, t_{PSI} and M_{Space} were selected to evaluate the efficiency and processing time of the processing strategies. A distinguishing is made between t_{total}, which covers the entire processing chain presented in Figure 3.4, and t_{PSI}, which only considers the PSI processing. The distinguishing is made to evaluate the influence of W_{subset} better. The parameters N_{PSC} and N_{PS} were selected to draw conclusions concerning the development of the PS density. The resulting values for each parameter are presented separately for each processing strategy in the following three paragraphs.

Strategy A: Growing Dataset

The key processing parameters of Strategy A, which is to always process all the available SAR images, are presented in Table 6.1. In addition to the above-listed key parameters, the table does also include W_{subset} and the time span, the time series covers. Table 6.1 and Figure 6.3 show that the needed hard disk space (green) increases steadily, as was expected, from 242 GB to 2,446 GB with an increase of the number of SAR images (top x-axis) in each subset (bottom x-axis).

As for the processing time, t_{total} increases linearly with W_{subset}. The interferometric pre-processing of one single interferometric SAR image pair takes about 14 minutes. If only t_{PSI} is considered, it can be observed that the processing time decreases significantly from 9.3 h to 7.3 h between Subset 1 and Subset 2, remains steady between 7 h and 8 h between Subset 2 and Subset 4 and then increases again up to 15.7 h (Subset 19). This trend can be observed in Figure 6.3. The figure also shows that the part of t_{total} needed for the interferometric pre-processing increases significantly with W_{subset}. While for the first subset 58 % of the total processing time was needed for the execution of the PSI algorithm and 42 % for the interferometric pre-processing, for the last subset only 19 % of t_{total}

was needed for the PSI processing and 81 % for the interferometric pre-processing. It is important to keep in mind, that in the case of Strategy A, the entire dataset is re-processed for each subset and no intermediate results are re-used.

Both N_{PSC} and N_{PS} decreases with an increase W_{subset}, as can bee seen in Table 6.1. However, the decrease is not linear. Between Subset 1 and Subset 2, N_{PSC} drops from 331,542 to 209,654 PSC. Following the initial drop of 121,888 PSC, the amount of PSC lost with each batch of new SAR images decreases. The difference between Subset 2 and Subset 3 is only 37,302 PSC, and between Subset 18 and Subset 19, only 1,868 PSC. The slower decrease in the number of PSC for larger datasets might be influenced by the makeup of the AOI, which mainly covers the city of Patras and its suburbs. For a mainly rural area, the number of PSC might continue to decrease more rapidly. Similar observations can be made for N_{PS}. Figure 6.4 displays N_{PSC} (blue) and N_{PS} (purple) for each subset (bottom x-axis) depending on W_{subset} (top x-axis). The figure also shows that, the percentage of PSC that are selected as PS. This ratio increases significantly with an increase in W_{subset} at first and then hits a plateau around Subset 5.

Comparing the trend of N_{PSC} and N_{PS} to the trend of t_{PSI}, indicates that t_{PSI} is mainly influenced by N_{PSC} and N_{PS} in the first phase and by W_{subset} in the third phase.

In a nutshell, as expected Strategy A results in a decrease in N_{PSC} and N_{PS} with an increase in W_{subset}. Both t_{total} and M_{Space} increase linearly with W_{subset}. As for t_{PSI} it briefly

Subset	Time Span	W_{subset}	M_{Space} [GB]	t_{total} [h]	t_{PSI} [h]	N_{PSC}	N_{PS}
1	11/2016 - 05/2017	30	242	16.0	9.3	331,542	246,857
2	11/2016 - 08/2017	45	364	17.5	7.3	209,654	173,226
3	11/2016 - 11/2017	60	487	21.3	7.7	172,352	152,986
4	11/2016 - 02/2018	75	609	24.7	7.6	142,796	133,340
5	11/2016 - 05/2018	90	732	28.7	8.1	127,559	122,436
6	11/2016 - 08/2018	105	853	32.6	8.6	117,362	114,064
7	11/2016 - 12/2018	120	976	36.6	9.1	111,862	109,047
8	11/2016 - 03/2019	135	1,097	40.6	9.5	105,726	103,359
9	11/2016 - 06/2019	150	1,221	44.6	10.2	100,931	98,959
10	11/2016 - 09/2019	165	1,344	48.7	10.8	97,420	95,604
11	11/2016 - 12/2019	180	1,466	52.7	11.3	93,712	92,078
12	11/2016 - 03/2020	195	1,588	56.7	11.9	91,588	90,016
13	11/2016 - 06/2020	210	1,711	60.8	12.5	90,335	88,806
14	11/2016 - 09/2020	225	1,833	64.8	13.1	88,524	86,993
15	11/2016 - 12/2020	240	1,956	68.9	13.6	87,060	85,546
16	11/2016 - 03/2021	255	2,078	72.8	14.1	84,631	83,129
17	11/2016 - 06/2021	270	2,203	76.8	14.7	83,411	81,874
18	11/2016 - 09/2021	285	2,324	81.0	15.4	82,293	80,740
19	11/2016 - 12/2021	300	2,446	84.9	15.7	80,425	78,932

Table 6.1.: Key parameters of Strategy A.

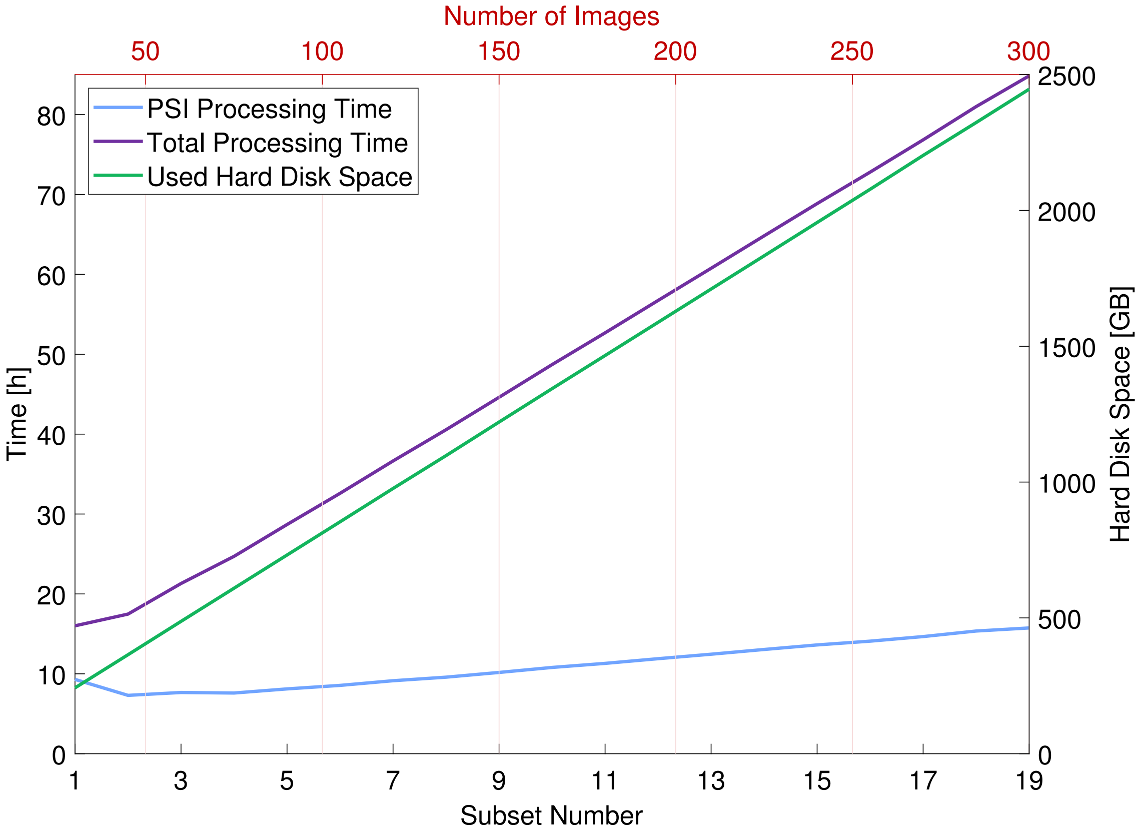

Figure 6.3.: The total processing time (purple), the PSI processing time (blue) and used hard disk space (green) depending on the processed subset (bottom x-axis) and the number of SAR images (top x-axis) in the subset for Strategy A.

Subset	Time Span	W_{subset}	M_{Space} [GB]	t_{total} [h]	t_{PSI} [h]	N_{PSC}	N_{PS}
1	11/2016 - 05/2017	30	242	16.2	9.5	331,542	246,857
2	05/2017 - 11/2017	30	222	20.8	14.1	394,029	309,328
3	11/2017 - 05/2018	30	239	14.6	7.9	307,034	219,033
4	06/2018 - 12/2018	30	218	18.4	11.7	365,698	284,159
5	12/2018 - 06/2019	30	241	13.9	7.2	298,916	207,838
6	06/2019 - 12/2019	30	218	17.4	10.7	354,235	268,144
7	12/2019 - 06/2020	30	220	17.5	10.8	354,204	271,103
8	06/2020 - 12/2020	30	220	25.1	18.4	433,800	352,838
9	12/2020 - 06/2021	30	243	14.5	7.8	310,806	220,270
10	06/2021 - 12/2021	30	224	18.4	11.7	378,623	284,155

Table 6.2.: Key parameters of Strategy B.

decreases and then increases with W_{subset}. In total 25,531 GB hard disk space and 930 h are needed to process Dataset C with Strategy A.

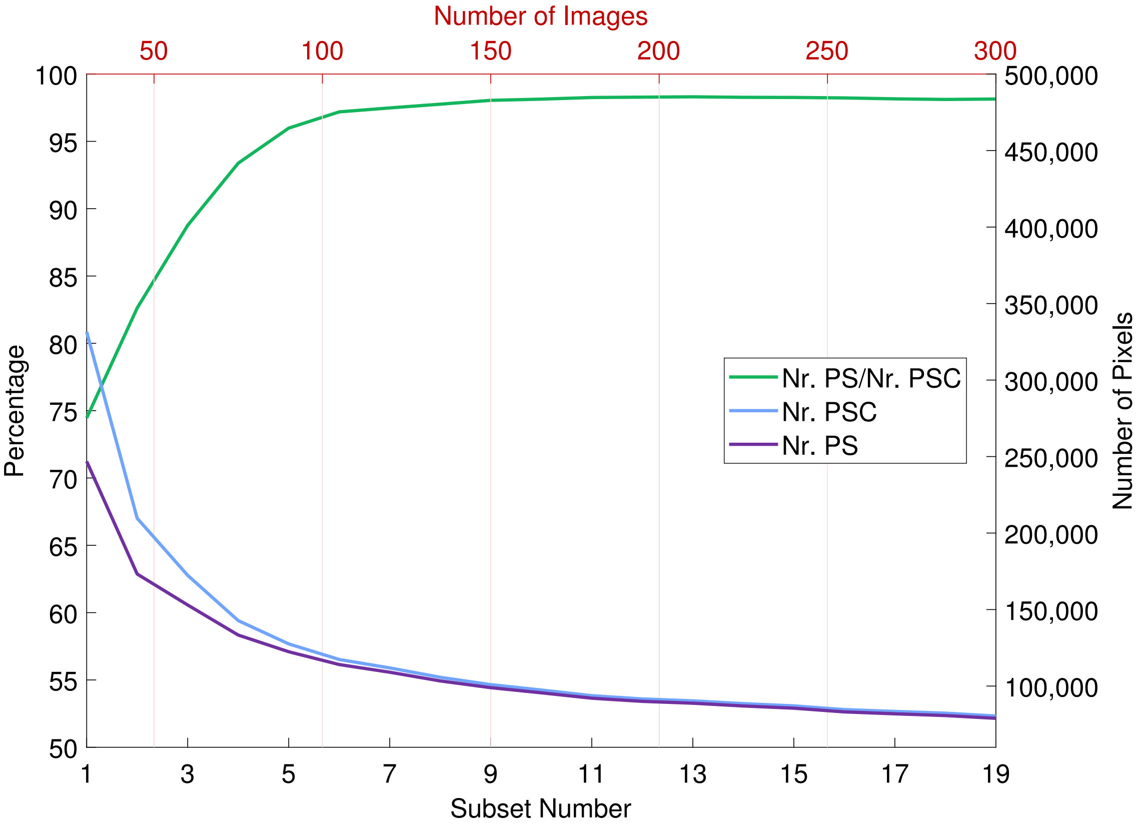

Figure 6.4.: Number of identified PSC (blue), PS (purple) and their ratio (green) depending on the processed subset (bottom x-axis) and the number of SAR images (top x-axis) in the subset for Strategy A.

Strategy B: Non-Overlapping Subsets

The key processing parameters of Strategy B, which is to process the steady stream of SAR images in consecutive non-overlapping subsets, are presented in Table 6.2. As for Table 6.1, Table 6.2 lists the number of SAR images and the time span the subsets cover, in addition to the above-listed key parameters. The used hard disk space stays relatively steady between 218 GB (Subset 6) and 243 GB (Subset 9), which is additionally shown in Figure 6.5 (green). This was expected, since W_{subset} was kept constant for all subsets.

Figure 6.5 also presents t_{total} (purple) and t_{PSI} (blue) with regard to the processed subset (bottom x-axis) and the temporal center point of the subset (top x-axis). Both follow the same trend, but with a constant offset between them. The offset is 6.7 hours, which is the amount of time needed for pre-processing 30 SAR images. The t_{PSI} varies between 7.2 h (Subset 5) and 18.4 h (Subset 8) and features a periodic pattern.

Figure 6.6 reveals a similar pattern for N_{PSC} (blue) and N_{PS} (purple) as was observed in t_{total} and t_{PSI}. The difference between N_{PSC} and N_{PS} is on average 86,651 pixels. The ratio between PS and PSC ranges between 70 % (Subset 5) and 81 % (Subset 8). The observed periodic pattern in N_{PSC}, N_{PS}, t_{PSI} and t_{total} is likely due to the time span the subsets cover. As stated above, Dataset C was restricted to the time period where a 6-day repeat pass time could be abided. Thus, the SAR image from the 21st December 2021 is the last image in the dataset. The size of the subsets was set to $W_{\text{subset}} = 30$ to allow for the observation of short-term effects. Both considerations lead to subsets for Strategy B that always cover either the winter half (November/December) or the summer half (May/June) of the year. In order to verify this assumption, a small number of additional subsets, which divide the year between spring (March) and autumn (September), were processed. The results are summarized in Table 6.3. Here, the difference between the number of N_{PSC} and N_{PS} identified in the subsets is steadier. In accordance, the ratio between PS and PSC is also more consistent and ranges around 72 %. Overall, the number of PS ranges

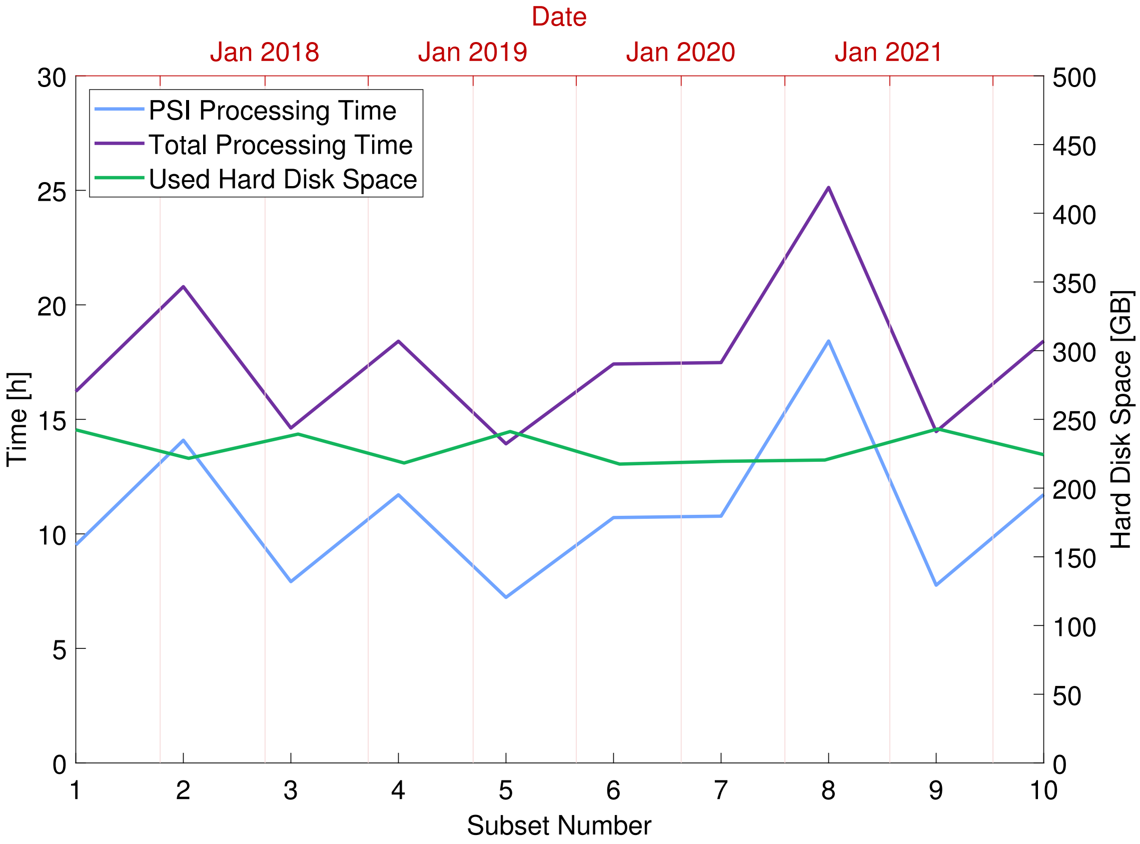

Figure 6.5.: The total processing time (purple), the PSI processing time (blue) and used hard disk space (green) with regard to the processed subset (bottom x-axis) and the temporal center point of the subset (top x-axis) for Strategy B.

Subset	Time Span	W_{subset}	M_{Space} [GB]	t_{total} [h]	t_{PSI} [h]	N_{PSC}	N_{PS}
1	03/2017 - 09/2017	30	249	15.8	9.0	312,729	226,342
2	09/2017 - 03/2018	30	241	17.2	10.4	341,493	248,011
3	03/2018 - 09/2018	30	218	17.6	10.9	344,768	254,380
4	09/2018 - 03/2019	30	209	15.7	9.0	328,200	233,226

Table 6.3.: Key parameters of processing a growing dataset in sequential non-overlapping subsets (Strategy B) with slightly shifted time spans compared to Table 6.2.

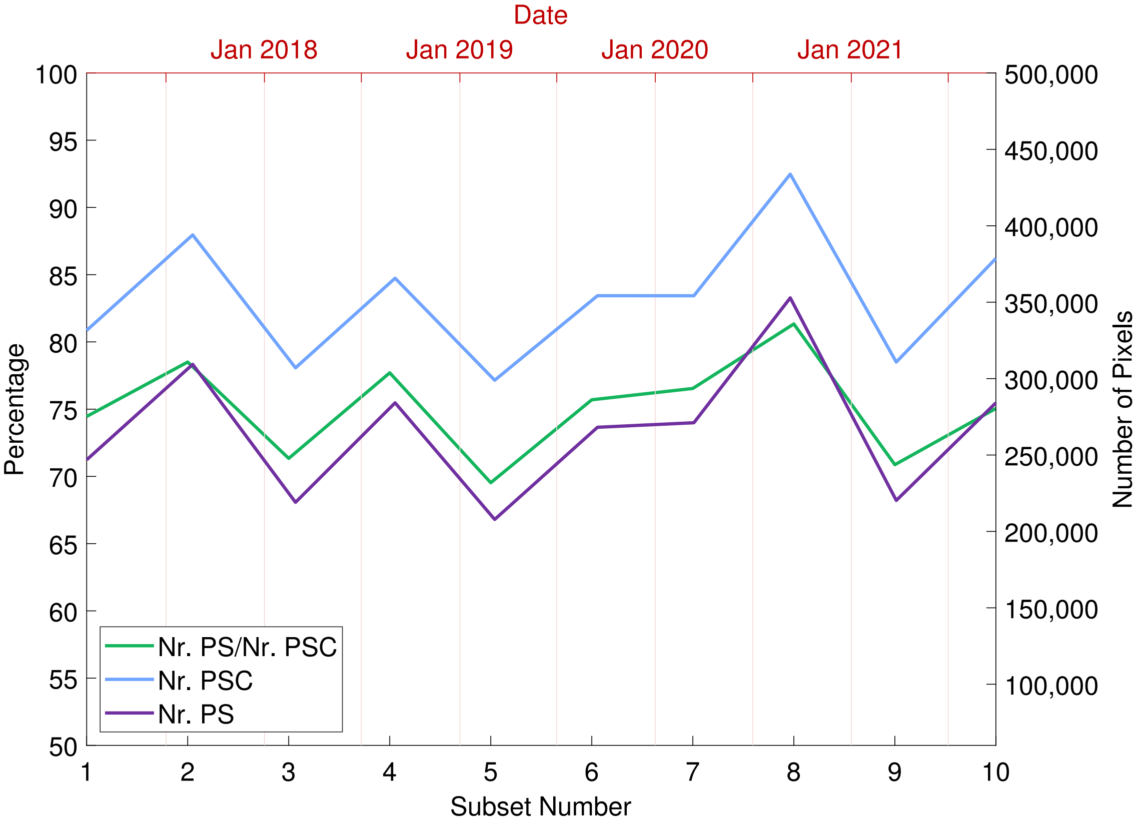

Figure 6.6.: Number of identified PSC (blue), PS (purple) and their ratio (green) with regard to the processed subset (bottom x-axis) and the temporal center point of the subset (top x-axis) for Strategy B.

between 226,342 (Subset 1) and 254,380 (Subset 3) and the difference between subsets ranges between 6,000 to 22,000 PS. The difference in N_{PS} between subsets in the original set-up, as can be seen in Table 6.2, is about 70,000 PS. Shifting the time spans lessened any periodic effect on the number of identified PS in each subset significantly.

Boiled down, it can be stated that Strategy B also behaved as expected. Neglecting any periodic effect, N_{PSC}, N_{PS}, t_{total}, t_{PSI} and M_{Space} remain relatively steady. In total 2,287 GB hard disk space and 176 h are needed to process Dataset C with Strategy B.

Strategy C: Overlapping Subsets

The key processing parameters of Strategy C, which is to process the steady stream of SAR images with a sliding-window approach, are presented in Table 6.4. As in the previous tables, Table 6.4 lists the number of SAR images and the time span the subsets cover, in addition to the key parameters listed at the beginning of Section 6.2.2. The used hard disk space increases slightly between Subset 1 and Subset 2, from 278 GB to 330 GB, and then varies between 300 GB and 360 GB. This trend is displayed in Figure 6.7 (green). This figure also shows t_{total} (purple) and t_{PSI} (blue). Similar to the case of Strategy B, there is an offset between the t_{total} (purple) and t_{PSI} (blue). In this case, the offset is constant at

3.7 h with the exception of Subset 1, where it is 6.7 h. This is due to the key feature of the PSISlider strategy, which is to re-use intermediate results, which plays a role starting from Subset 2. All secondary SAR images are co-registered to the same co-registration reference image. Thus, only the 15 new SAR images are subjected to interferometric pre-processing. The intermediate products from the remaining 15 SAR images are taken on from the previous subset. The differential interferograms are calculated with a local reference image, which can be switched between subsets. However, this local reference image is not exchanged as long as this local reference image is still in the current subset. Allowing again for re-using intermediate products, where possible. This results in the significantly varying PSI processing time, as evident in Figure 6.7. For example, the PSI processing time of Subset 2 is about half the PSI processing time of Subset 1. The same applies to Subset 3 and Subset 4, Subset 5 and Subset 6, and so on. Additionally, the same periodic effect that can be observed in the results of Strategy B plays a role in the results of Strategy C. About every 5th subset has a significantly higher PSI processing time than the other subsets. A similar pattern can be observed in the number of PS identified in each subset. For subsets with a higher processing time, the number of identified PS is over 280,000 (Subset 7, Subset 13 and Subset 19), while for the other subsets it ranges between 201,623 PS (Subset 10) and 274,332 PS (Subset 11). The pattern is presented in Figure 6.8. The ratio of PSC that are selected as PS also varies. It ranges from 57 % (Subset 10) to 76 % (Subset 3).

Subset	Time Span	W_{subset}	M_{Space} [GB]	t_{total} [h]	t_{PSI} [h]	N_{PSC}	N_{PS}
1	11/2016 - 05/2017	30	278	16.2	9.4	331,542	246,857
2	02/2017 - 08/2017	30	330	8.4	4.7	317,850	220,197
3	05/2017 - 12/2017	30	349	17.7	14.1	398,858	301,630
4	08/2017 - 02/2018	30	335	9.7	6.1	368,755	245,861
5	11/2017 - 05/2018	30	334	12.1	8.5	339,561	221,089
6	02/2018 - 08/2018	30	334	8.3	4.7	343,769	201,781
7	06/2018 - 02/2018	30	334	16.3	12.7	402,752	285,648
8	09/2018 - 03/2019	30	345	9.3	5.6	363,091	233,251
9	12/2019 - 05/2019	30	347	11.5	7.9	335,071	209,818
10	03/2019 - 09/2019	30	301	8.5	4.8	355,342	201,623
11	06/2019 - 12/2019	30	359	15.5	11.9	394,256	274,332
12	09/2019 - 03/2020	30	349	9.3	5.7	373,385	232,489
13	12/2019 - 06/2020	30	354	16.0	12.3	398,768	280,538
14	03/2020 - 09/2020	30	334	10.6	7.0	432,374	271,769
15	06/2020 - 12/2020	30	335	24.5	20.8	477,553	360,078
16	09/2020 - 03/2021	30	353	9.8	6.2	363,663	246,700
17	12/2020 - 06/2021	30	355	12.6	8.9	350,977	226,495
18	03/2021 - 09/2021	30	359	10.2	6.6	438,927	251,658
19	06/2021 - 12/2021	30	357	17.0	13.3	421,596	287,638

Table 6.4.: Key parameters of Strategy C.

To sum it up, Strategy C reduces both t_{total} and t_{PSI} significantly, while N_{PSC}, N_{PS} and M_{Space} remain relatively steady, as was expected. In total 6,440 GB hard disk space and 244 h are needed to process Dataset C with Strategy C.

6.3 Discussion

Reflecting on the beginning of this chapter, questions were raised about what a suitable PSI processing strategy could be for processing a steady stream of SAR images in the context of a monitoring task. One concern was the PS density. For this reason N_{PSC} and N_{PS} were recorded. As expected, evaluating the recorded values for N_{PSC} and N_{PS} for Strategy A showed that the expanding time span considered and the increase in W_{subset} results in a significant decrease in N_{PSC} and N_{PS}. In the case of Strategy B and Strategy C keeping W_{subset} constant, resulted in a relatively steady N_{PSC} and N_{PS}, neglecting any periodic effects.

Further, Strategy A also shows that t_{total}, t_{PSI} and M_{Space} increase with W_{subset}. In contrast, the hard disk space needed for Strategy B and Strategy C remains relatively steady.

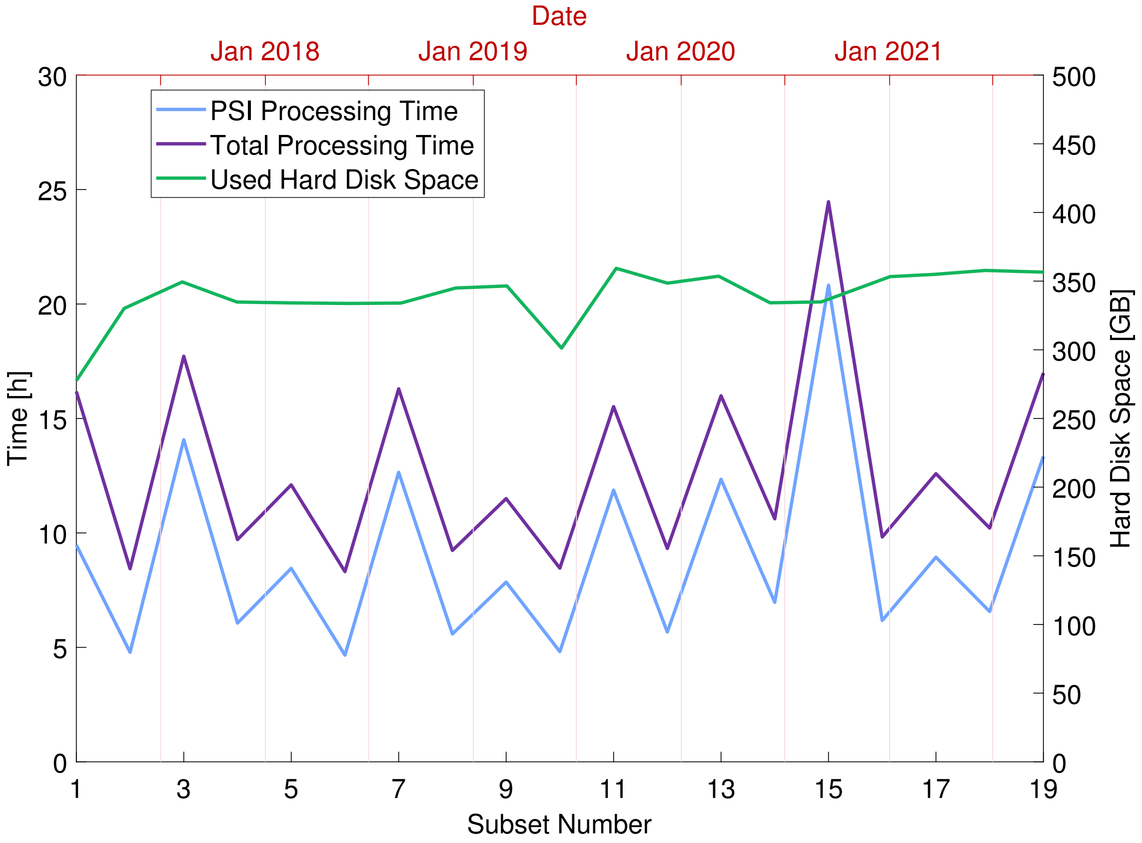

Figure 6.7.: The total processing time (purple), the PSI processing time (blue) and used hard disk space (green) with regard to the processed subset (bottom x-axis) and the temporal center point of the subset (top x-axis) for Strategy C.

This is again achieved by keeping W_{subset} constant. In the case of Strategy B, t_{total} and t_{PSI} also remain relatively steady, again neglecting any periodic effects. However, the implementation of the PSISlider processing chain for Strategy C resulted in a significant reduction of t_{total} and t_{PSI}. Additionally, Strategy C allows for a quicker pace in updates than Strategy B.

The most concerning issue of Strategy B is that the comparability of results in between subsets is not given. Contrary, implementing the PSISlider processing chain for Strategy C, ensures the comparability of results in between subsets by using two different reference images for co-registration and interferogram formation. The last concern raised at the beginning of the chapter was inefficiency during processing. As Strategy C allows for the re-use of intermediate results, it stands to reason that it operates more efficiently. However, this is also reflected in the values for the total processing time and total hard disk space. In the case of Strategy A, processing the steady stream 300 SAR images with regular updates took 930 h and needed 25,531 GB hard disk space. For Strategy B, 176 h and 2,287 GB were required, while for Strategy C, 244 h and 6,440 GB are needed. However, it needs to be taken into consideration that Strategy B only used 10 subsets, while Strategy C used 19 subsets. Assuming that Strategy B, neglecting periodic effects, needs 17 h to process one subset with $W_{\text{subset}} = 30$, processing 19 subsets would take roughly 323 h. Similarly, the

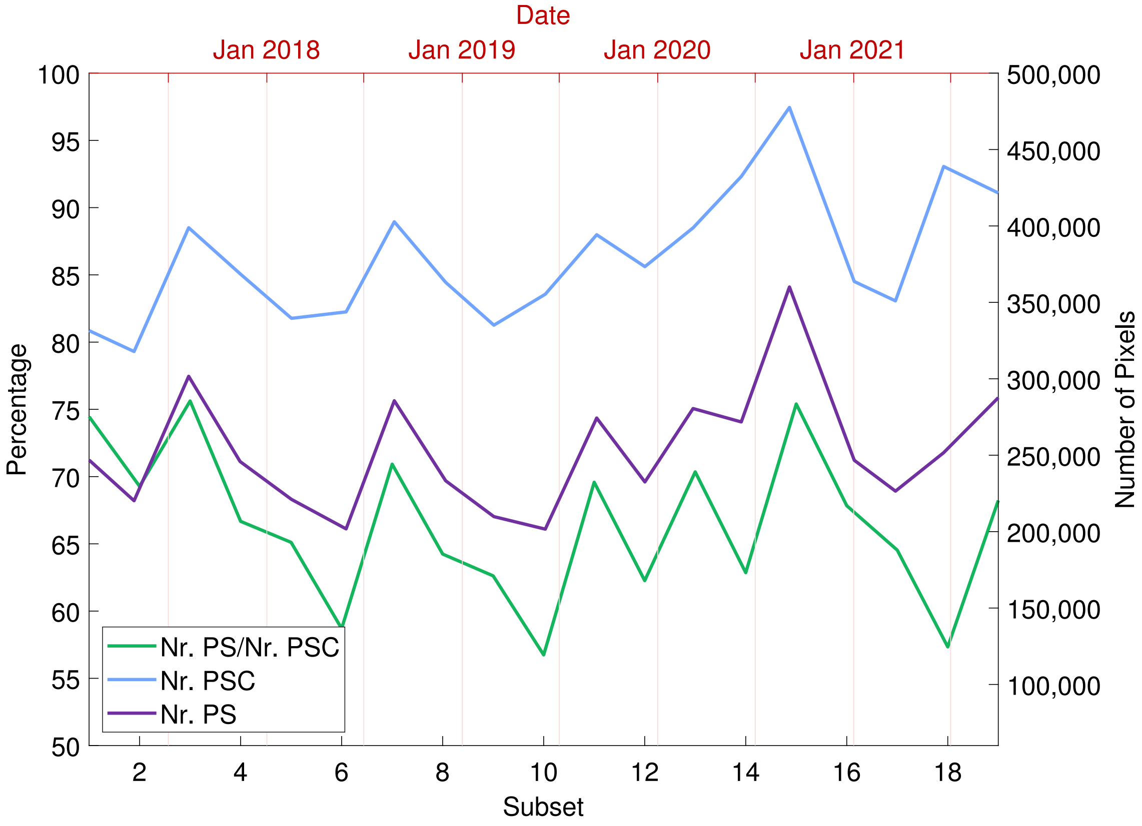

Figure 6.8.: Number of identified PSC (blue), PS (purple) and their ratio (green) with regard to the processed subset (bottom x-axis) and the temporal center point of the subset (top x-axis) for Strategy C.

total hard disk space for 19 subsets processed with Strategy B would be 4,345 GB. The larger amount of hard disk space needed for Strategy C is due to the intermediate results that need to be saved for later re-use.

To boil it down, Strategy C provides a relatively steady N_{PSC} and N_{PS}, while keeping t_{total}, t_{PSI} and M_{Space} limited. Additionally, the strategy allows for quickly paced updates and ensures comparability of intermediate results. All aspects, desirable for processing a steady stream of SAR images in the context of a monitoring task.

However, while employing Strategy C for a long-term monitoring task, it is important to consider the number of SAR images in each subset. In literature, typically around 20 SAR images are considered the minimum necessary number of images for ψ, and the larger the number, the more reliable the displacement estimates are [19, 51, 53, 222].

Synopsis and Outlook

7

Reflecting on the beginning of this thesis, the question arose as to how the PSI technique can contribute to the continuous monitoring of human settlements and large infrastructure elements. From this overriding topic, three sub-question emerged, which were addressed in Chapter 4, Chapter 5 and Chapter 6. Those research questions are the following:

(1) How can the results of advanced DInSAR processing be utilized to provide information on the dynamic evolution of the deformation process?

(2) How can advanced DInSAR datasets that are complex to process due to their high-resolution and shorter wavelength still be used to map highly spatially variable and rather quick deformation?

(3) What processing approach for PSI would allow for a continuous long-term monitoring of an area or object of interest, taking into account MP density and comparability with historic data?

Concerning the first question, in Chapter 4, a need for automatic post-processing procedures to extract relevant information on the temporal pattern of ground surface deformation datasets was identified. Advanced DInSAR processing results are often evaluated and interpreted based on their mean deformation velocity. The advantage is that the spatial pattern and extent of actively deforming areas can be easily assessed [38, 45]. The downside is that any information concerning an acceleration, deceleration or periodic behavior of the monitored deformation phenomena is neglected. However, in Sub-section 4.1 this type of information was identified as highly relevant for local authorities to assess and mitigate any threat due to surface deformation. Many geophysical or anthropogenically induced ground surface deformation phenomena do not follow a constant velocity deformation model. Ground surface deformation due to underground gas storage [28, 29], groundwater extraction [27], or the thermal expansion of large buildings [166] are periodic. At the same time, displacement rates of aseismic creep [22, 23] alongside tectonic faults or subsidence rates due to urbanization [30] can change over time and may result in a piecewise linear or quadratic trend. The post-processing tool PSDefoPAT®, presented in Chapter 4, was designed to identify the underlying time series model in the displacement time series resulting from advanced DInSAR processing. The tool assigns each displacement time series a best-fitting time series model using a sequence of statistical tests. Additionally, a standardized visualization of the PSDefoPAT® results was designed to facilitate an easy interpretation of the results.

The two case studies presented in Section 4.4 illustrate the additional information generated using PSDefoPAT®. In the case of the city of Patras, clusters of MPs that follow a specific time series model do roughly match known geological features such as active faults and thus, may help correct their recorded traces. Further, clusters of time series with a periodic component on the Rio-Antirio Bridge show which bridge components are affected by thermal expansion. The second case study, the Parapeiros-Peiros Dam, showed that PSDefoPAT® provides relevant information on the dynamics of its surface deformation, which are mainly anthropogenically driven. Most MP on the dam body feature a quadratic trend, i.e., their deformation velocity changes during the observation period as a reaction to the flooding of its reservoir. Both case studies highlight the significance of moving on from mainly using the mean deformation velocity maps to interpret the results from advanced DInSAR results.

Another concern, raised in Chapter 4, was that in the case of a continuous processing of a steady stream of SAR images, analyzing the amount of produced advanced DInSAR results would pose a bottleneck. Therefore, PSDefoPAT® was designed to operate fully automatically. The standardized visualization of the results is also automated.

The second question was addressed in Chapter 5. Challenges that can arise from tailoring a monitoring system for a specific large infrastructure element, such as an embankment dam, were addressed. Dams are subject to various surface deformations that can either be localized, such as varying subsidence rates alongside the crest of the dam body, or occur on a larger scale, such as slope instabilities along the shoreline of the water reservoir [47, 48]. Hence, a wide coverage is needed to monitor large-scale deformation and a high spatial resolution to monitor vulnerable areas. This demand can only be met using two sets of SAR images. For example, S1 SAR images that fulfill the requirement of wide coverage and high-resolution TSX SAR images that fulfill the requirement of high spatial resolution. However, their different spatial resolution and wavelengths make the datasets unequally complex to process in the case of mapping a spatially highly variable and rather quick deformation, in the context of PSI. The two processing steps affected the most by this are: (1) the PS selection and (2) the phase unwrapping process. In Chapter 5, it is suggested to combine the selection criteria defined by Ferretti et al. (2002) and by Hooper et al. (2004) so that they complement each other. The combined sets of PS are then processed jointly. Applying this approach to a TSX SAR time series, mapping the deformation of the Parapeiros-Peiros Dam during the filling of its reservoir, increased the number of PS on and near the dam body from 50,608 to 60,346. This effectively closed significant gaps on the dam body, which prevented the mapping of its surface deformation.

The second challenge, phase unwrapping, was met by reconstructing an idealized deformation induced phase based on displacement time series models extracted with PSDefoPAT® from a simpler-to-process dataset, in this case a S1 SAR image time series. Applying the approach to the TSX SAR image time series improved the phase unwrapping step in space and time and thus, resulted in improved displacement time series and smoother transition lines in the mean deformation velocity map.

Chapter 6 addresses the third question. Concerns regarding N_{PSC}, N_{PS}, t_{total}, t_{PSI} and M_{Space} in the case of the frequent processing of a continuously expanding time series were stressed and led to the question of an adequate processing strategy to allow for a continuous long-term monitoring of an area or object of interest. Three different strategies were presented and evaluated. The first strategy is to always process all available SAR images W_{total}, i.e., a growing dataset (Strategy A). The second strategy is to process the steady stream of SAR images in consecutive non-overlapping subsets (Strategy B), and the third strategy is to use overlapping consecutive subsets, similar to a sliding-window (Strategy C). In order to evaluate the different strategies, a steady stream of SAR images was simulated by dividing 300 S1 SAR images into subsets and processing them according to the three strategies. However, before that, the PSISlider processing chain, presented in Figure 6.2, was implemented to take full advantage of the possibility to re-use intermediate results given by Strategy C. Comparing the recorded values of N_{PSC}, N_{PS}, t_{total}, t_{PSI} and M_{Space}, showed that for Strategy A t_{total}, t_{PSI} and M_{Space} increase with W_{subset}, while N_{PSC} and N_{PS} decrease. Strategy B and Strategy C counter this by limiting W_{subset} and keeping it constant, which results in relatively steady values for N_{PSC}, N_{PS}, t_{total}, t_{PSI} and M_{Space}, neglecting any periodic effects. The most concerning issue of Strategy B was that the comparability of results in between subsets is not given. In contrast, the implementation of the PSISlider processing chain for Strategy C ensures the comparability of results between subsets by using two different reference images, one for the co-registration of all secondary images and one for the interferogram formation. The PSISlider processing chain also tackles the last concern presented in Chapter 6, which was inefficiency during processing. Since, with implementation of the PSISlider processing chain, Strategy C allows for the re-use of intermediate results, it stands to reason that it operates more efficiently than Strategy A and Strategy B. This is also reflected in the values for the total processing time and total hard disk space. In the case of Strategy A, processing the steady stream 300 SAR images with regular updates took 930 h. For Strategy B, 176 h were required, while for Strategy C, 244 h are needed. However, it needs to be taken into consideration that Strategy B only used 10 subsets, while Strategy C used 19 subsets. Assuming that Strategy B needs 17 h to process one subset with $W_{\text{subset}} = 30$, processing 19 subsets would take roughly 323 h. To boil it down, it could be shown that, as was expected, Strategy C is the most suitable strategy for continuous monitoring tasks. It provides a relatively steady N_{PSC} and N_{PS}, while keeping t_{total}, t_{PSI} and M_{Space} limited. Additionally, the strategy allows for quickly paced updates and ensures comparability of intermediate results. All aspects, desirable for processing a steady stream of SAR images in the context of a monitoring task.

Returning to the overarching question of how the PSI technique can contribute to the continuous monitoring of human settlements and large infrastructure elements. Chapter 4 showed that information on the temporal deformation pattern of larger areas, such as the city of Patras and its suburbs, and individual infrastructure elements, such as the Parapeiros-Peiros Dam, can be extracted from PSI processing results employing

PSDefoPAT®.

Chapter 6 showed with the implementation of the PSISlider processing chain that continuous processing can be set up without suffering from a continuous loss of PS, and an increase in processing time and in needed hard disk space, while also not losing the ability to compare current results to historic ones. All aspects are desirable for processing a steady stream of SAR images in the context of a monitoring task, such as SHM.

Chapter 5 showed how the conventional processing chain, presented in Figure 3.4, can be adapted to allow the mapping of spatially highly variable and rather quick deformation, which can occur in the context of SHM, with high-resolution SAR images. High-resolution data may be needed in addition to SAR data, which has a wider coverage, in the context of SHM to monitor vulnerable areas in greater detail.

Nonetheless, this leaves the question of how these three different aspects can be brought together, especially the usage of PSDefoPAT® in combination with the PSISlider processing chain. In Chapter 6, the PSISlider processing chain is used with 30 SAR images spread over half a year. However, such a time series would probably be too short to estimate most of the time series models implemented in PSDefoPAT®. Therefore, instead of applying PSDefoPAT® to the results of each subset, it could also be applied to the joint time series of all previous subsets. The resulting time series model could be used in a predictive manner. The displacement time series from the new subset could then be compared to the predicted time series course. This approach would enable the generation of alerts if a cluster of PS diverges significantly from the predicted time series course. In this context, it would be necessary to evaluate how long a time series needs to be to reliably estimate the implemented time series models and how the time series from the individual subsets can be effectively merged.

Another aspect is the incorporation of SAR sensors with wavelengths other than 3.1 cm (X-band) and 5.6 cm (C-band). The Argentinian L-band (23 cm) satellites SAOCOM [223] or the Japanese ALOS PALSAR satellites [224] come to mind. Chapter 5 showed that it can be beneficial to map surface deformation with more than one sensor, since the sensors are affected differently by the spatial variability and velocity of the observed deformation phenomenon. Studies have shown that L-band sensors outperform C-band sensors in vegetated areas and deformation phenomena with high deformation velocities [225, 226]. A higher PS density could be especially interesting for infrastructure elements situated in rural areas, as dams often are, or that are vegetated on purpose, such as levees. A higher tolerance to high deformation velocities could be beneficial for newly built infrastructure elements, such as the Parapeiros-Peiros Dam, or areas affected by mining [226].

Acknowledgement

At this point, I would like to express my sincere appreciation for the many people that supported me during my Ph.D. studies and without whose support this endeavour would not have been possible. First and foremost, I would like to express my sincere gratitude to my Ph.D. supervisor, Stefan Hinz, for his invaluable feedback and support. I would also like to thank him for giving me a great deal of freedom in conducting my research and setting my research focus.

Further, words cannot express my gratitude to my mentor and colleague, Antje Thiele, who guided me through my research process and always had an open ear for me. She provided me with thoughtful and constructive criticism to drive my research forward and improve my writing and presentation skills. I would also like to thank her for coordinating the cooperation and administrative work with the Karlsruhe Institute of Technology.

I would also like to express my deepest gratitude to Karsten Schulz for always discussing my research ideas with me and refining them with critical questions and insightful input. Additionally, he played a crucial role in shaping my research topic by involving me in his long-standing collaboration with the Department of Geology at the University of Patras.

In addition, this endeavour would not have been possible without the support of my colleagues. I'd like to express my gratitude to Erich Cadario. Any question, problem, or theoretical discussion I brought to him was always met with insightful and constructive input. He always provided me with constructive criticism and thought-provoking questions to improve my writing further. I am also grateful to Horst Hammer for his support during my Ph.D. studies. He always had an open ear for me and provided my with valuable input through critical questions and thoughtful and constructive criticism.

I would be remiss if I did not mention Aggeliki Kyriou and Konstantinos Nikolakopoulos from the Department of Geology at the University of Patras, who drew my attention to the Parapeiros-Peiros Dam and, with that, gave the impetus to my thesis.

Lastly, I would like to thank my parents, Susanne and Norbert Evers, my brother, Gerrit Evers, and my close friends, Sina Aßhoff, Sandra Große-Kampmann, and Juliane Yalcin, for their motivation and emotional support during this time.

Bibliography

[1] D. Massonnet, M. Rossi, C. Carmona, F. Adragna, G. Peltzer, K. Feigl, and T. Rabaute. "The displacement field of the Landers earthquake mapped by radar interferometry". In: *Nature* 364.6433 (1993b), pp. 138–142.

[2] H. Zebker, P. Rosen, R. Goldstein, A. Gabriel, and C. Werner. "On the derivation of coseismic displacement fields using differential radar interferometry: The Landers earthquake". In: *Journal of Geophysical Research: Solid Earth* 99.B10 (1994), pp. 19617–19634.

[3] S. Stein and E. Klosko. "7 - Earthquake Mechanisms and Plate Tectonics". In: *International Handbook of Earthquake and Engineering Seismology, Part A*. Ed. by W. Lee, H. Kanamori, P. Jennings, and C. Kisslinger. Vol. 81. International Geophysics. Academic Press, 2002, pp. 69–78. URL: `https://www.sciencedirect.com/science/article/pii/S0074614202802108`.

[4] J. R. Elliott, R. J. Walters, and T. J. Wright. "The role of space-based observation in understanding and responding to active tectonics and earthquakes". In: *Nature Communications* 7.1 (2016), p. 13844.

[5] R. Bürgmann and W. Thatcher. "Space geodesy: A revolution in crustal deformation measurements of tectonic processes". In: *The Web of Geological Sciences: Advances, Impacts, and Interactions*. Ed. by W. Lee, H. Kanamori, P. Jennings, and C. Kisslinger. Geological Society of America, Sept. 2013. URL: `https://doi.org/10.1130/2013.2500(12)`.

[6] H. Kimura and Y. Yamaguchi. "Detection of landslide areas using satellite radar interferometry". In: *Photogrammetric Engineering and Remote Sensing* 66.3 (2000), pp. 337–344.

[7] T. Strozzi, P. Farina, A. Corsini, Christian Ambrosi, M. Thüring, J. Zilger, A. Wiesmann, U. Wegmüller, and C. Werner. "Survey and monitoring of landslide displacements by means of L-band satellite SAR interferometry". In: *Landslides* 2 (2005), pp. 193–201.

[8] A. Theron, J. Engelbrecht, J. Kemp, W. Kleynhans, and T. Turnbull. "Detection of sinkhole precursors through SAR interferometry: radar and geological considerations". In: *IEEE Geoscience and Remote Sensing Letters* 14.6 (2017), pp. 871–875.

[9] H. Zebker and J. Villasenor. "Decorrelation in interferometric radar echoes". In: *IEEE Transactions on Geoscience and Remote Sensing* 30.5 (1992), pp. 950–959.

[10] R. Hanssen. *Radar interferometry: data interpretation and error analysis*. Vol. 2. Springer Science & Business Media, 2001.

[11] H. Zebker, P. Rosen, and S. Hensley. "Atmospheric effects in interferometric synthetic aperture radar surface deformation and topographic maps". In: *Journal of Geophysical Research: Solid Earth* 102.B4 (1997), pp. 7547–7563.

[12] R. Goldstein. "Atmospheric limitations to repeat-track radar interferometry". In: *Geophysical Research Letters* 22.18 (1995), pp. 2517–2520.

[13] A. Ferretti, C. Prati, and F. Rocca. “Permanent scatterers in SAR interferometry”. In: *IEEE Transactions on Geoscience and Remote Sensing* 39.1 (2002), pp. 8–20.

[14] A. Hooper, H. Zebker, P. Segall, and B. Kampes. “A new method for measuring deformation on volcanoes and other natural terrains using InSAR persistent scatterers”. In: *Geophysical Research Letters* 31.23 (2004).

[15] P. Berardino, G. Fornaro, R. Lanari, and E. Sansosti. “A new algorithm for surface deformation monitoring based on small baseline differential SAR interferograms”. In: *IEEE Transactions on Geoscience and Remote Sensing* 40.11 (2002), pp. 2375–2383.

[16] A. Ferretti, A. Fumagalli, F. Novali, C. Prati, F. Rocca, and A. Rucci. “A new algorithm for processing interferometric data-stacks: SqueeSAR”. In: *IEEE Transactions on Geoscience and Remote Sensing* 49.9 (2011), pp. 3460–3470.

[17] A. Ferretti, G. Savio, R. Barzaghi, A. Borghi, S. Musazzi, F. Novali, C. Prati, and F. Rocca. “Submillimeter accuracy of InSAR time series: Experimental validation”. In: *IEEE Transactions on Geoscience and Remote Sensing* 45.5 (2007), pp. 1142–1153.

[18] F. Cigna, R. Esquivel Ramírez, and D. Tapete. “Accuracy of Sentinel-1 PSI and SBAS InSAR displacement velocities against GNSS and geodetic leveling monitoring data”. In: *Remote Sensing* 13.23 (2021), p. 4800.

[19] N. Adam, A. Parizzi, M. Eineder, and M. Crosetto. “Practical persistent scatterer processing validation in the course of the Terrafirma project”. In: *Journal of Applied Geophysics* 69.1 (2009), pp. 59–65.

[20] P. Marinkovic, G. Ketelaar, F. van Leijen, and R. Hanssen. “InSAR quality control: Analysis of five years of corner reflector time series”. In: *Proceedings of the Fringe 2007 Workshop (ESA SP-649), Frascati, Italy* (2007), pp. 26–30.

[21] V. Drouin and F. Sigmundsson. “Countrywide observations of plate spreading and glacial isostatic adjustment in Iceland inferred by sentinel-1 radar interferometry, 2015–2018”. In: *Geophysical Research Letters* 46.14 (2019), pp. 8046–8055.

[22] E. Cetin, Z. Cakir, M. Meghraoui, S. Ergintav, and A. M. Akoglu. “Extent and distribution of aseismic slip on the Ismetpaşa segment of the North Anatolian Fault (Turkey) from Persistent Scatterer InSAR”. In: *Geochemistry, Geophysics, Geosystems* 15.7 (2014), pp. 2883–2894.

[23] Z. Cakir, A. M. Akoglu, S. Belabbes, S. Ergintav, and M. Meghraoui. “Creeping along the Ismetpasa section of the North Anatolian fault (Western Turkey): Rate and extent from InSAR”. In: *Earth and Planetary Science Letters* 238.1-2 (2005), pp. 225–234.

[24] V. Tofani, F. Raspini, F. Catani, and N. Casagli. “Persistent Scatterer Interferometry (PSI) technique for landslide characterization and monitoring”. In: *Remote Sensing* 5.3 (2013), pp. 1045–1065.

[25] A. Busetti, C. Calligaris, E. Forte, G. Areggi, A. Mocnik, and L. Zini. “Non-invasive methodological approach to detect and characterize high-risk sinkholes in urban cover evaporite karst: integrated reflection seismics, PS-InSAR, leveling, 3D-GPR and ancillary data. A NE Italian case study”. In: *Remote Sensing* 12.22 (2020), p. 3814.

[26] T. Oliver-Cabrera, S. Wdowinski, S. Kruse, and T. Robinson. “Detection of sinkhole activity in West-Central Florida using InSAR time series observations”. In: *Remote Sensing of Environment* 269 (2022), p. 112793.

[27] M. Béjar-Pizarro, P. Ezquerro, G. Herrera, R. Tomás, C. Guardiola-Albert, J. M. R. Hernández, J. A. F. Merodo, M. Marchamalo, and R. Martínez. “Mapping groundwater level and aquifer storage variations from InSAR measurements in the Madrid aquifer, Central Spain”. In: *Journal of Hydrology* 547 (2017), pp. 678–689.

[28] P. Teatini, N. Castelletto, M. Ferronato, G. Gambolati, C. Janna, E Cairo, D. Marzorati, D. Colombo, A. Ferretti, and A. Bagliani. “Geomechanical response to seasonal gas storage in depleted reservoirs: A case study in the Po River basin, Italy”. In: *Journal of Geophysical Research: Earth Surface* 116.F2 (2011).

[29] M. Even, M. Westerhaus, and V. Simon. “Complex surface displacements above the storage cavern field at Epe, NW-Germany, Observed by Multi-Temporal SAR-interferometry”. In: *Remote Sensing* 12.20 (2020), p. 3348.

[30] L. Solari, A. Ciampalini, F. Raspini, S. Bianchini, and S. Moretti. “PSInSAR analysis in the Pisa urban area (Italy): A case study of subsidence related to stratigraphical factors and urbanization”. In: *Remote Sensing* 8.2 (2016), p. 120.

[31] J. J. Sousa and L. Bastos. “Multi-temporal SAR interferometry reveals acceleration of bridge sinking before collapse”. In: *Natural Hazards and Earth System Sciences* 13.3 (2013), pp. 659–667.

[32] R. Tomás, M. Cano, J. Garcia-Barba, F. Vicente, G. Herrera, J. M. Lopez-Sanchez, and J. J. Mallorquí. “Monitoring an earthfill dam using differential SAR interferometry: La Pedrera dam, Alicante, Spain”. In: *Engineering Geology* 157 (2013), pp. 21–32.

[33] I. Özer, F. J. van Leijen, S. N. Jonkman, and R. F. Hanssen. “Applicability of satellite radar imaging to monitor the conditions of levees”. In: *Journal of Flood Risk Management* 12.S2 (2019), e12509.

[34] P. Snoeij, E. Attema, M. Davidson, B. Duesmann, N. Floury, G. Levrini, B. Rommen, and B. Rosich. “The Sentinel-1 radar mission: Status and performance”. In: *Proceedings of International Radar Conference" Surveillance for a Safer World" (RADAR 2009)* (2009), pp. 1–6.

[35] P. Potin, B. Rosich, N. Miranda, P. Grimont, I. Shurmer, A. O’Connell, M. Krassenburg, and J.-B. Gratadour. “Copernicus Sentinel-1 constellation mission operations status”. In: *Proceedings of IGARSS 2019-2019 IEEE international Geoscience and Remote Sensing Symposium* (2019), pp. 5385–5388.

[36] P. Potin, O. Colin, M. Pinheiro, B. Rosich, A. O’Connell, T. Ormston, J.-B. Gratadour, and R. Torres. “Status and Evolution of the Sentinel-1 mission”. In: *Proceedings of IGARSS 2022-2022 IEEE International Geoscience and Remote Sensing Symposium* (2022), pp. 4707–4710.

[37] European Space Agency. *From launch to images: the roadmap to Sentinel-1C operations*. URL: `https://sentinels.copernicus.eu/-/from-launch-to-images-the-roadmap-to-sentinel-1c-operationsl`. (accessed: 11.06.2025).

[38] A. Barra, L. Solari, M. Béjar-Pizarro, O. Monserrat, S. Bianchini, G. Herrera, M. Crosetto, R. Sarro, E. González-Alonso, and R. Mateos. “A methodology to detect and update active deformation areas based on Sentinel-1 SAR images”. In: *Remote Sensing* 9.10 (2017), p. 1002.

[39] O. Monserrat, A. Barra, G. Herrera, S. Bianchini, C. Lopez, R. Onori, P. Reichenbach, R. Sarro, R. M. Mateos, and L. Solari. “SAFETY project: Sentinel-1 based tools for geohazards monitoring and management”. In: *The International Archives of the Photogrammetry, Remote Sensing and Spatial Information Sciences* 42 (2018), pp. 351–355.

[40] R. Montalti, L. Solari, S. Bianchini, M. Del Soldato, F. Raspini, and N. Casagli. “A Sentinel-1-based clustering analysis for geo-hazards mitigation at regional scale: a case study in Central Italy”. In: *Geomatics, Natural Hazards and Risk* 10.1 (2019), pp. 2257–2275.

[41] J. Navarro, R. Tomás, A. Barra, J. Pagán, C. Reyes-Carmona, L. Solari, J. L. Vinielles, S. Falco, and M. Crosetto. “ADAtools: Automatic detection and classification of active deformation areas from PSI displacement maps”. In: *ISPRS International Journal of Geo-Information* 9.10 (2020), p. 584.

[42] F. Raspini, S. Bianchini, A. Ciampalini, M. Del Soldato, L. Solari, F. Novali, S. Del Conte, A. Rucci, A. Ferretti, and N. Casagli. “Continuous, semi-automatic monitoring of ground deformation using Sentinel-1 satellites”. In: *Scientific Reports* 8.1 (2018), p. 7253.

[43] D. Perissin and T. Wang. “Repeat-Pass SAR Interferometry With Partially Coherent Targets”. In: *IEEE Transactions on Geoscience and Remote Sensing* 50.1 (2012), pp. 271–280.

[44] N. Dörr, A. Schenk, and S. Hinz. “Fully Integrated Temporary Persistent Scatterer Interferometry”. In: *IEEE Transactions on Geoscience and Remote Sensing* 60 (2022), pp. 1–15.

[45] R. Tomás et al. “Semi-automatic identification and pre-screening of geological–geotechnical deformational processes using persistent scatterer interferometry datasets”. In: *Remote Sensing* 11.14 (2019), p. 1675.

[46] F. Raspini, S. Bianchini, A. Ciampalini, M. Del Soldato, R. Montalti, L. Solari, V. Tofani, and N. Casagli. “Persistent Scatterers continuous streaming for landslide monitoring and mapping: The case of the Tuscany region (Italy)”. In: *Landslides* 16 (2019), pp. 2033–2044.

[47] G. Hunter and R. Fell. *The deformation behaviour of embankment dams*. University of New South Wales, School of Civil and Environmental Engineering, 2003.

[48] C. Kutzner. *Earth and rockfill dams: Principles for design and construction*. Routledge, 2018.

[49] S. Buckreuss, U. Steinbrecher, and B. Schättler. “The TerraSAR-X mission status”. In: *Proceedings of 5th Asia-Pacific conference on synthetic aperture radar (APSAR)* (2015), pp. 357–361.

[50] R. Werninghaus and S. Buckreuss. “The TerraSAR-X mission and system design”. In: *IEEE Transactions on Geoscience and Remote Sensing* 48.2 (2009), pp. 606–614.

[51] A. Hooper, P. Segall, and H. Zebker. “Persistent scatterer interferometric synthetic aperture radar for crustal deformation analysis, with application to Volcán Alcedo, Galápagos”. In: *Journal of Geophysical Research: Solid Earth* 112.B7 (2007).

[52] A. Hooper and H. A. Zebker. “Phase unwrapping in three dimensions with application to InSAR time series”. In: *Journal of the Optical Society of America A* 24.9 (2007), pp. 2737–2747.

[53] M. Crosetto, O. Monserrat, M. Cuevas-González, N. Devanthéry, and B. Crippa. “Persistent scatterer interferometry: A review”. In: *ISPRS Journal of Photogrammetry and Remote Sensing* 115 (2016), pp. 78–89.

[54] M. Evers, A. Kyriou, K. Nikolakopoulos, and K. Schulz. “How to set up a dam monitoring system with PSInSAR and GPS”. In: *Proceedings of Earth Resources and Environmental Remote Sensing/GIS Applications XI* 11534 (2020), pp. 98–114.

[55] M. Evers, A. Thiele, H. Hammer, and S. Hinz. “PSDefoPAT—Persistent Scatterer Deformation Pattern Analysis Tool”. In: *Remote Sensing* 15 (2023), 1–26, paper no. 4646.

[56] M. Evers, H. Hammer, A. Thiele, and S. Hinz. “Psdefopat–Towards automatic model based psi post-processing”. In: *ISPRS Annals of the Photogrammetry, Remote Sensing and Spatial Information Sciences* 3 (2022), pp. 107–114.

[57] M. Evers, A. Thiele, H. Hammer, E. Cadario, K Schulz, and S. Hinz. “Concept to analyze the displacement time series of individual persistent scatterers”. In: *The International Archives of the Photogrammetry, Remote Sensing and Spatial Information Sciences* 43 (2021), pp. 147–154.

[58] M. Evers and A. Thiele. “Visualization of PSDefoPAT Results”. In: *EUSAR 2024; 15th European Conference on Synthetic Aperture Radar* (2024), pp. 359–364.

[59] M. Evers, A. Thiele, H. Hammer, and S. Hinz. “The Filling Process of an Embankment Dam Monitored with PSI”. In: *IGARSS 2022 - 2022 IEEE International Geoscience and Remote Sensing Symposium* (2022), pp. 1640–1643.

[60] M. Evers, E. Cadario, and A. Thiele. “PSDefoPAT for Phase Unwrapping: Knowledge Transfer from Sentinel-1 to TerraSAR-X”. In: *IGARSS 2024-2024 IEEE International Geoscience and Remote Sensing Symposium* (2024), pp. 11052–11055.

[61] M. Evers, H. Hammer, A. Thiele, and K Schulz. “Strategies for PS processing of large sentinel-1 datasets”. In: *The International Archives of the Photogrammetry, Remote Sensing and Spatial Information Sciences* 43 (2020), pp. 99–106.

[62] A. Moreira, P. Prats-Iraola, M. Younis, G. Krieger, I. Hajnsek, and K. Papathanassiou. “A tutorial on synthetic aperture radar”. In: *IEEE Geoscience and Remote Sensing Magazine* 1.1 (2013), pp. 6–43.

[63] L. Cutrona, W. Vivian, E. Leith, and G. Hall. “A high-resolution radar combat-surveillance system”. In: *IRE Transactions on Military Electronics* 2 (1961), pp. 127–131.

[64] C. Sherwin, J. Ruina, and R. Rawcliffe. “Some early developments in synthetic aperture radar systems”. In: *IRE Transactions on Military Electronics* 2 (1962), pp. 111–115.

[65] C. Wiley. “Synthetic aperture radars”. In: *IEEE Transactions on Aerospace and Electronic Systems* AES-21.3 (1985), pp. 440–443.

[66] R. Bamler and P. Hartl. “Synthetic aperture radar interferometry”. In: *Inverse Problems* 14.4 (1998), pp. 1–54.

[67] C. Oliver and S. Quegan. *Understanding synthetic aperture radar images*. SciTech Publishing, 2004.

[68] M. Skolnik. “Introduction to radar”. In: *Radar Handbook* 2 (1962), p. 21.

[69] A. Rogers and R. P. Ingalls. “Venus: Mapping the surface reflectivity by radar interferometry”. In: *Science* 165.3895 (1969), pp. 797–799.

[70] S. H. Zisk. “Lunar topography: First radar-interferometer measurements of the Alphonsus-Ptolemaeus-Arzachel region”. In: *Science* 178.4064 (1972), pp. 977–980.

[71] L. C. Graham. “Synthetic interferometer radar for topographic mapping”. In: *Proceedings of the IEEE* 62.6 (1974), pp. 763–768.

[72] H. Zebker and R. Goldstein. “Topographic mapping from interferometric synthetic aperture radar observations”. In: *Journal of Geophysical Research: Solid Earth* 91.B5 (1986), pp. 4993–4999.

[73] F. K Li and R. Goldstein. “Studies of multibaseline spaceborne interferometric synthetic aperture radars”. In: *IEEE Transactions on Geoscience and Remote Sensing* 28.1 (1990), pp. 88–97.

[74] R. Goldstein, H. Zebker, and C. Werner. “Satellite radar interferometry: Two-dimensional phase unwrapping”. In: *Radio Science* 23.4 (1988), pp. 713–720.

[75] D. Massonnet and T. Rabaute. “Radar interferometry: limits and potential”. In: *IEEE Transactions on Geoscience and Remote Sensing* 31.2 (1993a), pp. 455–464.

[76] R. Goldstein and H. Zebker. “Interferometric radar measurement of ocean surface currents”. In: *Nature* 328.6132 (1987), pp. 707–709.

[77] A. Gabriel, R. Goldstein, and H. Zebker. “Mapping small elevation changes over large areas: Differential radar interferometry”. In: *Journal of Geophysical Research: Solid Earth* 94.B7 (1989), pp. 9183–9191.

[78] D. Massonnet and K. Feigl. “Radar interferometry and its application to changes in the Earth’s surface”. In: *Reviews of Geophysics* 36.4 (1998), pp. 441–500.

[79] A. Ferretti, A. Monti-Guarnieri, C. Prati, F. Rocca, and D. Massonnet. *InSAR principles-guidelines for SAR interferometry processing and interpretation*. Vol. 19. 2007.

[80] A. Gabriel and R. Goldstein. “Crossed orbit interferometry: theory and experimental results from SIR-B”. In: *International Journal of Remote Sensing* 9.5 (1988), pp. 857–872.

[81] D. Just and R. Bamler. “Phase statistics of interferograms with applications to synthetic aperture radar”. In: *Applied Optics* 33.20 (1994), pp. 4361–4368.

[82] H. Yu, Y. Lan, Z. Yuan, J. Xu, and H. Lee. “Phase unwrapping in InSAR: A review”. In: *IEEE Geoscience and Remote Sensing Magazine* 7.1 (2019), pp. 40–58.

[83] K. Itoh. “Analysis of the phase unwrapping algorithm”. In: *Applied Optics* 21.14 (1982), pp. 2470–2470.

[84] T. J. Flynn. “Consistent 2-D phase unwrapping guided by a quality map”. In: *Proceedings of IGARSS’96. 1996 International Geoscience and Remote Sensing Symposium* 4 (1996), pp. 2057–2059.

[85] C. W. Chen and H. Zebker. “Network approaches to two-dimensional phase unwrapping: intractability and two new algorithms”. In: *Journal of the Optical Society of America A* 17.3 (2000), pp. 401–414.

[86] E. Rodriguez and J. M. Martin. “Theory and design of interferometric synthetic aperture radars”. In: *IEE Proceedings F (Radar and Signal Processing)* 139.2 (1992), pp. 147–159.

[87] M. S. Seymour and I. G. Cumming. “Maximum likelihood estimation for SAR interferometry”. In: *Proceedings of IGARSS’94-1994 IEEE International Geoscience and Remote Sensing Symposium* 4 (1994), pp. 2272–2275.

[88] E. López-Martínez C.and Pottier. “Coherence estimation in synthetic aperture radar data based on speckle noise modeling”. In: *Applied optics* 46.4 (2007), pp. 544–558.

[89] E. W. Hoen and H. Zebker. “Penetration depths inferred from interferometric volume decorrelation observed over the Greenland ice sheet”. In: *IEEE Transactions on Geoscience and Remote Sensing* 38.6 (2000), pp. 2571–2583.

[90] J. Askne and G. Smith. “Forest INSAR decorrelation and classification properties”. In: *Proceedings of the Fringe 96 Workshop: ERS SAR Interferometry* 406 (1997), p. 95.

[91] U. Wegmuller and C. L. Werner. “SAR interferometric signatures of forest”. In: *IEEE Transactions on Geoscience and Remote Sensing* 33.5 (2002), pp. 1153–1161.

[92] S. Usai. “The use of man-made features for long time scale INSAR”. In: *Proceedings of IGARSS’97. 1997 IEEE International Geoscience and Remote Sensing Symposium Proceedings. Remote Sensing-A Scientific Vision for Sustainable Development* 4 (1997), pp. 1542–1544.

[93] D. Massonnet and K. Feigl. “Discrimination of geophysical phenomena in satellite radar interferograms”. In: *Geophysical Research Letters* 22.12 (1995), pp. 1537–1540.

[94] D. Massonnet, P. Briole, and A. Arnaud. “Deflation of Mount Etna monitored by spaceborne radar interferometry”. In: *Nature* 375.6532 (1995), pp. 567–570.

[95] F. Meyer, R. Bamler, N. Jakowski, and T. Fritz. “The potential of low-frequency SAR systems for mapping ionospheric TEC distributions”. In: *IEEE Geoscience and Remote Sensing Letters* 3.4 (2006), pp. 560–564.

[96] F. Meyer. “A review of ionospheric effects in low-frequency SAR—Signals, correction methods, and performance requirements”. In: *IEEE Geoscience and Remote Sensing Symposium* (2010), pp. 29–32.

[97] F. Meyer and J. Nicoll. “The impact of the ionosphere on interferometric SAR processing”. In: *IEEE Geoscience and Remote Sensing Symposium* 2 (2008), pp. II–391.

[98] R. Brcic, A. Parizzi, M. Eineder, R. Bamler, and F. Meyer. “Ionospheric effects in SAR interferometry: An analysis and comparison of methods for their estimation”. In: *IEEE Geoscience and Remote Sensing Symposium* (2011), pp. 1497–1500.

[99] R Brcic, A. Parizzi, M. Eineder, R. Bamler, and F. Meyer. “Estimation and compensation of ionospheric delay for SAR interferometry”. In: *IEEE Geoscience and Remote Sensing Symposium* (2010), pp. 2908–2911.

[100] H. Liang, L. Zhang, X. Ding, Z. Lu, and X. Li. “Toward mitigating stratified tropospheric delays in multitemporal InSAR: A quadtree aided joint model”. In: *IEEE Transactions on Geoscience and Remote Sensing* 57.1 (2018), pp. 291–303.

[101] R. Hanssen, S. Lehner, and I. Weinreich. “Atmospheric heterogeneities from ERS tandem SAR interferometry and sea surface images”. In: *Proceedings of CEOS SAR Workshop, ESTEC, Noordwijk, The Netherlands* 39 (1998).

[102] S. Usai and R. Hanssen. “Long time scale INSAR by means of high coherence features”. In: *European Space Agency-Publications-Esa Sp* 414 (1997), pp. 225–228.

[103] A. Ferretti, C. Prati, and F. Rocca. “Permanent scatterers in SAR interferometry”. In: *Proceedings of IEEE 1999 International Geoscience and Remote Sensing Symposium. IGARSS’99 (Cat. No. 99CH36293)* 3 (1999), pp. 1528–1530.

[104] S. Zwieback, S. Hensley, and I. Hajnsek. “Soil moisture estimation using differential radar interferometry: Toward separating soil moisture and displacements”. In: *IEEE Transactions on Geoscience and Remote Sensing* 55.9 (2017), pp. 5069–5083.

[105] C. Werner, U. Wegmüller, T. Strozzi, and A. Wiesmann. “Interferometric point target analysis for deformation mapping”. In: *Proceedings of IGARSS 2003. 2003 IEEE International Geoscience and Remote Sensing Symposium. (IEEE cat. No. 03CH37477)* 7 (2003), pp. 4362–4364.

[106] B. M. Kampes. *Radar interferometry*. Vol. 12. Springer, 2006.

[107] D. Perissin and T. Wang. “Repeat-pass SAR interferometry with partially coherent targets”. In: *IEEE Transactions on Geoscience and Remote Sensing* 50.1 (2011), pp. 271–280.

[108] A. Hooper. “A multi-temporal InSAR method incorporating both persistent scatterer and small baseline approaches”. In: *Geophysical Research Letters* 35.16 (2008).

[109] O. Mora, J. J. Mallorqui, and A. Broquetas. “Linear and nonlinear terrain deformation maps from a reduced set of interferometric SAR images”. In: *IEEE Transactions on Geoscience and Remote Sensing* 41.10 (2003), pp. 2243–2253.

[110] D. A . Schmidt and R. Bürgmann. “Time-dependent land uplift and subsidence in the Santa Clara valley, California, from a large interferometric synthetic aperture radar data set”. In: *Journal of Geophysical Research: Solid Earth* 108.B9 (2003).

[111] A. Hooper, D. Bekaert, E. Hussain, and K. Spaans. *StaMPS/MTI manual*. Vol. 4.1 b. Accessed: 5-5-2025. School of Earth and Environment, University of Leeds, 2018, p. 44.

[112] C. W. Chen and H. A Zebker. “Two-dimensional phase unwrapping with use of statistical models for cost functions in nonlinear optimization”. In: *Journal of the Optical Society of America A* 18.2 (2001), pp. 338–351.

[113] A. Kalia. “Classification of landslide activity on a regional scale using persistent scatterer interferometry at the Moselle Valley (Germany)”. In: *Remote Sensing* 10.12 (2018), p. 1880.

[114] N. Schnitter. *A History of Dams: The Useful Pyramids*. Balkema, 1994. URL: `https://books.google.de/books?id=DP2sQgAACAAJ`.

[115] International Commission On Large Dams (ICOLD). *ICOLD CIGB > Role of Dams*. URL: `https://www.icold-cigb.org/GB/dams/role_of_dams.asp` (visited on 07/02/2025).

[116] R. B. Jansen. “Introduction”. In: *Advanced Dam Engineering for Design, Construction, and Rehabilitation*. Ed. by R. B. Jansen. Springer Science & Business Media, 2012, pp. 1–7.

[117] C. F. Corns. “Gravity Dam Design and Analysis”. In: *Advanced Dam Engineering for Design, Construction, and Rehabilitation*. Ed. by R. B. Jansen. Springer Science & Business Media, 2012, pp. 256–320.

[118] F. Salazar, J. San Mauro, D.J. Vicente, C.M. Baena, C. Granell, L. Gracia, and E. de-Pouplana I .and Oñate. “Computer-aided design and analysis of arch dams”. In: *Proceedings of 14th International Benchmark Workshop on Numerical Analysis of Dams* (2017), pp. 672–681.

[119] USBR – US Bureau of Reclamation. “Design of Double-Curvature Arch Dams Planning, Appraisal, Feasability Level”. In: *Technical Memorandum No. EM36-86-68110* (2013), pp. 672–681.

[120] International Commission On Large Dams (ICOLD). *ICOLD CIGB > Technology of Dams*. URL: https://www.icold-cigb.org/GB/dams/technology_of_dams.asp (visited on 07/02/2025).

[121] R. B. Jansen. “Earthfill Dam Design and Analysis”. In: *Advanced Dam Engineering for Design, Construction, and Rehabilitation*. Ed. by R. B. Jansen. Springer Science & Business Media, 2012, pp. 466–492.

[122] T. M. Leps. “Rockfill Dam Design and Analysis”. In: *Advanced Dam Engineering for Design, Construction, and Rehabilitation*. Ed. by R. B. Jansen. Springer Science & Business Media, 2012, pp. 368–387.

[123] E. C. Lawton, R. J. Fragaszy, and M. D. Hetherington. “Review of wetting-induced collapse in compacted soil”. In: *Journal of Geotechnical Engineering* 118.9 (1992), pp. 1376–1394.

[124] G. Wu. “Earthquake-induced deformation analyses of the Upper San Fernando Dam under the 1971 San Fernando earthquake”. In: *Canadian Geotechnical Journal* 38.1 (2001), pp. 1–15.

[125] M. Scaioni, M. Marsella, M. Crosetto, V. Tornatore, and J. Wang. “Geodetic and remote-sensing sensors for dam deformation monitoring”. In: *Sensors* 18.11 (2018), p. 3682.

[126] I. Nagayama, Y. Yamaguchi, T. Sasaki, A. Nakamura, H. Kawasaki, and D. Hirayama. “Damage to dams due to three large earthquakes occurred in 2003, in Japan”. In: *Proceedings of 36th Joint Meeting Panel on Wind and Seismic Effects* (2004).

[127] J.R. Swaisgood. “Embankment dam deformations caused by earthquakes”. In: *Proceedings of Pacific Conference on Earthquake Engineering* 14 (2003).

[128] G. Guler, H. R. Kilic, G. Hosbas, and K. Ozaydin. “Evaluation of the movements of the dam embankments by means of geodetic and geotechnical methods”. In: *Journal of Surveying Engineering* 132.1 (2006), pp. 31–39.

[129] M. C. de Lacy, M. I. Ramos, A. J. Gil, Ó. D. Franco, A. M. Herrera, A. Avilés M.and Domínguez, and J. C.s Chica. “Monitoring of vertical deformations by means high-precision geodetic levelling. Test case: The Arenoso dam (South of Spain)”. In: *Journal of Applied Geodesy* 11.1 (2017), pp. 31–41.

[130] S. I. Pytharouli and S. C. Stiros. “Investigation of the parameters controlling the crest settlement of a major earthfill dam based on the threshold correlation analysis”. In: *Journal of Applied Geodesy* 3 (2009), pp. 55–62.

[131] Q. M. Guedes and I. da Silva. “Technical report: Shell dam horizontal displacement monitoring–comparative study using geodetic measurement, optical plumb and GPS technologies”. In: *Journal of Applied Geodesy* 3.4 (2009), pp. 249–255.

[132] A. Wagner. “A new approach for geo-monitoring using modern total stations and RGB+ D images”. In: *Measurement* 82 (2016), pp. 64–74.

[133] Y. Zhou, A. Wagner, T. Wunderlich, and P. Wasmeier. “Calibration method for IATS and application in multi-target monitoring using coded targets”. In: *Journal of Applied Geodesy* 11.2 (2017), pp. 99–106.

[134] Z. Altamimi, P. Rebischung, L. Métivier, and X. Collilieux. “ITRF2014: A new release of the International Terrestrial Reference Frame modeling nonlinear station motions”. In: *Journal of Geophysical Research: Solid Earth* 121.8 (2016), pp. 6109–6131.

[135] A. Chrzanowski, A. Szostak, and R. Steeves. “Reliability and efficiency of dam deformation monitoring schemes”. In: *Proceedings of the 2011 Annual Conference of Canadian Dam Association (CDA/ACB), Fredericton, NB, Canada* 15 (2011), pp. 1–15.

[136] A. Azzoni, G. Mazzà, M. Scaioni, and G. Vassena. “The automatic collimator for dam monitoring ISAC 5000. Results of one year tests”. In: *Proceedings of the IAG Symposium on Geodesy for Geotechnical and Structural Engineering, Eisenstadt, Austria* (1998), pp. 331–336.

[137] D. Tarchi, H. Rudolf, G. Luzi, L. Chiarantini, P. Coppo, and A. J. Sieber. “SAR interferometry for structural changes detection: A demonstration test on a dam”. In: *Proceedings of IEEE 1999 International Geoscience and Remote Sensing Symposium. IGARSS’99 (Cat. No. 99CH36293)* 3 (1999), pp. 1522–1524.

[138] J. Erdélyi, A. Kopáčik, I. Lipták, and P. Kyrinovič. “Automation of point cloud processing to increase the deformation monitoring accuracy”. In: *Applied Geomatics* 9 (2017), pp. 105–113.

[139] A. Nickitopoulou, K. Protopsalti, and S. Stiros. “Monitoring dynamic and quasi-static deformations of large flexible engineering structures with GPS: Accuracy, limitations and promises”. In: *Engineering Structures* 28.10 (2006), pp. 1471–1482.

[140] T. D. Stark and H. Choi. “Slope inclinometers for landslides”. In: *Landslides* 5 (2008), pp. 339–350.

[141] L. Guerriero, G. Guerriero, G. Grelle, F. M. Guadagno, and P. Revellino. “Brief Communication: A low-cost Arduino®-based wire extensometer for earth flow monitoring”. In: *Natural Hazards and Earth System Sciences* 17.6 (2017), pp. 881–885.

[142] I. Hunstad, G. Selvaggi, N. D’Agostino, P. England, P. Clarke, and M. Pierozzi. “Geodetic strain in peninsular Italy between 1875 and 2001”. In: *Geophysical Research Letters* 30.4 (2003).

[143] W. Mukupa, G. W. Roberts, C. M. Hancock, and K. Al-Manasir. “A review of the use of terrestrial laser scanning application for change detection and deformation monitoring of structures”. In: *Survey Review* 49.353 (2017), pp. 99–116.

[144] M. Choudhury and C. Rizos. “Slow structural deformation monitoring using Locata–a trial at Tumut Pond Dam”. In: *Journal of Applied Geodesy* 4 (2010), pp. 177–187.

[145] M. Scaioni, B. Höfle, A.P. Baungarten Kersting, L. Barazzetti, M. Previtali, and D. Wujanz. “Methods from information extraction from lidar intensity data and multispectral lidar technology”. In: *The International Archives of the Photogrammetry, Remote Sensing and Spatial Information Sciences* 42 (2018), pp. 1503–1510.

[146] O. Monserrat, M. Crosetto, and G. Luzi. “A review of ground-based SAR interferometry for deformation measurement”. In: *ISPRS Journal of Photogrammetry and Remote Sensing* 93 (2014), pp. 40–48.

[147] M. Crosetto, O. Monserrat, G. Luzi, M. Cuevas, and N. Devanthéry. “Deformation monitoring using ground-based SAR data”. In: *Engineering Geology for Society and Territory-Volume 5: Urban Geology, Sustainable Planning and Landscape Exploitation* 5 (2015), pp. 137–140.

[148] C. Xing, J. Huang, and X. Han. “Research on the environmental effects of GB-SAR for dam monitoring”. In: *Advanced Materials Research* 919 (2014), pp. 392–397.

[149] F. Ferrigno, G.I. Gigli, R. Fanti, E. Intrieri, and N. Casagli. “GB-InSAR monitoring and observational method for landslide emergency management: the Montaguto earthflow (AV, Italy)”. In: *Natural Hazards and Earth System Sciences* 17.6 (2017), pp. 845–860.

[150] P. Milillo, R. Bürgmann, P. Lundgren, J. Salzer, D. Perissin, E. Fielding, F. Biondi, and G. Milillo. “Space geodetic monitoring of engineered structures: The ongoing destabilization of the Mosul dam, Iraq”. In: *Scientific Reports* 6.1 (2016b), p. 37408.

[151] G. Grenerczy and U. Wegmüller. “Persistent scatterer interferometry analysis of the embankment failure of a red mud reservoir using ENVISAT ASAR data”. In: *Natural Hazards* 59 (2011), pp. 1047–1053.

[152] USGS - United States Geological Survey. *Tectonic Plate Boundaries*. 2025. URL: `https://www.usgs.gov/programs/earthquake-hazards/google-earthtmkml-files` (visited on 04/22/2025).

[153] USGS - United States Geological Survey. *Earthquake Catalog*. 2025. URL: `https://earthquake.usgs.gov/earthquakes/search/` (visited on 04/22/2025).

[154] D. McKenzie. “Plate tectonics of the Mediterranean region”. In: *Nature* 226.5242 (1970), pp. 239–243.

[155] D. McKenzie. “Active tectonics of the Mediterranean region”. In: *Geophysical Journal International* 30.2 (1972), pp. 109–185.

[156] J.-M. Nocquet. “Present-day kinematics of the Mediterranean: A comprehensive overview of GPS results”. In: *Tectonophysics* 579 (2012), pp. 220–242.

[157] T. Doutsos and G. Poulimenos. “Geometry and kinematics of active faults and their seismotectonic significance in the western Corinth-Patras rift (Greece)”. In: *Journal of Structural Geology* 14.6 (1992), pp. 689–699.

[158] G. Ferentinos, M. Brooks, and T. Doutsos. “Quaternary tectonics in the Gulf of Patras, western Greece”. In: *Journal of Structural Geology* 7.6 (1985), pp. 713–717.

[159] A. Ganas. *NOAFAULTS KMZ layer Version 5.0 (V5.0)*. `https://doi.org/10.5281/zenodo.8075517`. Accessed: 2024-01-29.

[160] P. Elias and P. Briole. “Ground deformations in the Corinth rift, Greece, investigated through the means of SAR multitemporal interferometry”. In: *Geochemistry, Geophysics, Geosystems* 19.12 (2018), pp. 4836–4857.

[161] I. Parcharidis, S. Kokkalas, I. Fountoulis, and M. Foumelis. “Detection and monitoring of active faults in urban environments: time series interferometry on the cities of Patras and Pyrgos (Peloponnese, Greece)”. In: *Remote Sensing* 1.4 (2009), pp. 676–696.

[162] V. Sakkas, M. Garcia, M. Bianchi, and E. Lagios. “Squeesar Analysis Based on Sentinel-1 Data in the Seismic Active Area of Patras Gulf (W. Greece)”. In: *Proceedings of IGARSS 2018-2018 IEEE International Geoscience and Remote Sensing Symposium* (2018), pp. 208–211.

[163] V. Tsironi, A. Ganas, I. Karamitros, E. Efstathiou, I. Koukouvelas, and E. Sokos. “Kinematics of active landslides in Achaia (Peloponnese, Greece) through InSAR time series analysis and relation to rainfall patterns”. In: *Remote Sensing* 14.4 (2022), p. 844.

[164] N. Sabatakakis, G. Koukis, E. Vassiliades, and S. Lainas. “Landslide susceptibility zonation in Greece”. In: *Natural Hazards* 65 (2013), pp. 523–543.

[165] M. Del Soldato, C. Del Ventisette, F. Raspini, G. Righini, V. Pancioli, and S. Moretti. “Ground deformation and associated hazards in NW peloponnese (Greece)”. In: *European Journal of Remote Sensing* 51.1 (2018), pp. 710–722.

[166] S. Gernhardt, N. Adam, M. Eineder, and R. Bamler. “Potential of very high resolution SAR for persistent scatterer interferometry in urban areas”. In: *Annals of GIS* 16.2 (2010), pp. 103–111.

[167] G. Dounias, S. Lazaridou, S. Sakellariou, L. Somakos, K. Skourlis, and S. Mihas. “The behavior of Asteri Dam on Parapeiros River during first filling, Greece.” In: *Proceedings of 91st International Commission of Large Dams Annual Meeting, International Commission of Large Dams* (2023), pp. 1–10.

[168] F. De Zan and A. M. Guarnieri. “TOPSAR: Terrain observation by progressive scans”. In: *IEEE Transactions on Geoscience and Remote Sensing* 44.9 (2006), pp. 2352–2360.

[169] M. Zink, A. Moreira, I. Hajnsek, P. Rizzoli, M. Bachmann, R. Kahle, T. Fritz, M. Huber, G. Krieger, and M. Lachaise. “TanDEM-X: 10 years of formation flying bistatic SAR interferometry”. In: *IEEE Journal of Selected Topics in Applied Earth Observations and Remote Sensing* 14 (2021), pp. 3546–3565.

[170] European Space Agency. *Sentinel Toolbox Overview*. 2015. URL: `https://step.esa.int/main/` (visited on 09/06/2015).

[171] F. Cigna, C. Del Ventisette, V. Liguori, and N. Casagli. “Advanced radar-interpretation of InSAR time series for mapping and characterization of geological processes”. In: *Natural Hazards and Earth System Sciences* 11.3 (2011), pp. 865–881.

[172] S. Bianchini, F. Raspini, L. Solari, M. Del Soldato, A. Ciampalini, A. Rosi, and N. Casagli. “From picture to movie: Twenty years of ground deformation recording over Tuscany region (Italy) with satellite InSAR”. In: *Frontiers in Earth Science* 6 (2018), p. 177.

[173] M. Crosetto, L. Solari, M. Mróz, J. Balasis-Levinsen, N. Casagli, M. Frei, A. Oyen, D. Moldestad, L. Bateson, and L. Guerrieri. “The evolution of wide-area DInSAR: From regional and national services to the European Ground Motion Service”. In: *Remote Sensing* 12.12 (2020), p. 2043.

[174] L. Chang and R. Hanssen. “A probabilistic approach for InSAR time-series postprocessing”. In: *IEEE Transactions on Geoscience and Remote Sensing* 54.1 (2015), pp. 421–430.

[175] M. Berti, A. Corsini, S. Franceschini, and J.P. Iannacone. “Automated classification of Persistent Scatterers Interferometry time series”. In: *Natural Hazards and Earth System Sciences* 13.8 (2013), pp. 1945–1958.

[176] R. Boni, G. Pilla, and C. Meisina. “Methodology for detection and interpretation of ground motion areas with the A-DInSAR time series analysis”. In: *Remote Sensing* 8.8 (2016), p. 686.

[177] M. Bordoni, R. Boni, A. Colombo, L. Lanteri, and C. Meisina. “A methodology for ground motion area detection (GMA-D) using A-DInSAR time series in landslide investigations”. In: *Catena* 163 (2018), pp. 89–110.

[178] M. Costantini, M. Zhu, S. Huang, S. Bai, J. Cui, F. Minati, F. Vecchioli, D. Jin, and Q. Hu. “Automatic detection of building and infrastructure instabilities by spatial and temporal analysis of InSAR measurements”. In: *Proceedings of IGARSS 2018-2018 IEEE International Geoscience and Remote Sensing Symposium* (2018), pp. 2224–2227.

[179] S. M. Mirmazloumi, Y. Wassie, J. A. Navarro, R. Palamá, V. Krishnakumar, A. Barra, M. Cuevas-González, M. Crosetto, and O. Monserrat. “Classification of ground deformation using sentinel-1 persistent scatterer interferometry time series”. In: *GIScience & Remote Sensing* 59.1 (2022), pp. 374–392.

[180] D. Festa, A. Novellino, E. Hussain, L. Bateson, N. Casagli, P. Confuorto, M. Del Soldato, and F. Raspini. “Unsupervised detection of InSAR time series patterns based on PCA and K-means clustering”. In: *International Journal of Applied Earth Observation and Geoinformation* 118 (2023), p. 103276.

[181] D. C. Montgomery, C. L. Jennings, and M. Kulahci. “Time series analysis and forecasting”. In: *Introduction to Time Series Analysis and Forecasting* (2015), pp. 1–671.

[182] K. Neusser. *Time series econometrics*. Springer, 2016.

[183] B. Walczak and D.L. Massart. “Noise suppression and signal compression using the wavelet packet transform”. In: *Chemometrics and Intelligent Laboratory Systems* 36.2 (1997), pp. 81–94.

[184] S. Mallat. *A Wavelet Tour of Signal Processing: The Sparse Way*. Academic Press, Inc., 2008.

[185] R. L. Motard and B. Joseph. *Wavelet applications in chemical engineering*. Vol. 272. Springer Science & Business Media, 2013.

[186] S. G. Mallat. “Multifrequency channel decompositions of images and wavelet models”. In: *IEEE Transactions on Acoustics, Speech, and Signal Processing* 37.12 (1989), pp. 2091–2110.

[187] R. Cohen. “Signal denoising using wavelets”. In: *Project Report* (2012), pp. 1–29.

[188] D. L Donoho. “De-noising by soft-thresholding”. In: *IEEE Transactions on Information Theory* 41.3 (1995), pp. 613–627.

[189] T. Loutas and V. Kostopoulos. “Utilising the wavelet transform in condition-based maintenance: A review with applications”. In: *Advances in Wavelet Theory and Their Applications in Engineering, Physics and Technology*. Ed. by Dumitru Baleanu. Vol. 1. Janeza Trdine 9, 51000 Rijeka, Croatia: InTech, 2012, pp. 273–312.

[190] R. A. Fisher. “Tests of significance in harmonic analysis”. In: *Proceedings of the Royal Society of London. Series A, Containing Papers of a Mathematical and Physical Character* 125.796 (1929), pp. 54–59.

[191] M. Ahdesmaki, H. Lahdesmaki, and O. Yli-Harja. “Robust Fisher’s test for periodicity detection in noisy biological time series”. In: *Proceedings of IEEE International Workshop on Genomic Signal Processing and Statistics* (2007), pp. 1–4.

[192] R.L. Ott and M. Longnecker. *An introduction to statistical methods and data analysis*. Cengage Learning, 2016.

[193] D. J. Biau, B. M. Jolles, and R. Porcher. “P value and the theory of hypothesis testing: an explanation for new researchers”. In: *Clinical Orthopaedics and Related Research®* 468.3 (2010), pp. 885–892.

[194] E. Keogh, S. Chu, D. Hart, and M. Pazzani. “Segmenting time series: A survey and novel approach”. In: *Data Mining in Time Series Databases*. World Scientific, 2004, pp. 1–21.

[195] G. F. Malash and M. I. El-Khaiary. “Piecewise linear regression: A statistical method for the analysis of experimental adsorption data by the intraparticle-diffusion models”. In: *Chemical Engineering Journal* 163.3 (2010), pp. 256–263.

[196] M. Lovrić, M. Milanović, and M. Stamenković. “Algoritmic methods for segmentation of time series: An overview”. In: *Journal of Contemporary Economic and Business Issues* 1.1 (2014), pp. 31–53.

[197] T. O. Hodson. “Root mean square error (RMSE) or mean absolute error (MAE): When to use them or not”. In: *Geoscientific Model Development Discussions* 2022 (2022), pp. 1–10.

[198] J. B. Johnson and K. S. Omland. “Model selection in ecology and evolution”. In: *Trends in Ecology & Evolution* 19.2 (2004), pp. 101–108.

[199] C. Del Gaudio, I. Aquino, G.P. Ricciardi, C. Ricco, and R. Scandone. “Unrest episodes at Campi Flegrei: A reconstruction of vertical ground movements during 1905–2009”. In: *Journal of Volcanology and Geothermal Research* 195.1 (2010), pp. 48–56.

[200] M. Polcari, S. Borgstrom, C. Del Gaudio, P. De Martino, C. Ricco, V. Siniscalchi, and E. Trasatti. “Thirty years of volcano geodesy from space at Campi Flegrei caldera (Italy)”. In: *Scientific Data* 9.1 (2022), p. 728.

[201] William H Schulz, Jonathan P McKenna, John D Kibler, and Giulia Biavati. “Relations between hydrology and velocity of a continuously moving landslide—evidence of pore-pressure feedback regulating landslide motion?” In: *Landslides* 6.3 (2009), pp. 181–190.

[202] Kwan Ben Sim, Min Lee Lee, and Soon Yee Wong. “A review of landslide acceptable risk and tolerable risk”. In: *Geoenvironmental Disasters* 9.1 (2022), p. 3.

[203] H. Shi, J. Chen, S. Liu, and B. Sivakumar. “The role of large dams in promoting economic development under the pressure of population growth”. In: *Sustainability* 11.10 (2019), p. 2965.

[204] C. A. Brown and W. J. Graham. “Assessing the threat to life from dam failure 1”. In: *Journal of the American Water Resources Association* 24.6 (1988), pp. 1303–1309.

[205] M. L. DeKay and G. McClelland. “Predicting loss of life in cases of dam failure and flash flood”. In: *Risk Analysis* 13.2 (1993), pp. 193–205.

[206] CIGB ICOLD. “Automated dam monitoring systems: guidelines and case histories””. In: *International Commission on Large Dams* 151 (2000).

[207] D. Di Martire, R. Iglesias, D. Monells, G. Centolanza, S. Sica, M. Ramondini, L. Pagano, J. J. Mallorquí, and D. Calcaterra. “Comparison between Differential SAR interferometry and ground measurements data in the displacement monitoring of the earth-dam of Conza della Campania (Italy)”. In: *Remote Sensing of Environment* 148 (2014), pp. 58–69. URL: https://www.sciencedirect.com/science/article/pii/S0034425714000856.

[208] P. Milillo, D. Perissin, J. Salzer, P. Lundgren, G. Lacava, G. Milillo, and C. Serio. “Monitoring dam structural health from space: Insights from novel InSAR techniques and multi-parametric modeling applied to the Pertusillo dam Basilicata, Italy”. In: *International Journal of Applied Earth Observation and Geoinformation* 52 (2016a), pp. 221–229. URL: https://www.sciencedirect.com/science/article/pii/S0303243416300952.

[209] S. L. Ullo, P. Addabbo, D. Di Martire, S. Sica, N. Fiscante, L. Cicala, and C. V. Angelino. “Application of DInSAR Technique to High Coherence Sentinel-1 Images for Dam Monitoring and Result Validation Through In Situ Measurements”. In: *IEEE Journal of Selected Topics in Applied Earth Observations and Remote Sensing* 12.3 (2019), pp. 875–890.

[210] H. Chen and A. Swain. “The Grand Ethiopian Renaissance Dam: Evaluating its sustainability standard and geopolitical significance”. In: *Energy Development Frontier* 3.1 (2014), pp. 11–19.

[211] M. Rebmeister, A. Schenk, S. Hinz, F. Andrian, and M. Vonie. “High dam monitoring with ground-based sar: opportunities and challenges”. In: *ICOLD* 2023 (2023), 91st.

[212] A. Piter, M. Haghshenas Haghighi, and M. Motagh. “Challenges and Opportunities of Sentinel-1 InSAR for Transport Infrastructure Monitoring”. In: *PFG–Journal of Photogrammetry, Remote Sensing and Geoinformation Science* 92.5 (2024), pp. 609–627.

[213] M. Lachaise, M. Eineder, and T. Fritz. “Multi baseline SAR acquisition concepts and phase unwrapping algorithms for the TanDEM-X mission”. In: *2007 IEEE International Geoscience and Remote Sensing Symposium* (2007), pp. 5272–5276.

[214] M. Lachaise, T. Fritz, and R. Bamler. “The dual-baseline phase unwrapping correction framework for the TanDEM-X mission part 1: Theoretical description and algorithms”. In: *IEEE Transactions on Geoscience and Remote Sensing* 56.2 (2017), pp. 780–798.

[215] C. G. Poidomani, D. Costantini, P. Pasquali, and P. Jaeger. “National-Scale DEM Generation Using ERS Tandem Data in Alpine Regions”. In: *Proceedings of the ERS-ENVISAT Symposium "Looking down to Earth in the New Millennium"* (2000), pp. 1–5.

[216] Z. Chunxia, G. Linlin, E . Dongchen, and C. Hsingchung. “A case study of using external DEM in InSAR DEM generation”. In: *Geo-Spatial Information Science* 8 (2005), pp. 14–18.

[217] J. Ziemer, J. Jänichen, G. Stein, N. Liedel, C. Wicker, K. Last, J. Denzler, C. Schmullius, M. Shadaydeh, and C. Dubois. “Identifying Deformation Drivers in Dam Segments Using Combined X-and C-Band PS Time Series”. In: *Remote Sensing* 17.15 (2025), p. 2629.

[218] Richard Franke. “Smooth interpolation of scattered data by local thin plate splines”. In: *Computers & mathematics with applications* 8.4 (1982), pp. 273–281.

[219] R. Capes and E. Passera. *Product Description and Format Specification*. Accessed: 5-15-2025.

[220] F. Hu, J. Wu, L. Chang, and R. Hanssen. “Incorporating temporary coherent scatterers in multi-temporal InSAR using adaptive temporal subsets”. In: *IEEE Transactions on Geoscience and Remote Sensing* 57.10 (2019), pp. 7658–7670.

[221] Homa Ansari, Francesco De Zan, and Richard Bamler. “Sequential estimator: Toward efficient InSAR time series analysis”. In: *IEEE Transactions on Geoscience and Remote Sensing* 55.10 (2017), pp. 5637–5652.

[222] Carlo Colesanti, Alessandro Ferretti, Fabrizio Novali, Claudio Prati, and Fabio Rocca. “SAR monitoring of progressive and seasonal ground deformation using the permanent scatterers technique”. In: *IEEE Transactions on Geoscience and Remote Sensing* 41.7 (2003), pp. 1685–1701.

[223] Matias Palomeque, Joaquin Ferreyra, and Marc Thibeault. “Monitoring Results of the SAOCOM-1 Constellation: A mission overview and summary of results”. In: *IEEE Geoscience and Remote Sensing Magazine* (2024).

[224] Ake Rosenqvist, Masanobu Shimada, and Manabu Watanabe. “ALOS PALSAR: Technical outline and mission concepts”. In: *4th International symposium on Retrieval of Bio-and geophysical parameters from SAR data for land applications*. Innsbruck, Austria. 2004, pp. 1–7.

[225] Tazio Strozzi, Nina Jones, Rafael Caduff, and Urs Wegmüller. “L-Band DInSAR Surface Motion Products in Alpine Regions with SAOCOM”. In: *IGARSS 2024 - 2024 IEEE International Geoscience and Remote Sensing Symposium* (2024), pp. 10740–10743.

[226] Z. Du, L. Ge, X. Li, and A. Ng. “Subsidence Monitoring over the Southern Coalfield, Australia Using both L-Band and C-Band SAR Time Series Analysis”. In: *Remote Sensing* 8.7 (2016). URL: `https://www.mdpi.com/2072-4292/8/7/543`.

List of Figures

List of Tables

List of Symbols

M	Number of Segments for a Piecewise Linear Representation
R^2_{adj}	Adjusted Coefficient of Determination
H_1	Alternative Hypothesis
a_j	Approximation Coefficients
A_w	Amplitude Values
L	Physical Antenna Size
x	Azimuth
b	Baseline
ς	Baseline Angle
γ	Coherence
$\lvert\widehat{\gamma}\rvert$	Maximum Likelihood Estimator of the Coherence Magnitude
d	Displacement
D_A	Amplitude Dispersion Index
u_j	Detail Coefficients
ε	Error
η	Number of Predictor Variables
ϑ	Expected Phase for the Reference Body
F_0	Test Statistic
f_0	Carrier Frquency
ω_i	Fourier Frequencies
g^*	G-Statistic
H	Altitude of Satellite above a Reference Plane
h	Height of Ground Resolution Cell above a Reference Body
ξ	Incidence Angle
Q	Number of Interferograms
λ	Carrier Wavelength
α	Level of Significance
θ	Look Angle
m_A	Mean Amplitude
ζ	Mother Wavelet
N	Number of Data Points
n	Noise
$n(R)$	Refractivity Index
$N(R)$	Refractivity of the Atmosphere
H_0	Null Hypothesis

γ	Residual Phase Varibilaty
ν	Pressure
P	Propability
ψ	Observed Phase
ϕ	Absolute Phase
$\tilde{\psi}$	Filtered Phase
β	Regression Coefficient
m	Resolution Level of wavelet Transformation
s	Wavelet Scaling Parameter
S	Scaling Filter
σ	Standard Deviation
R	Slant Range Distance
$I(\omega)$	Spectral Estimate
t_j	Student's t-statistic
τ	Degree of Freedom for the Regression Model
ϖ	Temperature
t	Time
o	Wavelet Translation Parameter
κ	Universal Threshold
C_{jj}	Diagonal Element of the Variance-Covariance Matrix
W	Number of SAR Images
χ	Wavelet Coefficients
G	Wavelet Filter
e_j	Wavelet Filtering Coefficients
k	Wavenumber
y	Observed Time Series
$\hat{y}$	Estimated Time Series Model
z	Signal Back Scattered from the Earth

List of Abbreviations

AOI	Area-of-Interest
APS	Atmospheric Phase Screen
ATFZ	Aigia Triada Fault Zone
BGR	Federal Institute for Geosciences and Natural Resources
BIC	Schwarz-Bayesian Information Criterion
CP	Change Point
DEM	Digital Elevation Model
DInSAR	Differential Synthetic Aperture Radar Interferometry
DLR	German Aerospace Center
DS	Distributed Scatterer
DWT	Discrete Wavelet Transformation
EGMS	European Ground Motion Service
ESA	European Space Agency
GBSAR	Ground-based Synthetic Aperture Radar
GMS	Ground Motion Service
GNSS	Global Navigation Satellite Systems
gpt	Graph Processing Tool
InSAR	Synthetic Aperture Radar Interferometry
IPTA	Interferometric Point Target Analysis
IW	Interferometric Wide
LOS	Line-of-Sight
MAE	Mean Absolute Error
MP	Measuring Point
NORCE	Norwegian Research Center
OLS	Ordinary Least squares
PDF	Probability Density Function
PF	Patras Fault
PLR	Piecewise Linear Representation
PPF	Psathopyrgos Fault
PRF	Pulse Repetition Frequency
PS	Persistent Scatterer
PSC	Persistent Scatterer Candidate
PSDefoPAT	Persistent Scatterer Deformation Pattern Analysis Tool
PSI	Persistent Scatterer Interferometry
PSISlider	Sliding-Window Approach for PSI

PU	Phase Unwrapping
RAM	Random-Access Memory
RMSE	Root Mean Squared Error
RPF	Rion-Patras Fault
S1	Sentinel-1
SAR	Synthetic Aperture Radar
SBAS	Small Baseline Subset Interferometry
SHM	Structural Health Monitoring
SNAP	SeNtinel Application Plattform
SNAPHU	Statistical-Cost Network-Flow Algorithm for Phase Unwrapping
SNR	Signal-to-Noise Ratio
SSE	Sum of Squares due to the Residual Error
SSR	Sum of Squares due to the Regression Model
SST	Total Sum of Squares
StaMPS	Stanford Method for Persistent Scatterer
TLS	Terrestrial Laser Scanning
TOPSAR	Terrain Observation by Progressive Scans
TSX	TerraSAR-X
WT	Wavelet Transformation

Appendix

A

A.1 Persistent Scatterer Deformation Pattern Analysis Tool

<table>
<tr><td rowspan="3"></td><td colspan="5">Model 1: $y = \beta_2 \cdot \sin(2\pi\beta_3(t-\beta_4))$</td><td colspan="8">Model 2: $y = \beta_2 \cdot \sin(2\pi\beta_3(t-\beta_4)) + \beta_1 \cdot t + \beta_0$</td><td colspan="6">Model 3: $y = \beta_0 + \beta_1 \cdot t + \beta_2(t-cp)\delta$
With $\delta \begin{cases} 0, t < cp \\ 1, t \geq cp \end{cases}$</td></tr>
<tr><td colspan="3">Model Coefficients</td><td rowspan="2">R^2_{adj}</td><td rowspan="2">$RMSE$</td><td colspan="6">Model Coefficients</td><td rowspan="2">R^2_{adj}</td><td rowspan="2">$RMSE$</td><td colspan="4">Model Coefficients</td><td rowspan="2">R^2_{adj}</td><td rowspan="2">$RMSE$</td></tr>
<tr><td>β_2</td><td>β_3</td><td>β_4</td><td>β_0</td><td>β_1</td><td>β_2</td><td>β_3</td><td colspan="2">β_4</td><td>β_0</td><td>β_1</td><td>β_2</td><td>cp</td></tr>
<tr><td>set</td><td>−14</td><td>370</td><td>−47</td><td></td><td></td><td>31</td><td>−0.056</td><td>−15</td><td>190</td><td colspan="2">43</td><td></td><td></td><td>6.4</td><td>−0.037</td><td>0.140</td><td>635</td><td></td><td></td></tr>
<tr><td>$\sigma = 1$</td><td>−13</td><td>373</td><td>−54</td><td>0.991</td><td>1.3</td><td>31</td><td>−0.056</td><td>12</td><td>190</td><td colspan="2">−51</td><td>0.994</td><td>1.5</td><td>6.5</td><td>−0.037</td><td>0.138</td><td>624</td><td>0.998</td><td>1.0</td></tr>
<tr><td>$\sigma = 2$</td><td>−13</td><td>376</td><td>−61</td><td>0.980</td><td>2.1</td><td>31</td><td>−0.056</td><td>13</td><td>190</td><td colspan="2">−51</td><td>0.997</td><td>2.9</td><td>7.4</td><td>−0.040</td><td>0.127</td><td>588</td><td>0.991</td><td>2.6</td></tr>
<tr><td rowspan="3">$\sigma = 4$</td><td rowspan="3">−13</td><td rowspan="3">378</td><td rowspan="3">−67</td><td rowspan="3">0.967</td><td rowspan="3">4.7</td><td colspan="6">Mislabeled as: $y = \beta_2 \cdot \sin(2\pi\beta_3(t-\beta_4)) + \beta_1 \cdot t + \beta_5 \cdot t^2 + \beta_0$</td><td rowspan="3">0.992</td><td rowspan="3">6.3</td><td rowspan="3">6.2</td><td rowspan="3">−0.037</td><td rowspan="3">0.134</td><td rowspan="3">618</td><td rowspan="3">0.997</td><td rowspan="3">4.0</td></tr>
<tr><td>β_0</td><td>β_1</td><td>β_2</td><td>β_3</td><td>β_4</td><td>β_5</td></tr>
<tr><td>33</td><td>−0.064</td><td>9</td><td>189</td><td>−49</td><td>$6.5 \cdot 10^{-5}$</td></tr>
<tr><td rowspan="3">$\sigma = 8$</td><td rowspan="3">−13</td><td rowspan="3">380</td><td rowspan="3">−69</td><td rowspan="3">0.952</td><td rowspan="3">7.6</td><td colspan="6">Mislabeled as: $y = \beta_1 \cdot t + \beta_0$</td><td rowspan="3">0.914</td><td rowspan="3">13.2</td><td rowspan="3">3.6</td><td rowspan="3">−0.035</td><td rowspan="3">0.119</td><td rowspan="3">594</td><td rowspan="3">0.998</td><td rowspan="3">7.9</td></tr>
<tr><td>β_0</td><td>β_1</td><td>β_2</td><td>β_3</td><td colspan="2">β_4</td></tr>
<tr><td>31</td><td>−0.056</td><td></td><td></td><td colspan="2"></td></tr>
</table>

A.2 PSISlider Processing Chain

To facilitate the re-use of intermediate results within the scope of the PSISlider processing chain, adaptations to parts of the conventional advanced DInSAR processing chain, presented in Figure 3.4 in Section 3.3, were necessary. Tests to verify that they function as indented are presented in the subsequent sections.

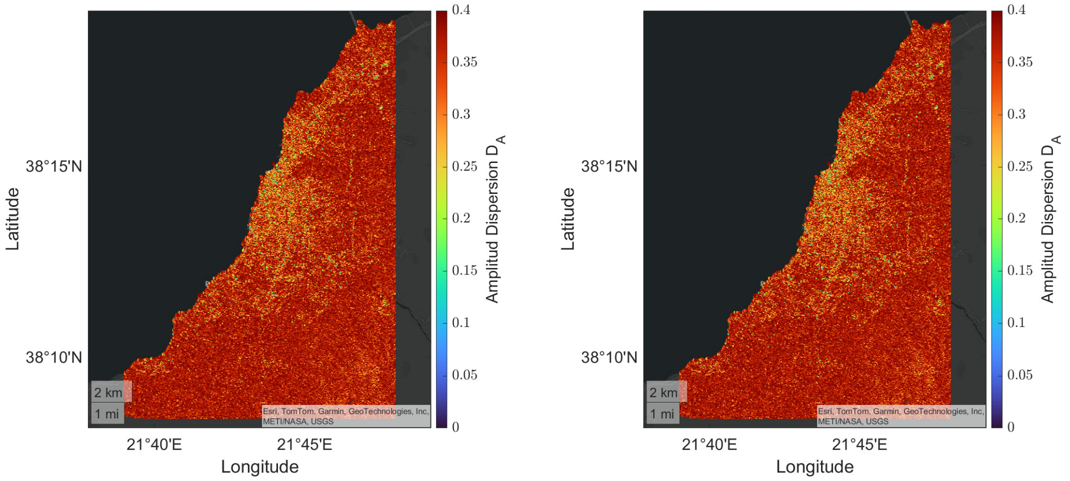

(a) Conventional processing chain **(b)** PSISlider processing chain

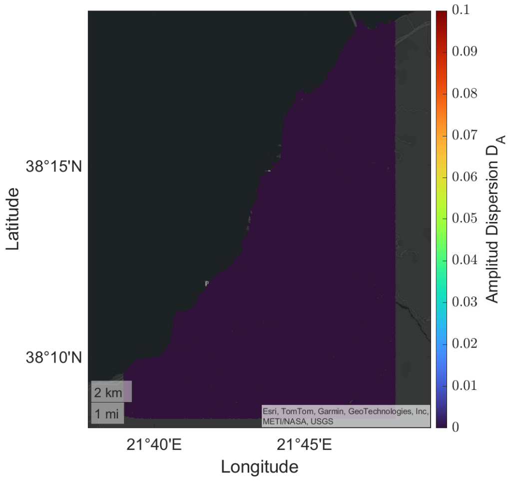

(c) Difference

Figure A.1.: Amplitude dispersion index D_A calculated with (a) the conventional processing chain, (b) the PSISlider processing chain and (c) their difference.

Re-Use and Adjustment of the Amplitude Dispersion Index

Calculating the Amplitude Dispersion Index D_A is part of the first step of StaMPS, the PSC Selection (outlined in detail in Sub-section 2.1.6). As presented in Sub-section 6.2.1, D_A is not completely re-calculated for each subset in the PSISlider processing chain. Instead, to calculate D_A for the current subset, D_A of the previous subset is corrected for the SAR images excluded and added to current subset. Figure A.1 shows D_A calculated with (a) the conventional processing chain, (b) the PSISlider processing chain and (c) their difference. The difference between the calculated D_A is in the range of 10^{-7} (dark blue) in the entire map presented in Figure A.1 (c), i.e., nearly identical. This verifies that calculating D_A with the conventional processing chain and the PSISlider processing chain yields comparable results.

Calculating the Differential Interferogram between Local Master and Slave SAR Images

As presented in Sub-section 6.2.1, to ensure comparability of the different subsets processed with the PSISlider processing chain, two different master SAR images need to be used for co-registration and calculating the differential interferograms. The master SAR images are referred to as the co-registration and local master. During interferometric pre-processing the slave SAR images and the local master SAR image are co-registered to the co-registration master image and their differential interferograms are calculated as presented in Figure 3.4 in Section 3.3. The differential interferogram between a slave SAR image and the local master SAR image is calculated by complex multiplication of the differential interferogram between local and co-registration master and the differential interferogram between slave and co-registration master. To verify the functionality of this concept, differential interferograms were calculated using:

1. only the SAR image from 04/22/2017 for co-registration and calculating the differential interferogram, and
2. the SAR image from 02/15/2017 for co-registration and the SAR image from 04/22/2017 as the local master to calculate the differential interferogram.

Exemplary resulting differential interferograms are displayed in Figure A.2. Visual inspection of corresponding differential interferograms shows that the differential interferograms are similar, which leads to the conclusion that the concept works as indented. Differential interferograms between slave SAR images and the local master SAR image can be calculated by complex multiplication of the differential interferogram between local and co-registration master and the differential interferograms between slaves and the co-registration master.

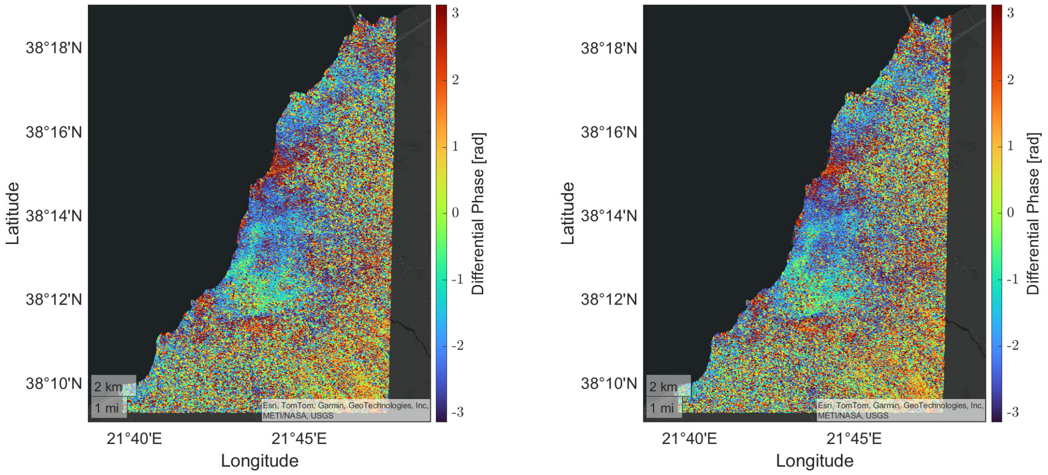

(a) 04/22/2017 & 11/23/2016: conventional processing chain

(b) 04/22/2017 & 11/23/2016: PSISlider processing chain

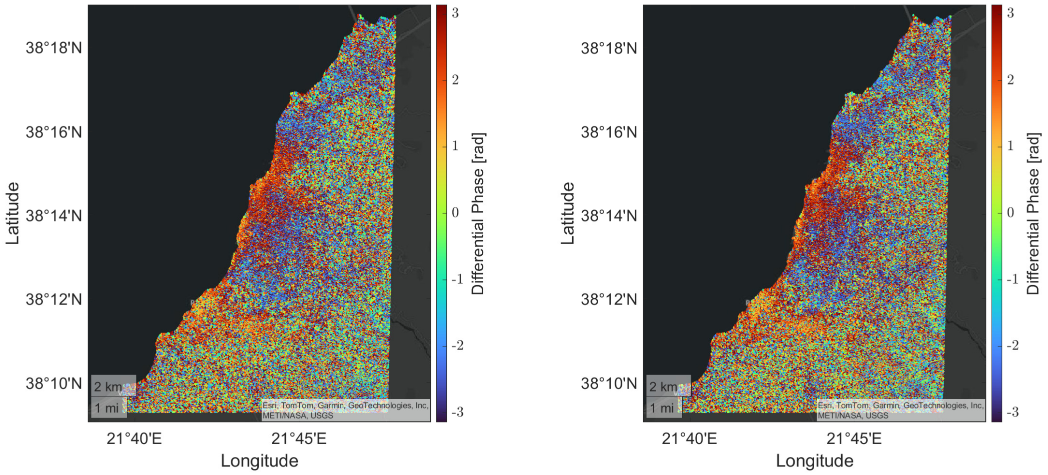

(c) 04/22/2017 & [01/10/2017: conventional processing chain

(d) 04/22/2017 & [01/10/2017: PSISlider processing chain

Figure A.2.: Exemplary resulting differential interferograms calculated with the conventional processing chain ((a) and (c)) and the PSISlider processing chain ((b) and (d))

Calculating the Spatial Baselines between Local Master and Slave SAR Images

Since vertical b_v and horizontal baselines b_h are needed for StaMPS, they need to be calculated for the slave SAR images and the local master SAR image within the scope of the PSISlider processing chain. This is achieved using java scripts that calculate the spatial baselines in accordance to the approach used in SNAP. Tests to verify that the implemented scripts provide the same spatial baseline values as the conventional advanced DInSAR processing chain, presented in Section 3.3, were carried out. Horizontal and vertical baselines calculated with:

1. the conventional advanced DInSAR processing chain with the SAR image from the 04/22/2017 as the only master image, and
2. the PSISlider processing chain with the SAR image from the 02/15/2017 as the co-registration master and the SAR image from the 04/22/2017 as the local master

are presented in Table A.1.

The differences in vertical Δb_v and horizontal baselines Δb_h presented in columns six and seven of Table A.1 are all zero. This shows that the implemented scripts provide the same spatial baseline values as the conventional advanced DInSAR processing chain, presented in Section 3.3.

Slave Date	Conventional PSI		PSISlider Strategy		Difference	
	b_v [m]	b_h [m]	b_v [m]	b_h [m]	Δb_v [m]	Δb_h [m]
11/17/2016	51.9235	4.1809	51.9235	4.1809	0	0
11/23/2016	57.7783	-113.6686	57.7783	-113.6686	0	0
11/29/2016	55.5019	51.5592	55.5019	51.5592	0	0
12/05/2016	67.0295	14.5740	67.0295	14.5740	0	0
12/11/2016	56.5211	-9.2225	56.5211	-9.2225	0	0
12/17/2016	65.2071	59.6492	65.2071	59.6492	0	0
12/23/2016	52.3344	-43.0037	52.3344	-43.0037	0	0
12/29/2016	61.9399	85.7096	61.9399	85.7096	0	0
01/04/2017	57.9828	-66.5863	57.9828	-66.5863	0	0
01/10/2017	56.1179	29.2224	56.1179	29.2224	0	0
01/16/2017	55.4488	-13.9656	55.4488	-13.9656	0	0
01/22/2017	49.4124	-90.1074	49.4124	-90.1074	0	0
01/28/2017	48.9099	60.2863	48.9099	60.2863	0	0
02/09/2017	45.3869	70.8973	45.3869	70.8973	0	0
02/21/2017	30.8028	-70.4519	30.8028	-70.4519	0	0
02/27/2017	24.8424	29.1412	24.8424	29.1412	0	0
03/05/2017	21.0552	-162.0064	21.0552	-162.0064	0	0
03/11/2017	10.4320	41.1241	10.4320	41.1241	0	0
03/17/2017	5.5802	-30.0193	5.5802	-30.0193	0	0
03/23/2017	-0.0272	-93.5874	-0.0272	-93.5874	0	0
03/29/2017	-8.0400	45.2587	-8.0400	45.2587	0	0
04/04/2017	-14.279	-51.0346	-14.2791	-51.0346	0	0
04/10/2017	-0.0356	52.4516	-0.0356	52.4516	0	0
04/16/2017	4.2720	-38.3496	4.2720	-38.3496	0	0
04/28/2017	0.2575	36.3931	0.2575	36.3931	0	0
05/04/2017	12.7199	-27.9786	12.7199	-27.9786	0	0
05/10/2017	6.0971	53.6427	6.0971	53.6427	0	0

Table A.1.: Horizontal and vertical baselines calculated with SNAP in a conventional PSI processing chain and the processing chain of the PSISlider strategy.

Colophon

This thesis was typeset with $\LaTeX\,2_\varepsilon$. It uses the *Clean Thesis* style developed by Ricardo Langner. The design of the *Clean Thesis* style is inspired by user guide documents from Apple Inc.

Download the *Clean Thesis* style at `http://cleanthesis.der-ric.de/`.